

Propagation and scattering of electromagnetic waves in low THz band in automotive radar applications



Shahrzad Minooe Sabery

A thesis submitted to the University of Birmingham

For the degree of

Doctor of Philosophy

School of Electronic, Electrical and System Engineering
College of Engineering and Physical Sciences
University of Birmingham

November 2021

UNIVERSITY OF
BIRMINGHAM

University of Birmingham Research Archive

e-theses repository

This unpublished thesis/dissertation is copyright of the author and/or third parties. The intellectual property rights of the author or third parties in respect of this work are as defined by The Copyright Designs and Patents Act 1988 or as modified by any successor legislation.

Any use made of information contained in this thesis/dissertation must be in accordance with that legislation and must be properly acknowledged. Further distribution or reproduction in any format is prohibited without the permission of the copyright holder.

To my amazing children

Jasmin & Zanyar

Declaration

I hereby declare that the work presented in this thesis, has not been submitted for any other degree or professional qualification, and that it is the result of my own independent work except where specifically indicated. Many of the theoretical and experimental ideas in this thesis came from discussion with my supervisors, Professor Marina Gashinova and Professor Peter Gardner and my co-supervisors, Dr Bystrov and Dr Norouzian.

Excerpts of this thesis have been published in the following peer-reviewed journal articles and international radar conference paper, as part of my PhD studying outcomes over the four years (2017-2021). All these papers have been submitted by myself as the corresponding authors together with the co-authors of these publications.

- **Sabery S**, Norouzian F, Gardner P, Hoare E, Cherniakov M, Gashinova M. Signal reduction by tree leaves in low THz automotive radar. In2018 48th European Microwave Conference (EuMC) 2018 Sep 23 (pp. 1445-1448). IEEE. (**Chapter 4**)
- **Sabery S**, Norouzian F, Gardner P, Bystrov A , Gashinova M. Signal reduction due to layer of water at low THz automotive radar. Paper has been accepted for 2021 European Microwave Conference (EuMC) (**Chapter 4**)
- **Sabery SM**, Bystrov A, Navarro-Cía M, Gardner P, Gashinova M. Study of Low Terahertz Radar Signal Backscattering for Surface Identification. Sensors. 2021 Jan;21(9):2954. (**Chapter 5**)
- **Sabery SM**, Bystrov A, Gardner P, Stroescu A, Gashinova M. Road Surface Classification Based on Radar Imaging Using Convolutional Neural Network. IEEE Sensors Journal. 2021 Jun 7. (**Chapter 6**)
- **Sabery SM**, Bystrov A, Gardner P, Gashinova M. Surface classification based on low terahertz radar imaging and deep neural network. In2020 21st International Radar Symposium (IRS) 2020 Oct 5 (pp. 24-27). IEEE. (**Chapter 6**)

Abstract

This thesis, firstly, due to the lack of knowledge in influence of harsh outdoor environment on the performance of the low-THz automotive sensors, the investigation has been done to demonstrate the performance of low-THz sensors in the presence of different radome contaminants (mud, oil, grit, etc.) and various weather conditions (rain, snow, fog, etc.) to prove the feasibility of using low-THz frequencies (100 GHz -1 THz) in automotive radar in uncontrolled environmental conditions.

Secondarily, this thesis reports and discuss the important and yet unsolved task on automotive surface recognition and shows the possibility of using Low THz radar for road surface classification by exploring the radar signal backscattering from surfaces with different roughness, and finally this thesis demonstrate the novel approach to surface classification based on the analysis of radar images obtained using the low THz imaging radar and demonstrate the advantage of low THz radar for surface discrimination for automotive sensing. The proposed experimental technique in combination with a convolutional neural network provides high surface classification accuracy.

Publications associated with this research

- Sabery SM, Bystrov A, Navarro-Cía M, Gardner P, Gashinova M. Study of Low Terahertz Radar Signal Backscattering for Surface Identification. *Sensors*. 2021 Jan;21(9):2954.
- Sabery SM, Bystrov A, Gardner P, Stroescu A, Gashinova M. Road Surface Classification Based on Radar Imaging Using Convolutional Neural Network. *IEEE Sensors Journal*. 2021 Jun 7.
- Sabery SM, Bystrov A, Gardner P, Gashinova M. Surface classification based on low terahertz radar imaging and deep neural network. In 2020 21st International Radar Symposium (IRS) 2020 Oct 5 (pp. 24-27). IEEE.
- Sabery S, Norouzian F, Gardner P, Hoare E, Cherniakov M, Gashinova M. Signal reduction by tree leaves in low-THz automotive radar. In 2018 48th European Microwave Conference (EuMC) 2018 Sep 23 (pp. 1445-1448). IEEE.
- Sabery S, Norouzian F, Gardner P, Bystrov A, Gashinova M. Signal reduction due to layer of water at low-THz automotive radar. Paper has been accepted for 2021 European Microwave Conference (EuMC)

Acknowledgements

I would like to extend my appreciation to the following people, who they have been supportive and extremely help full during my PhD.

Firstly, I would like to express my gratitude to my supervisors, Professor Marina Gashinova and Professor Peter Gardner. I hugely benefited from Marinna's knowledge and expertise and without Peter's guidance especially during pandemic, it would have been an impossible task to accomplish this PhD thesis.

I would like to extend my gratitude to my co-supervisors, Dr Fatemeh Norouzian and Dr Aleksandr Bystrov, for their motivation and providing invaluable advice and caring.

I am deeply grateful to Professor Mikhail Cherniakov, Dr Edward Horae, and Mr Alan Yates for all their support and assistance.

I would like to thank my fellow PhD students and research fellows in the MISL group for their support and friendship, Ana Stroescu, Muge Bekar, Ali Bekar, Yang Xiao, Anum Pirhani, Dr Emidio Merchetti, Dr Liam Daniel, Dr Dominic Phippen.

My amazing mother, Fereshteh, who has always been close to me and I am so thankful for her unconditional love, my father and my brothers.

My very precious children, Jasmin and Zanyar, who always give me motivation and strength to become better mom who they can be proud of. I have dedicated this thesis to them.

Last but not least, my beloved husband, for being patient and supportive during the past four years.

Table of contents

Declaration	iii
Abstract	iv
Publications associated with this research	v
Acknowledgements	vi
Table of contents	vii
List of figures	xii
List of tables	xvi
Abbreviations	xvii
Chapter 1: Introduction	1
1.1 Motivation	1
1.2 Thesis structure	12
Chapter 2: Literature review	14
2.1 Principles of radar system	14
2.1.1 Radar definition.....	14
2.1.2 Radar equation.....	17
2.1.3 Radar cross section	18
2.2 Radar waveform choices and signal processing.....	21
2.2.1 FMCW waveform	22
2.2.2 Stepped frequency waveform.....	26
2.3 Clutter.....	28
2.4 Radar signal propagation mechanism	30
2.4.1 Atmospheric attenuation.....	30
2.4.2 Reflection	32
2.4.3 Diffraction	35

Thesis title

Table of contents

2.5	Penetration depth	36
2.6	Millimetre-wave and THz sensing	37
2.6.1	Low THz radar.....	37
2.6.2	Low THz automotive radar	38
2.7	Artificial Neural Network.....	42
2.7.1	Activation function.....	45
2.7.2	Training the network.....	50
2.7.3	Loss function	50
2.7.4	Optimization algorithm	50
2.8	Convolutional neural network.....	51
2.8.1	Input layer	51
2.8.2	Convolutional layer	52
2.8.3	Pooling layer.....	53
2.8.4	Fully connected layer	53
Chapter 3: Methodology		54
3.1	Overview.....	54
3.2	Radar system	54
3.2.1	SFR VNA system	55
3.2.2	FMCW radar	62
3.3	Radome contamination.....	65
3.3.1	Measurement methodology	65
3.3.2	Theoretical model	68
3.4	Backscattering of Radar Signal from Rough Surface	70
3.4.1	Normalized RCS.....	70
3.5	High resolution imaging radar.....	72
3.6	Summary.....	77

Chapter 4: Signal reduction due to radome contaminant.....	78
4.1 Overview.....	78
4.2 Signal Reduction by tree leaves in Low THz Automotive Radar.....	80
4.2.1 Overview	80
4.2.2 Introduction	81
4.2.3 Theoretical model	83
4.2.4 Methodology.....	85
4.2.5 Measurement.....	86
4.2.6 Result and discussion	88
4.2.7 Conclusions	91
4.3 Signal reduction due to a layer of water at low THz frequency for automotive radar applications	92
4.3.1 Overview	92
4.3.2 Introduction	92
4.3.3 Theoretical model	94
4.3.4 Measurement methodology	98
4.3.5 Result and discussion	102
4.3.6 Conclusion	109
4.4 Attenuation through sand, oil, ice in low THz radome	110
4.5 Summary.....	113
Chapter 5: Low terahertz radar signal backscattering for surface identification.....	114
5.1 Overview.....	114
5.2 Introduction.....	115
5.3 Backscattering of Radar Signal from Rough Surface	117
5.4 Experimental Methodology.....	121
5.4.1 Empirical Scattering Model.....	121

Thesis title

Table of contents

5.4.2	Relative Permittivity of Surface Material.....	123
5.5	Measurement setup	127
5.6	Results and discussion	131
5.6.1	Normalized RCS in Vertical Polarization	132
5.6.2	Measured and Calculated Normalized RCS.....	137
5.6.3	Discussion.....	141
5.7	Conclusion	143
5.8	Summary.....	145
Chapter 6: Surface classification based on low THz radar imaging using convolutional neural network.....		146
6.1	Overview.....	146
6.2	Introduction.....	147
6.3	Surface classification based on Low Terahertz Radar Imaging and Convolutional Neural Network	150
6.3.1	The experimental setup	150
6.3.2	Experimental results and Analysis	154
6.3.3	Classification using CNN.....	161
6.3.4	Network Architecture	163
6.3.5	Sand paper classification result	165
6.4	Road Surface Classification Based on Radar Imaging Using Convolutional Neural Network.....	167
6.4.1	Methodology of Data Collection	167
6.4.2	Experimental results and analysis.....	171
6.4.3	Road surface classification with CNN.....	177
6.4.4	Road surface classification result.....	181
6.5	Summary and conclusion	183
Chapter 7: Conclusion and Future Work		184

Thesis title

Table of contents

7.1	Summary and Conclusion	184
7.2	Future plan	187
	References	188

List of figures

Figure 1.1: Automotive remote sensors: yellow-green – optical or LIDAR, blue – microwave (radar), orange - ultrasonic[5]	4
Figure 1.2: Sensing challenges[26]	6
Figure 1.3: The terahertz frequency band with capabilities which is a trade-off between microwaves and infrared and optical frequencies [32]	8
Figure 1.4: Atmospheric attenuation windows[38]	9
Figure 2.1: Radar system	15
Figure 2.2: Monostatic (a), bistatic (b) and multistatic (c) radar configuration	16
Figure 2.3: The normalized RCS PEC sphere[48]	21
Figure 2.4: frequency vs time relation of linear FMCW transmit and receive chirp	23
Figure 2.5: Stepped frequency waveform	27
Figure 2.6: volume clutter illuminated cell size in monostatic radar [57]	29
Figure 2.7: Clutter illuminated patch size in monostatic radar [57]	30
Figure 2.8: Specific attenuation due to atmospheric gases[58]	31
Figure 2.9: Ray representation of oblique incidence	33
Figure 2.10: Reflection from smooth, moderately rough, and very rough surface	33
Figure 2.11: Autounonomous Vehicle sensors	39
Figure 2.12: Example imaged scene, (a) video ground truth, (b) 150 GHz scanned radar image. Letters highlight image features: F—foliage, P—pedestrian, V—vehicle, O—obstruction (branch), T—track, G—gulley (water filled)—image normalised to image maxima [36]	41
Figure 2.13: Arthitecture of ANN	42
Figure 2.14: McCulloch and Pitts (MP) model of neuron	43
Figure 2.15: Activation function (a) ReLU, (b) Leaky ReLU[83]	46
Figure 2.16: Sigmoid activation function curve [84]	47
Figure 2.17: Tanh activation function curve [87]	49
Figure 2.18: Convolution operation	52
Figure 3.1: portable VNA and frequency converters	56
Figure 3.2: Schematic diagram of 300 GHz VNA and frequency convertors	57
Figure 3.3: Antennas (a) 300 GHz, (b) 670 GHz	59
Figure 3.4: Photo of PNA SFR radar system	59

Thesis title

List of figures

Figure 3.5: photo of VNA with up/down convertors. 61

Figure 3.6: Antennas: (a) 79 GHz, (b) 150 GHz, (c) 300 GHz, and (d) 670 GHz. 61

Figure 3.7: ELVA-1 300 GHz horn antennas 62

Figure 3.8: Summarized outline of 79 GHz FMCW radar 63

Figure 3.9: Photo of 79 GHz FMCW radar [98] 63

Figure 3.10: Experimental setup configuration (a) general view (b) actual system setup (c) antenna setup 67

Figure 3.11: Three-layer structure used to model the transmissivity through uniform layer of leaves 68

Figure 3.12: Single beam monostatic configuration for imaging radar. H is the antenna elevation; θ_E and θ_H are beamwidths of antenna pattern in E-plane and H-plane accordingly. R is the distance to the center of the footprint, defined by beam axis direction; R_c is the linear angular range at the distance R . [35]..... 73

Figure 3.13: Vehicle scanning the illuminated area in the front of the antennas mounted on the vehicle. 74

Figure 3.14: Curved image map from rotating scanning imaging antennas(a), camera image(b), 79GHz radar image (c) 75

Figure 4.1: signal reduction medium for automotive radar 78

Figure 4.2: Coffea arabica leaf (a) Transmitted intensity at 300 GHz (b) and volumetric water content reduction [106]..... 82

Figure 4.3: Evaluation of leaf water content based on time. 85

Figure 4.4: Photo of detached leaves of (a) Willow (b) Lauren and (c) Birch 85

Figure 4.5: Measuremet setup configuration 86

Figure 4.6: Measured transmissivity through three leaves respect to volume water content reduction 88

Figure 4.7: Calculated and measured result of transmissivity through leaves respect to WCR, using effective permittivity of leaves [106]..... 89

Figure 4.8: Measured and calculated results of transmissivity through equivalent uniform water layer, using water permittivity 90

Figure 4.9: Calculated transmissivity of pure water as a function of water thickness at 24 GHz, 77 GHz, 150 GHz, and 300 GHz at 23 °C. The error bars correspond to the uncertainty in the double Debye model parameters in equation (4. 8). [109] 95

Thesis title

List of figures

Figure 4.10: Error between measured and theoretical transmissivity for different values of pure water permittivity at 150 GHz [109] 96

Figure 4.11: Error between measured and theoretical transmissivity for different values of pure water permittivity at (a)300 GHz (b) 670 GHz..... 97

Figure 4.12: (a) Sample with specific illuminating area footprint (blue circle), (b)measurement setup 98

Figure 4.13: System schematic..... 100

Figure 4.14: Measured transmissivity through pure water, actual seawater, and water of three different salinities as a function of water thickness at 23 °C (a) at 300 GHz and (b) at 670 GHz..... 103

Figure 4.15: Measured transmissivity through 0.3 mm layer of pure water, sea water and water with 3.5% salinity versus frequency 104

Figure 4.16: Calculated and measured transmissivity through pure water at (a) 300 GHz and (b) 670 GHz, and water with salinity of 3.5% at (c) 300 GHz and (d) 670 GHz as a function of uniform thickness at 23 °C..... 108

Figure 5.1: Reflection from smooth, moderately rough, and very rough surface..... 117

Figure 5.2: Roughness characterization of road surface as a function of incident angle and radar frequency[141] 118

Figure 5.3: Automotive sensing scenario: H —Radar height over ground, α —Elevation beam width, R_0 —Ground range, θ —Incident angle, γ —Grazing angle. 120

Figure 5.4: TDS system measurement set up 124

Figure 5.5:Experimental setup configuration (a) schematic setup (b) actual setup. ... 127

Figure 5.6: The normalized RCS σ_{VV}^0 : (a) 79 GHz, (b) 150 GHz, (c) 300 GHz, and (d) 670 GHz. 135

Figure 5.7: normalized RCS σ_{VV}^0 as a function of electromagnetic roughness at a grazing angle of 10° 136

Figure 5.8: Measured and calculated normalized RCS: (a) grit 40 at 150 GHz, (b) grit 40 at 670 GHz, (c) grit 240 at 150 GHz, and (d) grit 240 at 670 GHz. 139

Figure 6.1: Experimental setup (a) system schematic (b) actual system configuration 151

Figure 6.2: 150 GHz radar images of sandpaper with grit (a) 40 and (b) 80, the rectangle shows the position of the sample 155

Thesis title

List of figures

Figure 6.3: 300 GHz radar images of sandpaper with grit (a) 40, (b) 80, (c) 120, (d) 240, and (e) 320. the rectangle shows the position of the sample 158

Figure 6.4: Backscattering coefficient for vertically polarized signal, lines represent the theoretically calculated curves, circles indicate the experimentally measured values 160

Figure 6.5: CNN schematic architecture for sand paper classification 163

Figure 6.6: Experimental setup configuration 169

Figure 6.7: Photos and radar maps of asphalt road (a),(b), countryside road (c),(d), and muddy road (e),(f). 174

Figure 6.8: Riverside image scene: camera image (a), radar map (b); the white, red and blue boxes denotes to area of river, gravel and rocky road 175

Figure 6.9: CNN simplified schematic structure for road surface classification task ... 179

List of tables

Table 1.1: SAE J3016 levels of driving automation [3].....	3
Table 2.1: Existing automotive radar characteristics [74]	39
Table 3.1: 300 GHz SFR radar parameter	57
Table 3.2: parameters of the 300 GHz and 670 GHz SFR radar	60
Table 3.3: 79 GHz FMCW radar specification	64
Table 4.1: Parameters of the measurement system.....	101
Table 4.2: Calculated permittivity of pure water and saline solutions at 300 GHz and 670 GHz	105
Table 5.1. Measured sandpaper relative permittivity	126
Table 5.2: Parameters of the measurement system.....	128
Table 5.3: Sandpaper Parameters.....	129
Table 5.4. Cross-polarized backscatter ratio q , dB	140
Table 6.1: Parameters of the measurement system.....	152
Table 6.2: Sandpaper Parameters.....	153
Table 6.3: Road Surfaces Cropped Images, 89×93 pixel	162
Table 6.4: Confusion Matrix of the Classification Results.....	166
Table 6.5: Parameters of the Measurement System	170
Table 6.6: road surface parameters	176
Table 6.7: Road Surfaces Cropped Images, 100×65 pixel	178
Table 6.8: Confusion Matrix of the Classification Results.....	182

Abbreviations

ACC	Adaptive Cruise Control
ADC	Analogue to Digital Converter
AI	Artificial Intelligence
AV	Autonomous Vehicle
B	Bandwidth
CPI	Coherent Processing Interval
CTA	Cross Traffic Alert
CW	Continuous Waveform
CNN	Convolutional Neural Networks
EM	Electromagnetic Magnetic
EMW	Electromagnetic Magnetic Wave
ETSI	European Telecommunications Standards Institute
FCC	Federal Communications Commission
FM	Frequency Modulation
FMCW	Frequency Modulation Continuous Waveform
FT	Fourier Transform
HRR	High range resolution
IF BW	Intermediate Frequency Bandwidth
IFFT	Inverse Fast Fourier Transform
LIDAR	Light Detection and Ranging
LLL	Landau, Lifshitz, Looyenga
LPF	Low Pass Filter
L LRR	Long Range Radar
MISL	Microwave Integrated Systems Laboratory
MLP	Multilayer Perceptron
MRR	Medium Range Radar
PEC	Perfect Electric Conductor
PM	Phase Modulation
PNA	Programmable Network Analyser
RADAR	Radio Detection and Ranging

RCS	Radar Cross Section
SAE	Society of Automotive Engineers
SFW	Stepped Frequency Waveform
SGD	Stochastic Gradient Descent
SGDM	Stochastic Gradient Descent with Momentum
SRI	Sweep Repetition Interval
SRR	Short Range Radar
Surface ID	Surface Identification
THz	TeraHertz
V VLF	Very Low Frequency
VNA	Vector Network Analyzers

Chapter 1: Introduction

1.1 Motivation

The last few years have been favorable for the autonomous vehicle (AV) technology. Major companies are considering AV as a solution to reduce road accidents and fatalities. A study on identifying the cause of road crashes in Europe shows the main cause of these accidents to be human error [1], which leads to death of 49 road deaths per minutes and totally about 25000 road death per a year in Europe [2]. Even in the case of non-fatal crashes, the economic costs are undeniably high, while with using the vehicles equipped with autonomous driving technologies, the number of accidents could significantly decrease which emphasize AV importance and its potential to overcome the human error and improve safety to road users. Furthermore, AV can increasing the road capacity, and as a result reduce the pollution, improve access to mobility and guarantee new jobs for the automotive and electronic sectors.

An integral element of prospective AV technology is a surface identification (Surface ID) system. This system should remotely classify the road surfaces and alert driver or AV computer about potential hazardous road surfaces, such as ice (especially “black ice”), standing water or changes in road pavement, which will allow the vehicle to remain safely under control as it transitions from one surface to another, reducing costly damage, avoiding injury and saving lives. Automatically adapting vehicle speed to surface conditions is an essential step in providing autonomous driving. In four-wheel drive vehicles, Surface ID system will enable two or four-wheel drive to be selected as appropriate, therefore helping to reduce CO2 emissions.

Spanning from fully manual to fully autonomous vehicles, there are six level of AV classification, which were defined in 2014 by Society of Automotive Engineers (SAE) [3] and named SAE J3016. This classification is based on the amount of driver involvement in the act of driving. The 6-level automation from level zero to level five is reproduced in Table 1.1 [3]. Level zero correlates to having no automation and instead complete human control of the vehicle. Levels one and two the driver needs to drive and must constantly supervise the driver support features while in level 3 to 5 the driver not driving when automated driving features are engaged. Level 3 automated vehicles are expected to enter the world by 2021, according to public claims by such automotive manufacturers as Ford, Honda, Toyota, Volvo, BMW, and Mercedes-Benz and others

Chapter 1: Introduction

which advertised to have a level 3 cars available for consumer purchase subject to their national regulations and automotive law [4]. Currently, the market remains dominated by partially autonomous level 2 vehicles.

Table 1.1: SAE J3016 levels of driving automation [3]

SAE Level	Name	Narrative Description	Execution of Steering and Acceleration/Deceleration	Monitoring of Driving Environment	Fallback Performance of Dynamic Driving Task	System Capability (Driving Modes)
Human driver monitors the driving environment						
0	No Automation	The full-time performance by the human driver of all aspects of the dynamic driving task, even when enhanced by warning or intervention systems	Human driver	Human driver	Human driver	N/A
1	Driver Assistance	The driving mode-specific execution by a driver assistance system of either steering or acceleration/deceleration using information about the driving environment and with the expectation that the human driver performs all remaining aspects of the dynamic driving task	Human driver and system	Human driver	Human driver	Some driving modes
2	Partial Automation	The driving mode-specific execution by one of more driver assistance systems of both steering and acceleration/deceleration using information about the driving environment and with the expectation that the human driver performs all remaining aspects of the dynamic driving task	System	Human driver	Human driver	Some driving modes
Automated driving system monitors the driving environment						
3	Conditional Automation	The driving mode-specific performance by an automated driving system of all aspects of the dynamic driving task with the expectation that the human driver will respond appropriately to a request to intervene	System	System	Human driver	Some driving modes
4	High Automation	The driving mode-specific performance by an automated driving system of all aspects of the dynamic driving task even if a human driver does not respond appropriately to a request to intervene	System	System	System	Some driving modes
5	Full Automation	The full-time performance by an automated driving system of all aspects of the dynamic driving task under all roadway and environmental conditions that can be managed by a human driver	System	System	System	All driving modes

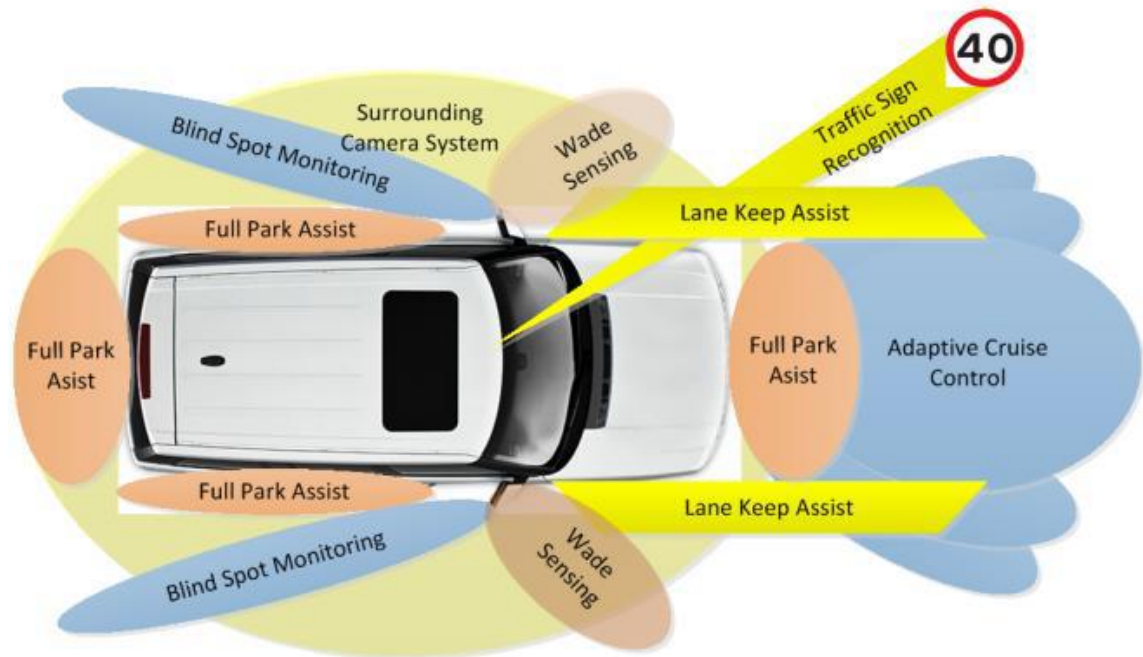


Figure 1.1: Automotive remote sensors: yellow-green – optical or LIDAR, blue – microwave (radar), orange - ultrasonic[5]

Different sensor technologies are used for AV (see Figure 1. 1) such as optic cameras [6-10], light detection and ranging (LIDAR) [11,12], sonar [13]-[5], and radar [14-22]. LiDAR use laser and because of high resolution has the advantage of detecting small objects, accurate depth perception, which allows LiDAR to measure the distance to an object within a few centimetres, up to 100 metres away. Optical cameras are cheap and lightweight and they produce an easily understandable colour image of the scene. In addition, stereo cameras provide depth map where distance to the object can be evaluated by disparity of cameras. However, severe weather conditions negatively affect the performance of LIDAR and optical cameras. Furthermore, optical cameras require adequate visible radiation levels and have poor performance in limited lighting conditions. The advantages of sonar are the small size of a transceiver, simplicity and cheapness combined with high range resolution. The limitation of sonar is related to the fact that being a mechanical wave the acoustic signal is affected by volumetric particulates in the non-uniform media (spray, rain), or exhaust, and wind, leading to significant inaccuracies of the results. Therefore, the sonar is mostly used in parking sensors at distances up to 6-8 metres. To provide partial or full autonomy, automotive sensors should be operational under all weather conditions, including rain, snow and fog, and at any time of the day. Unlike LIDAR, optical sensors and sonar, radar sensors

have the advantage of robust operation in harsh weather and lighting conditions [23-25]. This is, due to the ability of electromagnetic (EM) waves at frequencies below the infra-red band to propagate through optically non-transparent media such as fog, smoke and spray, with much lower loss. Figure 1. 2 shows acuity on Bystrove's [26] study for comparison of the remote sensor technologies in various lighting and weather condition.

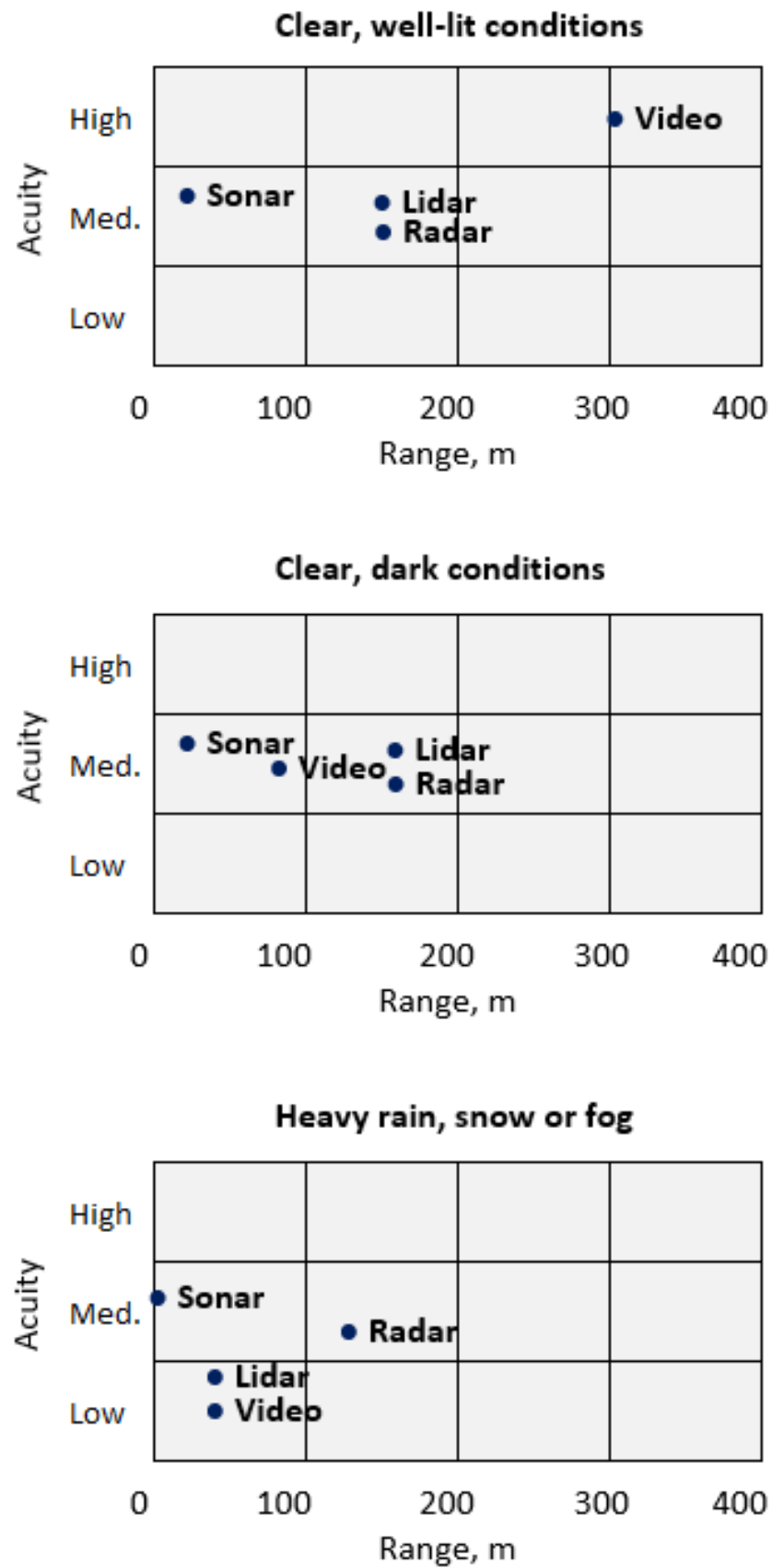


Figure 1.2: Sensing challenges[26]

Furthermore radar offers the following advantages in comparison to other AV sensors technology:

- Direct measurements of range and speed.
- The sensors can be mounted behind radar transparent materials (e.g. plastic vehicle bumper) with low reduction of sensitivity if needed for design aspects and environmental protection.
- Radar can detect multiple objects simultaneously.
- Radar can easily differentiate between stationary and moving objects

Currently, one of the trends in the development of automotive radars is to increase the operating frequency from 24 GHz to 79 GHz and higher. According to European Telecommunications Standards Institute (ETSI)[27] and the Federal Communications Commission (FCC)[28] Regulations , Mid-range radar operating at 24 GHz has a maximum bandwidth of 200 MHz. Short range 79 GHz radar has wider operational bandwidth of 4 GHz which results in much higher range resolution and more detailed road surface imaging. Antenna size reduction is another key aspect for automotive applications due to already dense in-vehicle packaging, and if achieved, this will result in lower integration costs. Therefore, there is a need for new sensing systems that fulfil the entire range of requirements for LIDAR, radar, and camera systems. Low Terahertz (low THz) range refers to the spectrum range from 0.1-1 THz which occupies the region between the upper end of the radio spectrum and the lower end of the Infra-Red spectrum (see Figure 1.3). This frequency range has benefits of significantly higher range resolution because of wider bandwidths available [29,30], which lead to more image-like scene characterization by such a radar. At the same time, unlike LIDAR and optical sensors, low THz sensors have the advantage of robust operation in harsh weather and lighting conditions [23-25]. Importantly, operation at higher frequencies leads to more compact electronics components, in particular antennas, thereby responding to challenges of more and more dense packaging of multiple sensors and processing systems for modern and future cars. Until recently, the high cost was an obstacle to the widespread implementation of low THz radar systems, but with the development of appropriate technologies [31], it has been steadily decreasing.

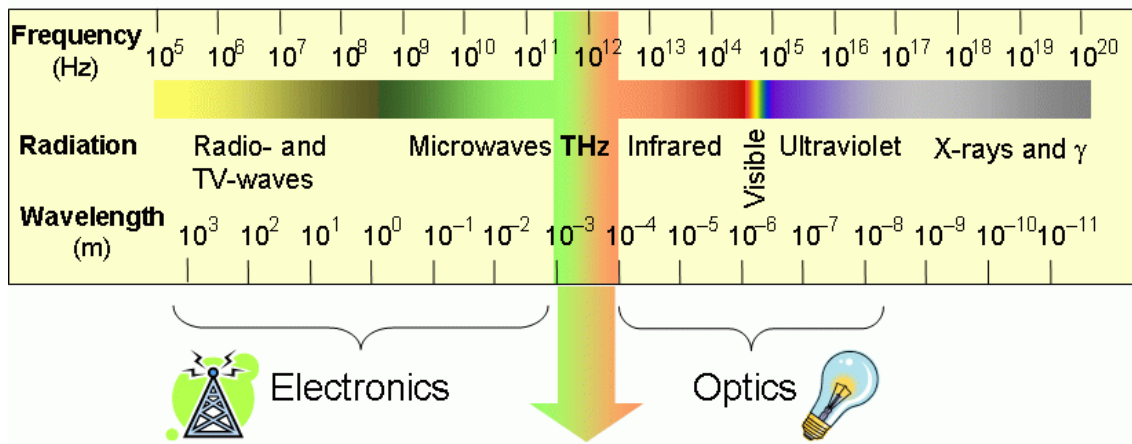


Figure 1.3: The terahertz frequency band with capabilities which is a trade-off between microwaves and infrared and optical frequencies [32]

Low THz has found for a wide range of indoor application such as standoff personnel screening(at 675 GHz)[33] , material characterization [34] and, importantly, low THz radar has been proposed as a candidate to provide high-resolution imagery for future autonomy [35-37]. High influence of atmospheric conditions (absorption by atmospheric gases, and also absorption and scattering by atmospheric aerosols) on signal propagation at higher frequencies, is recognized as the major limitation of employing low THz frequencies in outdoor applications. Thus, the influence of the harsh outdoor environment on the performance of the low THz sensors remains largely unknown and became an objective for Microwave Integrated Systems Laboratory (MISL) group in the University of Birmingham since 2016.

The well-known graph of atmospheric attenuation (absorption by atmospheric gases) versus frequency (between 100 GHz and 1 THz) shown in Figure 1.4 [38], which shows a region of local minimum attenuation between absorption peaks at frequencies referred to as “atmospheric windows” . The chosen low THz frequency for this thesis and the currently used automotive radar frequency both lie in such atmospheric windows. As can be seen from Figure 1.4 the atmospheric attenuation, primarily due to water vapour absorption, is significant in many spectral regions in the low THz band, especially in adverse weather conditions [24,39]. However, there are transmission windows around 340 GHz, 400 GHz, and 650 GHz, where atmospheric loss in clear air does not exceed 10 dB/km, 20 dB/km, and 60 dB/km, respectively. Therefore, for the automotive radar operational range of up to 100 meters, atmospheric loss will not

exceed 10 dB and makes a relatively small contribution to the power budget needed to guarantee the system efficiency [40].

As mentioned above there is a lack of knowledge on the influence of harsh outdoor environments on the performance of the low THz sensors, so **the first objective of this thesis is investigating the performance of low THz sensors in the presence of different radome contaminants (mud, oil, grit, etc.) and various weather conditions (rain, snow, fog, etc.) to prove the feasibility of using low THz frequencies in automotive radar in uncontrolled environmental conditions.**

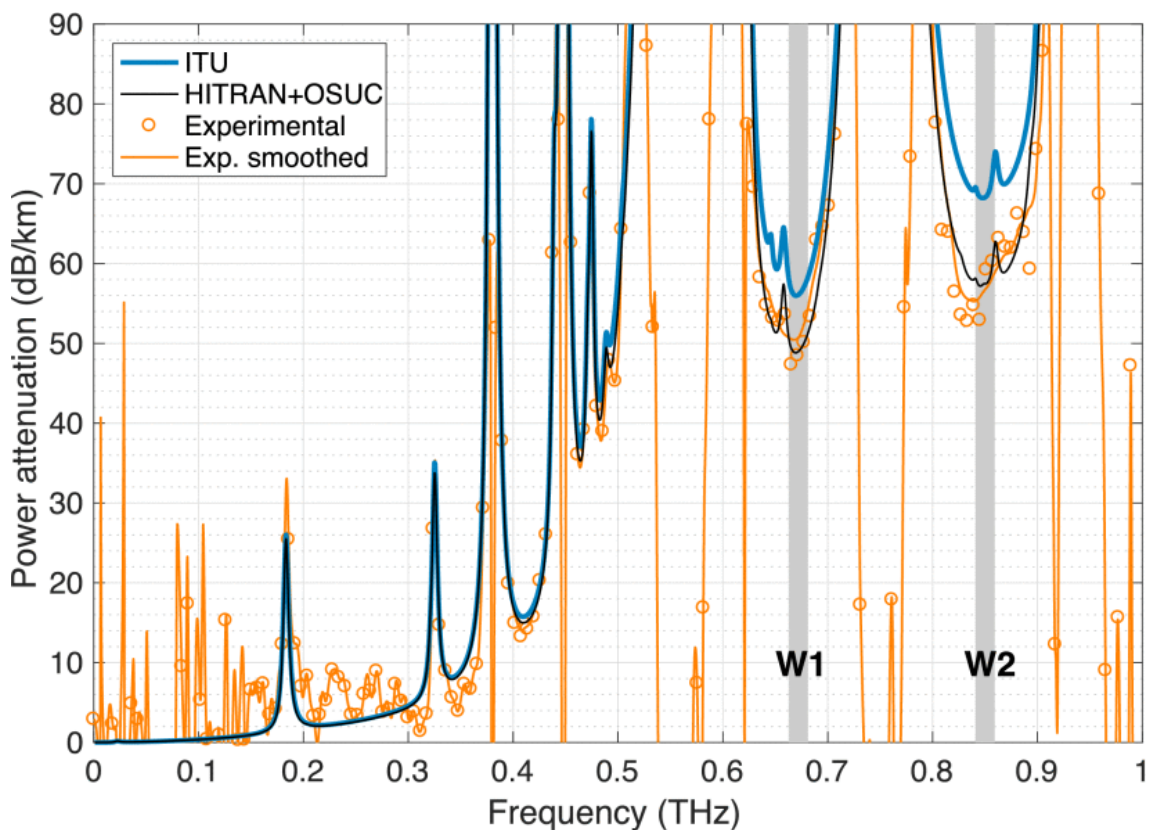


Figure 1.4: Atmospheric attenuation windows[38]

To overcome the challenge of remote road surface classification which still has remained an unsolved task in the implementation of AV, the low THz radar could be considered due to its wide operating bandwidth which is very sensitive to surface roughness and capable to provide high image resolution. This will allow high resolution road surface images to be obtained, to recognize different type of surfaces.

It is significantly important for automotive radar designers to consider the signal backscattering from the road surface while considering increase in frequency. Based on Fraunhofer criterion the surface is considered rough if the surface rms height h (root

mean square average of the heights above or below a mean reference line) satisfies the inequality $h \geq \lambda / (32 \cos \theta)$, where θ is the angle of incidence relative to the surface normal and λ is the signal wavelength. From the Fraunhofer criterion, it follows that with an increase in the frequency of the radar, its ability to distinguish surfaces improves. Consider, for example, rough asphalt with $h=1$ mm and smooth asphalt with $h=0.3$ mm. For a radar with a frequency of 79 GHz (wavelength of 3.8 mm) with an incidence angle of over 70° , both of these surfaces will be smooth and indistinguishable. At the same time, a radar with a frequency of 300 GHz (wavelength of 1 mm) will be able to distinguish them even at an incidence angle of 85° . Let us assume that the radar is mounted at a height of 1 m above the road. An angle of 70° corresponds to only 3 m, and an angle of 85° correspond to almost 12 m, so **the second objective of this PhD research is the investigation of the possibility of using Low THz radar for road surface classification by exploring the scattering of radar signal from surfaces with different roughness..** Initially, new improved method for measuring backscattering coefficient of rough surfaces has been proposed to estimate the normalized radar cross-section (RCS) of surfaces of different roughness as a function of radar and configuration, such as polarization, grazing angle, surface roughness parameters and dielectric constant, which will play an important role in understanding the complex problem of signal reflection from actual road surfaces.

The AV vehicle for having full or partial autonomy require to sense the vehicle's surrounding environment based on the received images from its sensors, in all weather and lighting condition. AS mentioned previously unlike LIDAR and optical camera low THz radar has advantageous of working in all weather and lighting condition so **the third objective of this PhD thesis is to investigate the performance of low THz imaging radar in the surface ID task.**

As Convolutional Neural Networks (CNNs) have been successfully applied to different classification tasks such as image analysis in medicine image segmentation, also with applications in the field of automated driving (like object detection), it seems promising to use a CNN-based approach for surface classification task.

In this PhD study a new approach was explored to surface classification based on the analysis of different images with various roughness, obtained using the Low Terahertz radar in the laboratory and the proposed experimental techniques in combination of

Chapter 1: Introduction

CNN have been used for surface classification task, and these results have led me to the final step of this PhD research which classifies actual road surfaces (asphalt, gravel, mud...) based on the actual road scene collected during outdoor trials and again used CNN for classification task

1.2 Thesis structure

- Chapter 2 describes a radar definition and basic radar operation also provide in details the background for the topics covered in the later chapters such as electromagnetic wave (EWM) propagation and scattering mechanism , and the concepts of radar cross section, clutter, penetration depth, radar waveform choices and signal processing, millimetre wave and THz sensing, radar imaging and neural network classification.
- Chapter 3 presented the methodology utilised in the experimentation and to analyse the data collected to produce significant results, which can be used for the design of low THz radars for future autonomous vehicles. The low THz radar systems which was used for this PhD research to collect the data for experimental purpose described and characterized in this chapter.
- Chapter 4 describe and characterized the signal attenuation through contaminant accumulate radome of automotive sensor in the range of low THz radar. The study of signal attenuation by tree leaves at 300 GHz radar as well as the results on signal attenuation by different water in low THz automotive radar have been presented in this chapter. Furthermore, the summary of results of attenuation of low THz signals due to radome contamination which has been done by MISL group are shown and discussed.
- Chapter 5 explore the scattering of signals within mm- and low Terahertz frequency range, represented by frequencies of 79 GHz, 150 GHz, 300 GHz, and 670 GHz, from surfaces with different roughness to demonstrate advantages of low THz radar for surface discrimination for automotive sensing.

Chapter 1: Introduction

- Chapter 6 shows surface classification based on the analysis of the radar image of the sand paper with different roughness which is obtained using the Low Terahertz radar at two frequencies of 150 GHz and 300 GHz. the convolutional neural network has been used in the classification of sandpaper with different roughness (grit). In next stage an approach has been considered to surface classification based on the analysis of the 79 GHz imaging radar data. The six type of actual road with different roughness has been considered and the gained 79 GHz roads radar images has been classified with convolutional neural network.
- Chapter 7 conclusions are drawn and potential further research topics are discussed.

Chapter 2: Literature review

2.1 Principles of radar system

2.1.1 Radar definition

The origin of radio (electromagnetic) wave detection dates back to the last decades of the 19th century. The German physicist Heinrich Hertz demonstrated that the radio waves could be reflected by metallic objects and dielectric material [41] and this investigation became a basis for target detection which was issued as a patent for “an obstacle detector and ship navigation” by German engineer Christian Huelsmeyer in 1904. He invented the device called Telemobiloscope which was able to detect the presence of distant objects by using radio waves [42]. The radar (Radio Detection and Ranging), as known today, was developed during the Second World War as an ideal technique for detecting military bomber aircrafts. The two purpose of such radars were detection and estimation of the location of objects remotely. However modern radar is being developed to enable target identification and classification, and even to produce images of objects. For example radar is now used to detect aircraft, ships, spacecraft, guided missiles, motor vehicles, and many practical applications are developed using radar, including medical imaging, security, weather forecasting, astronomy, navigation and more recently automotive radar.

The principle of radar system as can be seen in Figure 2. 1, is that the transmitter generate the Electromagnetic Magnetic (EM) signal and routed to the antenna via the duplexer (a device that permits both transmission and reception of EM waves with a single antenna). The antenna acts as a transducer to couple the EM into the surrounding area. Generally, the radar antenna will form a beam of EM energy by concentrating the propagating EM wave in a given direction. Thus, the beam can be designed to achieve desired angular coordinates by effectively pointing the antenna in the direction through a combination of mechanical and electrical means [43]. Only part of transmitted signal is intercepted by the target which is located within the antenna beam and is reradiated in all directions. The receiving antenna collects the returned energy and delivers it to the receiver via duplexer. The receiver amplifies the weak received signals and processes them in order to detect the presence of targets and to extract their locations (ranges) and relative velocities and to gather other information about the targets according to the radar application [41]. The distance to the target, R (range) is determined by

measuring the time T_R required by the transmitted radar signal to reach to the target and return, and is shown as a relation of

$$R = \frac{cT_R}{2} \quad (2.1)$$

where $c = 3 \times 10^8 \text{ m/s}$ is the speed of electromagnetic radiation.

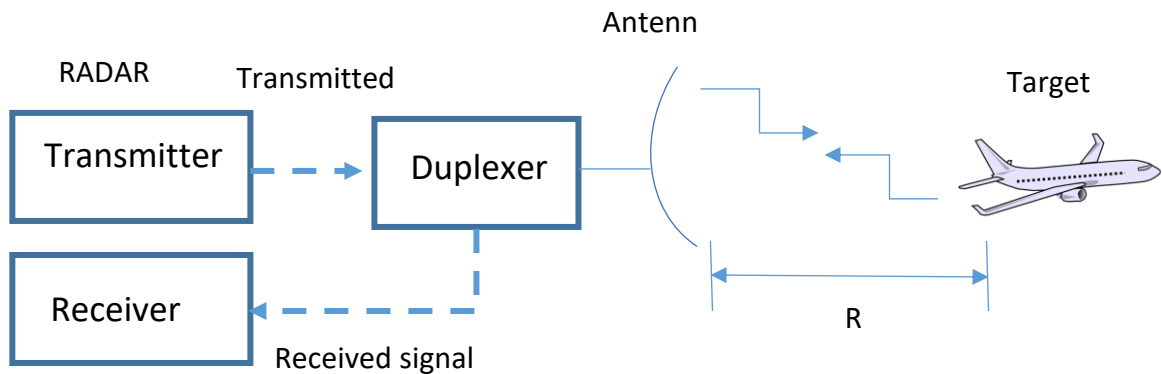


Figure 2.1: Radar system

It should be noted that the radar is the only type of sensor or device which is able to measure the range to the remote target in adverse weather (fog, rain, snow,) and poor lighting condition (day and night).

Radar systems can be classified in four different configurations based on its transmitter and receiver topology: monostatic, quasi-monostatic bistatic and multistatic.

- Monostatic radar: which is the most common type of the radar and exploits the backscattering from target. The transmitter and receiver are collocated as viewed from target. As the same antenna is used to transmit and receive the signal, a duplexer is needed to separate the transmit chain from receive chain and vice versa.
- Quasi-monostatic radar: the transmit and receive antennas are slightly separated but still appear to be at the same location as viewed from the target.
- Bistatic radar: A radar configuration having transmitter and receiver separated and located in different places, as shown in Figure 2. 2(b).

- Multistatic radar: Figure 2.2(c) shows the multistatic radar which consist one or more transmitter and more than one receiver.

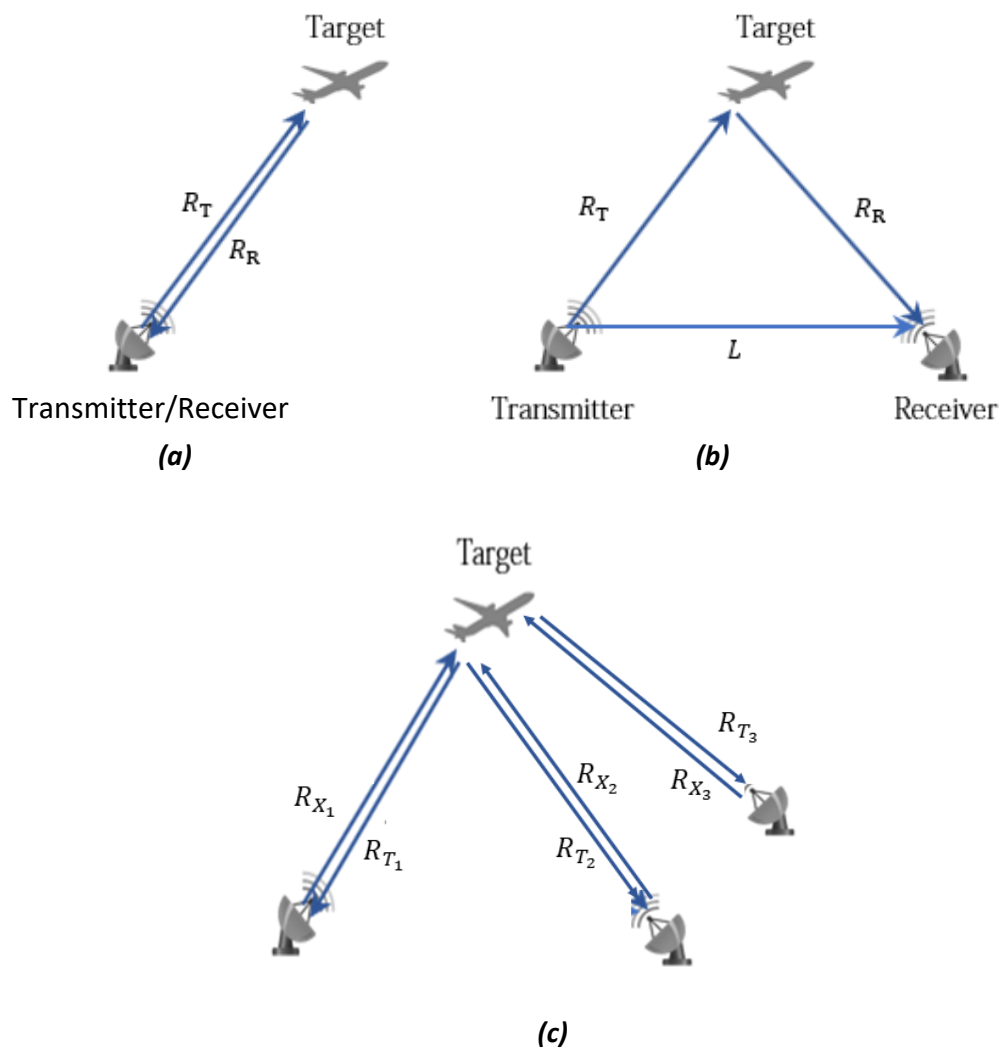


Figure 2.2: Monostatic (a), bistatic (b) and multistatic (c) radar configuration

2.1.2 Radar equation

The radar equation is a very useful mathematical expression that determines the radar performance and it is a necessary tool for radar system designers. It encompasses factors related to detect a target, transmitter, receiver, antenna and environment [44].

If the radar radiating power is denoted by P_t , and if G is antenna gain (we consider that transmitting and receiving antennas have the same gain) then the power density P_D at the distance R from the radar is [44]

$$P_D = \frac{P_t G}{4\pi R^2} \quad (2.2)$$

The measure of the amount of incident power intercepted by the target and radiated back in the direction of the radar is denoted as the radar cross section, so the reflected power density at the radar system is

$$P_0 = \frac{P_t G \sigma}{(4\pi)^2 R^4} \quad (2.3)$$

The amount of this reflected power received by the radar is found using the antenna effective area A_e which can be expressed as

$$A_e = \frac{G \lambda^2}{4\pi} \quad (2.4)$$

So by combining (2.3) and (2.4) the mean power received by the radar is

$$P_r = \frac{P_t G^2 \lambda^2 \sigma}{(4\pi)^3 R^4} \quad (2.5)$$

To have a more accurate and realistic model of radar performance, it is necessary to consider some radar disturbance such as the propagation medium and path loss, atmospheric noise, thermal noise introduced within radar, system losses (non-ideal component) and signal processing losses. Therefore the equation (2.5) should be multiplied for a factor $L < 1$ which includes all the mentioned losses.

The total noise at the output of the receiver N may be considered to be equal to thermal –noise which is unavoidable noise and generated by the thermal agitation of conduction electrons multiplied by a factor called the receiver noise figure F_n [44].

$$N = kTBF_n \quad (2. 6)$$

where k =Boltzmann's constant= $1.38 \times 10^{-23} J/deg$, T is temperature and generally assumed to be 290 Kelvin(K) and B is receiver bandwidth .

We can now compare the received power with the noise power which can be expressed in terms of signal to noise ratio (SNR) and can be written as

$$SNR = \frac{P_r}{N} = \frac{P_t G^2 \lambda^2 \sigma}{(4\pi)^3 R^4 kTBF_n} L \quad (2. 7)$$

From (2. 7) the maximum detection range R_{max} of a given radar can be obtained as

$$R_{max} = \left(\frac{P_t G^2 \lambda^2 \sigma}{(4\pi)^3 (SNR)_{min} kTBF_n} L \right)^{1/4} \quad (2. 8)$$

where SNR_{min} is the minimum value of SNR required to achieve the desired radar per.

2.1.3 Radar cross section

The quantification of targets detection performance and maximum detection range, is extremely important in radar applications. This requires the knowledge of the reflectivity of objects, which is characterized by Radar Cross Section (RCS). RCS is a measure of the proportion of the scattered power by target which is radiated towards the receiver [44,45] . There are a number of different factors that determine the RCS of an objects which include: the target material, the size of the target compared to the wavelength of the illuminating radar signal, frequencies, the absolute size of the target, the incident and reflected angle and the polarization of the transmitted and the received radiation in respect to the orientation of the target.

From equation 2.4, the monostatic radar RCS is

$$\sigma = \frac{(4\pi)^3 R^4 P_r}{P_i G^2 \lambda^2} \quad (2.9)$$

If we take the ratio of equation 2.2 to equation 2.1, we obtain the result

$$\sigma = \lim_{x \rightarrow \infty} (4\pi R^2 \frac{P_0}{P_D}) \quad (2.10)$$

where the limit has been added to emphasize the range R , at which the power density P_D is measured is in the far-zone region of the target [46].

P_0 and P_D are related to the electric field of their corresponding waves by :

$$P_0 = \frac{|E_{RX}|^2}{2\eta_0} \quad \text{and} \quad P_D = \frac{|E_{TX}|^2}{2\eta_0}$$

where η_0 , E_{RX} and E_{Tg} is wave impedance of air, the reflected field strength at radar and strength of incident field at the target, respectively.

So another way to express the RCS in terms of electric field amplitude is

$$\sigma = 4\pi \lim_{R \rightarrow \infty} \left[R^2 \frac{|E_{Rx}|^2}{|E_{Tg}|^2} \right] \quad (2.11)$$

The RCS of an object is dependent on the ratio between the target dimensions and wavelength, and the following three scattering regions can be seen for simple shape object [45,47]:

- Rayleigh region (*target size* $\ll \lambda$): the $RCS \propto \lambda^4$ and $RCS \propto (\text{target volume})^2$: At low frequency, when the size of the target in the propagation plane is small compared to wavelength. In this region target acts as a point scattered with almost negligible RCS contribution.
- Resonant or Mie region (*target size* $\sim \lambda$): in medium frequencies where the size of target is comparable with the incident wavelength, the incident wave phase changes significantly along the target surface.

- Optical region ($target\ size \gg \lambda$): in high frequencies the RCS is roughly the same size as the real area of the target. In this region the target size are much larger compared to the radar wavelength. This region is favorites of this PhD research as we mainly focused on mm wavelength which is much smaller than our measurement target.

A sphere is most commonly used as a calibration target in laboratory experiments or measurement field since the orientation or positioning of the sphere will not affect radar reflection intensity measurements [48]. In [49] the best solution for the RCS of sphere made of a perfect electric conductor (PEC) with the radius of r has been presented. The three scattering regions discussed previously from Perfect Electric Conductor (PEC) smooth metal sphere can be calculated by [50]

$$\delta = \frac{\lambda^2}{\pi} \left| \sum_{n=1}^{\infty} (-1)^n \left(n + \frac{1}{2} \right) (b_n - a_n) \right|^2 \quad (2.12)$$

$$a_n = \frac{j_n(ka)}{h_n(ka)} \quad (2.13)$$

$$ka = \frac{2\pi r}{\lambda} \quad (2.14)$$

$$b_n = \frac{kaj_{n-1}(ka) - nj_n(ka)}{kah_{n-1}(ka) - nh_n(ka)} \quad (2.15)$$

$$h_n(x) = j_n(x) + jy_n(x) \quad (2.16)$$

where, j_n and h_n are the radius, n -th order spherical Bessel and Hankel function, respectively.

Figure 2.3 shows the normalized radar cross section of PEC sphere as a function of its circumference measured in wavelength (ka) and the trend which identified the three regions was mentioned earlier obtained by calculating (2.11) at different wavelength.

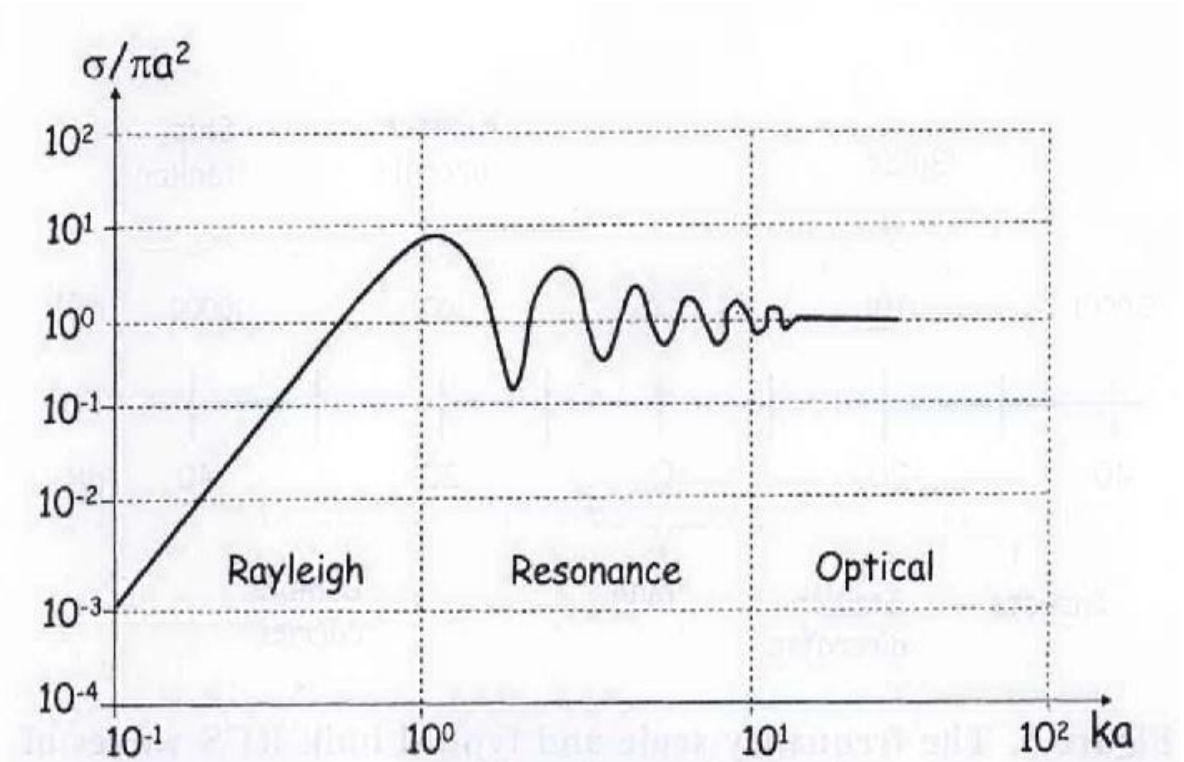


Figure 2.3: The normalized RCS PEC sphere[48]

2.2 Radar waveform choices and signal processing

As mentioned earlier, the target's range is estimated by measuring the EMW round trip travel time to and from the target. The target radial velocity (v_r) is estimated based on the Doppler frequency shift induced on the EMW from the motion of the target relative to the radar. It is very important to find out the form of the EMW transmitted by the radar (waveform) to determine the accuracy with which the targets' range and radial velocities are estimated. The radar waveforms can be classified into two general classes to determine the radar range: pulsed radar, which uses amplitude modulation, and continuous waveform (CW) radar which uses frequency modulation (FM) or phase modulation (PM) techniques.

Pulsed radar generates and transmits a narrow rectangular shape pulse modulating a sinewave carrier. By having the narrower pulse, the wider bandwidth will be achieved and therefore the range measurement would be more accurate in comparison to those radar using CW waveforms [51]. The pulse radar employs high peak power to concentrate all the energy in a short period of time which usually needs large, heavy and inefficient components, whereas, CW use low continuous power which allows the CW radar to be built using cheaper and more efficient component in comparison to those using pulse waveforms [51], for example the FMCW radars can be powered by batteries or solar panels in portable or remote deployment. Since the CW radar is not able to measure the target range, in order to overcome this inability the transmit and receive waveforms must have some sort of timing marks. By comparing the timing marks at transmit and receive, CW radars can extract target range. The timing mark can be implemented by modulating the transmit waveform, and one commonly used technique is frequency modulated continuous waveform (FMCW). In this thesis two main modulated waveforms are used: the stepped frequency waveforms (SFW) and (FMCW) which will be presented in details in the next sections.

2.2.1 FMCW waveform

The FMCW radar basically measures the range, velocity and angle of arrival of targets within the line of sight of the incident beam. FMCW radar transmits a signal called chirp. A chirp is a sine wave whose frequency increases (up-chirp) or decreases (down-chirp) linearly within the given time interval.

Figure 2. 4 shows the up-chirp transmitted and received signal which shows how the frequency is changing linearly with time interval.

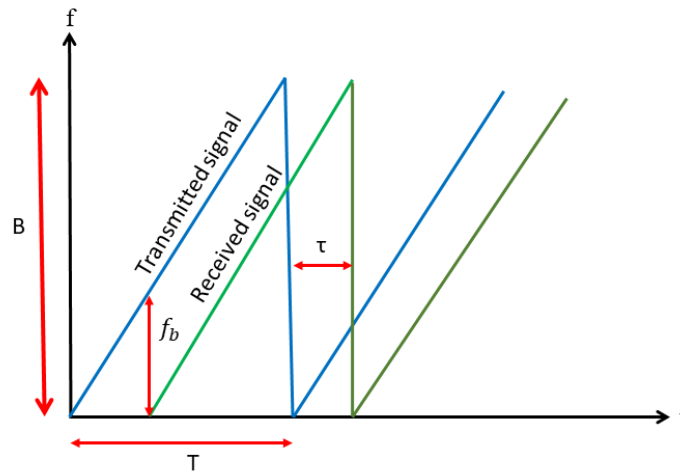


Figure 2.4: frequency vs time relation of linear FMCW transmit and receive chirp

FMCW signals can be processed either through matched filter or heterodyne detection. A matched filter is a filter with a transfer function which is equal to the mirror image of the transmitted signal, and delayed accordingly to ensure causality. In this approach the signal compresses in time domain and thus the output digitization needs fast analogue to digital convertor (ADC). In this research heterodyne detection is used which is explained below.

In the heterodyne detection, received chirp is mixed with the portion of the transmitted chirp and then low-pass filtered, and as a result the frequency difference between transmitted and received chirp will be generated which is called beat- frequency(f_b). In FMCW radar for measuring the range the beat-frequency is measured and can be obtained by:

$$f_b = \frac{B}{T} \tau \quad (2.17)$$

Where B is the frequency deviation which is called sweep bandwidth and T is the sweep time, τ is the round-trip time from transmitter to the target with the distance R (range) and back and can be expressed as

$$\tau = \frac{2R}{c} \quad (2.18)$$

By substituting equation (2. 18) in equation (2. 17), we can write equation (2. 19), which is related to the beat frequency to the range [52].

$$R = \frac{cT}{2B} f_b \quad (2. 19)$$

Since the effective beat frequency resolution Δf_b of baseband signal is $\frac{1}{T}$ (based on the effective 3dB bandwidth of CW signal of length T is 1/T), The range resolution ΔR corresponding to Δf_b can be written by:

$$\Delta R = \frac{c}{2B} \quad (2. 20)$$

A mathematical analysis of heterodyne transmitted up-chirp in a time interval T can be written by [53,54]:

$$v_t(t) = A_t \cos[\phi(t)] = A_t \cos(2\pi f_c t + \pi \frac{B}{T} t^2), \quad -\frac{T}{2} \leq t \leq \frac{T}{2} \quad (2. 21)$$

where A_t is the amplitude of the transmit signal and f_c is the carrier frequency.

The received chirp is a delayed copy of the transmitted chirp in equation (2. 21):

$$v_r(t) = A_r \cos[\phi(t - \tau)] = A_r \cos(2\pi f_c (t - \tau) + \pi \frac{B}{T} (t - \tau)^2) \quad (2. 22)$$

where A_r is the amplitude of the received signal.

The output of mixer in the receiver is obtained from multiplication of transmitted and received chirp and can be expressed using trigonometric identities and shown in equation (2. 23).

$$\begin{aligned} v_m(t) = & \frac{A_r A_t}{2} \cos(2\pi f_c t + \pi \frac{B}{T} t^2 - 2\pi f_c (t - \tau) - \pi \frac{B}{T} t^2 (t - \tau)^2) \\ & + \frac{A_r A_t}{2} \cos(2\pi f_c t + \pi \frac{B}{T} t^2 + 2\pi f_c (t - \tau) + \pi \frac{B}{T} t^2 (t - \tau)^2) \end{aligned} \quad (2. 23)$$

In equation (2.23), the second term has frequency of nearly twice the carrier frequency so after mixer it is removed by low pass filter (LPF). The remaining signal is beat-frequency as shown in the following:

$$S_b(t) = \frac{A_r A_t}{2} \cos\left(2\pi f_c \tau + 2\pi \frac{B}{T} t\tau - \pi \frac{B}{T} t^2\right) \quad (2.24)$$

The beat-frequency for the single chirp duration T can be computed by the derivative of the cosine argument:

$$f_b(t) = \frac{d}{2\pi dt} \left(2\pi f_c \tau + 2\pi \frac{B}{T} t\tau - \pi \frac{B}{T} t^2\right) = \frac{B}{T} \tau = \frac{B}{T} \frac{2r}{c} \quad (2.25)$$

The spectral analysis of the beat-frequency gives the information on range of a target so the Fourier transform (FT) is applied on a single chirp to extract the time delay and therefore range information. The FT of a single chirp is:

$$\begin{aligned} V(f) &= \int_{-T/2}^{T/2} A \cos[\phi_B(t)] e^{-j2\pi ft} dt = \\ &= \frac{AT}{2} \frac{\sin\left[\frac{2\pi(f-f_b)T}{2}\right]}{\frac{2\pi(f-f_b)T}{2}} e^{-j\phi_0 + j\omega_0 nT} + \frac{AT}{2} \frac{\sin\left[\frac{2\pi(f+f_b)T}{2}\right]}{\frac{2\pi(f+f_b)T}{2}} e^{j\phi_0 - j\omega_0 nT} = AT \quad (2.26) \end{aligned}$$

Equation (2.26) illustrates the spectrum of a single chirp is a sin x/x function centred at the beat-frequency related to the target time delay.

2.2.2 Stepped frequency waveform

High range resolution (HRR) profile are of interest to radar designers. It is known that the radar range resolution is proportional to its bandwidth so in order to achieve HRR, wide bandwidth is needed. However, use of wide Bandwidth signals often complicates the design of receiver and transmitter. To overcome these drawbacks and having HRR radar, Einstein,T.H. [55] introduced the stepped frequency waveform. The Stepped frequency waveform consists of a series of N narrowband pulses with the length of τ .The frequency is changing pulse to pulse by a fixed amount of Δf (see Figure 2.5) and the frequency of the n^{th} transmitted pulse is:

$$f_n = f_0 + (n-1)\Delta f, \quad n = 0,1,\dots,N-1 \quad (2. 27)$$

Where f_0 is nominal carrier frequency, Δf is the frequency step size, N is the number of pulse and $(n-1)\Delta f$ is the radar bandwidth.

The analytic expression of the SFW is:

$$s(t) = \sum_{n=0}^{N-1} x(t-nT_R) \exp[j2\pi(f_0 + n\Delta f)(t-nT_R)] \quad (2. 28)$$

where T_R is the Pulse Repetition Interval (PRI) and

$$x(t) = \text{rect}(t / \tau)$$

$$\text{rect}(t / \tau) = 1, \quad -\tau/2 < t < \tau/2$$

The coherent processing interval (CPI) which is known as a burst time is the total time to transmit and process the waveform and can be written as:

$$CPI = N(PRI) \quad (2. 29)$$

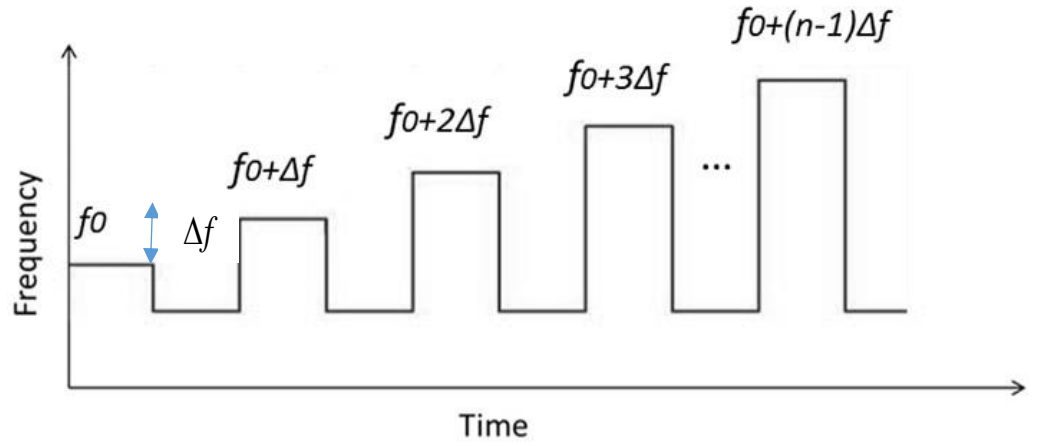


Figure 2.5: Stepped frequency waveform

The total bandwidth of SFW is:

$$B_{SFW} = N\Delta f \quad (2.30)$$

So the range resolution is:

$$\Delta R = \frac{c}{2B_{SFW}} = \frac{c}{2N\Delta f} \quad (2.31)$$

Therefore, as can be observed from equation (2.31), the increase in either number of pulses or frequency step size can result in the improvement in range resolution.

The maximum range is given by:

$$R_{\max} = N \frac{c}{2N\Delta f} = \frac{c}{2\Delta f} \quad (2.32)$$

In this thesis the SFW has been generated by vector network analyzers (VNA) which is capable to measure the scattering parameter (S_{21}) at different center frequencies within the available bandwidth in the frequency domain and convert it to the time domain through the inverse Fourier transform.

The range profile can be expressed from equation (2. 19) and shown by:

$$R = \left| \sum_{K=1}^K \sum_{f_n=f_0}^{f_s} W(f_n) S_{21}(f_n) e^{j2\pi f_n \frac{2r}{c}} \right|^2 \quad (2. 33)$$

where, f_0 is start frequency and f_n is stop, $W(f)$ is the Fourier transform of a window function used to reduce the side lobes.

2.3 Clutter

Radar Clutter is defined as unwanted returns from the environment and unwanted objects, which can disturb the performance of the radar systems. Clutter typically can be classified into two main categories: surface clutter and volume clutter. Ground terrain or sea returns are typical surface clutter while weather (rain, hail, snow) or chaff are the examples of volume clutter. It is essential for a radar system designer to consider the return from the targets in the presence of unwanted clutter in addition to receiver thermal noise. It is quite simple to calculate the surface clutter and volume clutter in monostatic radar due to its single antenna geometry, whereas this calculation is more complicated in bistatic radar.

The volume clutter V_c is shown by [56] :

$$V_c = \frac{R^2 \theta_{az} \theta_{el} \rho}{(L_p)^2} \quad (2. 34)$$

Where R , θ_{az} , θ_{el} are the target distance from antenna, antenna azimuth and elevation beamwidths in radians respectively and shown in Figure (2.6). $L_p=1.33$ is the beam shape loss and ρ is range resolution and can be calculated by

$$\rho = \frac{c}{2B} \quad (2. 35)$$

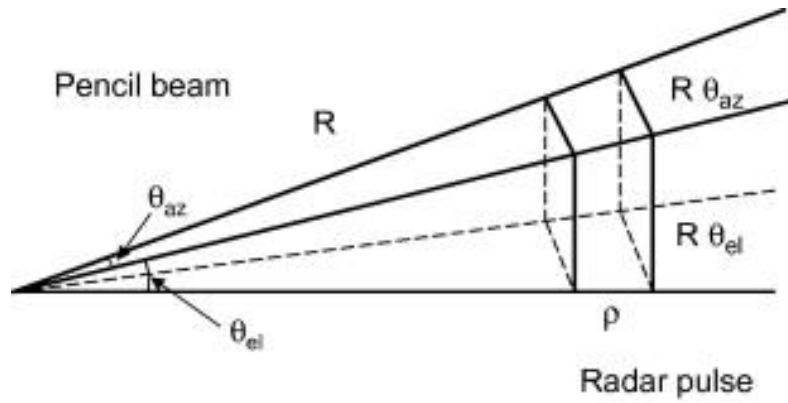


Figure 2.6: volume clutter illuminated cell size in monostatic radar [57]

The normalized volume clutter reflectivity η can be described as the total RCS of the volume of the distributed clutter sources σ , normalized by the volume clutter.

$$\eta_c = \frac{\sigma_c}{V_c} \quad (dBm^2/m^3) \quad (2.36)$$

So if the volume clutter reflectivity and the radar parameters are known, the received clutter power is given by [56]:

$$C = \frac{P_t G^2 \lambda^2 \delta_c F_c^4}{B(4\pi)^3 R^4 L_t L_{ac}} = \frac{P_t G^2 \lambda^2 R^2 \theta_{az} \theta_{el} \rho \eta_v F_c^4}{B(4\pi)^3 R^2 L_t L_{ac} (L_p)^2} \quad (2.37)$$

where L_t , L_{ac} and F_c are transmission line loss, atmospheric attenuation and pattern propagation factor for the radar-to-clutter path respectively.

The normalized surface clutter reflectivity δ° is shown in equation (2.38) and can be described by the RCS of the distributed in the illuminated patch, normalized by the clutter patch area A_c (see Figure 2.7):

$$\delta^\circ = \frac{\delta}{A_c} \quad (dBm^2/m^2) \quad (2.38)$$

$$A_c = \rho R \theta_{az} \sec(\phi_{gr}) \quad (2.39)$$

where, ϕ_{gr} is the local grazing angle(see Figure 2.7).

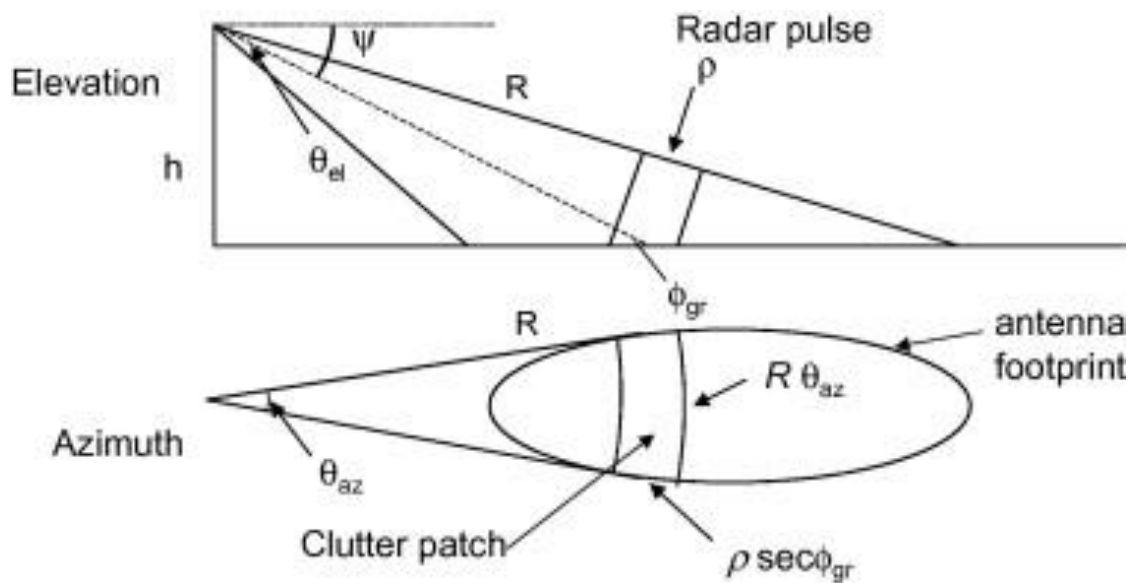


Figure 2.7: Clutter illuminated patch size in monostatic radar [57]

2.4 Radar signal propagation mechanism

The effects of radar EM wave propagation on the performance of a radar system can be discussed under five basic propagation mechanisms: atmospheric attenuation, diffraction, refraction, reflection and scattering. Atmospheric attenuation is the loss of radar energy which is mainly due to the absorption from water vapour and gaseous existing in the atmosphere (Oxygen and liquid hydrometeors) and generally increases with increasing frequency. Absorption is often neglected at wavelengths of 10 cm and longer, but becomes increasingly important at shorter wavelengths. When the EM waves hit an object, they are either transmitted, reflected, refracted, diffracted or scattered depending on the shape, size and material of the object and the wavelength of the EMW.

2.4.1 Atmospheric attenuation

Atmospheric attenuation is mainly due to incidence of certain gases (oxygen and water vapour) molecules in the atmosphere which cause dissipation of EM energy at certain frequencies. Figure 2.8 shows the specific value of atmospheric attenuation at frequencies of up to 1 THz for a pressure of 1013 hPa, temperature of 15° C for the cases of a water-vapour density of 7.5 g/m³ and a dry atmosphere [58]. As can be seen from the figure the atmospheric attenuation, primarily due to oxygen and water vapour

absorption, is significant in many spectral regions in the low THz band, however within a number of absorption windows e.g. around 150 GHz, 300 GHz, 400 GHz and 650 GHz the low atmospheric attenuation is observed which is of interest of this PhD research.

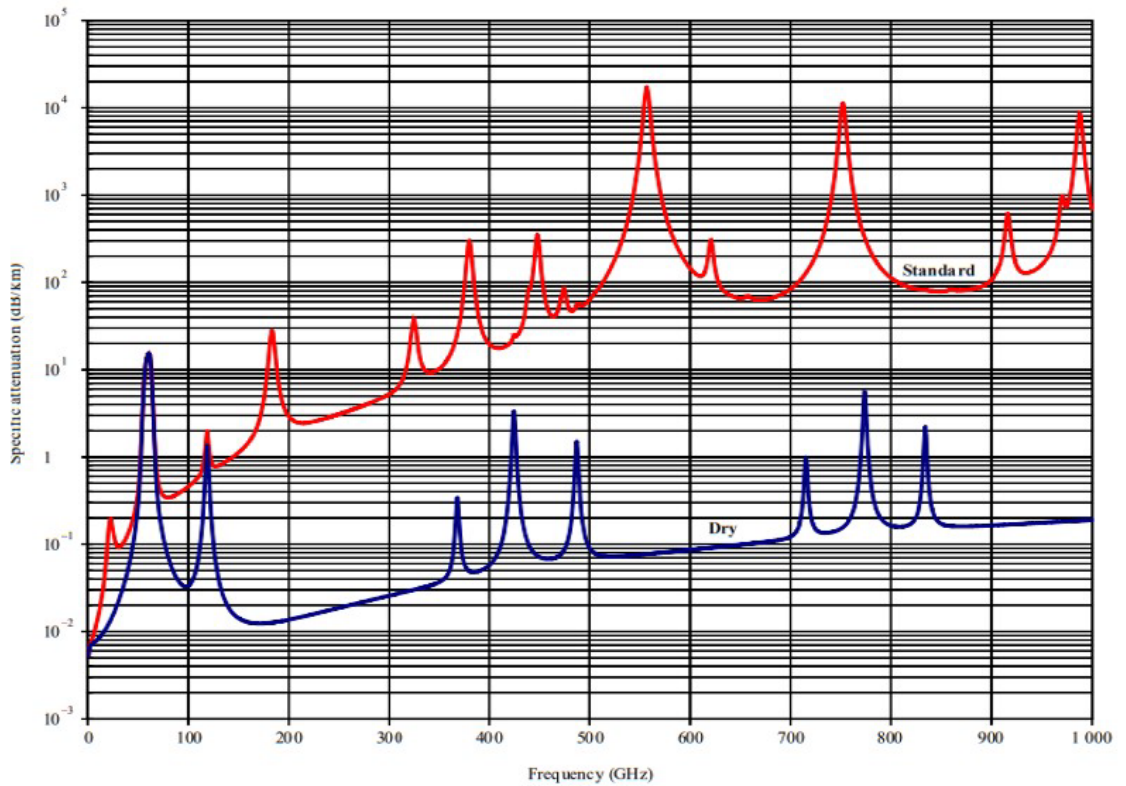


Figure 2.8: Specific attenuation due to atmospheric gases[58]

Other major causes of attenuation in the atmosphere are rain, snow, cloud and fog, of which rain and wet snow have the most effect on radar attenuation compared to clouds, fog and dry snow [56]. One of the aims of this PhD research is to investigate the effect of rain and snow on low THz radar and evaluate feasibility of low THz radar in outdoor environment.

2.4.2 Reflection

When transmitted EM waves encounter a change from one medium (air) to other medium or surface (considered as a target) with the dimension much greater than the wavelength of EM waves, some part of the energy is transmitted to the new medium and some part of it is absorbed and transformed to heat and the remainder of the energy is reflected (see Figure 2.9). If the encountered surface is a perfect conductor (metal), the electric charges are free to move on the surface and as a result all the EM waves are reflected back to the source. The ray representation of incident wave, reflected wave and transmitted wave are shown in Figure 2.9. When a reflection occurs the incident angle, θ_1 is the same as the reflected angle θ'_1 . The Fresnel reflection coefficient ρ is the ratio between the reflected electric field E_r and incident electric field E_i in the medium of origin. The reflection coefficient depends on the angle of incidence, the polarization and the frequency of the propagating wave [59] and can be written as [46]:

$$\rho = \frac{E_r}{E_i} = \frac{\eta_2 - \eta_1}{\eta_2 + \eta_1} \quad (2.40)$$

The wave impedance for medium 1 and medium 2 is $\eta_1 = \eta_0 / \sqrt{\epsilon_1}$ and $\eta_2 = \eta_0 / \sqrt{\epsilon_2}$ respectively.

where η_0 , ϵ_1 , ϵ_2 , λ_0 are free space impedance, relative permittivity of medium 1, relative permittivity of medium 2, free space wavelength respectively. So equation 2.40 leads to:

$$\rho = \frac{\sqrt{\epsilon_1} - \sqrt{\epsilon_2}}{\sqrt{\epsilon_1} + \sqrt{\epsilon_2}}$$

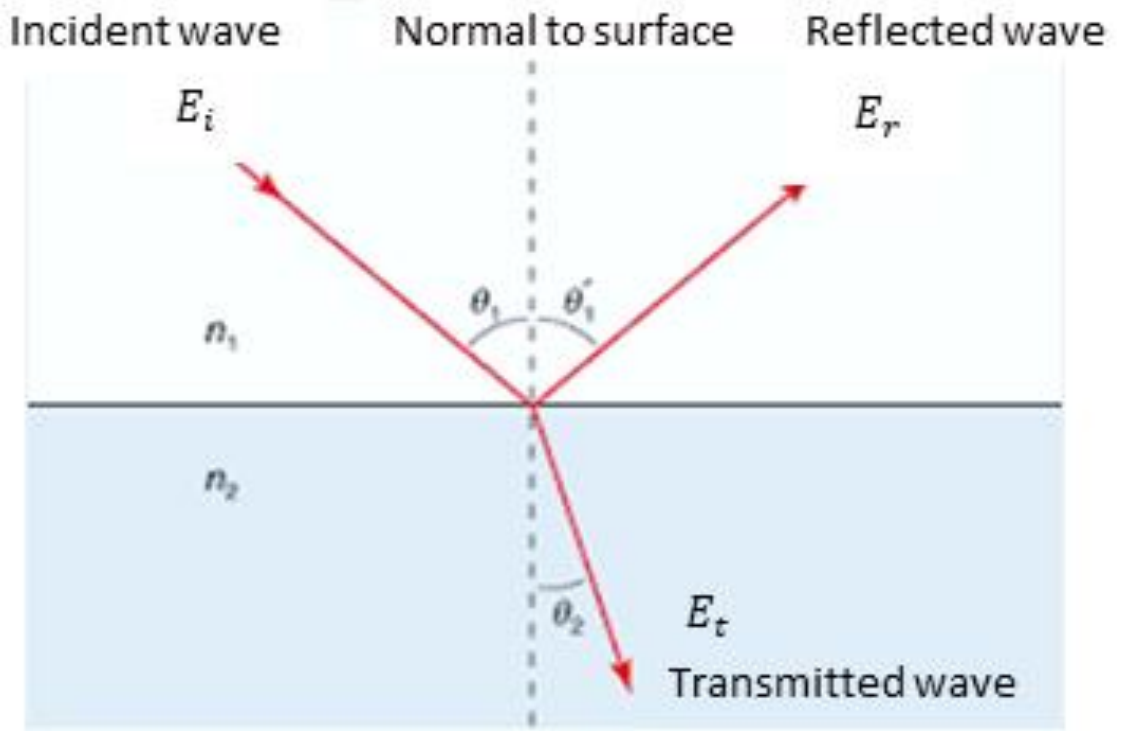


Figure 2.9: Ray representation of oblique incidence

2.4.2.1 Diffuse and specular reflection

Two main mechanisms of signal scattering on surfaces with different roughness are shown in Figure 2.10. In the case of a perfectly smooth surface only specular reflection will occur. When the surface becomes rougher, the ratio of specular reflection component will decrease and the diffuse reflections, re-radiating signal in all directions, will become more prominent. In a case of very rough surface, the diffuse reflection prevails over specular.

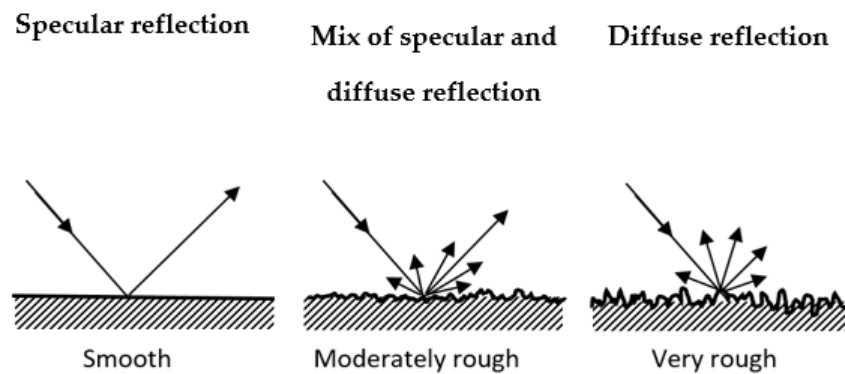


Figure 2.10: Reflection from smooth, moderately rough, and very rough surface

The type of scattering is defined by the surface rms height (root mean square average of the heights above or below a mean reference line) relative to wavelength. Based on the Fraunhofer criterion the surface is considered as rough if the surface rms height h satisfies the inequality

$$h \geq \frac{\lambda}{32 \cos \theta} \quad (2.41)$$

where θ is the angle of incidence relative to the surface normal and λ is the signal wavelength [60].

To evaluate the surface roughness relative to the wavelength, it is convenient to use electromagnetic roughness kh , where $k=2\pi/\lambda$ is the free space wave number. Fraunhofer criterion (2.41) can be expressed in terms of electromagnetic roughness as

$$kh \geq 0.2/\cos \theta \quad (2.42)$$

This implies another definition for surface roughness [61], according to which a surface may be considered relatively smooth if its $kh < 0.2$ and very rough if its $kh \geq 2$.

What is the difference between scattering and reflection?

It is worth noting the difference between reflection and scattering as the terms seem to have a very close meaning. As mentioned above, reflection occurs when propagating EM waves strike an object with the dimension much greater than the wavelength of EM waves while the scattering occurs when EM waves travel through a medium containing objects which are small relative to the wavelength of EM waves, and the number of these objects per unit volume is large [59]. Scattered waves are, in practice, produced by rough surfaces, foliage, lamp posts and precipitation.

2.4.3 Diffraction

Diffraction occurs when the radio path between the Transmitter and receiver is obstructed by a surface that has sharp irregularities (edges). The secondary waves resulting from obstacles are present throughout the space and even behind the obstacle, giving rise to transmission even without Line-Of-Sight. This gives rise to several phenomena: radio signals can propagate around the curved surface of the earth, beyond the horizon and behind obstructions. The field strength of a diffracted wave in the shadowed region is the vector sum of the electric field components of all the secondary wavelets in the space around the obstacles.

The amount of diffraction depends on the frequency and the size of the objects compared with wavelength. The lower the frequency, the more the wave is diffracted. The mechanism of diffraction is especially important at very low frequency (VLF), however in radar systems due to very small wavelength compared to earth's dimensions, little energy is diffracted [44].

Diffraction depends on the amplitude, phase and polarization of the incident wave at the point of diffraction [59,62]. In the proposed PhD research, we are mainly work with low THz radar (79 GHz- 670 GHz) and the targets of interest are electrically much greater than the wavelength, so diffraction effects are not significant and we don't consider them.

2.5 Penetration depth

When an EM waves is incident on the surface of a material, some part of it may reflected from that surface and some part transmitted into the material. This EM wave interacts with the atoms and electrons inside the material. Depending on the nature of the material, the EM wave might penetrate very far into the material, or may die out very quickly.

Penetration depth is a measure of how deep EM wave can penetrate into a surface material. It is defined as the distance from the surface into the dielectric at which the traveling wave power drops to e^{-1} from its value at the surface and can be expressed as [46]:

$$D_p = \frac{1}{k_a} \quad (2.43)$$

where k_a is the power absorption coefficient and its related to dielectric loss factor and can be written by:

$$k_a = -2k_0 \text{Im}\{\sqrt{\varepsilon}\} \quad (2.44)$$

Where $k_0 = \frac{2\pi}{\lambda}$ is a wave number and ε is the complex permittivity $\varepsilon' - j\varepsilon''$.

So another way of expressing penetration depth in terms of relative permittivity and loss factor can be written by:

$$D_p = \frac{\lambda}{2\pi(2\varepsilon')^{1/2}} \left\{ \left[1 + \left(\frac{\varepsilon''}{\varepsilon'} \right)^2 \right]^{1/2} - 1 \right\}^{-1/2} \quad (2.45)$$

2.6 Millimetre-wave and THz sensing

The interest in the THz region dates back to the 1920s [63] and during the last 40 years it has seen fantastic development due to the exceptional properties of the THz waves as well as its various possible applications. THz electromagnetic waves are located at the boundary between the microwave and infrared regions and offer an effective bridge between electronic and photonic technologies and represent a large scope of unused, unexplored bandwidth. THz radiation is transparent to non-polar, non-metallic solids material like plastic, wood and ceramic, however, metallic materials completely block or reflect THz waves. Although non-polar liquids are transparent in THz regime, polar liquids like water cause high attenuation and because of high volume of water in human skin, it attenuates most of THz rays. THz radiation is not considered dangerous for humans as THz rays would be harmlessly dissipated as heat in the first 100 microns of skins tissues [64]. Furthermore, THz radiation can propagate well in non-transparent media such as dust, fog and smoke with low losses due to smaller wavelength in comparison to object size.

The Earth's atmosphere is a strong absorber of THz radiation due to the chemical composition of the atmosphere (oxygen and water vapour) as seen in Figure 2.8 ,however certain relatively low attenuation windows(Figure 2.8) are available that reduce the effect of this problem. THz radiation has been successfully investigated for many applications such as security [64] , non-invasive through-layer vision [65] , and medical imaging [66] and more recently automotive sensing [67] .

2.6.1 Low THz radar

Although the THz band runs from 0.1 THz to 3 THz, in this thesis we are considering the lower part of THz band which is known as the low THz band and we mainly focus on frequencies of 79 GHz, 150 GHz, 300GHz and 670 GHz. The atmospheric attenuation is less severe and the technology more mature in this portion of the band [68]. Currently, by rapid improvement in developing high power compact transmitters [69,70] and Monolithic Microwave Integrated Circuits (MMIC), the low THz radar system architecture has been constantly improved, allowing the implementation many new applications in a short and medium range [71]. Importantly because the spectrum is not in use or licenced currently, the wide operational bandwidth available in low THz, which

leads to significantly higher range resolution is achievable and increases the sensitivity to the surface texture, leading to more image-like scene characterization by such a radar. Another significant benefit of using the low THz frequencies for radar is, operation at higher frequencies leads to more compact electronics components, in particular antennas. Also low THz sensors have the advantage of robust operation in harsh weather and lighting conditions. Until recently, the high cost was an obstacle to the widespread implementation of low THz radar systems, but with the development of appropriate technologies, it has been steadily decreasing.

2.6.2 Low THz automotive radar

Since the 1960's automotive radar has been under research and development by academic and industrial companies. Developments in the 1960s began at around 10 GHz [71], increasing the potential operating frequency to 24 GHz [72], 47 GHz [73], and 95 GHz [68], and currently settling at 76-77 and 77-81GHz.

Table 2.1 summarize the current radar sensors for short, medium and long range applications. In automotive radar, short range radar (SRR) is typically used for measurements of up to 30 m ahead of the vehicle and detect objects over a wide angular region and usually used for applications such as parking aid and obstacle detection (pedestrian, cyclist). The medium range radar (MRR) application refers to measurement range up to 150 m and apply to applications with a medium distance and speed profile, like Cross Traffic Alert (CTA). The range between 10 m to 250 m is used for long range radar (LRR) measurement, over a narrow angular region which is used for Adaptive Cruise Control (ACC), emergency braking, collision warning. AV can have multiple SRRs, MRRs and LRRs with addition to other sensors (optic cameras, Lidar,...) to provide full or partial autonomy. These sensors are shown in Figure 2.11.

Table 2.1: Existing automotive radar characteristics [74]

	LRR	MRR	SRR
Frequency band	76-77 GHz	77-81 GHz	77-81 GHz
Bandwidth	600 MHz	600 MHz	4 GHz
Maximum output power (EIRP)	55 dBm	-9 dBm/MHz	-9 dBm/MHz
Distance range	10-250 m	1-100 m	0.15-30 m
Range resolution	0.25 m	0.25 m	-0.075 m
Velocity accuracy	0.6 m/s	0.6 m/s	0.6 m/s
Angular accuracy	0.1°	0.5°	1°
Antennas azimuth 3dB beamwidth	±15°	±40°	±80°
Antennas elevation 3dB beamwidth	±5°	±5°	±10°

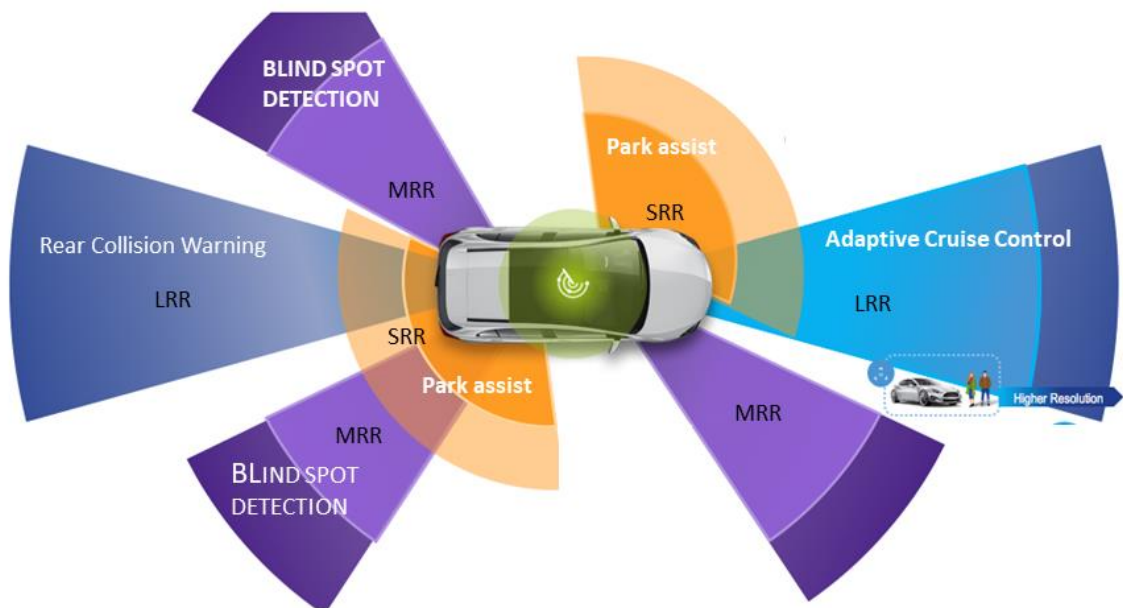


Figure 2.11: Autounomous Vehicle sensors

As mentioned in chapter 1.1, major companies are considering AV as a solution to reduce road accidents and fatalities, and they are producing tens of millions of radar sensors annually and thereby the question of mutual interference and co-existence will have to be addressed. Increased available bandwidth is one of the methods of use to mitigate some of these effects. As answer to the request to enlarge the allocated bandwidth, the low THz radar systems explained in section 2.6 introduce a new generation of radars which is the subject of the current research and development work taking place at the Microwave Integrated System Laboratory (MISL), University of Birmingham. This band, currently unallocated, offers the possibility of using large absolute bandwidths, with the same fractional bandwidth occupied by the commercial automotive radars, and therefore potentially reducing the problem of mutual interferences between radars [75]. Another advantage of low THz radar for automotive industry is wide operating bandwidth providing increased range resolution which leads to obtaining images similar to optical. Based on the Fraunhofer criterion (equation 2.39) the high frequency leads to an increase of surface roughness relative to signal wavelength. As a result, a high amount of diffuse scattering is received from the full extent of an object. Furthermore, small antenna size which leads to minimization of the system and as a result minimizes the cost of integration of the system.

Figure 2.11 illustrate an example of an off-road scenario which is taken by low THz radar (150 GHz) imagery [36]. The range, and angular position from each imaged object in the scene can be seen clearly. The high diffuse backscattering, texture sensitivity and high resolution of the radar imagery are immediately apparent, which shows the obvious difference between targets and demonstrates that high frequencies are more favorable to produce high quality images.

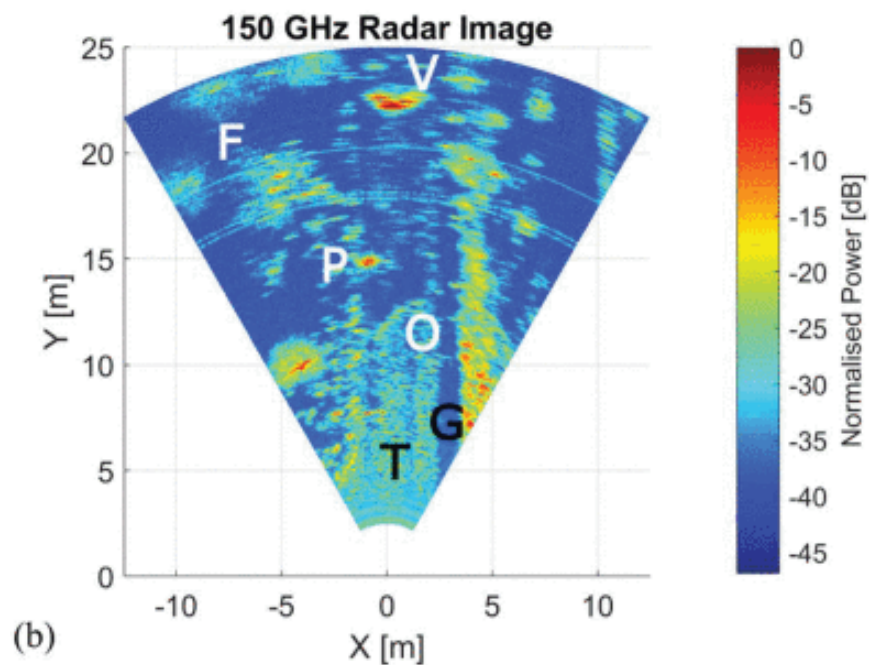


Figure 2.12: Example imaged scene, (a) video ground truth, (b) 150 GHz scanned radar image. Letters highlight image features: F—foliage, P—pedestrian, V—vehicle, O—obstruction (branch), T—track, G—gully (water filled)—image normalised to image maxima [36]

2.7 Artificial Neural Network

Neural networks (NN), which is known as artificial neural networks (ANN), are subfield of machine learning which imitate the way that human brain learns through set of algorithms and enables systems to automatically learn and improve from experience and by the use of data [76] and solve the problem.

Typical ANNs as shown in Figure 2.13 are comprise of the following layers:

- Input layer which picks up the input signals and passes to the hidden layer.
- One or more hidden layers (If ANN consists of more than two hidden layers, can be considered a deep neural network (DNN)) which responsible for majority of learning task(calculation and feature extraction)
- Output layer which deliver the final result.

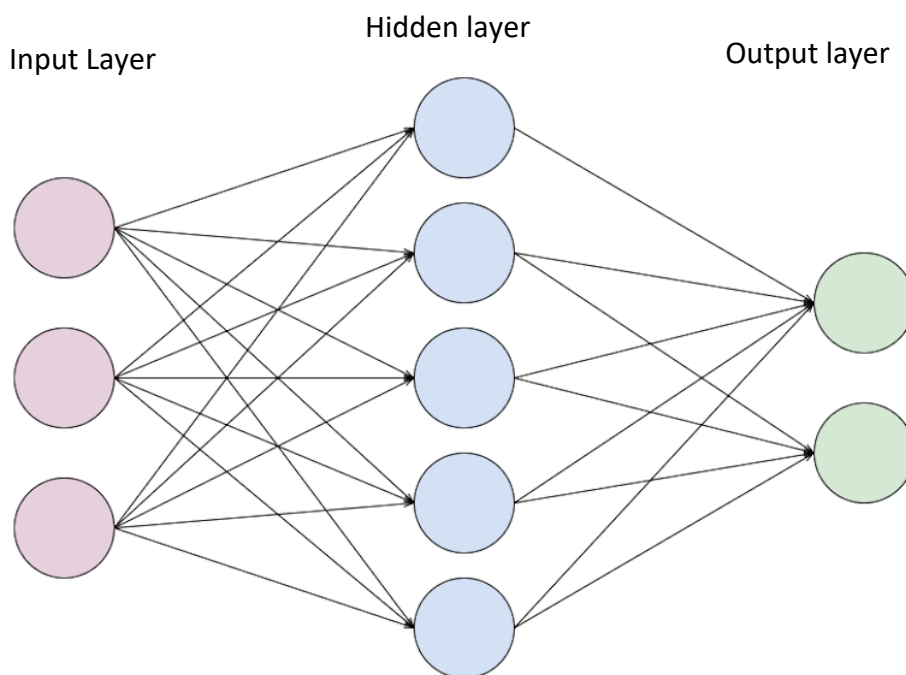


Figure 2.13: Arthitecture of ANN

Each layer in ANN architecture has multiple artificial neurons (nodes) and each neuron connects to the next layer with an associated weight and bias. Based on McCulloch and Pitts (MP) [77] model the weights are multiplied with the input signal, and a bias is added to all of them (see equation 2. 46). This processes is called feedforward. The output signal is generated by applying the activation function over the weighted sum of the inputs (see equation 2. 47). Activation functions decide which nodes should be active (fire) for feature extraction and send it to the next hidden layer or as an output and which node shouldn't be sending to the next layer. There are specific activation functions available that can be applied, depending upon the sort of task we are performing such as sigmoidal, Tan hyperbolic, Binary which are explained in the next section. The Figure 2.14 shows the MP model of ANN followed by its processing.

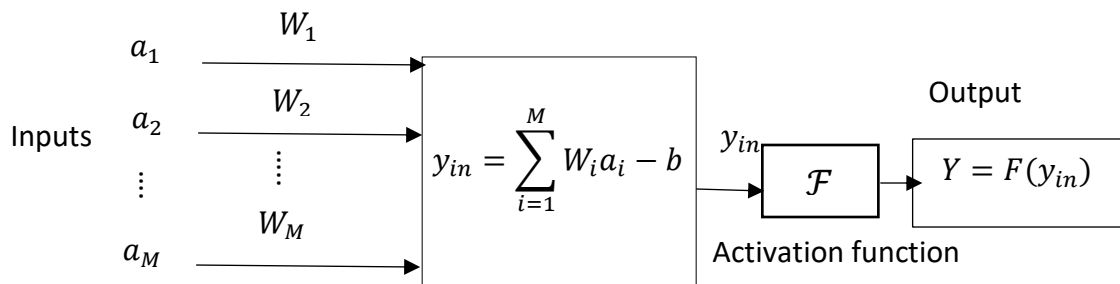


Figure 2.14: McCulloch and Pitts (MP) model of neuron

Equation 2. 46 and 2. 47 describe the MP model as below:

$$y_{in} = \sum_{i=1}^M W_i a_i - b \quad (2. 46)$$

where y_n is activation value, M is number of input signal, W_i is the synapse weight associated with the i th input, a_i is signal input and b is bias.

$$Y = F(y_{in}) \quad (2. 47)$$

where Y denotes the output signal which is a nonlinear function $F(y_{in})$ of the activation function(y_n).

Like the human brain, machines are capable to learn in different ways, so to design a learning process in ANN, we should first have a model of the environment in which a neural network operates, so we must know what information is available to the network. We refer to this model as a learning paradigm [78]. There are two main learning paradigms: supervised and unsupervised learning. In a supervised learning, certain data are labelled in a dataset to help classify output data and predict outcomes [79]. Some of the applications of supervised learning are speech recognition, pattern recognition, handwriting recognition, image classification. In unsupervised learning the algorithm is not provided with any pre-assigned labels or scores for the training data [80] so the ANN understands the data structure provided as input on its own.

For the purpose of image classification in supervised learning, each image needs to be labelled within the certain class and the goal is that the network should learn some specific features of the image during the training process and become capable of identifying the labels of un-seen images in a testing process. Formerly, the ANNs were initially used for image classification before they were extended to the more prominent convolutional neural network (CNN). The latter has solved several of the drawbacks of ANN. Some of the benefits of CNN to ANN for image classification task are illustrated as a bellow:

- CNN utilizes weight-sharing which reduces the number of weights in comparison to ANN, therefore as a result the network is faster and has lower memory requirements.
- The 2-dimensional image can be fed to the CNN directly without converting to a 1-dimensional image (which is necessary for ANN). This gives the benefit of maintaining the spatial properties of the image.
- By using actual raw image data as an input, the pre-processing of image is no longer needed.

So in this PhD research the CNN was chosen to classify the low THz radar image for the purpose of surface classification task, which is described in detail in chapter 6.

In order to reduce the complexity in understanding the CNN architecture some of the main concepts which are shared by both networks (ANN and CNN) like the neuron activation function (Rectified Linear Unit, Sigmoid Function, Softmax Function, Tanh function), network training, loss function and optimization algorithm are initially discussed in this section in relation to ANN architectures, and The framework of CNN architectures is covered in section 2.8.

2.7.1 Activation function

As mentioned before the activation function decides, whether a neuron should be activated (fire) and send to the next layer or not be activated. The main purpose of the activation function is to introduce non-linearity into the output of a neuron to make it capable to learn and perform more complex tasks .The activation function is responsible for transforming the weighted sum of inputs to the neuron into an output value to be fed to the next hidden layer or output. In any ANN or CNN, prediction accuracy depends on the number of layers used in the neural network architecture and most importantly, the type of activation function which is used. There are different activation functions but the most commonly used are non-linear activation function. Some non-linear activation functions such as Sigmoid, Tanh, Softmax, ReLU are explained below.

2.7.1.1 RELU activation function

Since 2017 the Rectified Linear Unit (ReLU) function is known as the most popular activation function in deep neural networks (DNN) [81] and has been applied in many applications of DNN such as computer vision, word processing, voice recognition, image classification .The RELU function, shown in equation 2. 48, returns the maximum of input x and zero. If the input is less than 0 (negative value), the ReLU activation function returns zero (0) and if the input value is greater than 0 (positive value), the ReLU function output is the same as original input value. Figure 2. 15a shows the curve and scope of ReLU activation function.

$$F(x) = \max(x, 0) \quad (2. 48)$$

Some recent study [82] claims that the ReLU function can be considered as one of the fastest activation functions and it's aiming to reduce the complexity and computation time and works well in large neural networks. However there is a limitation faced by this activation function which is named "Dying ReLU ". The Dying ReLU problem means that

many ReLU neurons die and become inactive, and for all inputs they output zero. In this case, no gradient flows and if the number of inactive neurons in the neural network is high, the performance of the model is affected. To solve this problem the leaky ReLU function can be used (see equation (2. 49) [83].

$$F(x) = \begin{cases} a_i x_i, & x_i \leq 0 \\ x_i, & x_i > 0 \end{cases} \quad (2. 49)$$

Where x_i is the input of the nonlinear Leaky ReLU activation function $F(x)$ on the i th channel, and a_i is a coefficient controlling the slope of the negative part.

The Leaky ReLU has been showed in Figure 2. 15b where the slope on the negative range is slightly changed, causing the ReLU function range to leak.

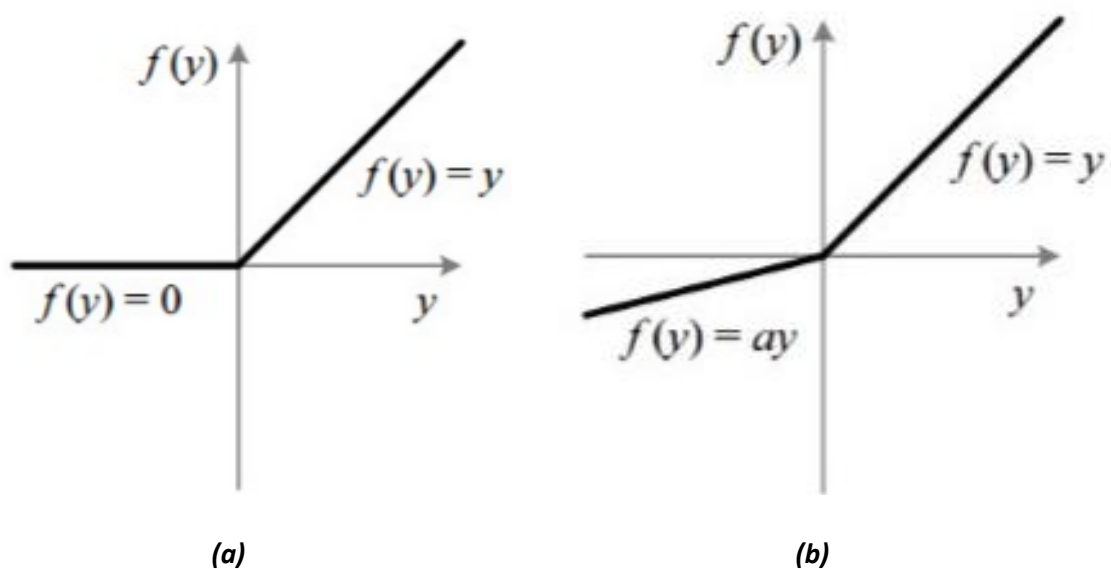


Figure 2.15: Activation function (a) ReLU, (b) Leaky ReLU[83]

2.7.1.2 Sigmoid function

The Sigmoid activation function is a non-linear function which takes any real value as input and delivers outputs between 0 and 1. Figure 2. 16 shows the curve and scope of Sigmoid activation function and mathematically it can be presented as [84]:

$$F(x) = \frac{1}{1 + e^{-x}} \quad (2. 50)$$

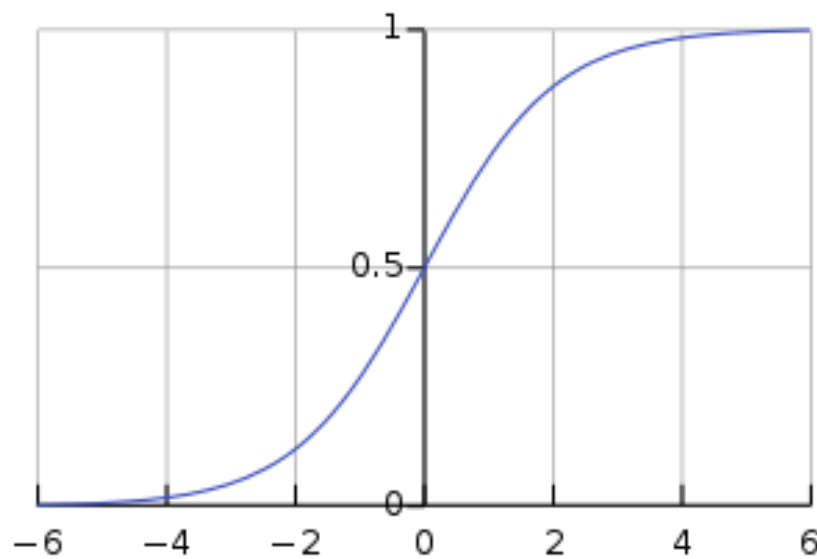


Figure 2.16: Sigmoid activation function curve [84]

The Sigmoid function and its derivative are simple and reduce the computation time, but since the derivative interval is short, we have a data loss problem in this function, so the more hidden layers our neural network has, or in other words, the deeper it is, the more information is compressed and deleted in each layer and as a result, more data is lost. Therefore due to this drawback it is preferable not to use these functions in deep neural networks, however, it can still be used to implement simple neural networks and logistic regression [84].

2.7.1.3 SoftMax Function

This activation function has almost the same function as the Sigmoid function, but with some differences that make it a more efficient and widely useful function. As mentioned previously, the output of Sigmoid is the value between 0 and 1 and it's suitable for cases where we want to get the probability of a particular class so this activation function is not preferred in multi-class classification, however Softmax function unlike Sigmoid function can be used for multi-class classification. The Softmax function produce the output (within the range of 0 and 1) with the sum of the probabilities which has been equal to 1 [85] . For instance, if the neural network aims to classify five various classes, the output is a vector with five values having a total equal to one. The soft max activation function is often used in the last layer of the neural network classifier (fully connected layer).

The mathematical equation of the Softmax function is as follows [86]:

$$\sigma(x_j) = \frac{e^{x_j}}{\sum_{i=1}^k e^{x_i}} \quad \text{for } j = 1, \dots, k \quad (2.51)$$

where x is the input vector to the softmax function and k is the number of the classes in the multi class classifier.

2.7.1.4 Hyperbolic tangent function (Tanh)

Tanh function which takes a real value which lies in the range between -1 and 1 as shown in equation 2. 52 [85] .

$$F(x) = \frac{(e^x - e^{-x})}{(e^x + e^{-x})} \quad (2. 52)$$

The Tanh become the preferred function over sigmoid function as it has gradients which are stronger, also, it is centralized the output to zero. However, similar to Sigmoid function, this function suffer from vanishing of the gradient [85].

Figure 2. 17 shows the curve and scope of Tanh activation function as below:

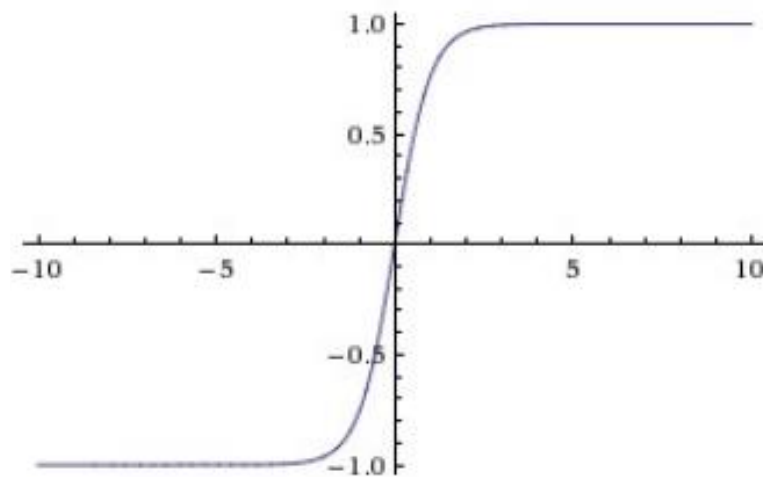


Figure 2.17: Tanh activation function curve [87]

After defining the hidden layers and activation function, the loss function and optimizer needs to be specified.

2.7.2 Training the network

One of the most widely used methods for training the neural networks is “back propagation of error “. In this method, there are two steps in each iteration: the first step is the feed forward, which, as mentioned before, is done by multiplying the input data in weights and then summing it with bias and the predicted output that is probably different from the actual output. This is where the network determine how much error the feed forward step had by using the loss function. The next step, is back propagation which goes back through the network and updates the weights and bias (with an optimizer algorithm) in a way that produces a result closer to the actual output and with less error in the next iteration. This repetition (feed forward and back propagation) is done until minimizing the error for each output neuron and the network as a whole, thereby minimizing the difference between prediction output and actual output.

2.7.3 Loss function

Selecting the appropriate type of loss function depends on several factors such as the type of machine learning algorithm, the time cost of running the algorithm,... . In general, loss functions can be divided into two main categories:

- Regression loss functions: Mean Square Error, Mean absolute Error, Mean Bias Error
- Classification loss functions: Hing loss, Categorical Crossentropy

2.7.4 Optimization algorithm

An optimizer algorithm is applied in backpropagation to update the weights and bias of each neuron in order to minimize the loss function. Some of the best optimization methods used in machine learning model are Gradient Descent, Stochastic Gradient Descent (SGD), Stochastic Gradient Descent with momentum (SGDM) and Adam optimizer. More details of each of these optimizer can be found in [88].

2.8 Convolutional neural network

Artificial Intelligence has seen vast growth in recent years in bridging the gap between human and machine capabilities. Researchers in this field are working on various aspects of it to make special innovations happen. One of these aspects is computer vision with the specific algorithm of CNN. The goal is to enable machines to see the world like human, and to perceive it in a way similar to humans and apply this gained knowledge to many tasks such as image and video recognition, image analysis, image classification, and recommendation systems [86]. The structure of the CNN is actually inspired by the visual cortex of the brain. In 1962, two scientists, Hubel and Wiesel, introduced an interesting experiment on a cat brain [89]. They showed that by seeing the edges in different images, certain neurons in the visual cortex of the brain are stimulated. For example, by seeing the horizontal lines, certain neurons are stimulated, and by seeing the perpendicular lines, different neurons are stimulated and show sensitivity. They found that all of these neurons were arranged together in the form of columnar structures, and the result of their cooperation was that we could have a good visual perception of our surroundings. The basis of the work of the CNN is like the visual cortex of our brain. In fact, on a CNN, there are several layers, each with a specific layer to identify specific items. Finally, the output of the model is complete visual perception.

The typical structure of a Convolutional Neural Network is mainly composed of input layer, convolution layer, pooling layer, fully connected layer and output layer, as explained below.

2.8.1 Input layer

The input of the whole CNN is known as an input layer. In CNN for image classification task the input is normally a representation of a 2D image which can be expressed as a matrix of pixel values from 0 to 255, which describes the pixel's grey level at that point.

2.8.2 Convolutional layer

The convolutional layer (CVL) is responsible for feature extraction from input image. Each CVL applies filters (kernels) on a matrix of input image for feature extraction such as blur, sharpen, and edge detection. The matrix of feature map which generated by sliding the filter over the input image is shown in [Figure 2. 18](#).

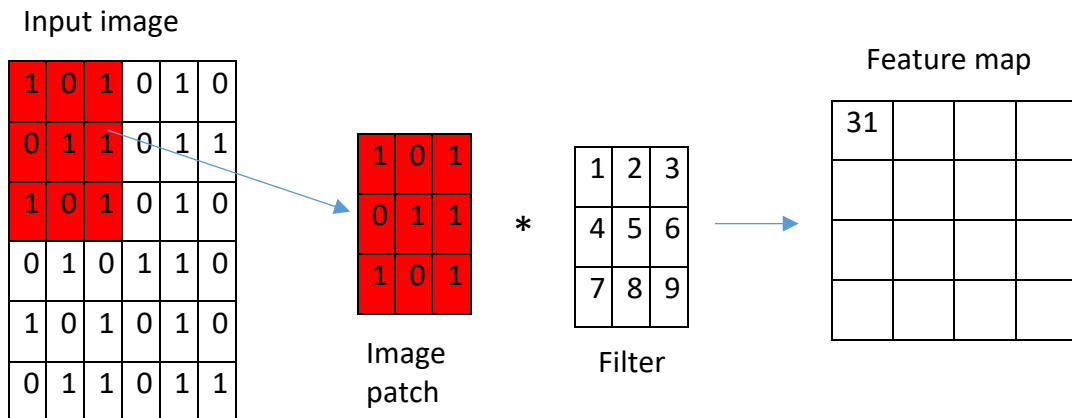


Figure 2.18: Convolution operation

The size of the output feature map is based on the stride and filter size, therefore for the input image with a matrix size of $(H \times H)$ and sliding filter with a matrix size of $(F \times F)$ and a stride of (S) , the output feature map with the size of $(W \times W)$ is given by [90]:

$$W = \left\lceil \frac{H - F}{S} \right\rceil + 1 \quad (2.53)$$

Stride defines the movement of the filter, if for example we set the stride=2, the filter takes two steps at the time. The stride default value is equal to zero.

After the convolution has completed the activation function which is explained in section 2.7.1 will apply to all values in the filtered image, in order to apply nonlinear feature.

2.8.3 Pooling layer

The pooling layer is also called subsampling or down sampling layer. This layer is responsible to reduce the size of each previous feature map and retains the most important information. There are two most used types of method of pooling: Max Pooling and Average Pooling [91] : Max Pooling returns the maximum pixel value from the part of the image covered by the filter (image patch). Max Pooling also does the "Noise Suppressant" function. It removes all the noise activation at the same time as reducing the size. Average Pooling returns the average of all values from the part of the image covered by the filter (image patch). The output after max pooling would be a feature map containing the most prominent features from the previous feature map while the output after average pooling would be the average features in the image patch, so it can be said that Max Pooling is much better than Average Pooling.

2.8.4 Fully connected layer

The fully connected layer (FCL) is usually used in the last layers of the network. As mentioned previously, the main features of the input have been extracted by the CV layer and the generated feature maps are down sized by pooling layer, then the output of the feature maps of the final pooling layer are transformed into 1D arrays and connected to one or more FCLs. In that case, every input is connected to every output by a learnable weight [92] and map the extracted features into the final output, such as classification. Each FCL is followed by a non-linear activation function. The activation function applied to the last FCL should be selected appropriately for each task. For example for multiclass classification tasks, the Softmax activation function should be used while for binary classification the Sigmoid activation function is the best choice [92].

Chapter 3: Methodology

3.1 Overview

This chapter explores the overall methodology, which was designed to produce significant results applicable utilised to the design of low THz radar in future autonomy.

In the following sections, firstly, the low THz radar systems used for this PhD research to collect the data for experimental purposes are described and characterized. The overall methodology for measuring the attenuation caused by radome contamination is described, however the measurement set up for each specific contamination described in details in chapter 4. Also this chapter describes the methodology for producing high resolution two dimensional (2D) imaging for automotive applications. The specified measurement methodology which was specifically developed and designed for forming low THz images in laboratory conditions and real outdoor scenarios is explained in details in chapter 6.

3.2 Radar system

In this study, two classes of experimental radar systems are described:

- The vector network analyser (VNA) which is used as a Stepped Frequency Radar (SFR) system to generate the SFR waveform, transmit the signal and receive the response through the attached antennas and finally save it for processing and further evaluation. In the PhD research the VNA is applied for measuring the signal reduction through radome contaminants within the range of low THz radar, VNA also used for measuring the signal backscattering from different rough surfaces at the range of low THz frequencies as well as for experiments on various rough surface radar imaging at low THz frequencies.
- 79 GHz FMCW radar system using fan-beam horn antennas, which has been used in the field experiments to classify the different road surfaces.

3.2.1 SFR VNA system

As mentioned in section 2.2.2, the SFR systems transmit pulses at different carrier frequencies in order to perform discrete modulation over time. VNA is used as a Stepped Frequency Radar, because it has the ability to measure the phase and amplitude between transmit and receive ports over a wide frequency range. VNA is capable to measure the transmission coefficient (S_{21}) and reflection coefficient (S_{11}) as shown in equations (3.1) and (3.2) for two port VNA.

$$S_{21} = \frac{V_2^-}{V_1^+} \quad (3.1)$$

$$20\log(S_{21}) = 20\log\left(\frac{V_2^-}{V_1^+}\right) = 10\log\left(\frac{P_{rx}}{P_{tx}}\right)$$

$$S_{11} = \frac{V_1^-}{V_1^+} \quad (3.2)$$

where V_2^- , V_1^+ are amplitudes of incoming voltage from receiver port, outgoing voltage from transmitter port respectively.

In this PhD research three different VNA is used to generate SFW signals:

- 300 GHz portable VNA (Agilent Fieldfox N9918A) for measuring the transmission coefficient through different radome contaminant (leaf, sand, oil,...)
- PNA N5232a in the range of low THz (150GHz - 670 GHz) to measure transmittivity through water-containing contaminants on antenna radome.
- VNA PNA-X N5247B to measure the backscattering from different surface roughness in the range of low THz frequencies.

3.2.1.1 300 GHz SFR

Figure 3.1 illustrate the 300 GHz radar system comprise an portable VNA(Agilent Fieldfox N9918A) connected to frequency up/ down convertor developed by VivaTech [93] in collaboration with MISL group, University of Birmingham. The mentioned system has been used for measuring the transmissivity through uniform layer of leaves [94].



Figure 3.1: portable VNA and frequency converters

The VNA generates stepped-frequency (SF) signals from 2 to 18 GHz which are up-converted to 282-298 GHz and transmitted by the square horn antenna with 10° 3dB beamwidth in both elevation and azimuth planes. The received signal is down-converted to 2-18 GHz and the scattering parameters (S_{21}) are measured. The converters and VNA are synchronised to an external 10 MHz reference signal provided by a rubidium oscillator.

Figure 3.2 shows the system schematic and the main parameters of the 300 GHz stepped frequency system are shown in Table 3. 1.

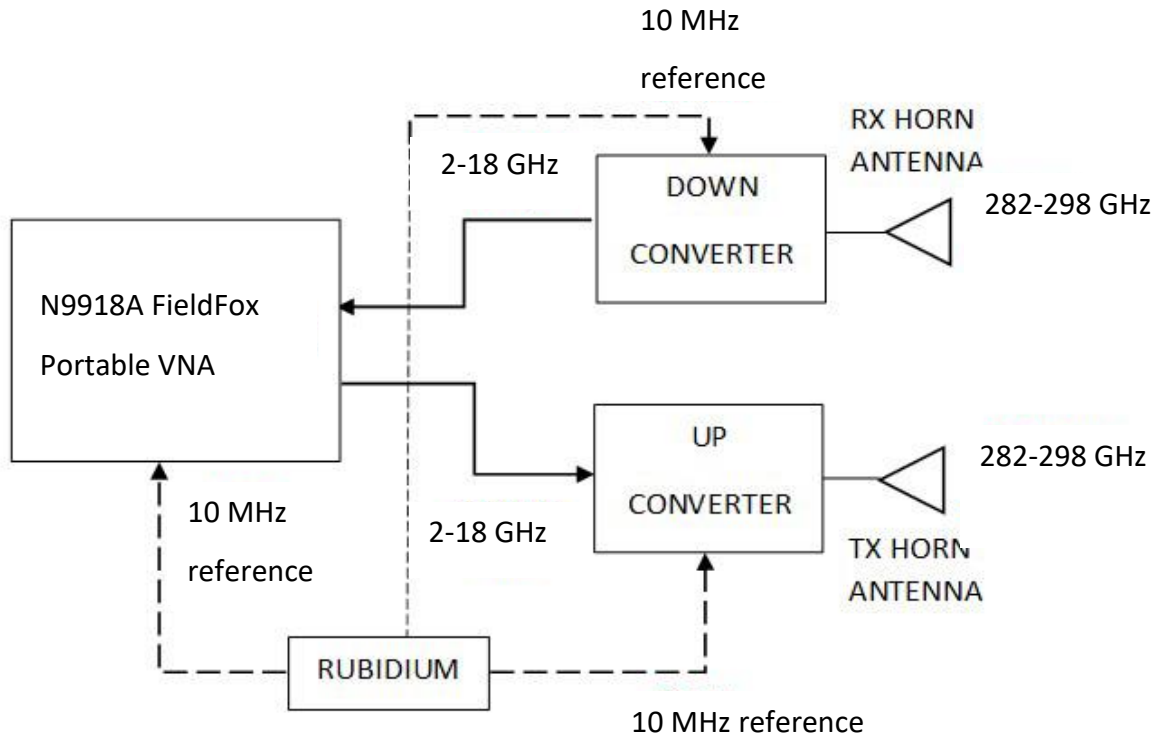


Figure 3.2: Schematic diagram of 300 GHz VNA and frequency converters

Table 3.1: 300 GHz SFR radar parameter

parameter	SFR
Frequency band	282-298 GHz
Bandwidth	16 GHz
output power	-17 dBm
Antenna gain	24 dBi
Antenna azimuth 3dB beamwidth	10°
Antenna elevation 3dB beamwidth	10°
IF bandwidth	1 KHz
Antennas type	Horn antenna

In order to increase the measurement accuracy through VNA and to achieve better dynamic range, the noise floor should be kept to a minimum. The following features help to reduce the noise floor:

- High Averaging: There are two types of averaging: point or sweep averaging. The Point averaging calculate the averaging on each data point before going to the next data point. The sweep averaging take the average of total sweeps. The higher the averaging factor, the less noise floor.
- Minimise the IF Bandwidth: The received signal is converted from its source frequency to a lower intermediate frequency (IF). Based on the model of VNA generally the IF bandpass filter bandwidth is adjustable down to a minimum of 1 Hz to the maximum of 15 MHz. In this PhD thesis the IF bandwidth has been chosen empirically for all used VNA's (with respect to VNA range allowance to ensure the noise floor was kept to a minimum while still achieving a reasonable acquisition time. In different experiments it varied from 100 Hz up to 1 kHz.

However we should note that both techniques of averaging and reducing IF bandwidth leads to increasing the acquisition time.

Additionally, the VNA needs to warm up (for minimum 30 minute) and stabilize before calibration and measurement which help to minimize thermal drift errors

3.2.1.2 SFR PNA

Data collection for measuring the transmissivity through a layer of water at frequencies of 300 GHz and 600 GHz were carried out with a SFR radar system composed of a 2-port Keysight Programmable Network Analyser (PNA N5232a) and linear up/down converters developed by VivaTech (Nice, France) in collaboration with the University of Birmingham. The PNA generates a stepped-frequency signal (4-20 GHz) which is up-converted to 282-298 for 300 GHz radar and 656- 672 GHz for 670 GHz radar and transmitted by T_x antenna. The received signal is received by an identical receiver antenna R_x and down-converted (4-20 GHz) and the scattering parameters are measured. Figure 3.3 shows the rectangular horn antennas at 300 and 670 GHz. The converters and VNA are phase locked to an external 10 MHz reference signal provided

by a rubidium oscillator. The system outline is visible in Figure 3.3 and the system parameters are summarized in Table 3.2.



Figure 3.3: Antennas (a) 300 GHz, (b) 670 GHz

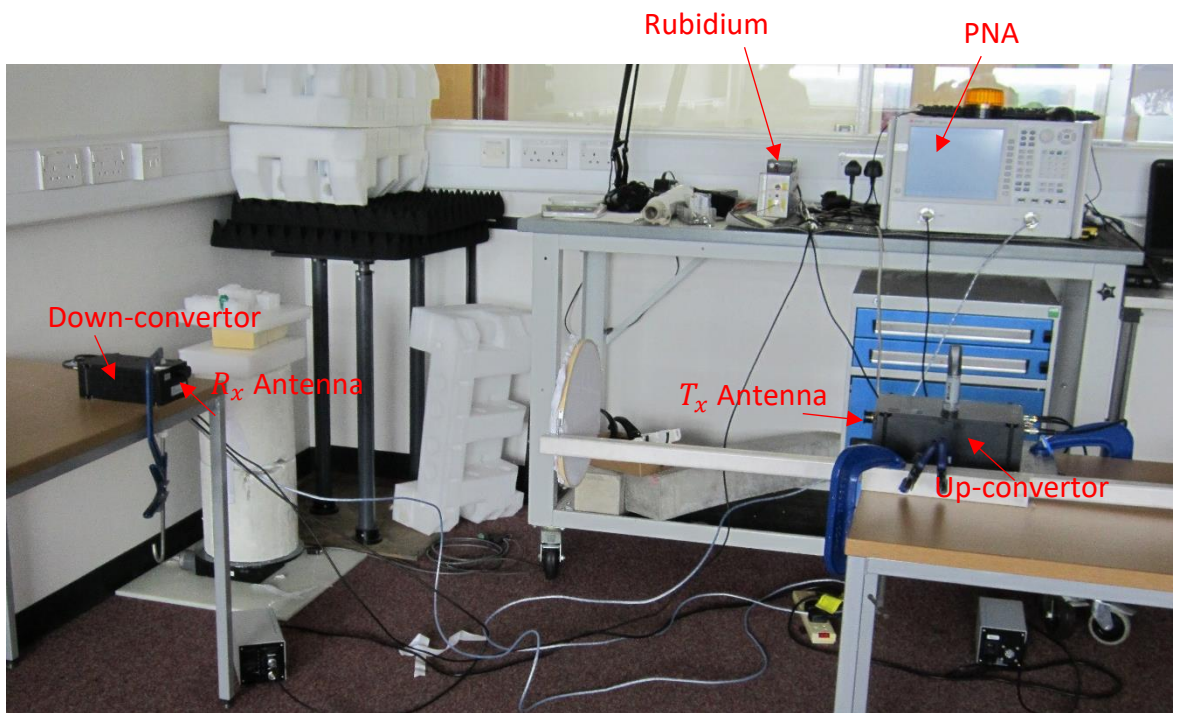


Figure 3.4: Photo of PNA SFR radar system

Table 3.2: parameters of the 300 GHz and 670 GHz SFR radar

Parameters	300 GHz	670 GHz
Frequency band	282-298 GHz	656-665 GHz
Sweep Bandwidth	16 GHz	9 GHz
Output power	-17 dB	-10 dB
Antenna type	rectangular horn	Square horn
Antenna Azimuth	10° (-3 dB)	10° (-3 dB)
Beamwidth		
Antenna Elevation	10° (-3 dB)	10° (-3 dB)
Beamwidth		
IF bandwidth	100 Hz	1 KHz
Antenna gain	25 dBi	20 dBi
Antenna dimension	6x8x22 mm	3x4x6 mm
Fairfield	128 mm	71 mm
Range resolution	9.4 mm	16.7 mm

3.2.1.3 SFR VNA

Figure 3.5 shows the Keysight N5247B VNA which is capable of measuring the full two-port scattering parameters in the frequency range from 10 MHz up to 1.1 THz using the frequency converter units [95]. The mentioned VNA has been used in practical measurements of signal reduction through a single leaf at low THz (150 GHz-900 GHz) as well as measuring the backscattering of different rough surfaces at low THz frequencies range (79, 150, 300, 670 GHz). The system was also used with scanning imaging antennas, as shown in figure 3.6, to collect data to produce high resolution image of different rough surfaces at frequencies of 150 and 300 GHz in order to classify them.

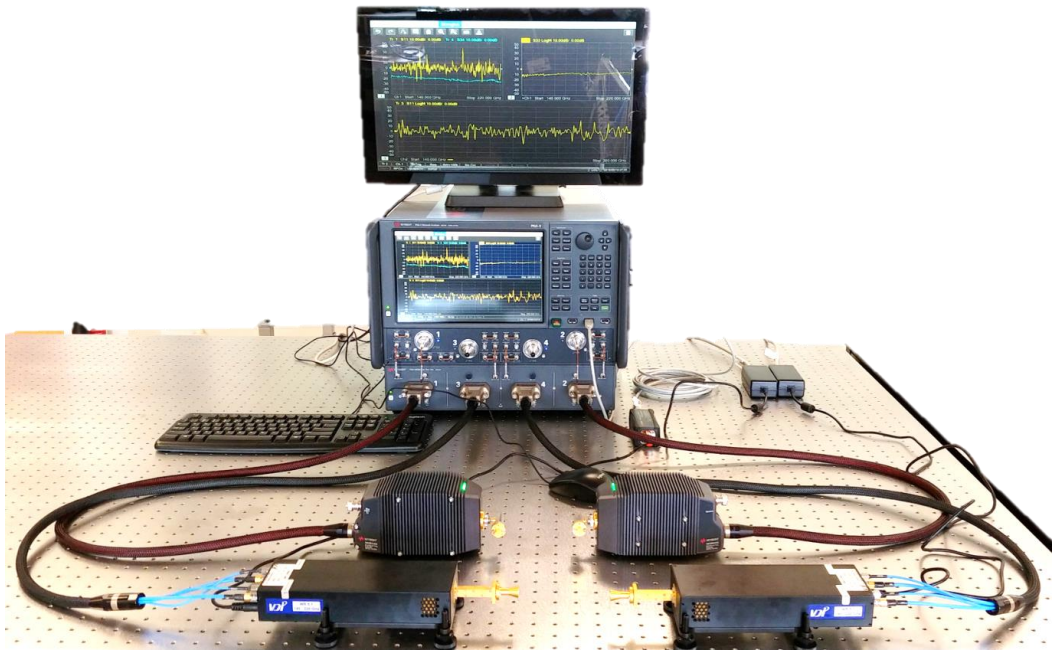


Figure 3.5: photo of VNA with up/down converters.



a

b

c

d

Figure 3.6: Antennas: (a) 79 GHz, (b) 150 GHz, (c) 300 GHz, and (d) 670 GHz.

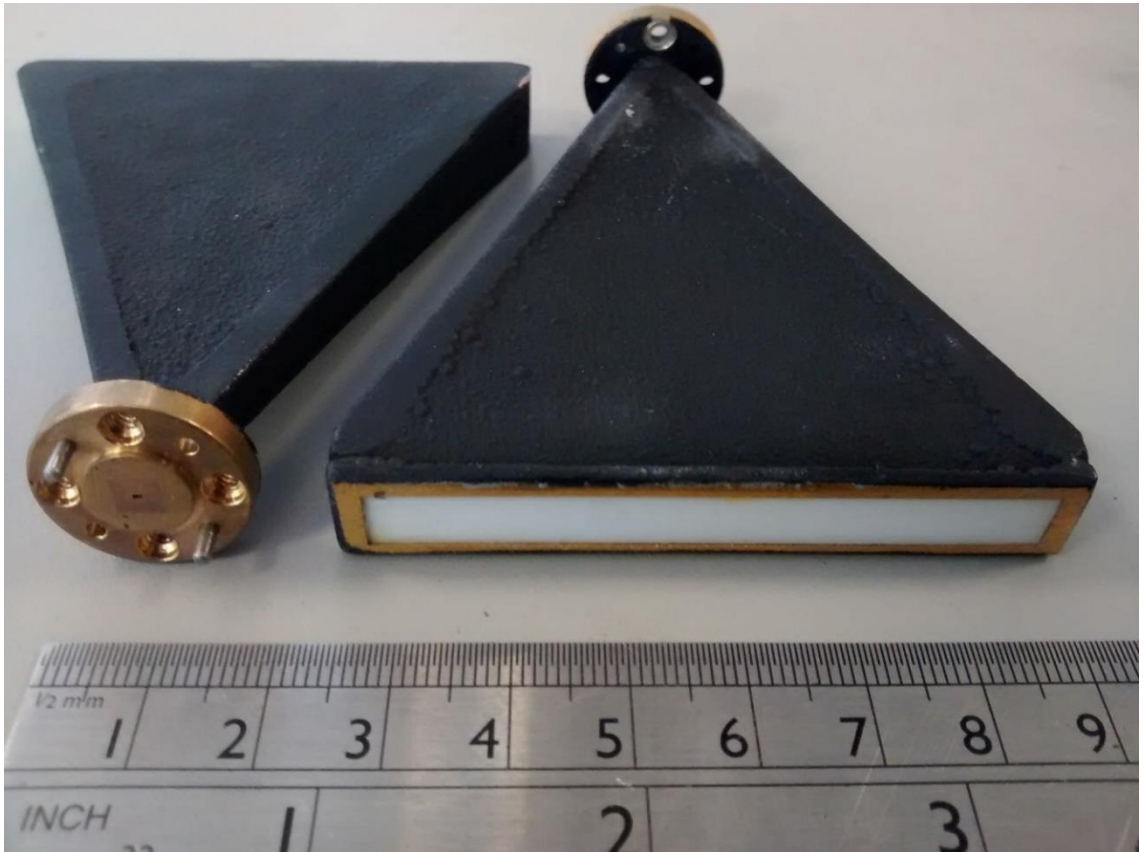


Figure 3.7: ELVA-1 300 GHz horn antennas

3.2.2 FMCW radar

The 79 GHz FMCW radar which was specially developed by ELVA [96] for MISL group in University of Birmingham, has been used for image data collection of different road surfaces with various roughness and texture. A photo of 79 GHz FMCW radar and a block diagram of overall system operation are shown in Figure 3.8 and 3.9 respectively.

13GHz signal is amplified by a power amplifier and up-converted to 79GHz by using ($\times 6$) multiplier fed by 13.1 GHz sweep synthesizer. The receiver, using an IQ mixer, mixes the transmitted signal with a replica of the received signal and is sampled through use of a picoscope [97] .

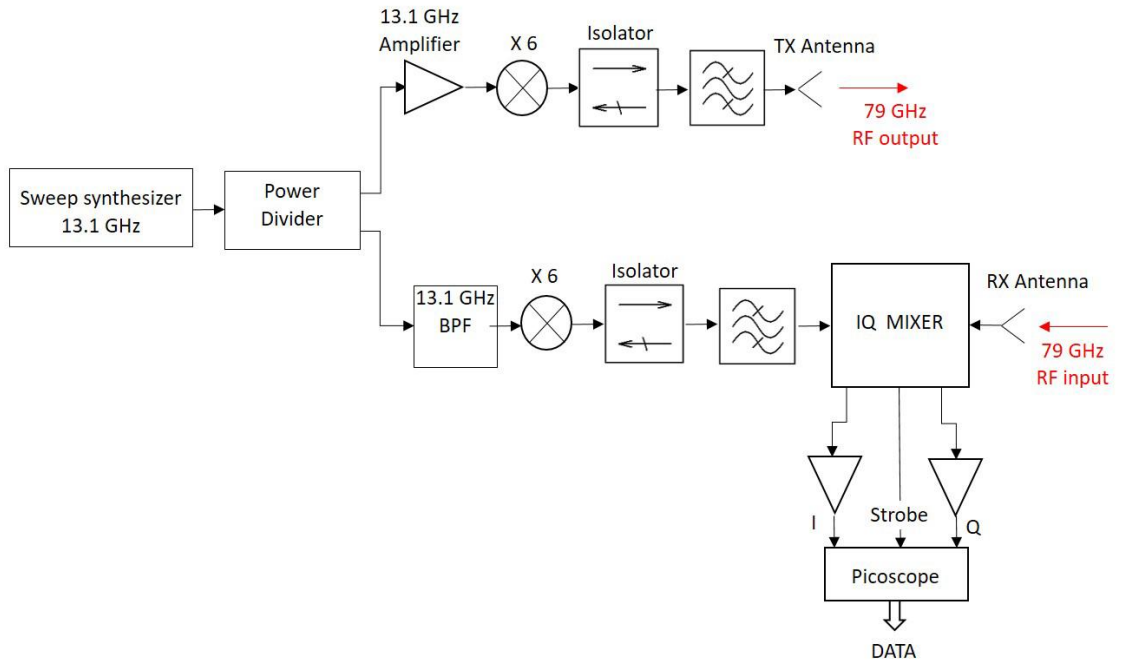


Figure 3.8: Summarized outline of 79 GHz FMCW radar

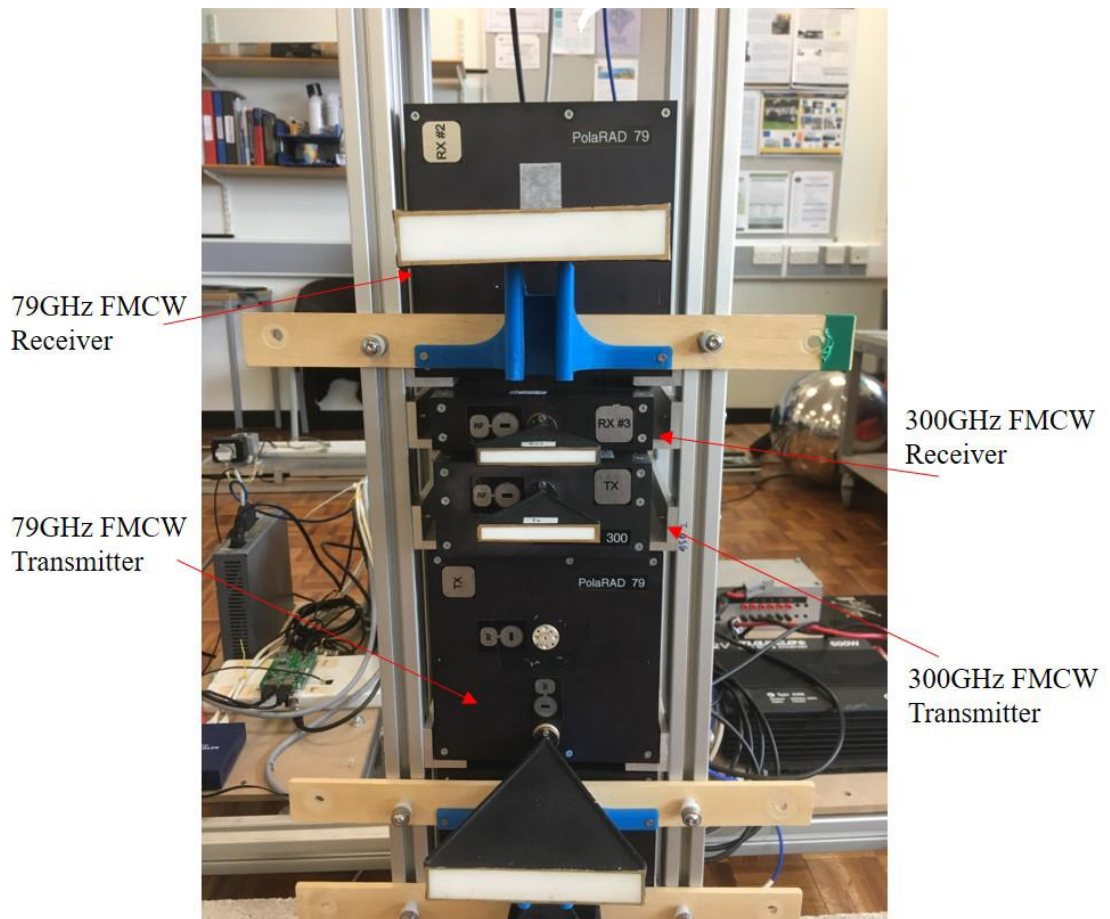


Figure 3.9: Photo of 79 GHz FMCW radar[98]

The 79 GHz radar signal bandwidth was set to 5 GHz to achieve about 3 cm range resolution ($\Delta r = \frac{c}{2B}$) and cover full automotive frequency allowance of 5 GHz (76–81 GHz). In order to obtain high-resolution radar images, two fan-beam horn antennas were used, having a narrow beamwidth (2.2°) in azimuth direction to provide a high angular resolution in azimuth and a wider beamwidth (15°) in vertical direction to deliver the required wide illuminated footprint along the path. The system specification is provided in Table 3.3.

Table 3.3: 79 GHz FMCW radar specification

Parameter	79 GHz FMCW
Frequency band	77-82 GHz
Wavelength	3.8 mm
Bandwidth	5 GHz
Output Power	15 dBm
Antenna type	Fan beam horn antenna
Azimuth Beamwidth	2.2° (-3 dB)
Elevation Beamwidth	15° (-3 dB)
Range resolution	30 mm
Receiver noise figure, dB	10
Sweep time, ms	1
Sweep repetition interval (SRI), ms	4.3

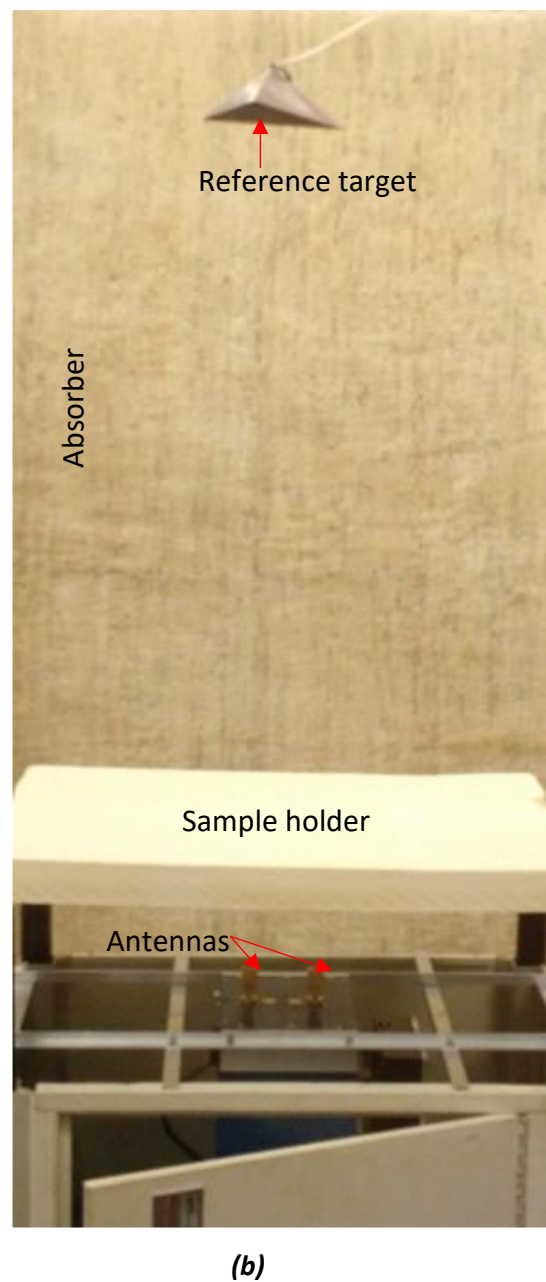
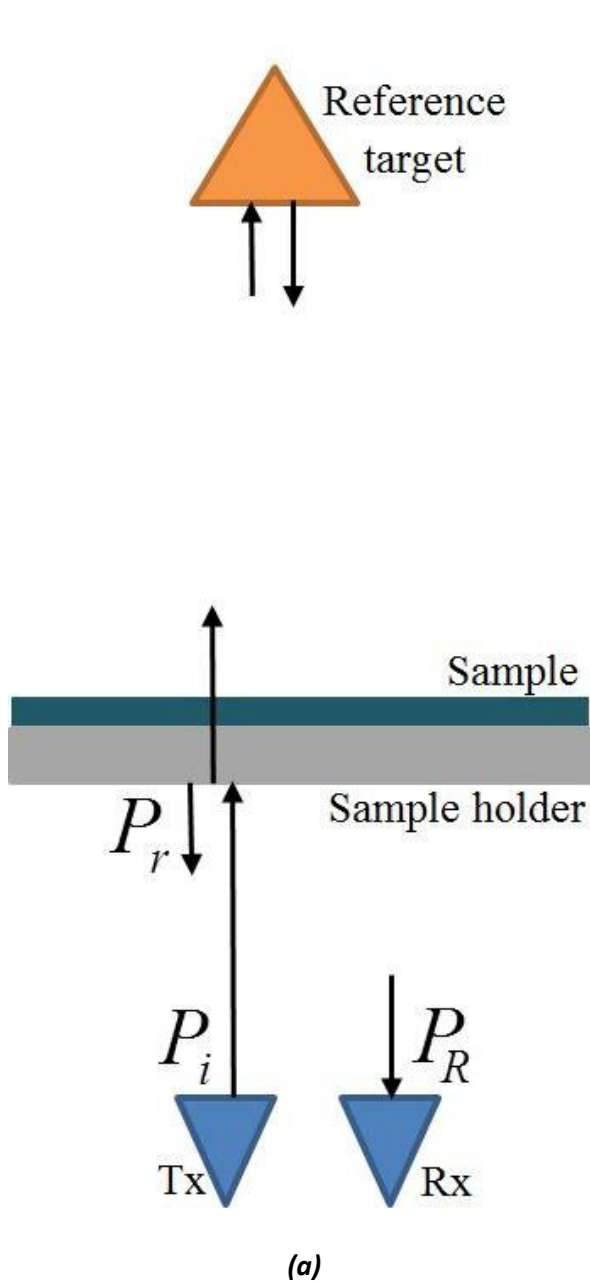
3.3 Radome contamination

At the start of this PhD research, a lack of the knowledge of signal reduction in presence of radome contaminant (oil, dust, leaves,...) at low THz frequencies was a big motivation for MISL group in the University of Birmingham to research the feasibility of low THz radar in outdoor scenario. This section describes the overall measurement methodology and measurement setup which has been applied by MISL group for measuring the signal reduction in presence of radome contaminant at low THz frequency range in laboratory condition.

3.3.1 Measurement methodology

The measurement setup is explained in [94]. Figure 3.10(a) shows the general view of measurement set up where P_r , P_R , T_x and R_x represent the incident power, reflected power from the bottom of sample (assuming the sample holder attenuation is negligible), received power at the receiver antenna, transmit antenna and received antenna respectively. When the signal comes from the transmitter and reaches the bottom of sample, part of the incident power (P_i) reflects back to the transmit antenna (P_r). The rest of the signal transmits through the sample holder as well as the sample, hits the target and finally travels back to the receiver (P_R). The actual measurement setup is shown in Figure 3.10 (b). The quasi-monostatic radar system (consisting of collocated T_x and R_x antennas) is located under the sample holder looking up at the reference target which is the suspended corner reflector with known RCS of 29.4 dBsm (decibels per square meter) at 300 GHz. A sample of contaminant is placed on a sample holder, between the antennas and the reference target in the path of the signal to obscure the radar beam. The sample holder was chosen from rigid material to provide robust and stable surface which can tolerate the weight of a sample without bending. It also needed to be easy to replace after each experiment. Furthermore the sample holder needed to have low reflection and low signal attenuation, a thickness equal to an integer number of half wavelengths and a low dielectric constant. The chosen sample holder was foam, made of closed cell polyurethane which demonstrated less than 2 dB attenuation at low THz frequencies and having the thickness of 50 mm which equals an integer multiple of half wavelengths at 150 GHz (2 mm) and 300 GHz (1 mm) and a dielectric constant of approximately 1.2 at both mentioned frequencies. The antenna's beamwidth in both elevation and azimuth is 10° for both frequencies. The distance

between the sample holder and antennas, and antenna and target is 200 mm and 220 mm respectively. The area that the sample needs to cover should be greater than the footprint of the illuminating beam, defined by the radiation pattern 3 dB roll-off, to guarantee that most of the energy passes through the sample. Based on the mentioned distances and antenna's beamwidth, the sample must cover an area exceeding 35 mm × 35 mm. The main benefit of this measurement setup is that various samples can be applied without the need for further alignment.





(c)

Figure 3.10: Experimental setup configuration (a) general view (b) actual system setup (c) antenna setup

We use term ‘transmissivity ‘ to indicate the signal level reduction due to presence of sample combined with other possible propagation mechanisms (scattering, absorption, reflection and refraction) which can be computed as:

$$T(dB) = 10 \log \left(\frac{P_R}{P_{R_0}} \right) \quad (3.3)$$

where P_{R_0} and P_R represent the received powers when reflected by the reference target through the sample holder without the sample and with presence of the sample, respectively.

3.3.2 Theoretical model

In order to evaluate the transmissivity through contaminant built up on the antenna radome at low THz frequencies the Fresnel theory [99] is used. The model is developed for a three layer structure, air-contaminant-air as shown in Figure 3.11.

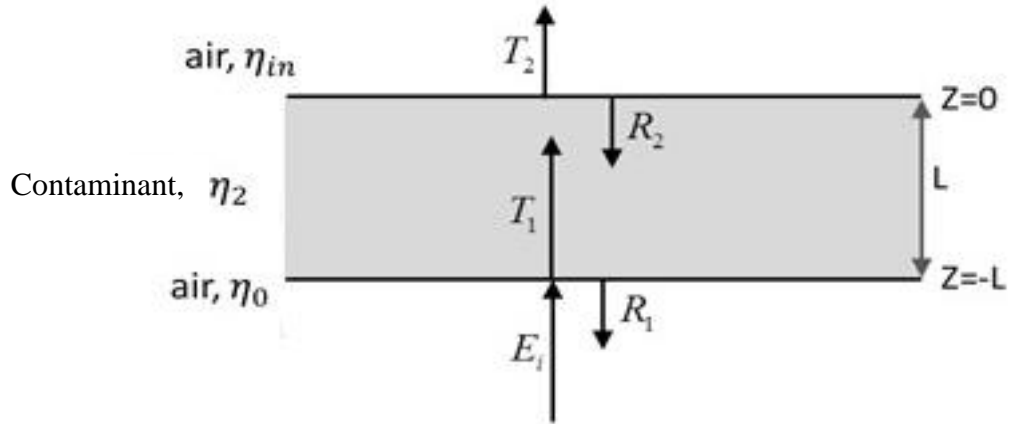


Figure 3.11: Three-layer structure used to model the transmissivity through uniform layer of leaves

The transmissivity in the third layer (air) can be computed as bellow

$$T = \frac{4\eta_0\eta_{in}}{(\eta_0 + \eta_{in})^2} \quad (3.4)$$

where η_0 is the wave impedance of air and η_{in} is the input impedance at the interface of radome contaminant and air and can be calculated using transmission line theory [100] :

$$\eta_{in} = \eta_2 \frac{\eta_0 \cosh(\gamma l) + \eta_2 \sinh(\gamma l)}{\eta_2 \cosh(\gamma l) + \eta_0 \sinh(\gamma l)} \quad (3.5)$$

where l is the thickness of layer of contaminant and η_2 is the wave impedance in the second medium(radome contaminant) and can be described by:

$$\sqrt{j\omega\mu/(\sigma + j\omega\mu)} \quad (3.6)$$

Chapter 3: Methodology

where σ is the conductivity of material, μ is the magnetic permeability and ε is the dielectric permittivity of radome contaminant, γ is propagation constant and can be calculated by:

$$\alpha + j\beta = j\omega\sqrt{1 - j\frac{\sigma}{\omega\varepsilon}} \quad (3.7)$$

where α and β are attenuation constant and phase constant respectively.

The complex permittivity is the most influential parameter defining the transmissivity through radome contaminant which depends on the material, operating frequency, temperature, humidity,... The values of permittivity of leaves and water under their measuring frequencies will demonstrate in section 4.2.4 and 4.3.3, respectively.

3.4 Backscattering of Radar Signal from Rough Surface

The lack of comprehensive and consistent surface scattering studies over both the millimetre-wave and THz range simultaneously motivates this PhD research. Hence, the second aim of this PhD research is to study and characterize the effect of signal backscattering from rough surfaces in the range of millimetre-wave and low THz frequencies (79 GHz-670 GHz) within the context of Surface ID for automotive sensing. To achieve this goal and attain accurate measurement, sandpaper of different coarseness (grit) was used as a reference surface. The results can easily be extended to the case of real road surfaces if their roughness and complex permittivity are quantified. This section provides precise description of the experimental methodology for measuring the signal backscattering from different sandpaper of different coarseness (grit).

3.4.1 Normalized RCS

The reflective properties of a surface are characterized by its normalized RCS. The normalized RCS of a distributed target is an ensemble average of the RCS σ per unit area:

$$\delta^0 = \langle \sigma \rangle / A \quad (3.8)$$

where A is the illuminated area. In chapter 5 Section 5.5 we will show how this ratio can be determined using a VNA.

The return power when the target is illuminated by a monostatic radar can be calculated using radar equation:

$$P_r = \frac{P_t G^2 \lambda^2 \sigma}{(4\pi)^3 R^4} \quad (3.9)$$

where P_t and P_r are transmitted and received power, G is antenna gain, R is the distance to the target, and σ is radar cross section. Thus, knowing the characteristics of the system, we can calculate σ from equation (3.9).

This calculation can be simplified, and measurement accuracy improved by calibrating the system and excluding the values of G and λ from the calculation. To calibrate the system, we carried out the free space measurement by placing the receiver at the distance $2 \times R_0$ from the transmitter. Then the power received by the antenna is described by Friis Transmission formula:

$$P_{Rf} = \frac{P_t G^2 \lambda^2}{(4\pi)^2 4R^2} \quad (3.10)$$

From equations 3.9 and 3.10 it follows that

$$\delta = \pi R^2 \frac{P_r}{P_{Rf}} \quad (3.11)$$

The squared magnitude of the VNA transmission coefficient S_{21} is equal to the ratio of received power to transmitted power [101]

$$|S_{21}|^2 = P_r / P_t \quad (3.12)$$

Therefore, RCS can be calculated as:

$$\delta = \pi R_0^2 \frac{|S_{21}|^2}{|S_{21f}|^2} \quad (3.13)$$

where S_{21f} is the measured transmission coefficient in free space. Thus, by measuring S-parameters for the surface under test and in free space, and calculating the illuminated area, we can find the normalized RCS δ_0 as defined in equation 3.8. In chapter 5 we will describe precisely the measurement setup for measuring normalized radar cross-section (RCS) of rough surfaces and present a method to calculate the normalized RCS of surfaces of different roughness as a function of radar and topology parameters, such as polarization and aspect angle. Also, the obtained measurement results have been demonstrated which analysed for compliance with Fraunhofer criterion and were compared with normalized RCS, calculated based on an improved empirical model.

3.5 High resolution imaging radar

As mentioned in Chapter 1, unlike LIDAR and optical cameras, radar has advantages of operating in harsh weather and any lighting condition, so the imaging radar is used to capture a 2D (azimuth, range) image map of the road surfaces and objects in a road environment. Radar imagery generally refers to the system which forms the image of an object or road surface by registering the intensity of reflected signal to determine the amount of backscattering signal. The backscattering signal is then built into a two-dimensional image map. The high resolution image can be applied for object and road surface classification and feature detection. The method which is applied in this PhD research to gain the backscattering map of the scene and the image of road surface and objects in the road is based on a physical beam mapping method. In order to create the high resolution radar image for a medium range automotive application the following general requirements are needed:

- The antennas with wide E-plane (elevation) beam Θ_E to provide the required wide illuminated footprint along the path and narrow H-plane (azimuth) beam Θ_H to provide fine angular resolution. Figure 3.12 illustrates the antenna footprint on the ground in monostatic setup.
- Wide operational bandwidth to deliver the high range resolution. In this thesis, the wide bandwidth has been achieved by 150 and 300 GHz SFW radar (section 3.2.1.3) and a 79 GHz FMCW radar (section 3.2.2).

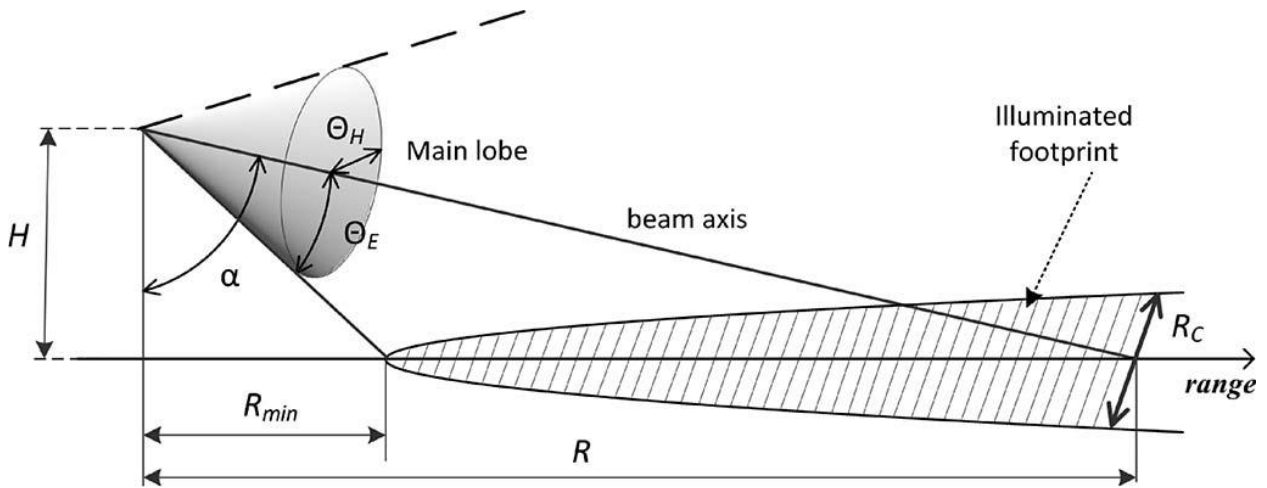


Figure 3.12: Single beam monostatic configuration for imaging radar. H is the antenna elevation; Θ_E and Θ_H are beamwidths of antenna pattern in E-plane and H-plane accordingly. R is the distance to the center of the footprint, defined by beam axis direction; R_c is the linear angular range at the distance R . [35]

The high resolution image is created by narrow-beam scanning antenna (in azimuth) which illuminates to a small part of the scene in each scan angle and scanning the scene electronically with rotating table. The rotating table rotation and the data acquisition are run by codes which had been written in Matlab and save the backscattered signal data one after each other to hard disc . The 2D image is produced by augmenting range profiles produced at each azimuth position (scanning angles). Figure 3.13 shows the vehicle scanning the illuminated area in the front of the antennas mounted on the vehicle. The polar range profile then converted to the Cartesian x-y surface. The 2D intensity image map as a function of range and azimuth angle were generated in MATLAB. The 2D radar image are composed of many pixels, which each pixel in the radar image represents the radar backscatter for that area. Figure 3.14 shows the schematic image map (a) example of scene camera image (b) with correspondence 79 GHz radar image (c).

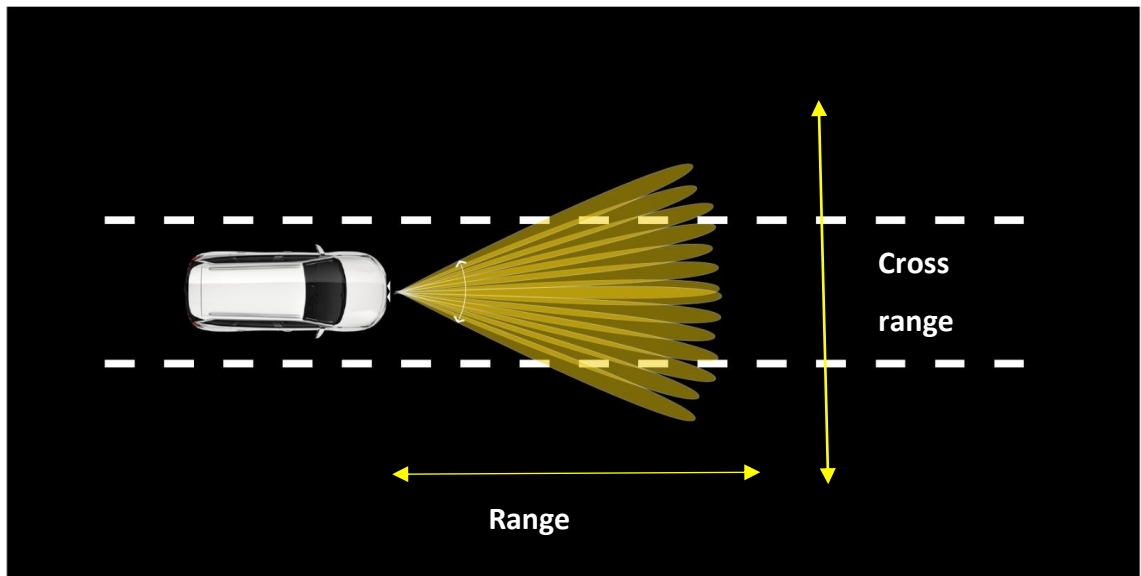
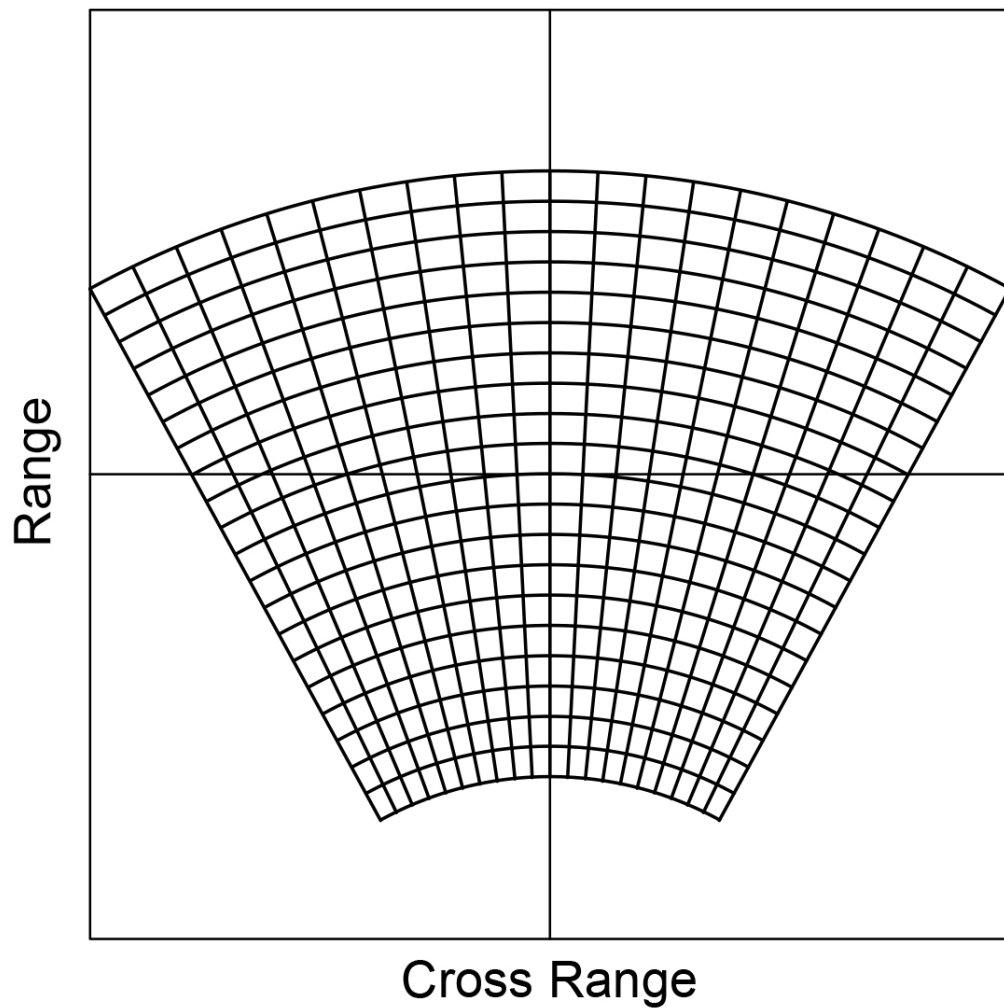


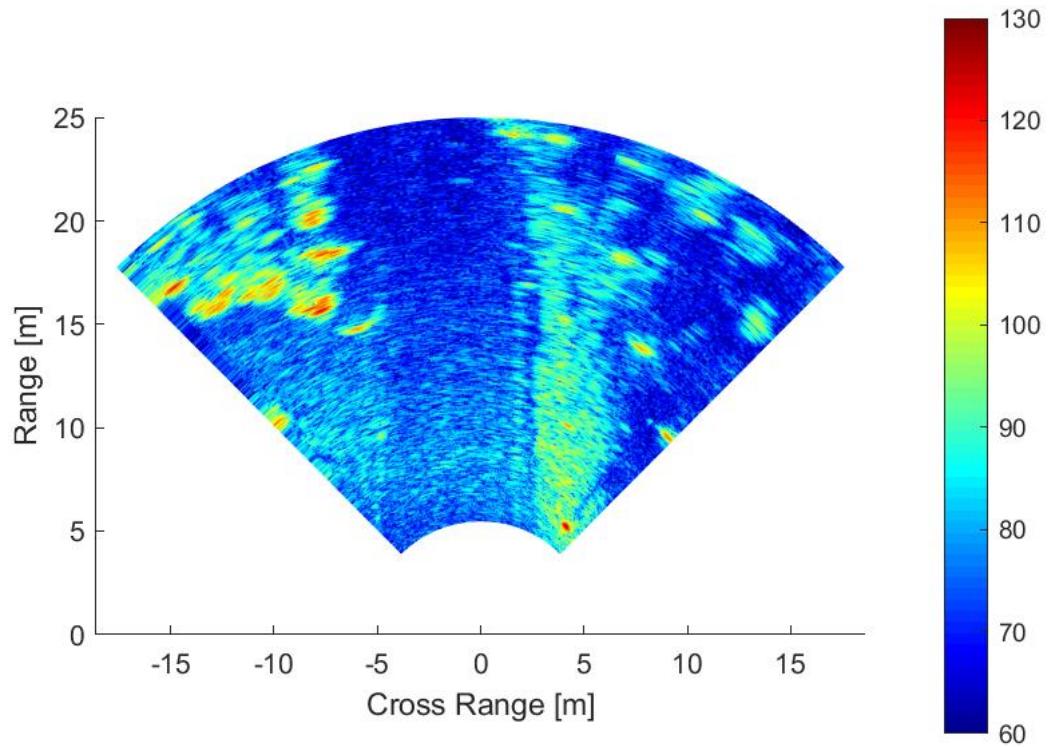
Figure 3.13: Vehicle scanning the illuminated area in the front of the antennas mounted on the vehicle.



(a)



(b)



(c)

Figure 3.14: Curved image map from rotating scanning imaging antennas(a), camera image(b), 79GHz radar image (c)

Chapter 3: Methodology

In this PhD research in order to verify the methodology, we explore the performance of imaging radar at 150 GHz and 300 GHz in classification of surfaces with different roughness in the laboratory conditions and classify the radar image with application of neural network, which is explained in details in chapter 6 section 6.3. These gained results lay the foundation for our further work on the development of automotive radar for surface classification. So in our next stage we applied the developed approach to the radar image of actual road scenes collected during outdoor trials (actual road scenarios), and classify through neural network, for which the methodology , analytical approach and the gained result will be described in details in chapter 6 section 6.4.

3.6 Summary

This chapter firstly, discuss the low THz radar systems used for this PhD research in order to collect the data for indoor and outdoor experiments. For the experimental purpose two type of radar systems have been used: The Stepped Frequency Radar (SFR) in the range of low- THz frequencies (150GHz- 670 GHz) and 79 GHz FMCW radar.

Secondly, the overall methodology and measurement set up for characterisation of the attenuation caused by radome contamination (including oil, dust and leaves) at low THz frequencies is described.

Thirdly the overall methodology of measuring the signal backscattering from different sandpaper of different coarseness (grit) has been discussed in this chapter and the method of measuring the normalized RCS is shown, and finally this chapter describes the methodology for producing high resolution two dimensional (2D) imaging for automotive applications.

Chapter 4: Signal reduction due to radome contaminant

4.1 Overview

As mentioned before, low-Terahertz (low THz) radar is the new research trend for automotive applications, as it can provide higher image resolution compared to traditional automotive radars. The knowledge of the performance of radars in harsh and uncontrolled outdoor environment is fundamentally important for the development of automotive sensors.

As shown in Figure 4.1, the areas of potential signal reduction in automotive radars occur in three media: radome contamination (leaves, ice, sand,..); wave propagation through atmospheric conditions such as snow, rain, fog and hail; and radar installation behind the car's surface components. Understanding these mentioned areas is critical before applying low THz technologies into automotive applications.

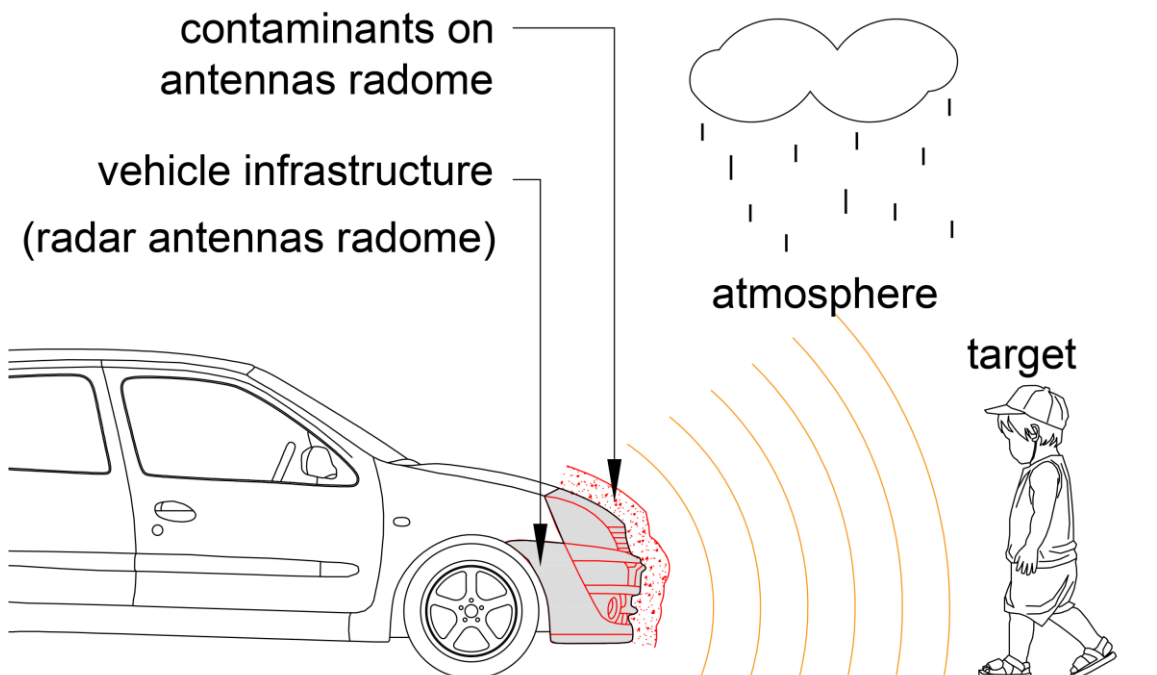


Figure 4.1: signal reduction medium for automotive radar

Chapter 5: Low terahertz radar signal backscattering for surface identification

This chapter focused on characterising the signal attenuation through contaminants accumulated on the radome of automotive sensor in the range of low THz radar which was carried out by the author of this thesis and MISL group at university of Birmingham. The chapter combines original results obtained by the author regarding the signal attenuation caused by radome contaminant (water, leaves) at low THz range, as well a review of works undertaken at MISL as part of the project TRAVEL. In the following sections, firstly the study of signal attenuation by tree leaves at 300 GHz radar published by the author [94] is shown. Secondly, results on signal attenuation by different water in low THz Automotive Radar are shown, which written by the author of this thesis and accepted by European Microwave Conference (EuMC) and will be published in January 2022 [102]. Thirdly, the summary of results of attenuation of low THz signals due to radome contamination which has been done by MISL group and published on [103-105] are shown.

4.2 Signal Reduction by tree leaves in Low THz Automotive Radar

4.2.1 Overview

In this section, the attenuation of signal propagating through leaves which can build up on the antenna radome is investigated. In the following sub sections, three sorts of leaves (Laurel, Birch, and Willow) are chosen in this measurement as likely obscurants which can stick to automotive radar radome and cause signal degradation. Transmissivity through a uniform layer of the leaves with different water contents is measured with 300 GHz radar. The water content is estimated in leaves drying gradually. The complex permittivity of the leaves with different water contents is estimated and these values are used to calculate the transmissivity through the uniform layer of leaves. Comparison of transmissivity in equivalent water layer with that of leaves having the same water content is made. Measured transmissivity through leaves is compared with that obtained by a theoretical model. The mentioned research was published by auther of this thesis in [94].

4.2.2 Introduction

For automotive sensing the degradation of radar signal propagation through layers of obscurant built up on a sensor radome is an important issue as the chance of covering radome of the car sensor by leaves (especially during autumn) is high and this can cause a temporary outage of sensor functioning. A leaf will interact with Electromagnetic (EM) wave and can cause signal reduction. In [106], the complex permittivity of coffee leaves with respect to the leaves' water content are studied for frequencies between 0.3-1.8 THz. The measured and calculated values of real part of the refractive index for water layer and fresh leaves show a good agreement. However, for the absorption rate observed at higher frequency range (0.6-1.8 THz) there is a large discrepancy between the measurement and calculated results. The improved permittivity model is proposed in [106] by accounting for the scattering through Rayleigh roughness factor. When the leaves are fresh it is shown that transmission losses are around -10dB and then the transmission losses increase to -0.9 dB after leaves are left for 21 days drying in natural conditions (see figure 4.2). The effect of leaves with different water content on absorption coefficient is also studied in [107] at 94 GHz: it was shown that there is an increase in the transmission due to natural water loss in *Fatsia japonica* and *Catalpa bignonioides* leaves during 200 hours of natural drying. The transmittance when the *japonica* and *Catalpa bignonioides* leaves are fresh is shown to be -9 and -6 dB, respectively, however this value increases until they become almost dry and become -3.09 and 0.44, respectively. The aim of this study which was published in [94] is to study the effect of leaves on low THz wave propagation. Transmissivity through a uniform layer of leaves is calculated based on Fresnel theory [99]. The measurement results of transmissivity at 300 GHz through a uniform layer of leaves are presented for three different species - laurel, birch and willow. This research shows how the knowledge of transmission performance, as well as the dielectric permittivity of leaves will have possible effect on the automotive radar performance.

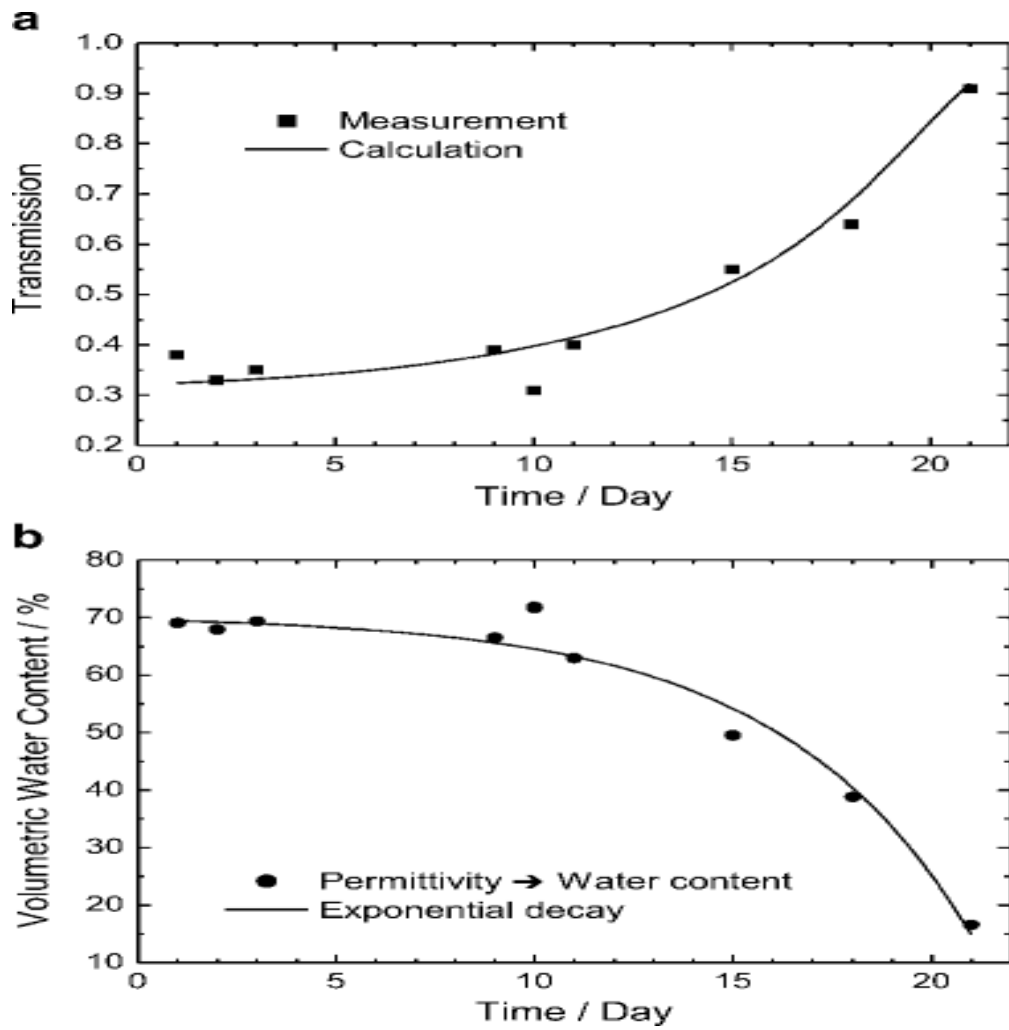


Figure 4.2: *Coffea arabica* leaf (a) Transmitted intensity at 300 GHz (b) and volumetric water content reduction [106]

4.2.3 Theoretical model

In order to evaluate the transmissivity through leaves built up on the antenna radome at low THz frequencies the Fresnel theory [99] is used. The model is developed for a three layer structure, air-leaves-air as discussed in section 3.3.2.

The complex permittivity is the most influential parameter defining the transmissivity through leaves. Leaves have the complex structure made of biological tissues (solid plant material), air and water. The complex permittivity of a complex mixture can be explained by Effective Medium Theory (EMT) as developed by Landau, Lifshitz, Looyenga (LLL model) [100]. LLL model describes permittivity of a two-compound mixture and a third-order extension of LLL model taken from [108] is used in this work:

$$\sqrt[3]{\epsilon_L(f)} = \xi_W \sqrt[3]{\epsilon_W(f)} + \xi_S \sqrt[3]{\epsilon_S(f)} + \xi_A \sqrt[3]{\epsilon_A(f)} \quad (4.1)$$

Here ξ_W , ξ_S , ξ_A are volume concentrations of water, solid plant material and air respectively, which can be calculated by the following formulas:

$$\xi_S = \frac{T_3}{T_1} \quad \xi_W = \frac{M_1 - M_2}{T_1 \rho_W A} \quad \xi_A = 1 - \xi_S - \xi_W$$

The indices 1, 2, 3 stand for the measured values of fresh leaves, drought stressed leaves and pressed leaves respectively. M is the mass of leaves, T is the thickness of leaves, A is the area of uniform layer of leaves and ρ represents the specific gravity of water.

To evaluate the concentration of solid material, the leaves (which contains air and solid material) are pressed under a load of 1 tonnes for few minutes to remove all air within the leaves. The leaves thickness are evaluated by measuring their thickness using a micrometer screw and determining their means from fresh until they are almost dry. In our measurement on Laurel leaves the average thickness of fresh leaves and dry leaves was approximately 0.35mm and 0.2 mm, respectively, while the average leaf thickness after pressing was measured as 0.13 mm. The change in thickness attributes to the loss of air.

In [109], the complex permittivity of water at frequency of 300 GHz is obtained as:

$$\varepsilon_W = 4.5 - 4.8j$$

The complex dielectric permittivity of solid plant material is taken as in [106]:

$$\varepsilon_S = 3.12 - 0.25j$$

The leaves' water content reduction is evaluated by measuring their weight until they are almost dry. Because the rates of water reduction are slightly different for individual leaves, the average weight of leaves is used. This averaging is one of the causes of measurement error but it can be used to generate a statistically representative set of measurements. The Water Content Reduction (WCR) of leaves is calculated by:

$$(WCR)\% = \frac{FW - DW}{FW} \quad (4. 2)$$

where FW is weight of leaves when fresh and DW is weight of leaves when dry.

Figure 4. 3 shows the rate of water content reduction over the time. The error bars of WCR are calculated by standard deviation of their weights at different periods of time. It can be seen that the leaves' water content reduces with similar rate over the certain time for all species of leaves. The rapid rate of losing water content within the first 10 hours changes to slow rate within following 10 hours to 65 hours of drying. As the Willow leaves are thinner than leaves of birch and laurel their rate of WCR is faster for the first 40 hours. Water content reduces 10% during first 2 hours and reached nearly 42%, after 10 hours. The laurel and birch leaves have almost the same WCR trend.

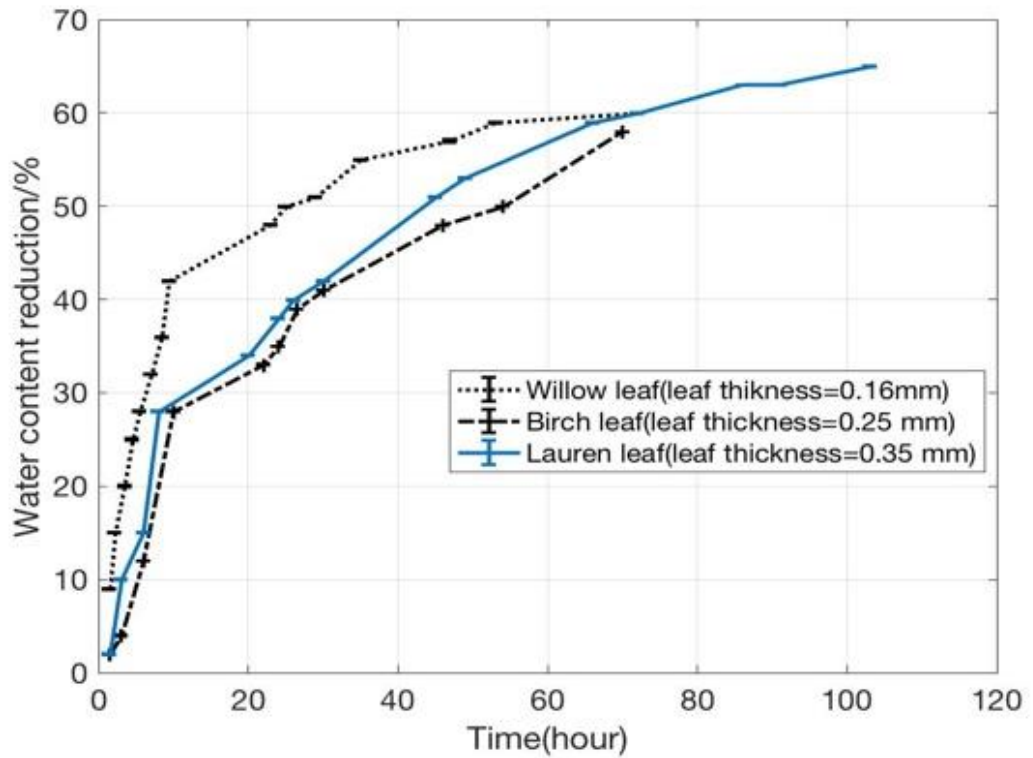


Figure 4.3: Evaluation of leaf water content based on time.

4.2.4 Methodology

The main focus of this study is on evaluating the signal reduction of low THz waves when passing through uniform layer of leaves. In order to achieve the goal of this research and attain more accurate practical measurement, the transmissivity through 3 different species (Laurel, Birch, Willow) are measured and the effect of their water content on signal transmission at 300 GHz are studied. Laurel, Birch and Willow are denoted as L, B and W, accordingly.

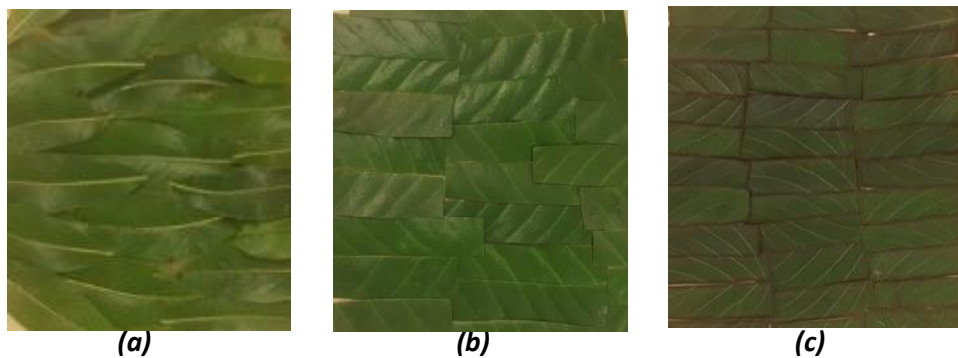


Figure 4.4: Photo of detached leaves of (a) Willow (b) Lauren and (c) Birch

4.2.5 Measurement

The SFR radar which was explained in section 3.2.1.1, sweeping from 282 to 298 GHz, used for measurement, is developed by VivaTech in collaboration with the University of Birmingham.

The measurement setup is described in detail in 3.3.1. As shown in Figure 4.5 the monostatic radar is located under the sample holder looking up at the reference target –a suspended corner reflector or sphere with known RCS. Samples (leaves) are placed on the sample holder. The intensity of signal propagating through the sample and reflected from the target is compared to that when no sample is present.

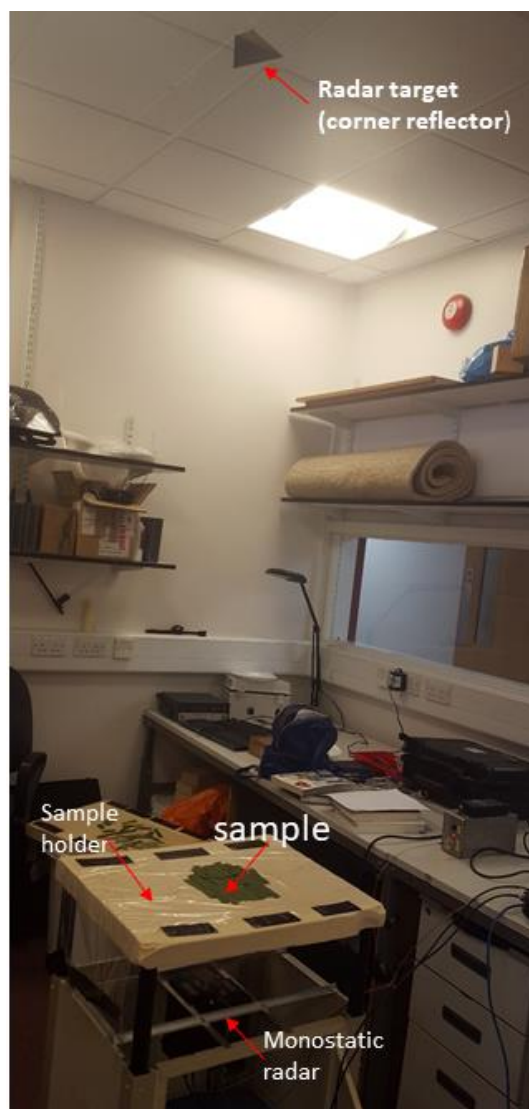


Figure 4.5: Measurement setup configuration

The received signal is recorded in the frequency domain and transformed to the time domain using an Inverse Fast Fourier Transform (IFFT).

The signal transmissivity due to the presence of a uniform layer of leaves combined with other possible propagation mechanisms (scattering, absorption, reflection and refraction) can be calculated by equation 3.3.

As shown in Figure 4.4 leaves Laurel 4.5b and Birch 4.5c cut into a similar sized square pieces to cover the area without overlapping or gaps to form the uniform layer. These leaves are arranged to have area larger than 7 cm to impose the sample within the footprint of illuminating beam and allow most of the energy transmitting through the leaves. The leaves are left on the sample holder for about 70 hours till they lose almost all their water content. The transmission through the leaves is measured during this time. Reference sets of leaves are chosen to quantify the rate of their water content reduction. The room temperature and humidity are measured by EasyLog | EL-USB-2 [110]: the temperature of 22 ± 2 Celsius ($^{\circ}\text{C}$) and humidity of 45 ± 5 per cent are observed throughout the measurement campaign.

Some spread of measured values from different sets of leaves may arise due to the presence of small air gaps between individual leaves (increased during the drying process) and also due to different rates of water reduction for individual leaves.

4.2.6 Result and discussion

Figure 4.6 illustrates the transmissivity through a uniform layer of Laurel leaves vs. WCR at 300 GHz. As expected there is an increase in transmissivity as leaves lose their water content with the max reduction of -20 dB when leaves are fresh. In the range of 30% to 40% of WCR, a fall in transmissivity is recorded which can be explained by change of size of leaves as they lose water and therefore appearance of air gaps between them. The signal loss due to presence of fresh leaves of Laurel, Willow and Birch are -20 dB, -16 dB and -12 dB, respectively. The general trend shows a dramatic increase in transmissivity until they lost almost all of their water. The transmissivity of -2.2 dB, -3.9 dB and -1.5 dB are measured for water stressed leaves L, W and B.

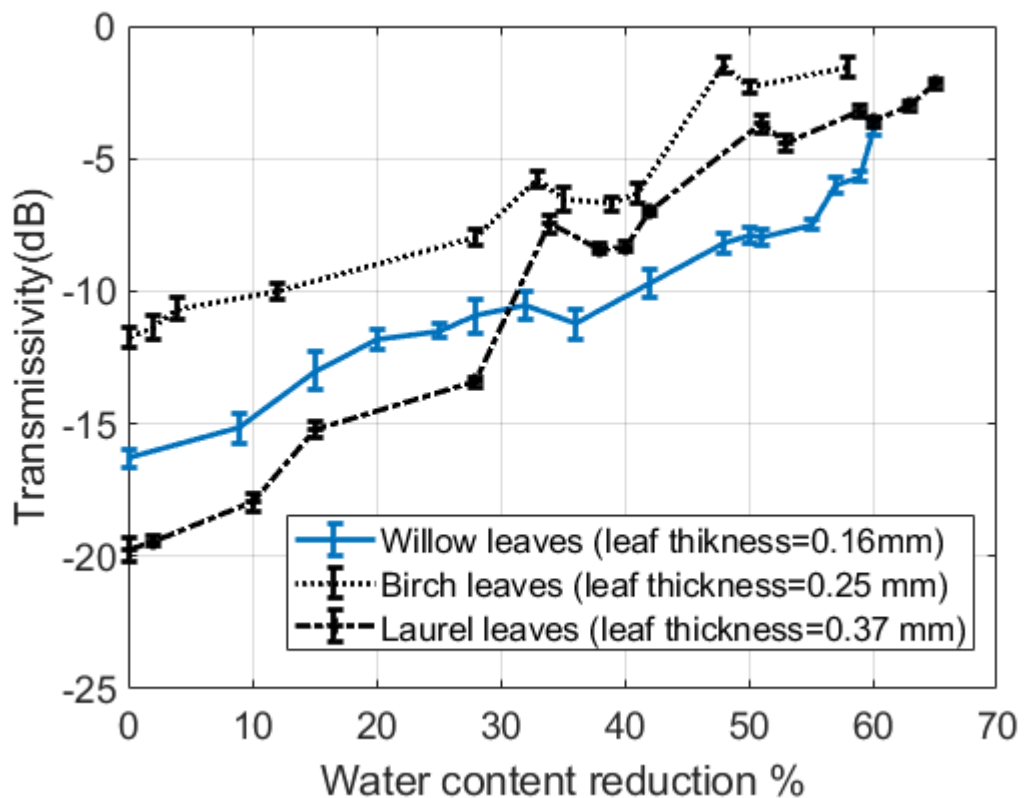


Figure 4.6: Measured transmissivity through three leaves respect to volume water content reduction

The measured and calculated results of transmissivity through uniform layer of Laurel leaves at 300 GHz with respect to WCR are plotted in Figure 4.7. Discrepancies between the measurements and the calculated results can be explained by the possible gaps between the leaves, different rates of water reduction in leaves (as it shown in Figure 4.4, the group of leaves sit together and generate uniform layer of leaves) and also scattering inside the leaves. Both measured and calculated results show an increase in transmissivity with a decrease of water content which confirms the fact that the water within the leaves is the main cause of signal reduction.

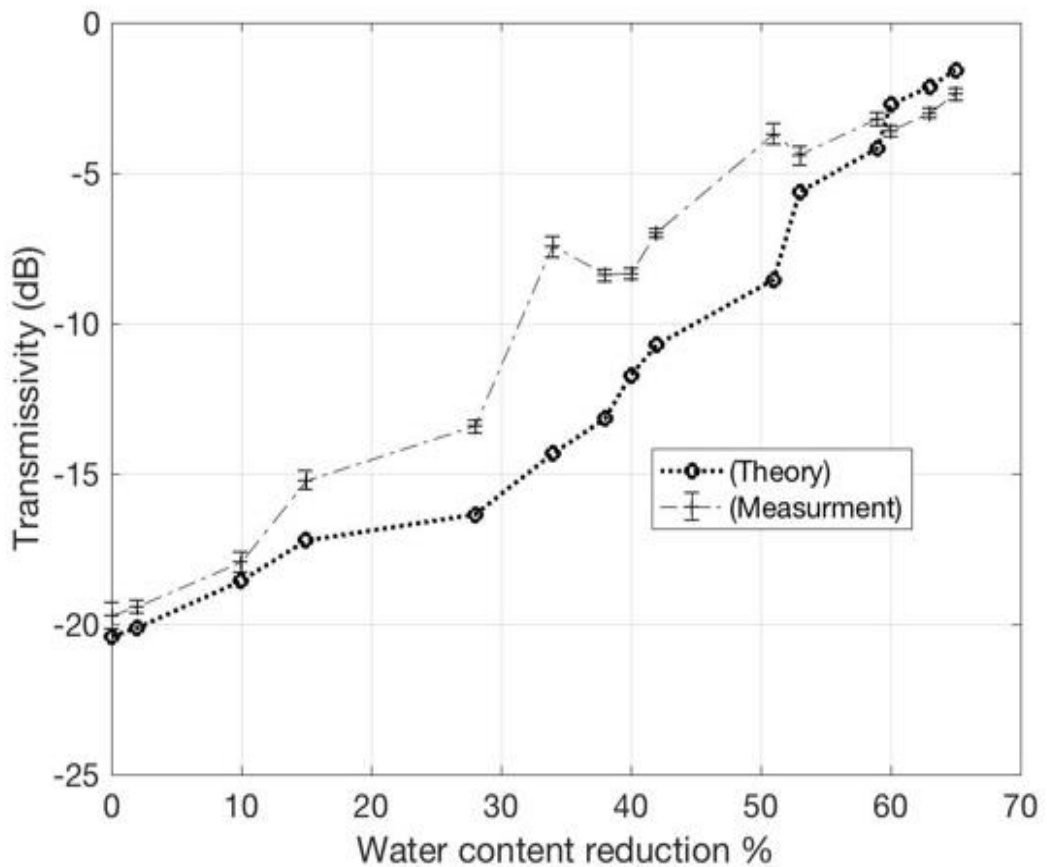


Figure 4.7: Calculated and measured result of transmissivity through leaves respect to WCR, using effective permittivity of leaves [106]

To study the contribution of water on transmissivity through leaves, an equivalent uniform layer of water (assuming negligible scattering inside the leaves) is considered. The value of volumetric water content of leaves has been calculated as $5 \times 10^{-4} \text{ g/mm}^3$. Then, the equivalent water thickness for each WCR state is calculated. The transmissivity is calculated by equation (3.4) and the value of permittivity of water is obtained from [109]. Measurement and theoretical results of transmissivity through leaves with respect to equivalent uniform water layer at 300 GHz are depicted in Figure 4.8. The agreement between the measured and calculated transmissivity is very good. The correlation between measured and calculated transmissivity and water thickness proves again that the water inside leaves is the main cause of signal reduction.

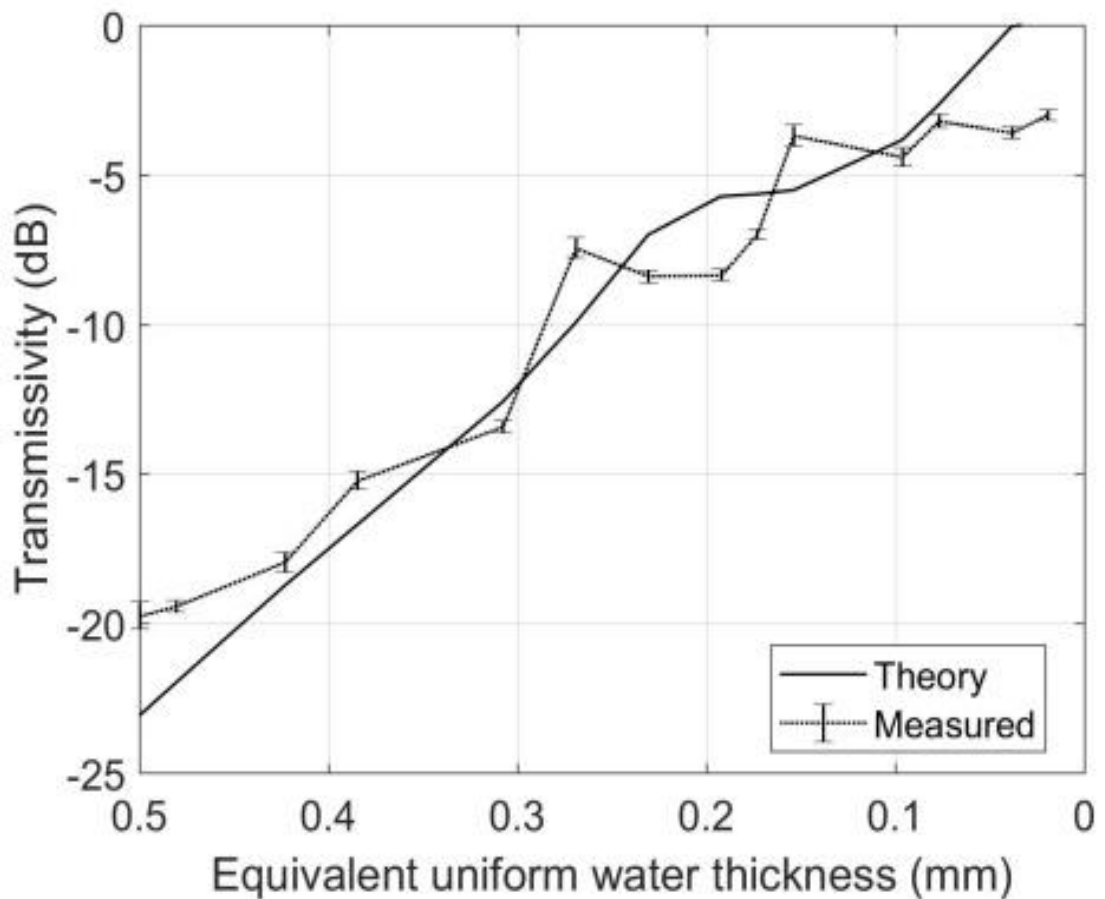


Figure 4.8: Measured and calculated results of transmissivity through equivalent uniform water layer, using water permittivity

4.2.7 Conclusions

In this study, the experimental and theoretical results of transmissivity through uniform layer of leaves at 300 GHz are presented. The transmissivity is calculated in two ways: (i) by using effective permittivity of leaves and (ii) considering equivalent water layer for different WCR and using water permittivity. The second model shows a better agreement with the measured results. Therefore, further studies on the effect of water containing obscurants should be focussed around developing equivalent water layer model to evaluate reduction of signal strength.

4.3 Signal reduction due to a layer of water at low THz frequency for automotive radar applications

4.3.1 Overview

The knowledge of the performance of radars in harsh and uncontrolled outdoor environment is fundamentally important for the development of automotive sensors. It is known that the presence of water in the atmosphere and on the radome are the main causes of losses in the propagation channel and will cause degradation in the performance of AV sensors in adverse weather condition, so that in our study we are carrying out investigations on the transmissivity through layer of water on low THz signals. The transmissivity through uniform layer of pure water, salty water with different levels of salt and actual seawater are measured and analysed at 300 GHz and 670 GHz and compared with the obtained results at 150 GHz [109]. Also, in this section the estimation of the permittivity of pure water and salty water with different levels of salt and actual seawater from the measured transmission coefficient is discussed. The measured results are compared with a theoretical model based on Fresnel transmission theory and show good agreement between the theoretical model and practical results.

4.3.2 Introduction

As mentioned above, In order to analyse the feasibility of low THz automotive sensors it is necessary to study their performance in harsh and uncontrolled outdoor environment. As mentioned in section 2.4.1 the atmospheric attenuation, primarily due to water vapour absorption, is significant in many spectral regions in the low THz band as shown in [38], especially in adverse weather conditions [24], [39]. However, there are transmission windows around 340 GHz, 400 GHz, and 650 GHz, where atmospheric loss in clear air does not exceed 10 dB/km, 20 dB/km, and 60 dB/km, respectively [38]. The results obtained in [111] for frequencies of 77 GHz and 300 GHz show that even in heavy rain the attenuation of the radar signal did not exceed 20 dB/km, and in [112] measured attenuation during snowfall was below 15 dB/km. Therefore, for the automotive radar operational range of up to 100 meters, atmospheric loss will not exceed 10 dB and makes a relatively small contribution to the power budget needed to guarantee the system efficiency [40].

In section 4.2 of this thesis the signal attenuation through radome covering by tree leaf was discussed, additionally the radar performance operation at low THz frequencies in the presence of other radome contaminants (sand, oil, ice, etc.) [103-105] formed on the radome has been studied by MISL group in the university of Birmingham. The transmissivity through uniform layers and randomly distributed droplets of pure and salty water at 150 GHz and 300 GHz was investigated in our laboratory [109]. The transmissivity at 670 GHz presented in this PhD research is measured with a spatially separated transmitter and receiver, in a traditional communication setup; whereas, the measurement methodology in [109] was quasi-monostatic. Because of this, the transmissivity at 300 GHz is also measured with the same experimental setup to compare the measurement results of the two setups, and also to investigate the effect of increased frequency on the attenuation of the signal in the water layer.

The transmission loss due to presence of water in the signal propagation path has been widely studied at microwave and mm-wave frequencies [113-117], and the results show a high dependence of loss on the carrier frequency and considerable loss even with a very thin layer of water. In [113], the transmissivity increases when the radome water thickness is increased, which generates a transmission loss of up to 20 dB at 20 GHz when the water thickness is 1.5 mm. In [116], the attenuation of near-Infrared radiation was measured through different water film thicknesses between 100 and 380 μm . The high attenuation in water films was confirmed, even for very small water film thickness.

In this study, a preliminary study on the attenuation of signals at 300 GHz and 670 GHz in the presence of a uniform layer of water in the propagation path is reported. The new experimental and theoretical results of the total loss due to presence of pure water and water contaminated with salt at both frequencies of 300 GHz and 670 GHz are shown and compared with measured results at 150 GHz obtained from [109]. The obtained results demonstrate the potential of using low THz sensors for outdoor applications.

4.3.3 Theoretical model

The Fresnel theory as discussed in section 3.3.2 were used, for a three layer structure, air-water-air to evaluate the transmissivity through water built up on the antenna radome at low THz frequencies.

As mentioned in section 3.3.2 the complex permittivity of the water is the important parameter defining the transmissivity through water. The relative complex permittivity of water $\varepsilon_r = \varepsilon_r' - j\varepsilon_r''$, is a function of frequency and temperature. The Double Debye model [118-120] is a popular model which has been used for calculation of complex permittivity of pure water and is given by the relation:

$$\varepsilon(\omega) = \varepsilon_\infty + \frac{\varepsilon_s - \varepsilon_1}{1 + i\omega T_1} + \frac{\varepsilon_1 - \varepsilon_\infty}{1 + i\omega T_2} \quad (4.3)$$

Where $\varepsilon_\infty, \varepsilon_s, \varepsilon_1$ is the dielectric constant in the high frequency limit, static dielectric constant and the intermediate dielectric constant respectively. T_1 is the first Debye relaxation time, and T_2 is the second Debye relaxation time.

The value of permittivity reported in the literature for pure water at frequency of 150 GHz is between 5.03 and 7.5 for real part (ε_r') and between 8.07 and 10.4 for imaginary part (ε_r''). These values at frequency of 300 GHz are account between 3.8 and 6.6 for ε_r' and between 4.19 and 6.23 for ε_r'' [118-121]. From 600 GHz to 700 GHz the reported permittivity's [122-124] is between 2 and 5 for real part (ε_r') and between 2 and 6 for imaginary part (ε_r''). The permittivity parameters of saline water at mentioned frequencies are missing from literature.

Figure 4.9 [109] shows a simulation result of transmissivity at frequencies of 24 GHz and 77 GHz (current automotive frequencies), 150 GHz, 300 GHz. The theoretical values are calculated using the permittivity obtained from literature which was mentioned above. The values of permittivity of pure water at 77 GHz and 24 GHz are taken from [120,125]. As can be seen from Figure 4.9 for water thickness smaller than 0.5 mm (the maximum water accumulated on the automotive radar), the difference between current automotive radar (77 GHz) and 150 GHz and 300 GHz is about 10 dB which demonstrates the potential of using the low THz radar for outdoor applications as this requirement is achievable with very short wavelength signals.

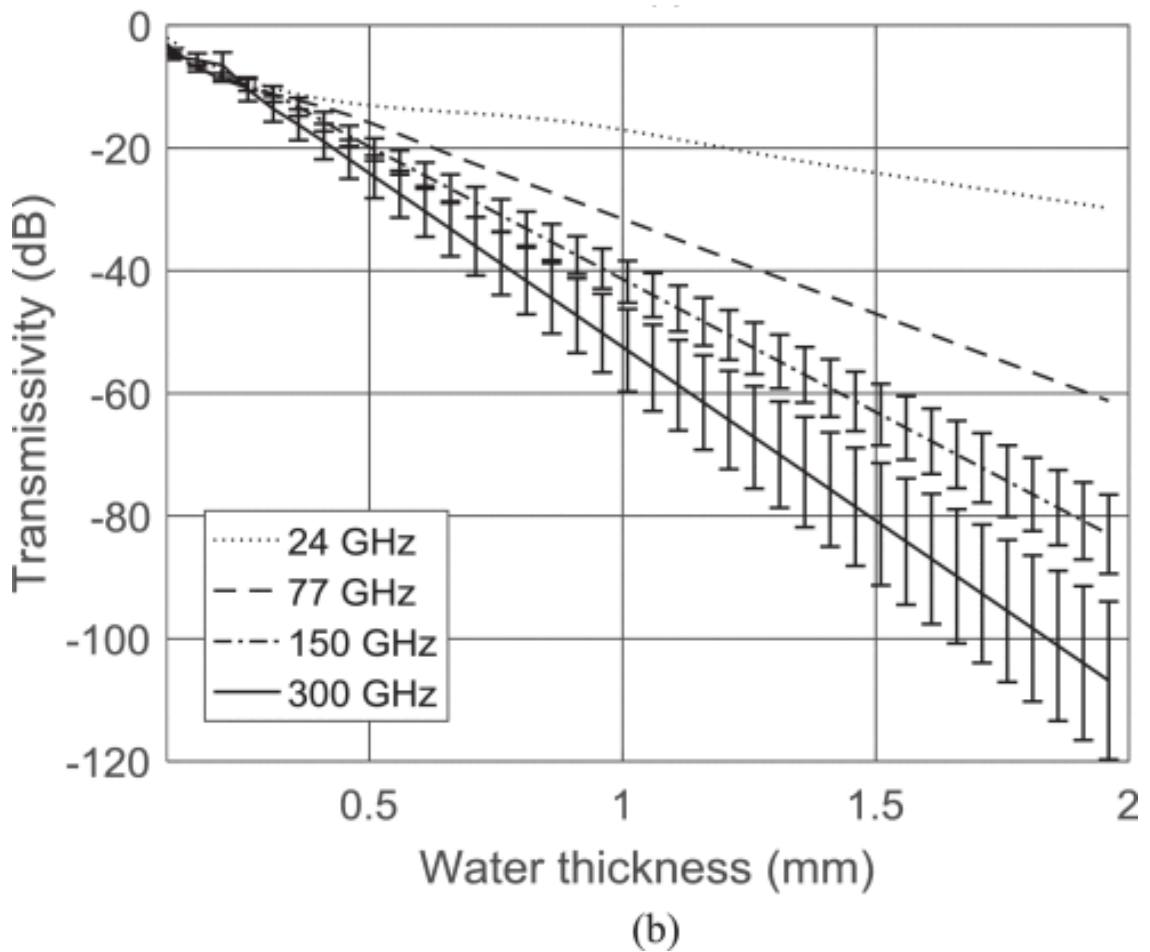


Figure 4.9: Calculated transmissivity of pure water as a function of water thickness at 24 GHz, 77 GHz, 150 GHz, and 300 GHz at 23 °C. The error bars correspond to the uncertainty in the double Debye model parameters in equation (4. 8). [109]

Due to unavailability and inconsistency between reported values for permittivity of water at low THz range, the permittivity of pure water and saline water with different levels of salt (constrained by the range of reported permittivity values in literature) was obtained from value of measured transmission coefficient and explained in details below.

In [126] a different experimental method for computing the material permittivity has been described. In this study the free-space technique has been used for calculation of complex permittivity of pure and saline water from measured transmission coefficient. The complex permittivity has been evaluated by using a root-finding algorithm [126], which minimizes the estimation error between theoretical and measured values of transmissivity, constrained by the range of reported permittivity values for pure water.

The permittivity was calculated by the equation:

$$E(\varepsilon_r', \varepsilon_r'') = \sum_{i=1}^N |T_{meas}(t_i) - T_{th}(t_i, \varepsilon_r', \varepsilon_r'')| \quad (4.4)$$

where N is the number of measurements, t_i is the thickness of i -th water layer, T_{meas} is the measured transmissivity, and T_{th} is calculated transmissivity.

The error calculated using equation 4.4 for the different combination of ε_r' and ε_r'' at frequencies of 150 GHz (f_1), 300 GHz (f_2) and 670 GHz (f_3) are shown in Figures 4.10, 4.11 (a) and (b) respectively and the final permittivity calculated minimizing the estimation error between theory and measurement for mentioned frequencies are shown as:

$$\varepsilon_r(f_1) = 7 - j10$$

$$\varepsilon_r(f_2) = 6.4 - j4.52$$

$$\varepsilon_r(f_3) = 5.69 - j2.08$$

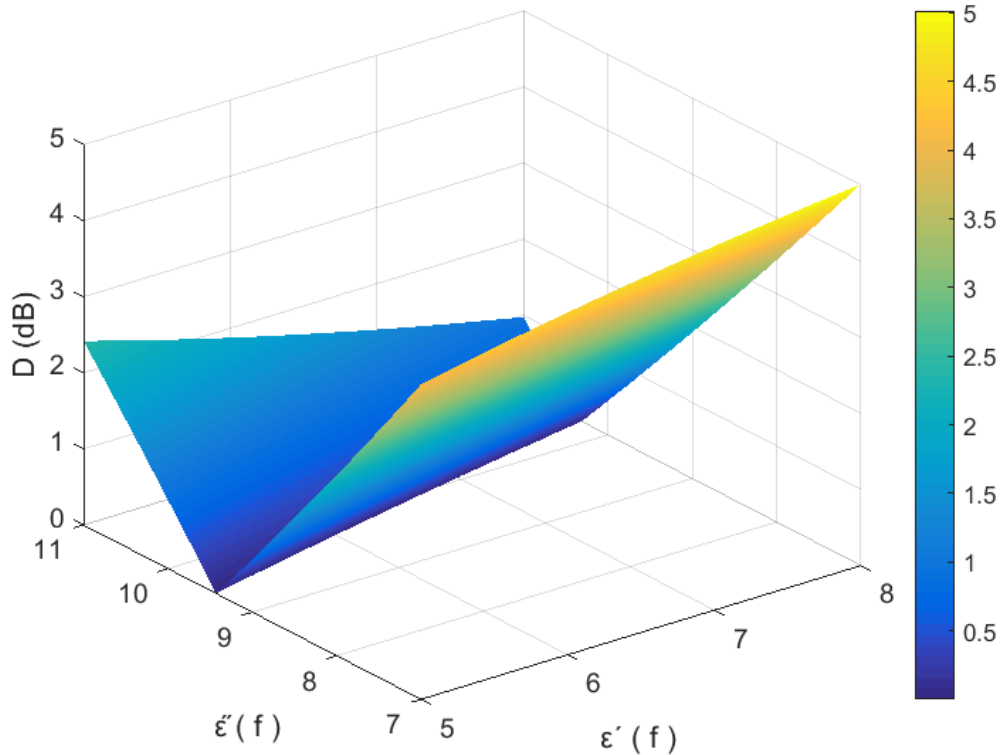
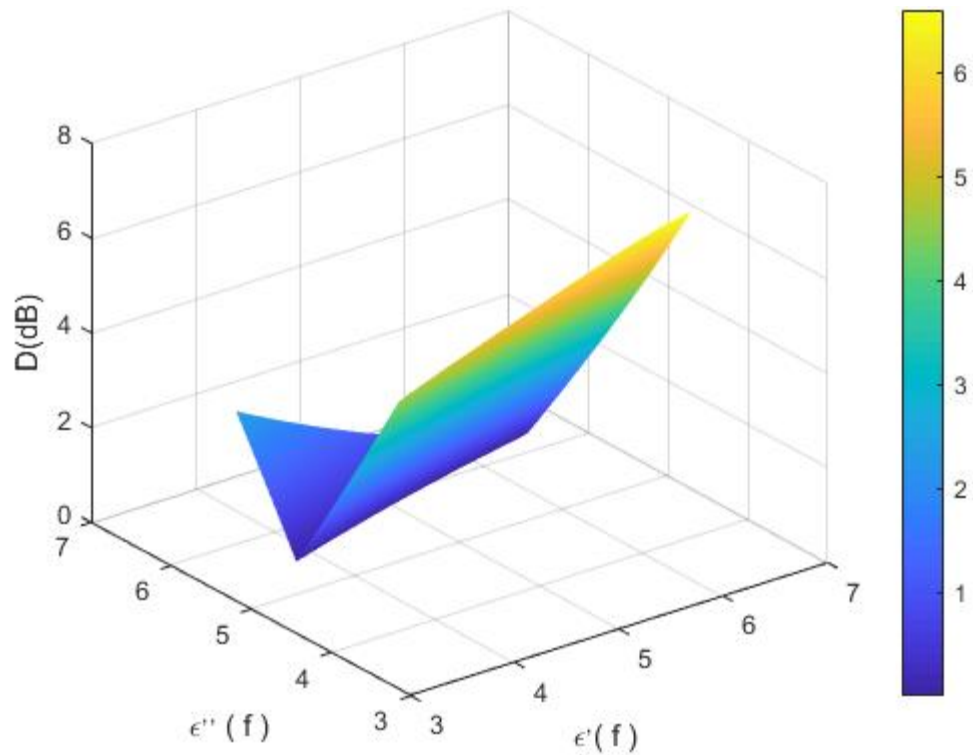
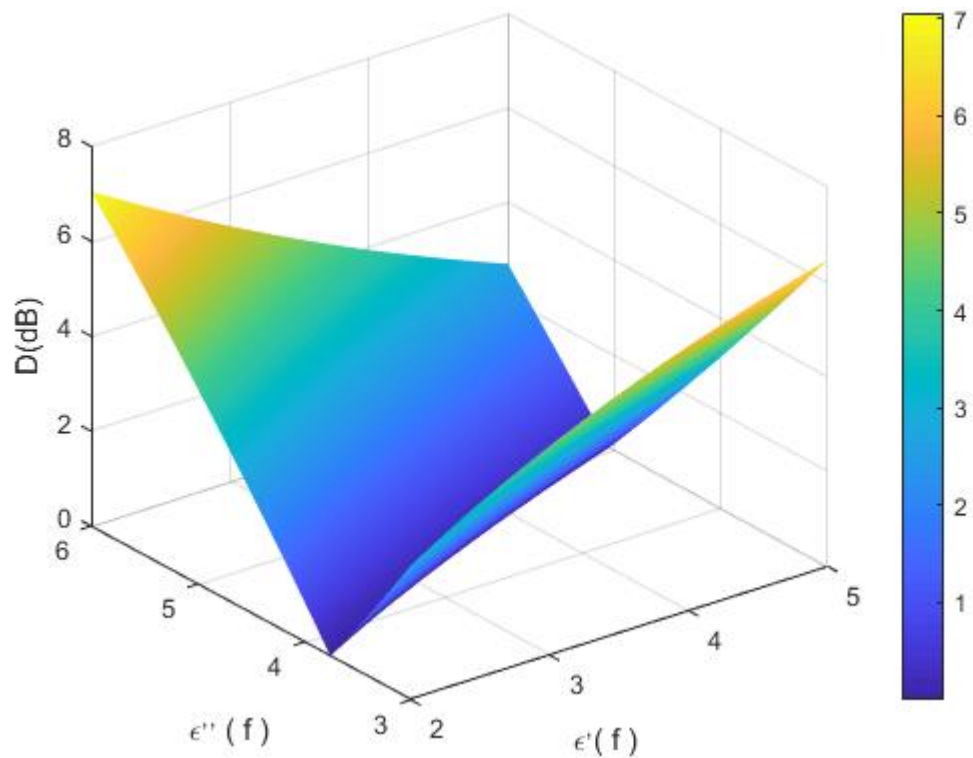


Figure 4.10: Error between measured and theoretical transmissivity for different values of pure water permittivity at 150 GHz [109]



(a)



(b)

Figure 4.11: Error between measured and theoretical transmissivity for different values of pure water permittivity at (a)300 GHz (b) 670 GHz

4.3.4 Measurement methodology

Figure 4.12b shows the experimental setup. The transmitter and receiver antennas are facing each other with spatial separation of 1.5 meter. The sample is placed in the direct propagation path between the transmitting and receiving antennas. The sample is situated in the far field of the antennas. The antennas are square horns with azimuth and elevation 3dB beamwidth of 10° , and 20 dBi gain. As shown in Figure 4.12a, the area of the sample is 10 times greater than the area illuminated by the 3dB beam to ensure the passage of most energy through the sample. Transmissivity through different thicknesses of water layer is characterized by comparing the transmission through the wet paper tissues and through the dry paper tissues (reference).

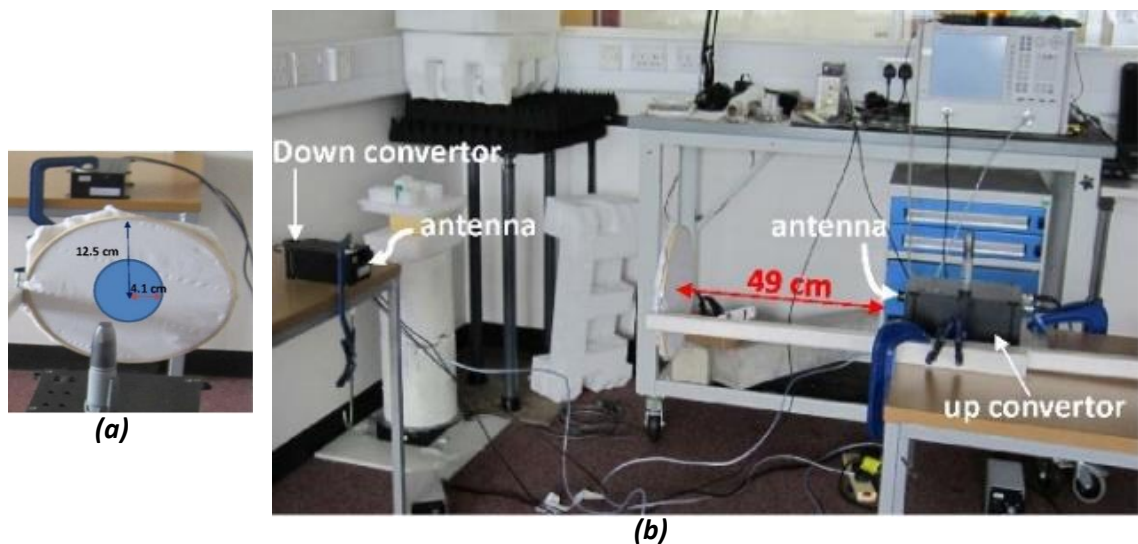


Figure 4.12: (a) Sample with specific illuminating area footprint (blue circle), (b) measurement setup

The main challenge in this measurement is producing thin layer of water due to physical properties of water (cohesion, adhesion and surface tension). The similar technique as explained in [109] is employed here to produce a thin layer of water by wetting tissue paper. In order to produce the thin layer of water, the specific known amount of water which was measured by syringe and spread on a tissue paper with known area; so by using the equation for the volume of a cylinder ($V = 2hr\pi$) the level water thickness can be computed. By using this method the accuracy of 0.05 mm is achievable to provide a uniform layer of water. Several tissue papers are stacked together to produce a thicker layer of water. As the wet tissue paper needs to be placed vertically between the antennas, a hoop is used to hold the wet tissue straight and vertically.

Analysis of the effect of water salinity on low THz propagation is undertaken in this PhD research as the deposited salt on a car radome in a coastal area can block the EM waves also during winter/autumn deposited salt on the road can stick to the radome and cause similar blockage effect. In order to analyse the effect of a layer of sea water or contaminated water with salt (for example salt from grit), saline water was produced with different levels of salinity in the laboratory. The salinity of water is expressed in grams of salt per kilogram of water (g/kg) and known as Practical Salinity Unit (PSU). The water salinity can also written as part per thousand (Ppt) or percentage figure (%), where 15 PSU is equivalent to 15 Ppt and is equal to 15%. Salt composition in sea water is not uniform throughout the world. Seawater salinity is mainly approximate between 32PSU and 37PSU [127], So in our experiment three salinities have been chosen (31PSU, 35PSU and 38PSU) as samples as well as the actual seawater from the Aegean Sea which was measured and analysed for comparison to investigate how saline water deposited on a radome can affect the signal attenuation in low THz waves.

In this study all the measurement have been carried out for 4 or more realization. Possible error might arise due to the presence of air gaps, non-perfect uniformity of the water layer, non-uniformity of the tissue paper and evaporation of water during multiple measurements, which slightly change the water layer thickness.

Data collection using this system has been carried out with a radar system composed of a 2-port Keysight Programmable Network Analyser (PNA N5232a) and linear up/down converters developed by VivaTech (Nice, France) as described in section 3.2.1.2. The VNA generates a stepped-frequency signal which is up-converted and transmitted. The received signal is down-converted and the scattering parameters are measured. The converters and VNA are phase locked to an external 10 MHz reference signal provided by a rubidium oscillator.

The signal level reduction (labelled as transmissivity) due to presence of the uniform layer of water is the result of various propagation phenomena, such as scattering, absorption, reflection, and refraction. It can be computed as:

$$T = 10 \log \frac{\sum_{i=1}^{i=n} P_{r_1}(f_i)}{\sum_{i=1}^{i=n} P_{r_0}(f_i)} \quad (4.5)$$

where n is the total number of sweeps, P_{r_1} is the received power with presence of sample (water), P_{r_0} is the received power without the sample.

Specifications of the system components are provided in Table 4.1, and Figure 4.13 shows a schematic of the system.

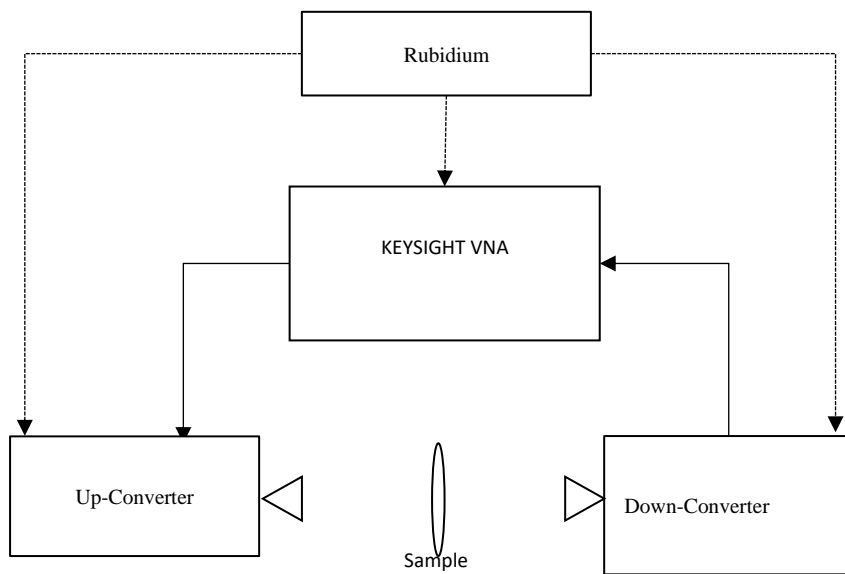


Figure 4.13: System schematic

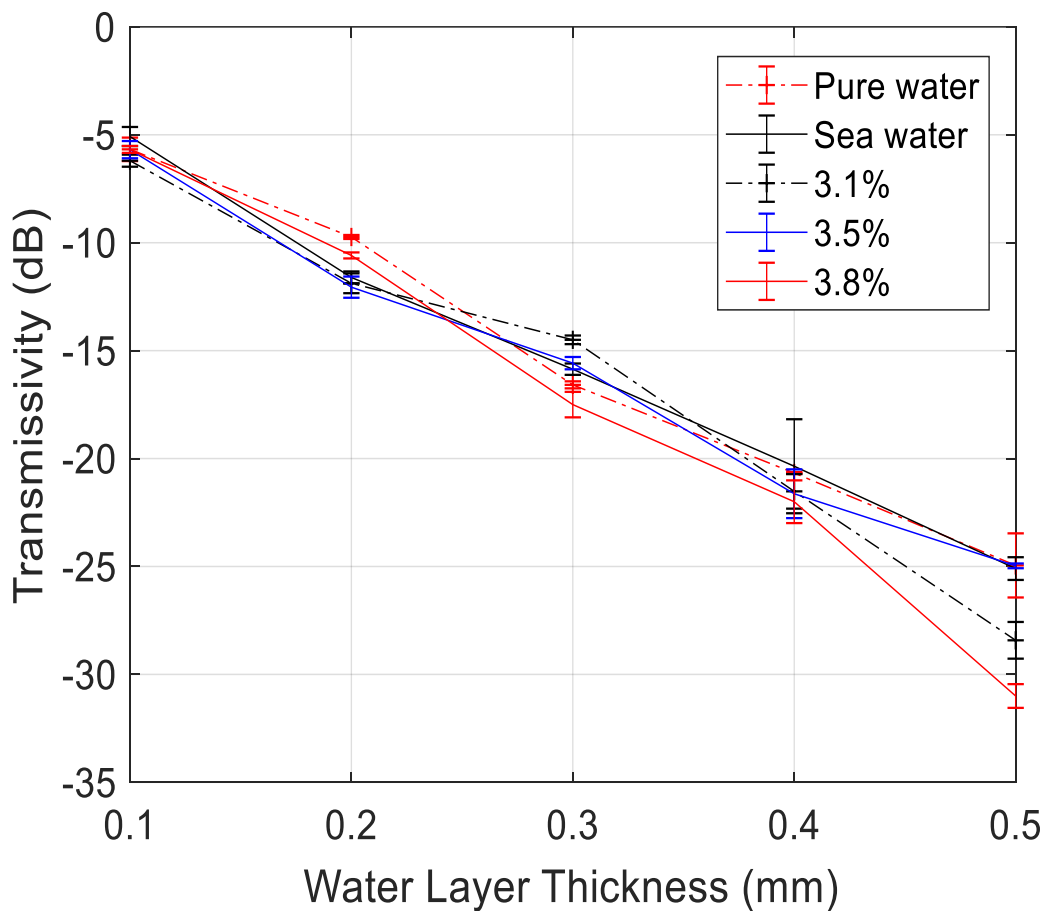
Table 4.1: Parameters of the measurement system

Parameters	300 GHz	670 GHz
Frequency band	282-298 GHz	656-665 GHz
Sweep Bandwidth	16 GHz	9 GHz
Output power	-15 dB	-10 dB
Antenna Azimuth	10° (-3 dB)	10° (-3 dB)
Beamwidth		
Antenna Elevation	10° (-3 dB)	10° (-3 dB)
Beamwidth		
Antenna gain	25 dBi	20 dBi
Antenna dimension	6x8x22 mm	3x4x6 mm
Far field	128 mm	71 mm
Range resolution	9.4 mm	16.7 mm

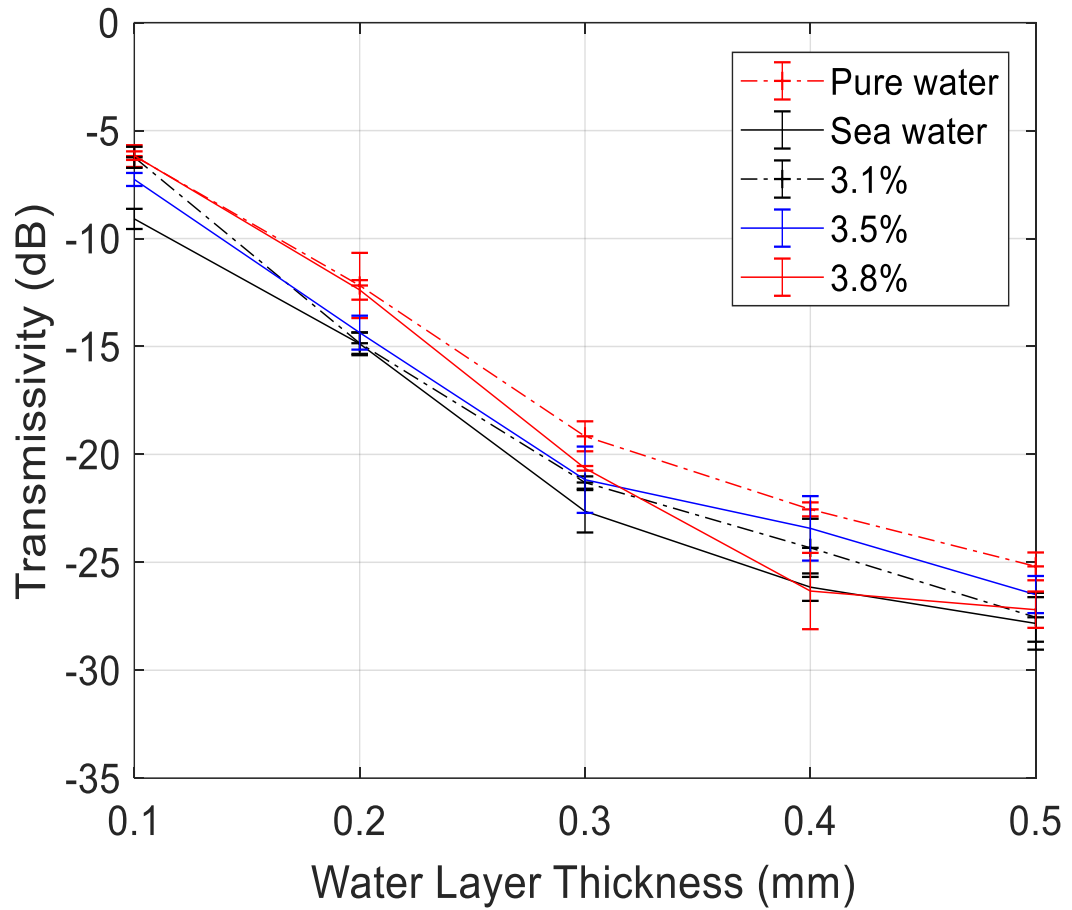
4.3.5 Result and discussion

In this section, the measurement result of transmissivity through uniform layer of pure water and saline water with three level of salinity (31%, 35%, 38%) and actual seawater are presented and compared with theoretical model based on Fresnel theorem.

The measured transmissivity through uniform layer of pure, saline (three salinity levels) and sea water at 300 GHz and 670 GHz are illustrated in Figure 4.14 (a) and Figure 4.14. (b), respectively. The measured results are shown as functions of water thickness in a range of 0.1 mm to 0.5 mm with 0.1 mm steps. The measured results are averaged over four or more sample realization and the error bars show the obtained standard deviation. The trends of the graphs show that the transmissivity is decreasing with increasing water thickness. The results show a slight decrease in the transmissivity with increasing water salinity at both frequencies. The small difference in the measured transmissivity through pure and contaminated water shows that contamination in the water covering the radome has a small impact on the transmissivity.



(a)



(b)

Figure 4.14: Measured transmissivity through pure water, actual seawater, and water of three different salinities as a function of water thickness at 23 °C (a) at 300 GHz and (b) at 670 GHz.

A comparison between the measurement results obtained by the explained experimental setup in this thesis and quasi-monostatic setup explained in [109] at 300 GHz shows acceptable agreement between them, considering one-way path propagation. Therefore, the measured transmissivity at 150 GHz presented in [109] is used to plot the transmissivity through 0.3 mm uniform layer of pure, saline (3.5%) and actual sea water versus frequency, shown in Figure 4.15. As expected, a decreasing trend in transmissivity is observed when the frequency is increased for the same thickness of water.

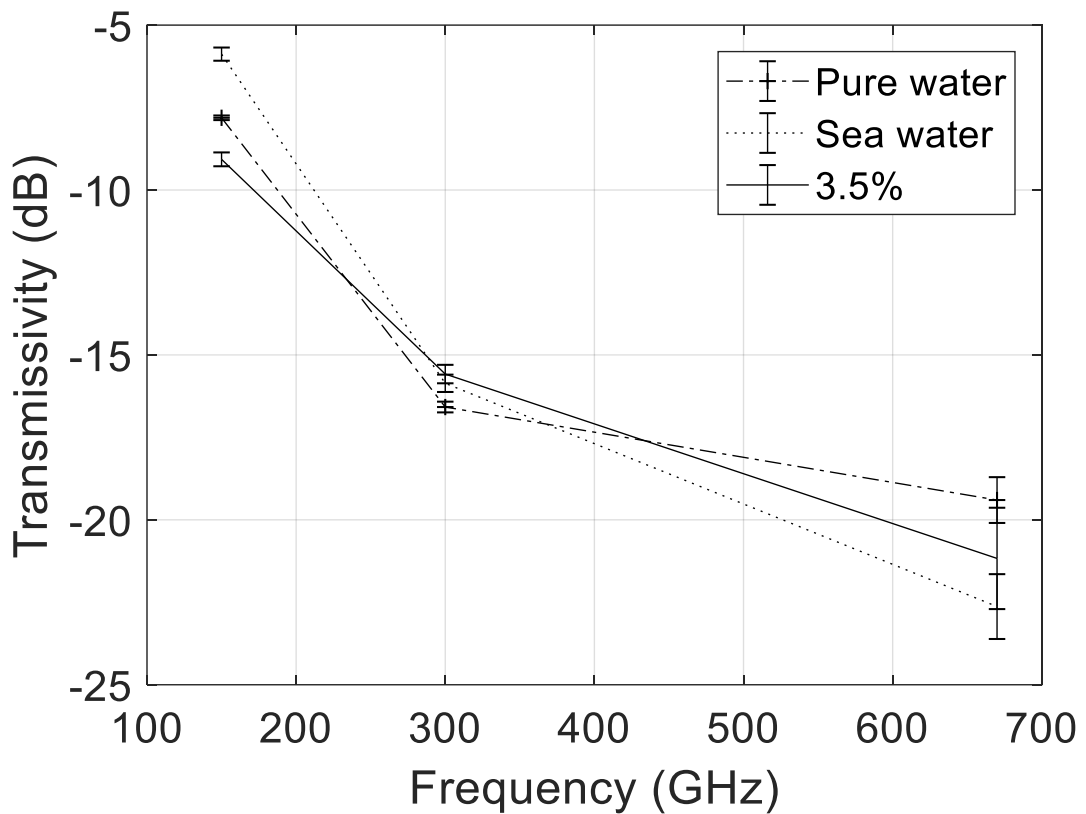


Figure 4.15: Measured transmissivity through 0.3 mm layer of pure water, sea water and water with 3.5% salinity versus frequency

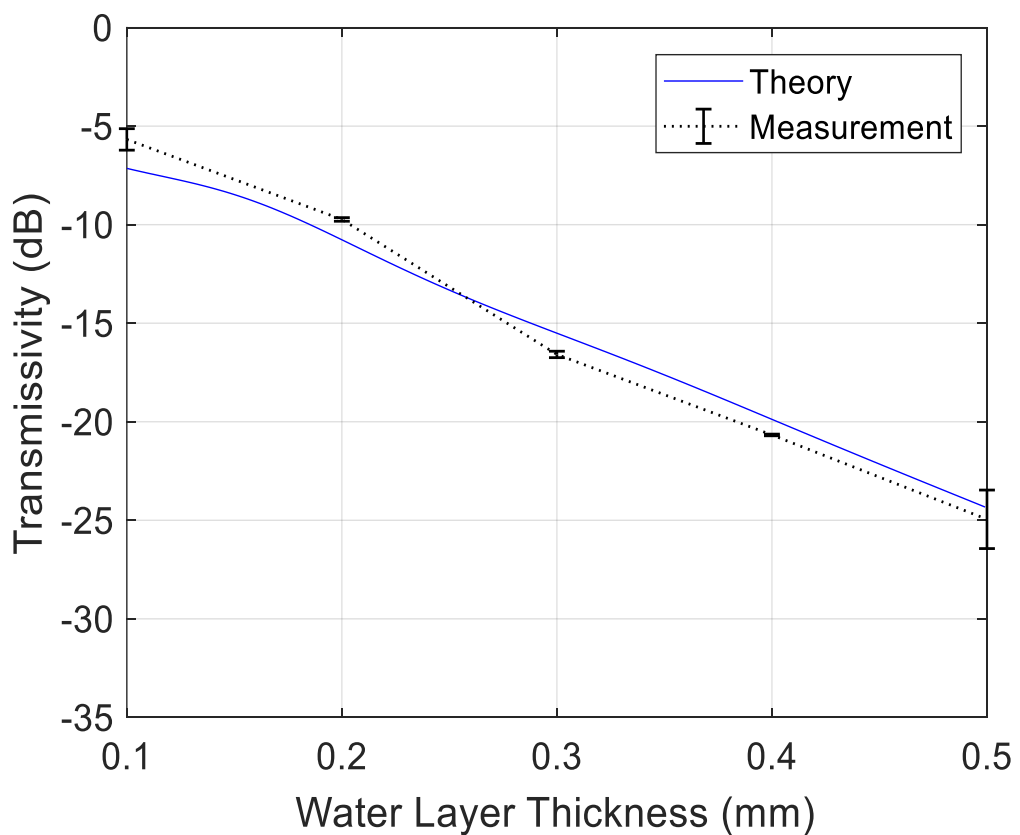
As mentioned earlier there is a little information in literature on the permittivity parameters of saline water and sea water at low THz frequencies. In [125] the permittivity of sea water has been measured for frequencies up to at least 90 GHz. The permittivity of NaCl with molarity of 2 mol/L (molarity = PSU/58.45) at frequency of up to 1 THz has been reported in [128] . Finally in [129] the measurement result of the Permittivity of saline water with salinity range from 0.1 mol/L to 3 mol/L in the frequency ranges from 0.1 THz to 2.7 THz has been reported. The permittivity of saline water with salinity close to sea water level at our working frequencies range (150 GHz, 300 GHz, 670GHz) is missing in literature. So the permittivity obtained by equation 4.4 with the root-finding algorithm mentioned in Section 4.3.3.

The obtained permittivity for pure water and water with 3.5% salinity at both frequencies are shown in Table 4. 2.

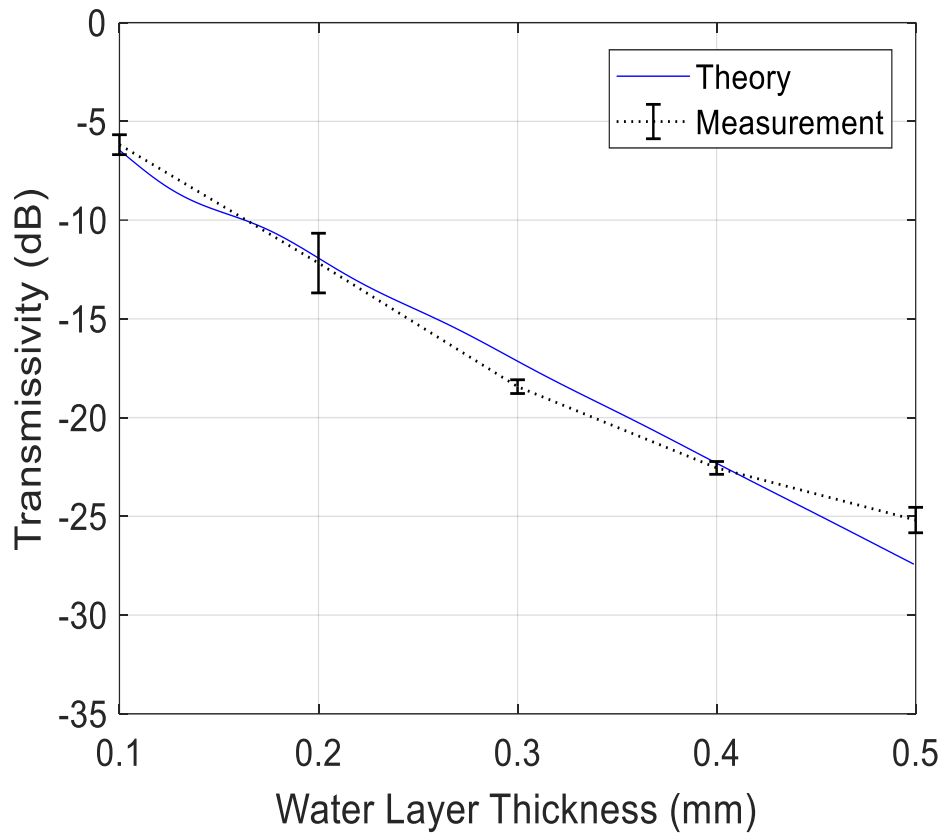
Table 4.2: Calculated permittivity of pure water and saline solutions at 300 GHz and 670 GHz

	300 GHz		670 GHz	
	ϵ_r'	ϵ_r''	ϵ_r'	ϵ_r''
Pure water	6.44	4.52	5.69	2.08
3.1% salinity	4.62	4.41	4.32	2.10
3.5%salinity	5.67	4.5	4.7	2.13
3.8% salinity	5.74	5.01	4.31	2.06
Sea water	6.64	4.59	3.73	2.13

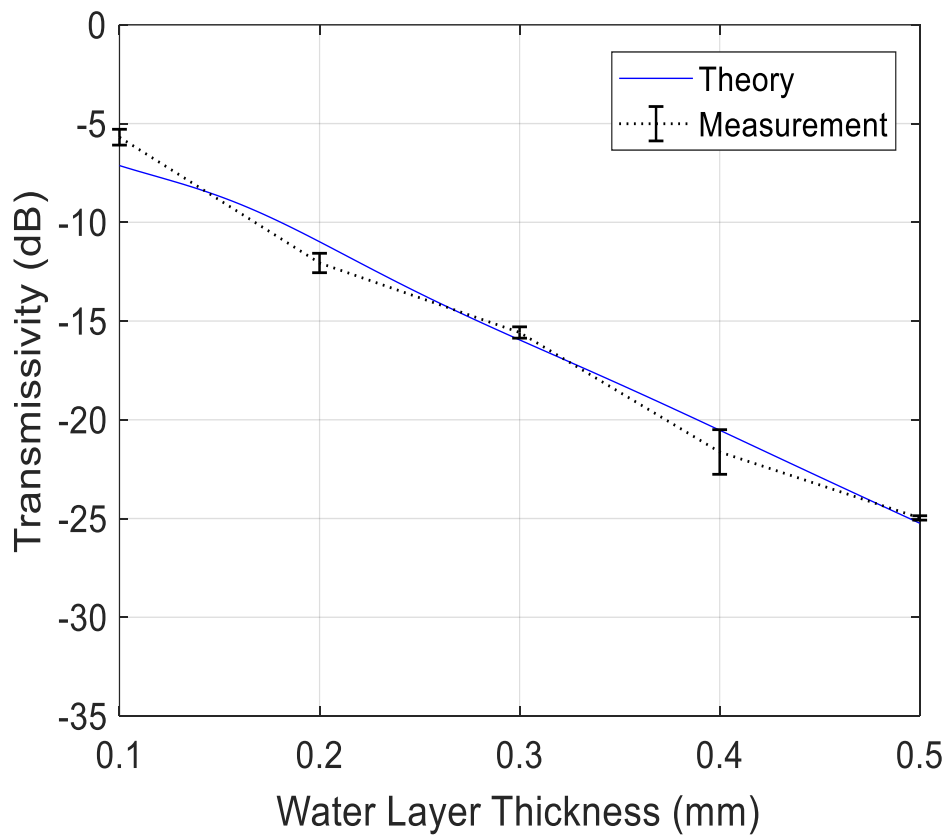
Figure 4. 16 depicts the measured and theoretical transmissivity of pure water and water with salinity of 3.5% as a function of thickness at frequencies of 300 GHz and 670 GHz. The theoretical values are calculated using the permittivity obtained with the root-finding algorithm. All the graphs show a good agreement between the theoretical and measured transmissivity. The small discrepancies are likely due to the presence of air gaps, non-perfect uniformity of the water layer, non-uniformity of the tissue paper and evaporation of water during multiple measurements, which slightly change the water layer thickness.



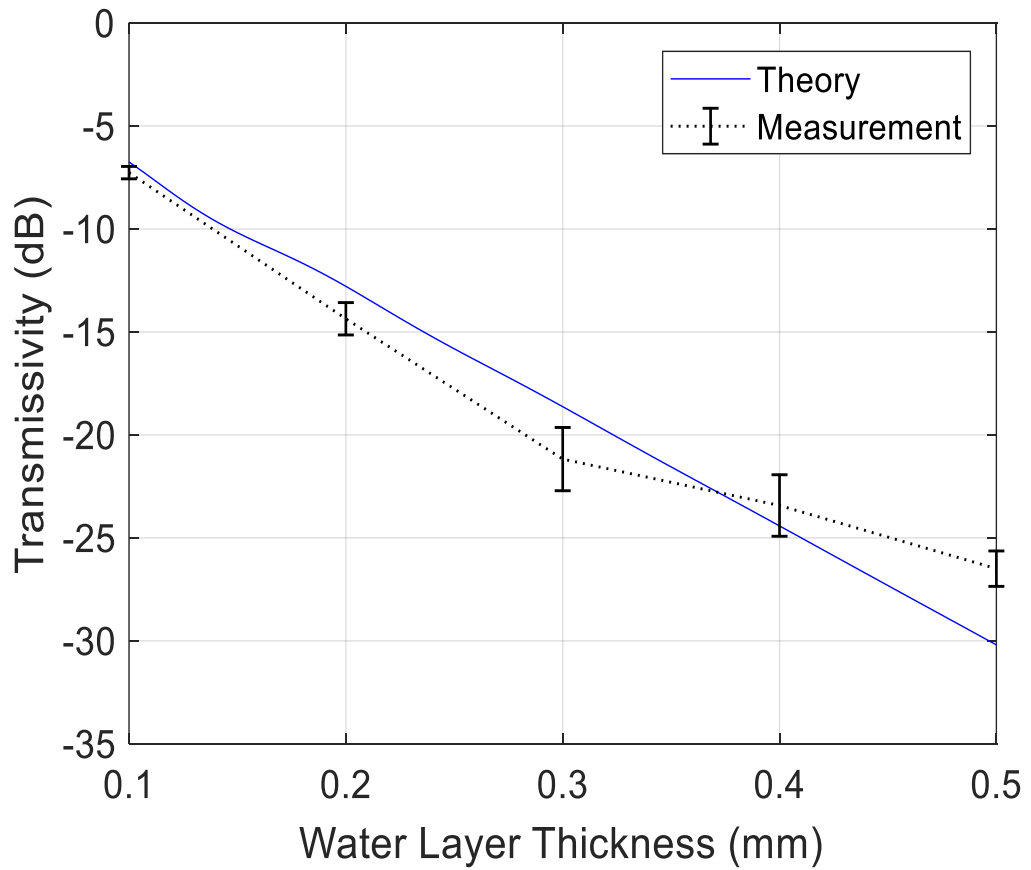
(a)



(b)



(c)



(d)

Figure 4.16: Calculated and measured transmissivity through pure water at (a) 300 GHz and (b) 670 GHz, and water with salinity of 3.5% at (c) 300 GHz and (d) 670 GHz as a function of uniform thickness at 23 °C.

4.3.6 Conclusion

Measured and theoretical results of the transmissivity through a uniform layer of water at 300 GHz and 670 GHz are presented in this study. Good agreement is demonstrated between the results obtained through measurements and a theoretical model based on the Fresnel theory. When compared with those obtained in our previous study [109] at 150 GHz, the results show an increase in attenuation due to the presence of a uniform thickness of water, with an increase in frequency.

4.4 Attenuation through sand, oil, ice in low THz radome

As mentioned earlier the radome contamination in automotive sensors can cause a considerable signal power reduction. The EMW can interact with these radome contaminants and as a result cause signal attenuation and adverse effects on radar performance, up to complete signal blockage and sensor failure. At the time this PhD research started, published information on the impact of radome contaminants on wave propagation is rather limited even at 77 GHz and practically absent for low THz bands. so in University of Birmingham MISL group comprehensive experimental and theoretical research on the signal attenuation of many common contaminants that occur in automotive practice, namely: gasoline and diesel [105], sand [103], water [109], ice [104] and fallen leaves [94] has been carried out in the range of low THz frequencies. The measurement methodology is explained in section 3.3.1 and for theoretical modelling Fresnel theory [99] which was developed for a three layer structure has been used. A more detailed explanation of the measurement methodology and theoretical modelling can be found in the referenced literature. Table 4.3 shows the summarized results of two way transmission loss through mentioned radome contaminations.

Table 4. 1: Two way signal reduction (in dB) on a contaminated radome[30]

Contaminant		Frequency		
		77 GHz	150 GHz	300 GHz
Water (0.45mm) [109]	PW	30	29	38
	SW (3.5%)	<u>23.2</u>	22	31
	DW	NA	34.6	40
Sand (Particle size:0.2 mm) (thickness:1 mm) [103]	Dry	NA	~0	10
	Moist (10 %)	NA	12.6	26
Ice (1 mm)[104]		<u>0.4</u>	1.4	3.2
diesel[105]		<u>0.6</u>	0.8	1.1
gasoline		<u>1</u>	1.4	1.5
Leaf (0.37 mm)[94]	fresh	30	34	40
	dry	<u>~0</u>	<u>~0</u>	4
Water droplet with coverage area in %[109]	10%	NA	2	2
	20%	NA	4	1.6
Abbreviations: PW-Pure water, DW-Contaminated water with road dirt, SW-Salty water				

The values which are shown bold are the highest measured signal reductions. The underlined values shown in Table 4. 3 are just from the calculation. By comparing the results presented in Table 4. 3 we can conclude, the presence of water on the radome surface or contaminant containing water has the dominant effect in signal degradation at all frequencies. As mentioned in section 4.3.5 signal reduction due to the uniform layer of the water mainly depends on water layer thickness as well as percentage of salt in the water and operational frequency and strong signal attenuation has been observed due to uniform layer of water. However that case is not a real life road scenario. The most common case in real road scenarios is randomly distributed water droplets

obscuring the radome which was investigated in [109], indicating that random distributed water on the antenna radome have a less detrimental effect on the wave propagation in comparison with a uniform layer of water. Losses are influenced by the water droplet size, density and distribution. Results in [79] show that the wave propagation through water droplets on the antenna radome at high frequency does not reduce the performance of the radar sensors significantly. This is attributable to the fact that gaps between droplets have an electrical dimension larger than the wavelength, increasing the transmissivity through a screen of randomly distributed droplets. Such effect demonstrates the potential of using the low THz sensors for outdoor applications as this requirement is achievable with very short wavelength signals.

In [103] the transmissivity through sand when sand layer thickness is increasing (from 0 mm to 45 mm stepped by 3 mm) was measured at 150 GHz and 300 GHz. To get better understanding into the effects within a sand-filled medium, the transmissivity through five species of calibrated particle with different size as well as natural sand was measured at 150 GHz and 300 GHz. The results shows that transmissivity is decreasing when the sample thickness increases for both frequency ranges. Moreover, the result indicates that coarser sand particles produce greater attenuation than finer particles at both mentioned frequencies. However, in real road scenario the smaller particles of sand are more likely to attach to the radome, possibly forming a uniform layer. Comparison between gained results at 150 GHz and 300 GHz indicate that the signal reduction at 300 GHz is higher than at 150 GHz. According to [104,105] ice, diesel and gasoline are almost transparent at 77 GHz and the attenuation increases slightly at 150 GHz and 300 GHz. Transmissivity through leaves was explained in details in section 4.2.

Based on the finding research which has been carried out by MISL group we can conclude that by shifting the automotive frequency from the current automotive frequency (below 100 GHz) to low THz frequency region does not introduce dramatic increase in attenuation through atmosphere over the range of operation (up to 2 m) on automotive radars.

4.5 Summary

This chapter reports results in regards of signal reduction due to radome contamination. In section 4.2 the attenuation of signal propagation through uniform layer of leaves which can build up on the antenna radome was investigated by the author of this thesis. The transmissivity through three sorts of leaves (Laurel, Birch, and Willow) was measured constantly with 300 GHz radar from when the leaves were fresh until they completely lost their water content through natural evaporation. The increase in transmissivity was observed while the leaves were losing their water content. The signal loss due to presence of fresh leaves of Laurel, Willow and Birch are -20 dB, -16 dB and -12 dB, respectively, while the transmissivity of -2.2 dB, -3.9 dB and -1.5 dB are measured for water stressed leaves Laurel, Willow and Birch. The results prove that the water inside the leaves is the main cause of signal reduction. The transmissivity figures are calculated in two ways: (i) by using effective permittivity of leaves and (ii) considering equivalent water layer for different WCR and using water permittivity. The second model shows a better agreement with the measured results.

In section 4.3 the transmissivity through a uniform layer of pure water, salty water with different levels of salt and actual seawater are measured and analysed at 300 GHz and 670 GHz by the author of this thesis and compared with the obtained results at 150 GHz [109]. The results show that the transmissivity is decreasing with increasing water thickness. Also a slight decrease in the transmissivity is observed with increasing water salinity at both frequencies. Additionally the results indicate that an increase in attenuation due to the presence of a uniform thickness of pure water, salty water and actual sea water, with an increase in frequency.

And finally in section 4.4 the attenuation through radome contamination (sand, Ice, gasoline and diesel) which was carried out by MISL group was discussed briefly. The measurement result of sand accumulated on a radome at 150 GHz and 300 GHz indicate that coarser sand particles produce greater attenuation than finer particles at both mentioned frequencies, furthermore the attenuation due to radome accumulated by sand at 300 GHz is higher than at 150 GHz.

Other common radome contaminant such as ice, diesel and gasoline are almost transparent at 77 GHz and the attenuation increase slightly at 150 GHz and 300 GHz.

Chapter 5: Low terahertz radar signal backscattering for surface identification

5.1 Overview

This chapter explores the scattering of signals within mm- and low Terahertz frequency range, represented by frequencies of 79 GHz, 150 GHz, 300 GHz, and 670 GHz, from surfaces with different roughness to demonstrate advantages of low THz radar for surface discrimination for automotive sensing. This study has been published in [130]. The work was done by the author of this PhD research under supervision of the paper's co-authors, Professor Gashinova, Professor Gardner, Dr Bystrov and Dr Navarro-Cia . The response of four surfaces (sandpaper) with different roughness was measured and their normalized radar cross sections were estimated as a function of grazing angle and polarization. The Fraunhofer criterion was used as a guideline for determining the type of backscattering (specular and diffuse). The proposed experimental technique provides high accuracy in the measurement of backscattering coefficient (normalized radar cross-section) and its dependence on the frequency of the signal, polarization, and grazing angle. An empirical scattering model was used to provide a reference, which is based on calculation of Fresnel reflection coefficients for different polarizations and grazing angles. To compare theoretical and experimental results of the signal scattering on test surfaces, the permittivity of sandpaper has been measured under supervision of Dr Miguel Navarro-Cia using time-domain spectroscopy in the school of Physics and Astronomy of University of Birmingham. It was shown that the empirical methods for diffuse radar signal scattering developed for lower radar frequencies can be extended for the low THz range with sufficient accuracy. The results obtained will provide reference information for creating remote surface identification systems for automotive use, which will be of particular advantage in surface classification, object classification and path determination in autonomous automotive vehicle operation.

5.2 Introduction

In chapter 1, I introduced the advantageousness of low THz radar in AV. The use of such radars allows an AV to effectively classify road objects and perform route planning [131,132].

Surface classification is an important outstanding problem in the implementation of autonomous vehicles. The extensive review of the papers on surface identification (Surface ID) using radar techniques can be found in [133]. As follows from the review, the most promising method for solving this problem is the analysis of the features of the backscattered signal with different polarization [19].

The principles of Surface ID are based on the theory of electromagnetic signal reflection from surfaces. Surface scattering is a function of surface roughness, characterized by its statistical parameters such as rms height and correlation length, radar frequency, grazing angle, and the effective permittivity of the material of the surface [134]. The problem of signal scattering from random surfaces has been investigated for many years [135]. There are two well-known solutions accounting for different ratios of wavelength and surface heights: (i) the Kirchhoff approximation, when surface roughness is larger or comparable to the wavelength and (ii) the small perturbation model, which performs better if the variation of surface heights is small relative to the wavelength [61]. Several models have been developed that combine these two, but they all have limitations on the signal frequency, on the surface dielectric constant and roughness characteristics [46]. Various empirical approaches are also widely used in the analysis of backscattering, where theoretical models are expanded or modified based on empirical observations to improve the performance of the original model in the interpretation of experimental data [15,136].

Advances in modern electronics have led to the emergence of commercially available radar components with frequencies above 100 GHz and this frequency range is currently of particular interest to automotive radar developers. At the same time, in most publications the analysis of radar signal backscattering is carried out in the frequency range up to 100 GHz and there is a limited number of studies investigating scattering of signals above 200 GHz. Most of these publications present research on diffuse scattering from rough surfaces in THz communication channels using time-domain spectrometers [137,138]. These works cover bistatic scattering measurements in the frequency range

from 100 GHz to 1 THz from a set of specially manufactured scattering targets with known roughness parameters. In [139] surface scattering was measured using a vector network analyzer (VNA) for 325-500 GHz and a dedicated system for 650 GHz. Of particular interest is [140], which examines 222 GHz polarimetric monostatic radar backscatter response of different types of real surfaces, such as asphalt, concrete, dirt, and grass of various length.

The lack of a comprehensive and consistent surface scattering studies over both the millimeter-wave and THz range simultaneously motivates this study. Hence, the aim here is to study and characterize the effect of signal backscattering from rough surfaces in the range of millimeter-wave and low THz frequencies (79 GHz-670 GHz) within the context of Surface ID for automotive sensing. The groundwork reported here for control samples (i.e., sandpapers with known geometrical parameters) identifies the impact of all critical parameters (e.g., surface roughness and dielectric properties, grazing angle, and polarization) on the surface backscattering and lays the foundations to make predictions for real road surfaces. Preliminary results related to this study were presented in [141]. In this study, an improved experimental technique for measuring normalized radar cross-section (RCS) of rough surfaces has been proposed and a method to calculate the normalized RCS of surfaces of different roughness as a function of radar and topology parameters was presented, such as polarization and aspect angle. The obtained measurement results were analyzed for compliance with the Fraunhofer criterion and were compared with normalized RCS, calculated based on an improved empirical model.

In this chapter firstly, the type of signal scattering based on the Fraunhofer criterion is discussed. Then, the methodology of backscattering coefficient measurement is described, the empirical model of signal scattering is discussed, and the results of sandpaper dielectric permittivity measurement are presented. The measured normalized RCS of sandpaper samples of four different levels of coarseness of the abrasive particles (grit) are presented in Section 5.4 and overall results are discussed in section 5.6. Finally, in Section 5.7, the conclusions and plans are formulated.

5.3 Backscattering of Radar Signal from Rough Surface

To classify surfaces with different roughness using radar, we should understand the nature of the reflection of the signal from such surfaces. Two main mechanisms of signal scattering on surfaces with different roughness are shown in Figure 5.1. In a case of perfectly smooth surface only specular reflection will occur. When the surface becomes rougher, the ratio of specular reflection component will decrease and the diffuse reflections, re-radiating signal in all directions, will become more prominent. In a case of very rough surface, the diffuse reflection prevails over specular.

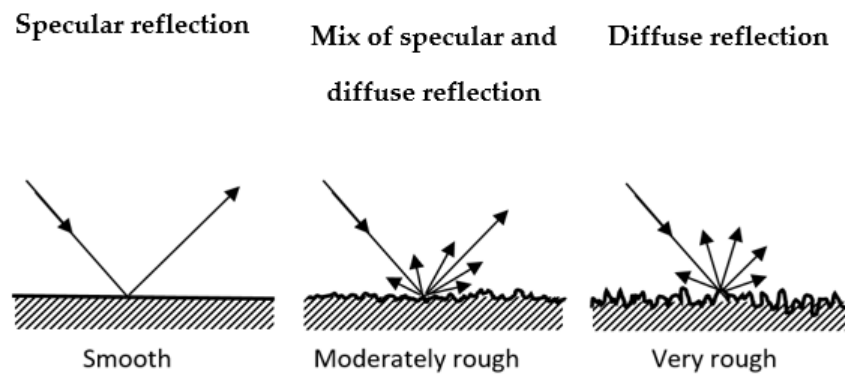


Figure 5.1: Reflection from smooth, moderately rough, and very rough surface

The type of scattering is defined by the surface rms height (root mean square average of the heights above or below a mean reference line) relative to wavelength. Based on the Fraunhofer criterion, the surface is considered as rough if the surface rms height h satisfies the inequality

$$h \geq \frac{\lambda}{32 \cos \theta} \quad (5.1)$$

where θ is the angle of incidence relative to the surface normal and λ is the signal wavelength [60].

To evaluate the surface roughness relative to the wavelength, it is convenient to use electromagnetic roughness kh , where $k=2\pi/\lambda$ is the free space wave number. Fraunhofer criterion (5.1) can be expressed in terms of electromagnetic roughness as

$$kh \geq 0.2/\cos \theta \quad (5.2)$$

This implies another definition for surface roughness [61], according to which a surface may be considered relatively smooth if its $kh < 0.2$ and very rough if its $kh \geq 2$.

Figure 5.2 shows graphs of rms height calculated in accordance with equation (5.1) defining the surface as rough with respect to different radar frequencies. Diffuse scattering dominates in regions above lines for each frequency, ensuring non-zero return to radar receiver as surface will become rough. Threshold lines with a constant value of h correspond to three typical road surfaces: 0.2 mm for smooth concrete, 0.33 mm for smooth asphalt, and 0.9 mm for rough asphalt [15].

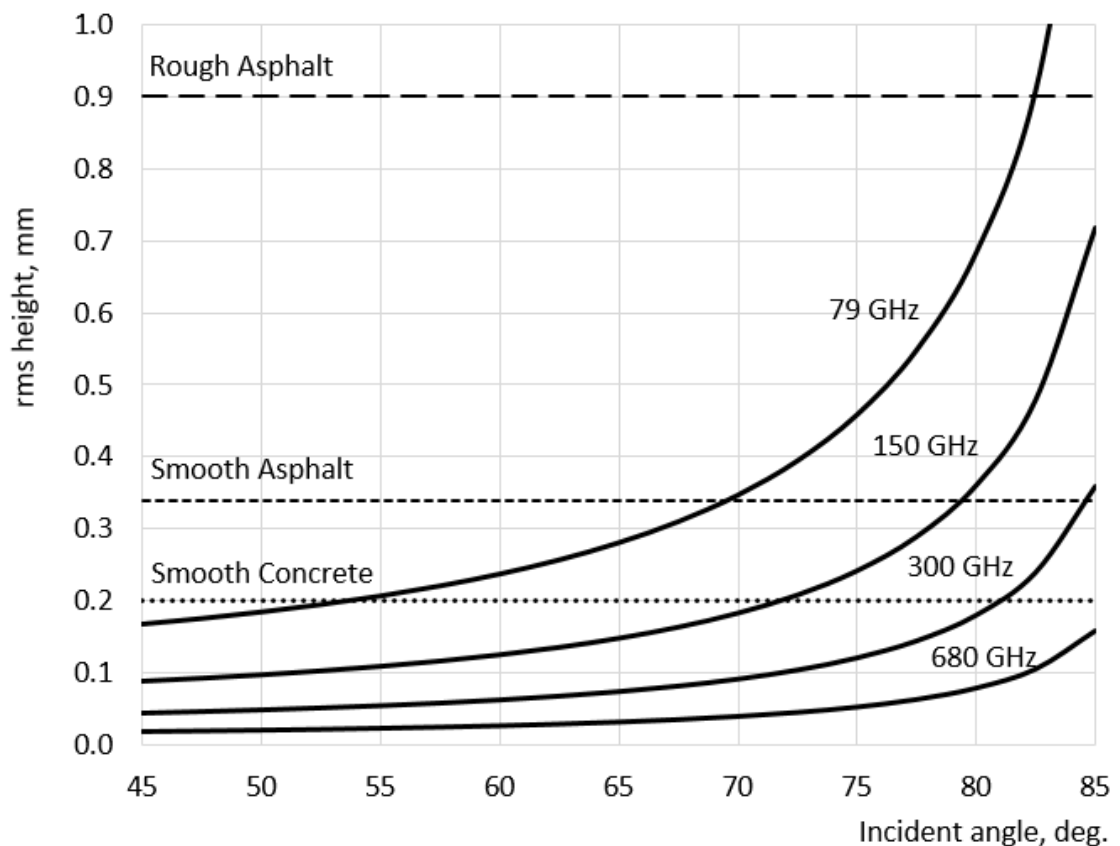


Figure 5.2: Roughness characterization of road surface as a function of incident angle and radar frequency[141]

The returned radar signal is defined by the RCS of the surface considered as a distributed target. As follows from the radar equation [142], the probability of target detection in a noisy environment depends on its RCS. In the cases that are considered, target detection means the ability to extract surface features from the backscattered signal. From a consideration of Figure 5.2, we can draw preliminary conclusions about the potential applicability of a radar operating at different frequencies for surface classification.

From Figure 5.2 it follows that a 79 GHz radar will not be able to distinguish smooth asphalt from smooth concrete at angles over 70° (the corresponding rms values are below the curve for 79 GHz, which suggests that they all appear effectively smooth). At the same time, 300 GHz radar can distinguish these surfaces to an angle of about 85°, and a 680 GHz radar is potentially able to distinguish smooth asphalt from smooth concrete up to an angle over 85°. Therefore, by increasing the radar frequency the ability to identify the type of road surface at higher incidence angle θ will improve. From here, we can make a conclusion about good prospects for using low THz radars for surface recognition.

In the case of automotive radars, low grazing (high incidence) angles are expected. Suppose we want to recognize a road surface at the distance of $R_0 = 10$ m in front of the car (Figure 5.3). At a speed of 40 km/h, the car will cover such a distance in about a second. This is the time in which the automatic system must determine the optimum terrain response settings for the surface ahead to maintain momentum and vehicle control as one surface transitions to another. The maximum height at which the radar can be installed on a passenger car is approximately $H = 1.5$ m (e.g., mirror on the windshield). Under the conditions considered, the incident angle θ will be approximately 81.5° which corresponds to a low grazing angle $\gamma = 8.5^\circ$. If the radar is positioned within the bumper of the car at a height of 60 cm, the grazing angle will be only 3°.

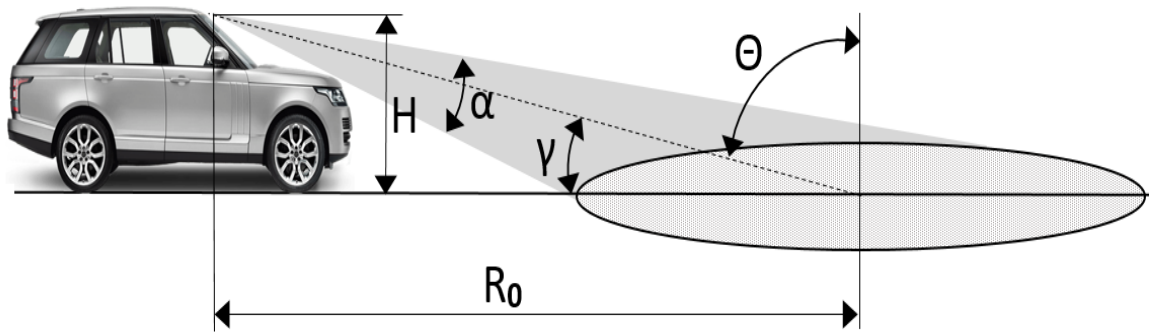


Figure 5.3: Automotive sensing scenario: H —Radar height over ground, α —Elevation beam width, R_0 —Ground range, ϑ —Incident angle, γ —Grazing angle.

In practical automotive radar implementation, at small grazing angle, the illuminated surface footprint will extend over a wide ground range. Let us say that the elevation beam width $\alpha = 10^\circ$, then the illuminated area of the road would lie from 6 m to 24 m, which corresponds to the range of grazing angles from 13.5° to 3.5° . Therefore, when analyzing the backscattered signal, we must consider the backscattering at different grazing angles. Applying time gating, we can choose a strip of surface lying at a certain angle. Analysis of the dependence of the backscattered signal power on the grazing angle provides additional information about the properties of the surface.

5.4 Experimental Methodology

The focus of this research is on studying the low THz signal backscattering from surfaces with different roughness. To achieve this goal and attain accurate measurement, sandpaper of different coarseness (grit) was used as a reference surface. The results can easily be extended to the case of real road surfaces if their roughness and complex permittivity are quantified. This section provides a concise and precise description of the experimental results, their interpretation, as well as the experimental conclusions that can be drawn.

The reflective properties of a surface are characterized by its normalized RCS and described in section 3.4.1.

5.4.1 Empirical Scattering Model

The empirical approaches to rough surface scattering are based on theoretical models and experimental observations. One of the best-known empirical models of radar backscattering response of natural surfaces was proposed in [136] for $0.1 < kh < 6.0$ and $2.5 < kl < 20$, where l is the correlation length; it was experimentally verified at 1.5–9.5 GHz. This model allows calculating co-polarization and cross-polarization ratios $\delta_{HH}^{\circ} / \sigma_{VV}^0$ and $\delta_{VH}^{\circ} / \sigma_{VV}^0$. Hereinafter, the first subscript indicates the transmitter antenna and the second subscript indicates the receiver antenna polarization.

According to this model, the co-polarized backscatter ratio can be described by the equation:

$$p = \frac{\sigma_{HH}^o}{\sigma_{VV}^o} = \left(1 - \left(\frac{2\theta}{\pi}\right)^{\frac{1}{3\Gamma_0}} e^{-kh}\right)^2 \quad (5.3)$$

where Γ_0 is the Fresnel reflectivity coefficient at nadir (i.e. $\theta = 0$), which depends on the relative permittivity ϵ_r of the surface material: $\Gamma_0 = \left|\frac{1-\sqrt{\epsilon_r}}{1+\sqrt{\epsilon_r}}\right|^2$.

Cross-polarized backscatter ratio can be calculated as

$$q = \frac{\sigma_{VH}^o}{\sigma_{VV}^o} = 0.23\sqrt{\Gamma_0}(1 - e^{-kh}) \quad (5.4)$$

The magnitude of σ_{VV}^o is described by the expression:

$$\sigma_{VV}^o = g \cos^3 \theta [\Gamma_V + \Gamma_H] / \sqrt{p} \quad (5.5)$$

where p is given by equation (5.3), $g = 0.7[1 - \exp(-0.65(kh)^{1.8})]$, Γ_V and Γ_H are Fresnel reflectivity for vertically and horizontally polarized waves, respectively, at the incidence angle θ . After calculating σ_{VV}^o using equation (5.5), the normalized RCS for other polarizations can be found from equations (5.3) and (5.4).

From equation (5.3) follows, that at small incidence angles the ratio of co-polarized signals p is close to one and decreases with increasing angle. The higher the roughness of the surface, the smaller the difference between normalized RCS at different polarizations. In addition, this ratio depends on the dielectric constant of the material. The cross-polarized ratio q is always much less than one and shows a stronger sensitivity to the surface roughness and a weaker dependence on the dielectric properties. In this study, tests are performed to show how this model matches the results of measuring signal backscattering at low THz frequencies.

5.4.2 Relative Permittivity of Surface Material

To use this empirical model, the dielectric properties of the surface material should be known. Sandpaper with grits 40, 80, 120, and 240, manufactured by Sealey Group (St Edmunds, UK), was chosen as a test surface (models PP232840, PP232880, WD2328120, and WD2328240, respectively). Sandpaper grits are categorized according to the coarseness of the abrasive particles used. The sandpaper is composed of backing material (paper or woven fibre) with $\epsilon_r = 2.0$, covered with abrasive (aluminum oxide grains) with $\epsilon_r = 9.7$, and adhesive (resin) with $\epsilon_r = 1.5-2.5$ at 1 MHz frequency [143]. The value of effective dielectric permittivity can be obtained from the dielectric constants and volume fractions of constituents of the test material. However, such data is not available in the open literature.

To retrieve the dielectric constant of sandpaper over the complete low THz range, the Menlo Systems THz time-domain spectrometer TERA K15 Mark II in a quasi-optical configuration was used along with a material parameter extraction algorithm [144], similarly to [145]. This retrieval algorithm minimizes the difference between the measured (defined as ratio of the sample spectrum to the reference spectrum computed by Fourier transform of the corresponding waveforms) and theoretical complex transfer functions using the Nelder-Mead simplex algorithm [146], whereby the thickness- and frequency-dependent complex refractive index of the sample are extracted after numerical optimization.

To estimate the thickness of the sample, the system measures temporal separation between the leading pulse and its echo and between successive echoes within the sample. The soundness of the algorithm is validated by comparing the thickness output by the retrieval algorithm and that provided by the sandpaper manufacturer.

To minimize the influence of scattering from the test surface in the retrieval method, we worked with a focused beam configuration using TPX (Polymethylpentene) plano-convex lenses [147] as shown in Figure 5.4. In such configuration, the diffuse scattering within ± 10 deg. approximately [148,149] was collected owing to the relay lens in the detection side and contributed to the retrieval method.

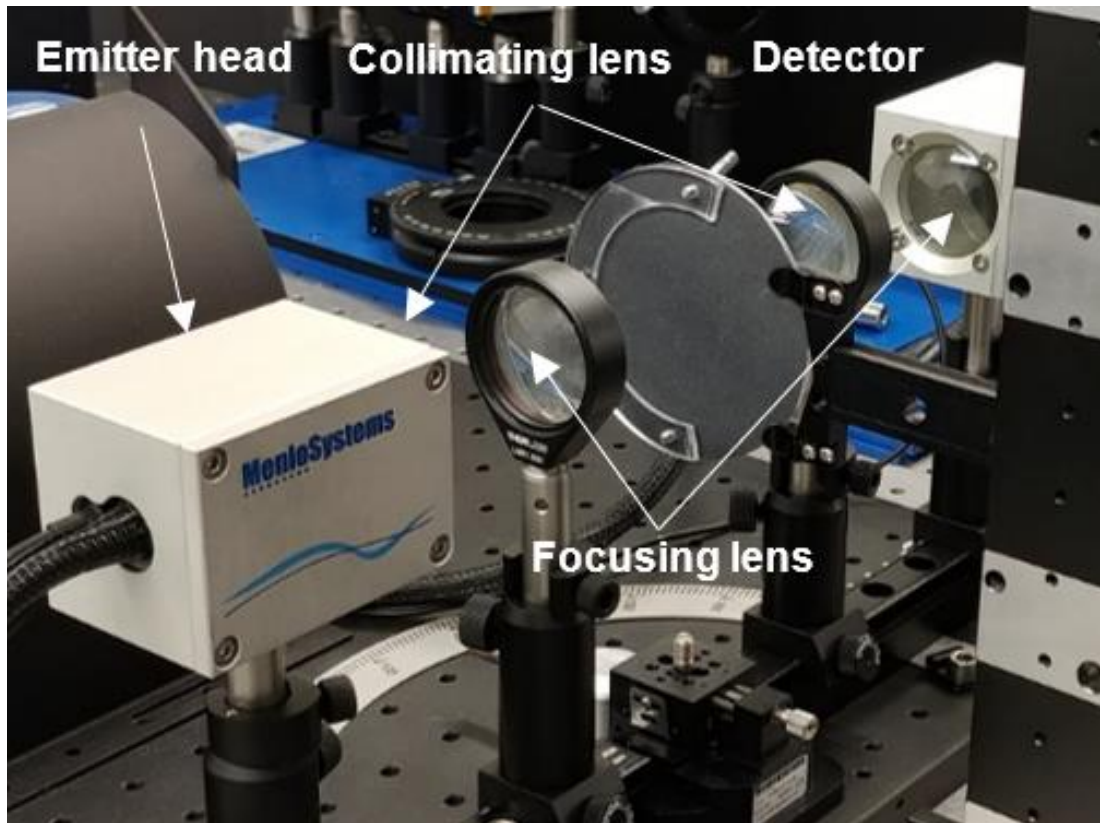


Figure 5.4: TDS system measurement set up

A collimated configuration was also employed for large grit number (fine grit) sandpaper to check consistency of the data. An 80 mm diameter round sandpaper sample was placed in the sample holder at the focal plane of the optical system where the frequency-dependent beam-waist was estimated to be larger than 1 mm below 700 GHz [147,148]. To decrease systematic errors, a series of three independent reference and sample measurements was taken.

For the characterization of the average power of return from rough surface, effective parameters suffice. Assumed homogenization of the medium is the conventional approach for the modelling of microwave structures where an effective dielectric permittivity is assigned to the multi-layered structure (which can be seen as the weighted average of dielectric properties of individual layers such as abrasive, substrate,

etc.). The simulation results presented below confirm this assumption as the dielectric permittivity used to generate analytical results agree very well with measurements.

The average measured permittivity values of sandpaper as well as their standard deviations at low THz frequencies are shown in Table 5.1. Due to the coarse roughness of the 40-grit sandpaper sample, the retrieval algorithm only converged for one of the three runs. Hence, the absence of standard deviation in Table 5.1 for this case.

The loss tangent, which is the measure of signal loss due to the dissipation of electromagnetic energy in the sandpaper, can be defined as

$$\tan \delta = \varepsilon'' / \varepsilon' \quad (5.6)$$

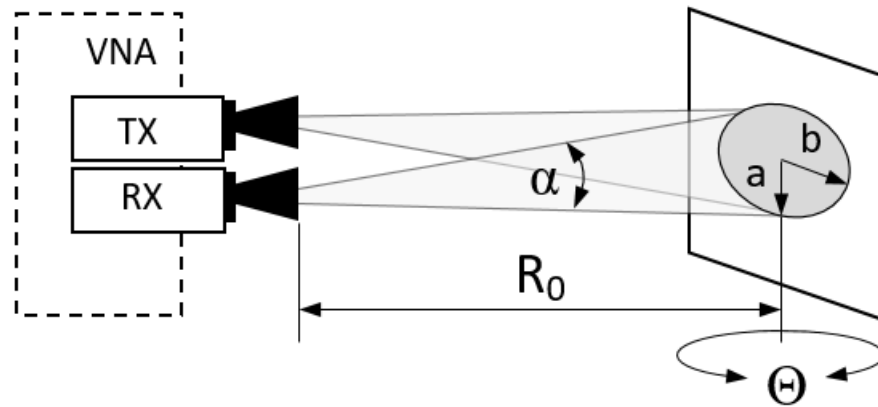
where ε' and ε'' are the real and the imaginary components of permittivity. The measured values of $\tan \delta$ are given in Table 5.1. In most cases, they are in the range of 0.20-0.30.

Table 5.1. Measured sandpaper relative permittivity

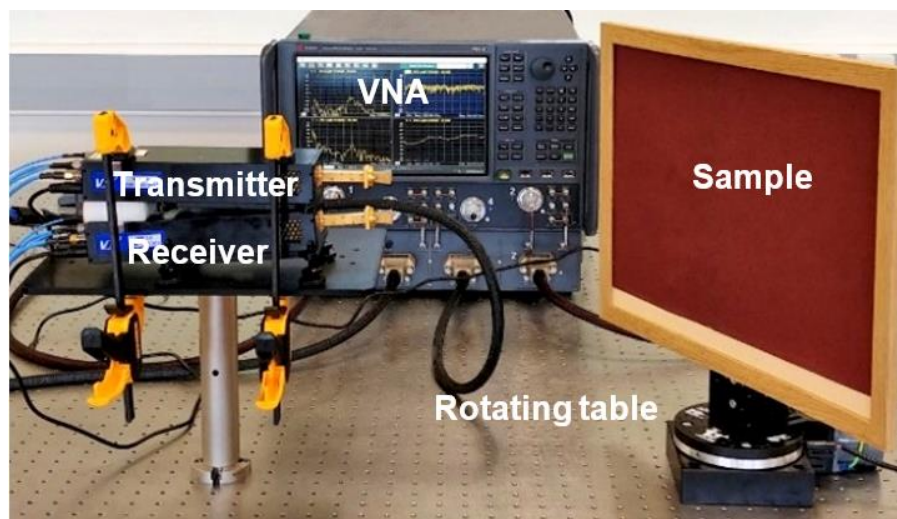
Frequency		Sandpaper grit			
		40	80	120	240
150 GHz	ϵ_r	3.6	3.6	4.4	4.9
	$\sigma_{\epsilon r}$	-	0.1	0.3	0.2
	$\tan \delta$	0.25	0.25	0.29	0.24
300 GHz	ϵ_r	3.4	3.4	3.9	4.6
	$\sigma_{\epsilon r}$	-	0.1	0.5	0.2
	$\tan \delta$	0.27	0.28	0.30	0.22
670 GHz	ϵ_r	2.9	3.5	3.1	4.3
	$\sigma_{\epsilon r}$	-	0.1	0.3	0.2
	$\tan \delta$	0.25	0.22	0.49	0.20

5.5 Measurement setup

For the backscattering experiments, we used the Keysight N5247B VNA which was described in sub section 3.2.1.3. The experimental setup is shown in Figure 5. 5.



a



b

Figure 5.5: Experimental setup configuration (a) schematic setup (b) actual setup.

The measuring system that corresponds to a quasi-monostatic radar with two closely spaced Tx and Rx antennas was stationary, only the test surface rotated and therefore the distance between the centre of the illuminated area and antennas, always remained the same. The rotation step was 5° , and the incidence angle varied from zero, when the antennas were perpendicular to the surface, to 80° , when they were almost parallel to the surface. Scattering coefficients were measured for co-polarized (vertical and

horizontal polarization) and cross-polarized transmit and receive signals at frequencies of 79 GHz, 150 GHz, 300 GHz, and 670 GHz. Different polarizations were obtained by rotating either Tx or Rx modules. Specifications of the system and set-up parameters are provided in Table 5.2, the photo of the used antennas for mentioned measurement are shown in Figure 3.6 in subsection of 3.2.1.3.

Table 5.2: Parameters of the measurement system

	Frequency, GHz			
	79	150	300	670
Frequency band, GHz	77-81	142-158	282-298	656-672
Wavelength, mm	3.8	2.0	1.0	0.4
Sweep bandwidth, GHz	4	16	16	16
Transmitted power, dBm	6	-6	-9	-25
Antenna azimuth beamwidth (-3dB)	10°	10°	10°	10°
Antenna elevation beamwidth (-3dB)	10°	10°	10°	10°
Antenna gain, dBi	20	24	25	20
Antenna aperture dimensions, mm	11×15	17×18	6×8	3×4
Far field range, mm	76	202	128	71
Range resolution, mm	37.5	9.4	9.4	9.4

For 79 GHz measurement we chose 4 GHz bandwidth which is defined by the European frequency regulation [27] for automotive radars in the 79 GHz frequency band. At higher frequencies, the wider bandwidths can be readily achieved to improve range resolution. Therefore, to resolve extended targets/surfaces with the imaging radar the 16 GHz

bandwidth has been used for 150 GHz, 300 GHz and 670 GHz radar measurement and the bandwidth kept the same to compare the results. The sandpaper rms height was measured in [150], and they are shown in Table 5.3 together with measured total thickness with backing paper/fabric and calculated electromagnetic roughness. The parameters given in [150] should be considered approximate, since there are no strict standards for sandpaper and the roughness can vary from batch to batch within certain limits.

Table 5.3: Sandpaper Parameters

Grit	Thickness, mm	Surface rms, mm	Electromagnetic roughness kh			
			79 GHz	150 GHz	300 GHz	670 GHz
40	1.25	0.11	0.18	0.34	0.69	1.55
80	0.46	0.06	0.10	0.19	0.38	0.84
120	0.43	0.03	0.05	0.09	0.19	0.42
240	0.28	0.01	0.02	0.03	0.06	0.14

The sample with dimensions of 28 cm by 46 cm was fixed in a frame mounted on a rotating table at 30 cm from the antennas. This distance is sufficient, since the far field distance of the antennas, estimated by

$$d_F = 2D^2/\lambda \quad (5.7)$$

where D is the maximum linear dimension of the antenna (Table 5.2), did not exceed 20 cm.

From consideration of Figure 5.5a, it follows that the illuminated area is an ellipse with semi-minor and semi-major axes:

$$a = R_0 \tan \frac{\alpha}{2} \quad \text{and} \quad b = R_0 \tan \frac{\alpha}{2} \frac{\cos \frac{\alpha}{2}}{\cos(\frac{\alpha}{2} + \Theta)} \quad (5.8)$$

where α is the antenna beamwidth. Thus, in the case under consideration, only the semi-major axis b depends on the aspect angle to the sample, increasing with the increase of incidence angle, while the semi-minor axis a is 26 mm. At an incidence angle of 82° the sandpaper sample is not anymore beam filling and this defines the largest incidence angle for which measurements can be made. To remove diffraction and other possible reflections, the signal was range-gated from 15 cm to 45 cm.

Antenna beamwidth $\alpha = 10^\circ$ (Table 5.2), and by approximating that $\cos\left(\frac{\alpha}{2}\right) = \cos(5^\circ) \approx 1$, the area of the ellipse $A = \pi ab$ can be expressed as

$$A \approx \frac{\pi R_0^2 \tan^2 \frac{\alpha}{2}}{\cos(\frac{\alpha}{2} + \Theta)} \quad (5.9)$$

Knowing RCS (equation 3.13) and A (equation (5.9)), the normalized RCS can be calculated by equation (3.12). The mentioned experimental setup allows taking measurements more conveniently than traditional methods with a fixed sample and moving antennas [19], because it does not require the use of a rotating frame for antennas and modules and the distance remains unchanged at any incidence angle. However, this method is applicable only for lightweight samples that can be mounted vertically.

THz radiation penetration depth D_p , defined as the distance from the surface into the dielectric at which the traveling wave power drops to e^{-1} from its value at the surface, can be expressed as [60]:

$$D_p = \frac{\lambda}{2\pi(2\varepsilon')^{1/2}} \left\{ \left[1 + \left(\frac{\varepsilon''}{\varepsilon'} \right)^2 \right]^{1/2} - 1 \right\}^{-1/2} \quad (5.10)$$

It should be noted that we are not applying the empirical model for scattering at 79 GHz. Therefore, considering Table 5.1 data and Equation (5.10), the maximum penetration depth is reached at 150 GHz and is in the range from 0.7 to 0.8 mm, which is more than the thickness of most sandpapers (see Table 5.3). In this case electromagnetic radiation is propagated in the air outside the sandpaper boundary, and reflections from objects outside the paper are cut off by time gating. At higher frequencies, the penetration does not exceed the thickness of the sandpaper. Thus, there is reflection from the surface and volume, and our experiment can be regarded as a special case of the scenario considered in [136].

5.6 Results and discussion

In this section the results of normalized RCS measurement for sandpaper with grits of 40, 80, 120, and 240 at different low THz frequencies (79, 150, 300, 670 GHz) are presented and compared with the empirical model, which is described in Section 5.4.1. As can be seen from Table 5.3, the considered combinations of roughness and frequencies cover all possible ranges - from very smooth to rough surface. At a frequency of 79 GHz, all surfaces will be smooth or relatively smooth, and at a frequency of 670 GHz, most of them will be rough or relatively rough. The frequencies of 150 GHz and 300 GHz are intermediate options between these two extremes.

To avoid dependence of the result on any potential texture, which may happen during abrasive layer deposition or bends, we have changed orientation of the sample by rotating it within the same imaging plane. For convenience of measurement, each sample was rotated by a step angle and measured, clockwise and anticlockwise. In the paper we refer to different measurements of the same sample. In the figures below, normalized RCS are represented as smoothed curves using a third-degree polynomial approximation.

5.6.1 Normalized RCS in Vertical Polarization

As a reference point, we chose a radar with a centre frequency of 79 GHz and 4 GHz bandwidth. The measured normalized RCS σ_{VV}° at 79 GHz is shown in Figure 5. 6a for different sandpapers. The results were averaged over six or more measurements; the error bars show the obtained standard deviation.

As can be seen from Figure 5. 6a, except for the final part of the graphs (grazing angle above 70°), the difference between σ_{VV}° of four sandpaper grits is within the accuracy of the measurement. At large grazing angles, the backscattering is highest because the geometry is close to specular reflections direction. However, this is outside the range of angles of interest for automotive pre-emptive sensing. When the angle decreases, the backscattering signal decreases for all samples equally. Indeed, based on the values of sandpaper electromagnetic roughness (Table 5. 3), all these samples are electrically “smooth”. Signal is mostly reflected away from the radar and the difference in backscattered signals would be insufficient for reliable classification.

The angular width of the specular reflection region depends on the antenna beamwidth. As the grazing angle decreases, the power P_r of the backscattered signal drops down to almost noise level. In accordance with equation (3. 11), this power drop is a result of a decrease in the normalized RCS σ^0 (equation 3. 8).

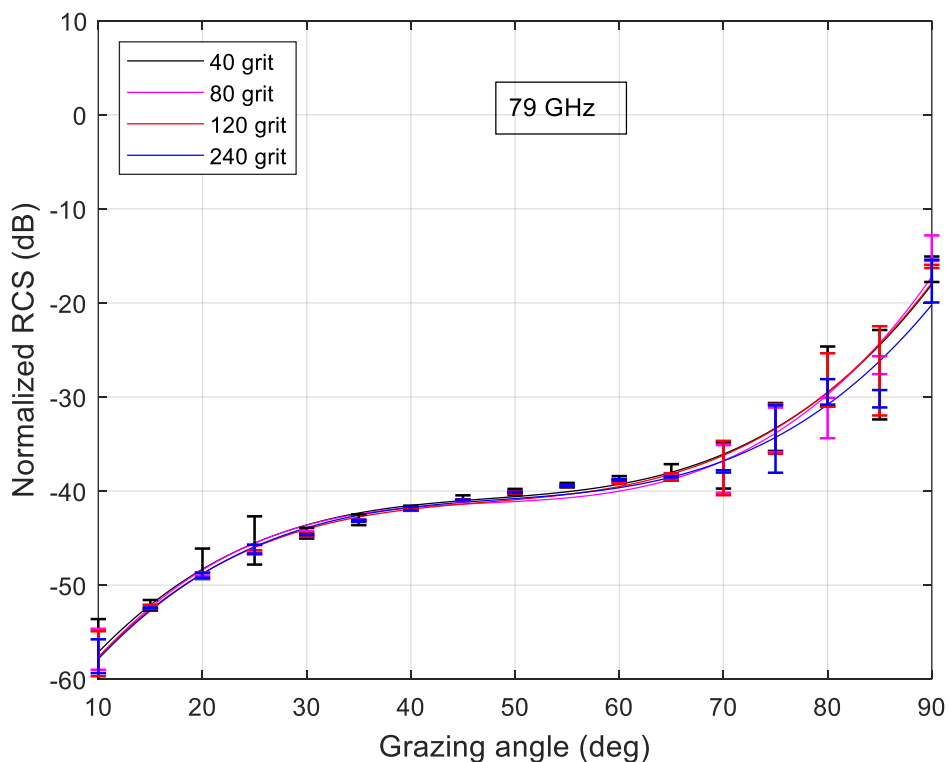
In Figure 5. 6b, the result of normalized RCS σ_{VV}° measurement at 150 GHz is shown as a function of a grazing angle. The graph clearly shows the difference in reflection from 40-grit sandpaper compared to all other grits. Indeed, based on Table 5. 3 in the first case we have a moderately rough surface with electromagnetic roughness 0.34 and in all other cases a smooth surface with electromagnetic roughness less than 0.2.

In accordance with the Fraunhofer criterion (equation 5. 1), the diffuse reflection region for sandpaper with grit 40 occurs at a grazing angle above 35°. The normalized RCS of 40-grit sandpaper reduces at lower angles however it remains considerably higher than for smoother sandpapers.

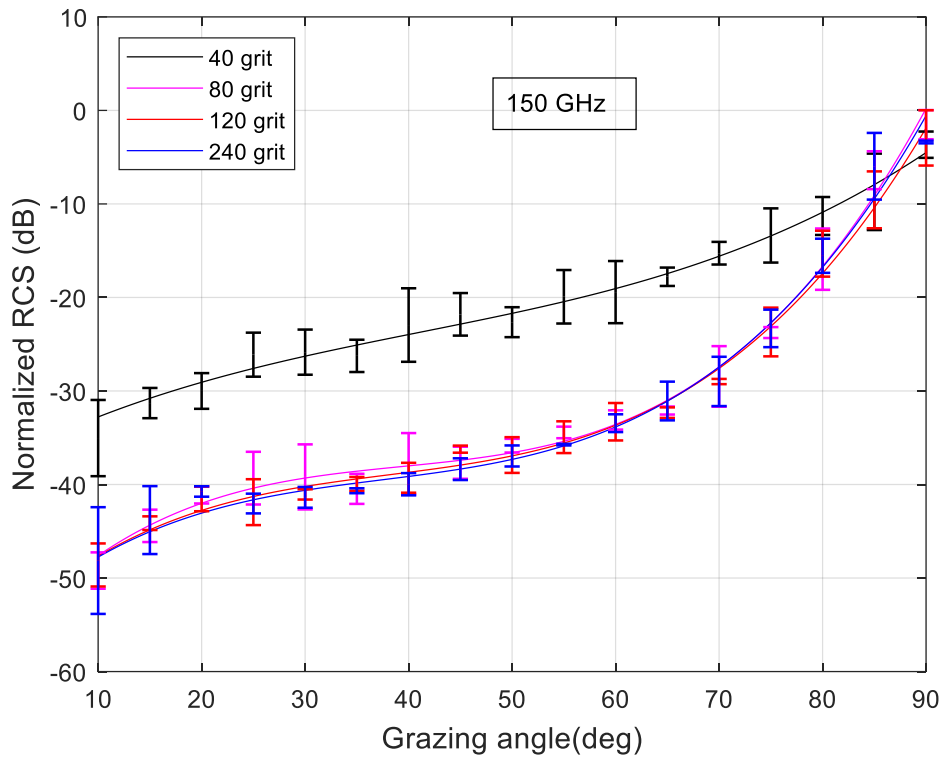
Figure 5. 6c depicts the result of σ_{VV}° measurement at 300 GHz as a function of a grazing angle for sandpapers with 40, 80, 120 and 240 grit. The reflection of a signal from 40-grit sandpaper is diffuse in almost the entire range of grazing angles, and in accordance with equation (5. 1) it has a specular reflection mechanism only below 17°.

No considerable differences were found in backscattering from sandpaper with grit 80 and 120. This is in some contradiction with the data in Table 5.3 where at a frequency of 300 GHz the electromagnetic roughness of sandpaper with grit 80 is 0.41 (mainly diffuse reflection), and sandpaper with grit 120 is 0.19 (mostly specular reflection). As discussed above in the Section 5.4.1, the properties of the backscattered signals are determined not only by the roughness of the surface, but also by its dielectric constant.

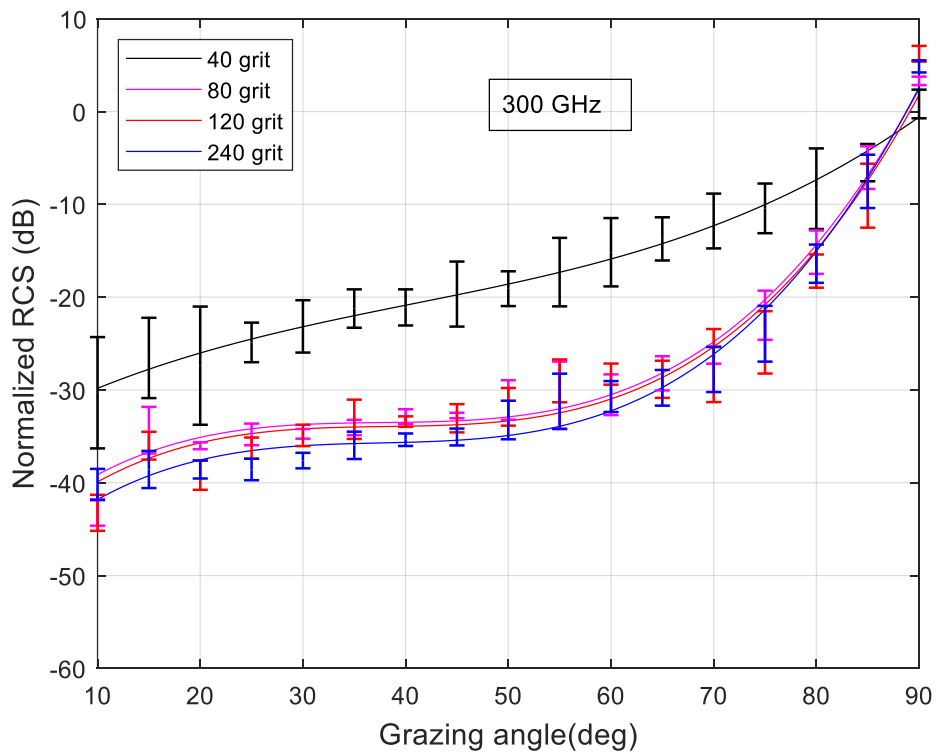
The results for σ_{VV}° as a function of the grazing angle are shown in Figure 5. 6d for 670 GHz. Graphs presented in Figure 5. 6d significantly differ from the previous results Figure (5. 6a–c), Reflection from all types of sandpaper, except for sandpaper with grit 240, is predominantly diffuse. According to the Fraunhofer criterion, this reflection pattern is preserved, depending on the size of the grit, until the angle decreases to 15°–25°. With a further decrease in the grazing angle, the normalized RCS rapidly decreases. At the same time, an expected trend for return power is observed: the higher the roughness of the surface, the greater the power of the reflected signal. Reflection from 240-grit sandpaper is generally specular; the graph is characterized by a peak at high grazing angles with the width depending on the width of the antenna beam, and a rapid decrease at lower angles.



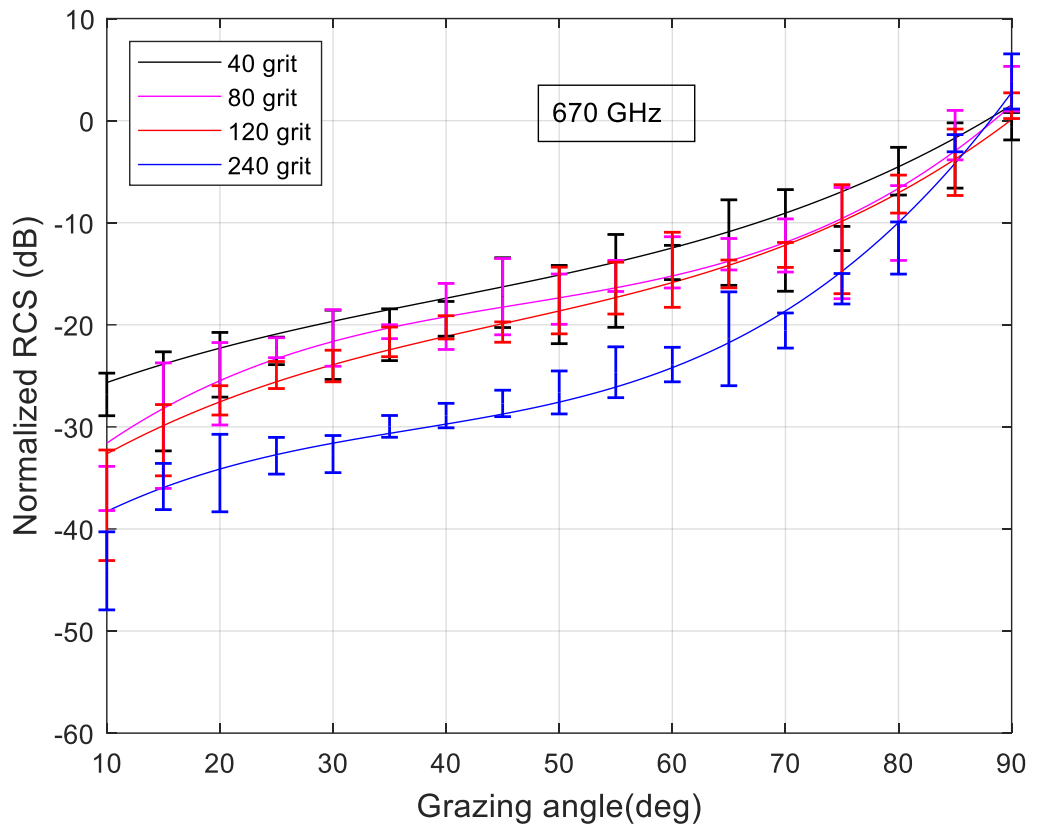
(a)



(b)



(c)



(d)

Figure 5.6: The normalized RCS σ_{VV}° : (a) 79 GHz, (b) 150 GHz, (c) 300 GHz, and (d) 670 GHz.

Figure 5.7 shows discrete values of normalized RCS σ_{VV}° versus electromagnetic roughness (see Table 5.3) for different sandpapers at a grazing angle of 10° . The general trend for the normalized RCS to increase with increasing kh is clearly seen.

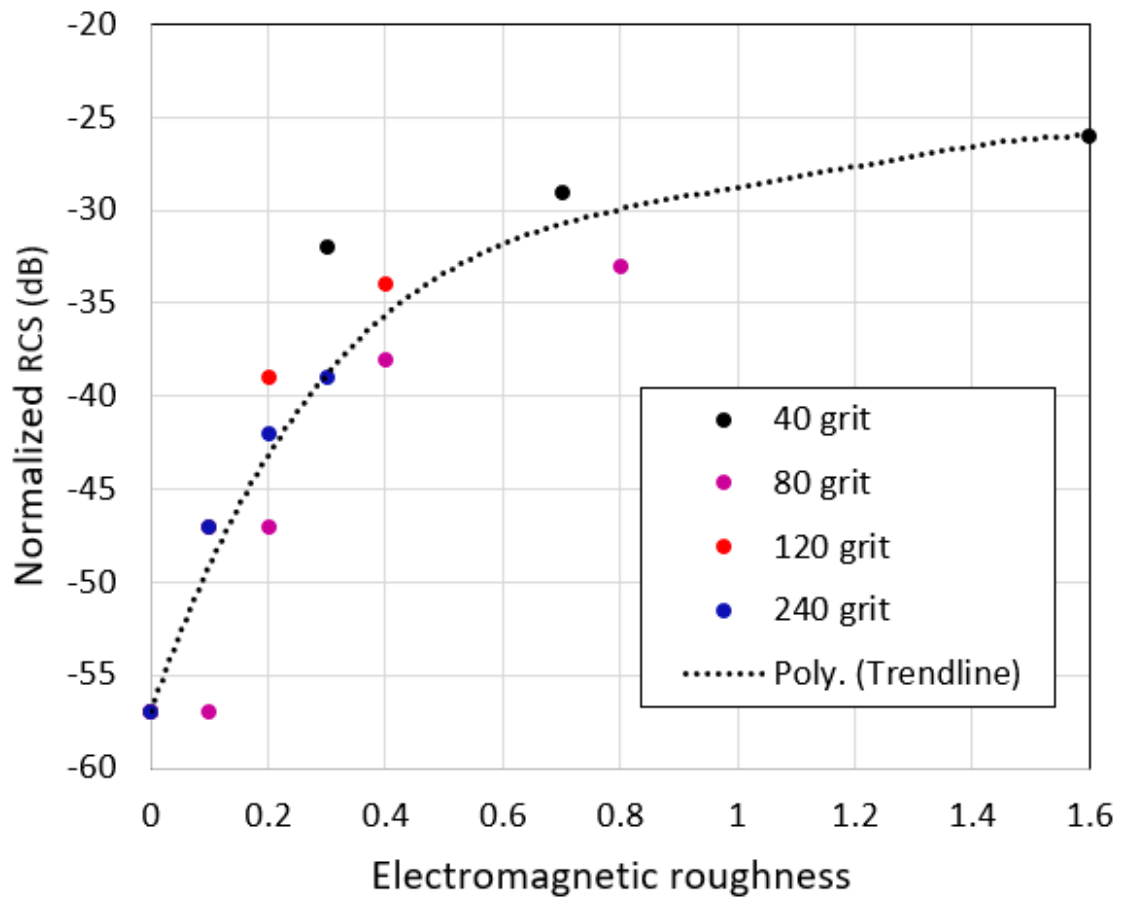


Figure 5.7: normalized RCS σ_{VV}° as a function of electromagnetic roughness at a grazing angle of 10° .

5.6.2 Measured and Calculated Normalized RCS

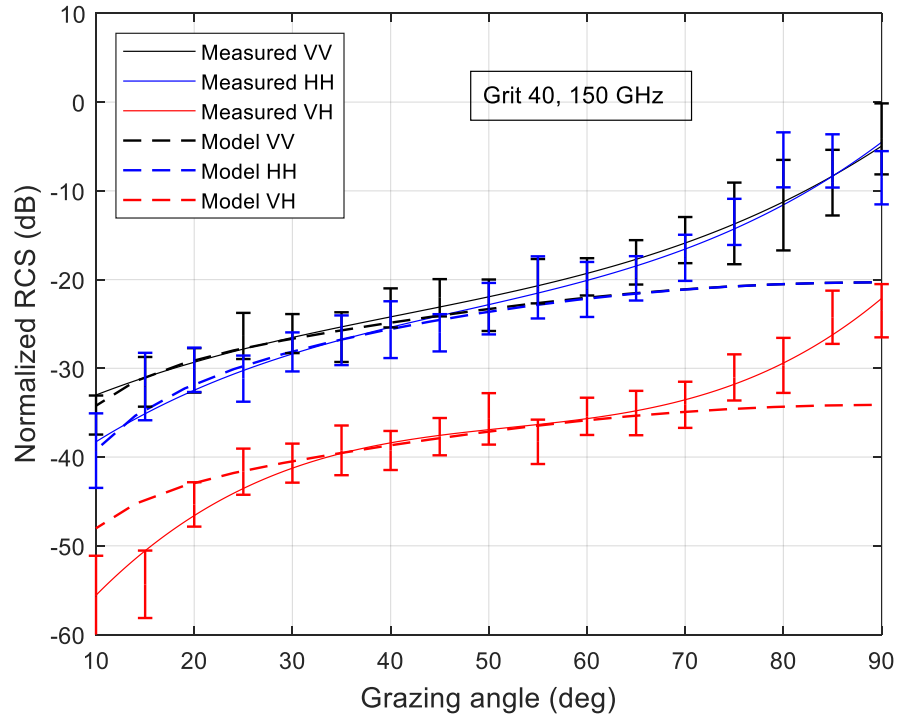
Figure 5.8 depicts the measured and calculated normalized RCS at different signal polarizations: σ_{VV}° , σ_{HH}° , and σ_{HV}° as a function of grazing angle increment. In this section, only reflection from sandpaper with two extreme values of roughness (grit 40 and grit 240) at two frequencies (150 GHz and 600 GHz) are considered, since the above examples illustrate well the general dependencies. The theoretical values are calculated using the empirical model explained in Section 5.4.1.

All considerations regarding the behaviour of the graphs at different frequencies depending on the roughness of the surface, made during the discussion of Figure 5.6a-d are valid for this case. As can be seen from the Figure 5.8a-d, at higher grazing angles the graphs for signals with horizontal and vertical polarization coincide within the measurement accuracy. It follows from Equation (3.13) that in all cases $\sigma_{HH}^\circ/\sigma_{VV}^\circ \leq 1$, and a noticeable difference between normalized RCS manifests itself with a decrease in the grazing angle. Calculations show that with an increase in the relative permittivity of the surface material, this difference also increases. In the example under consideration, ϵ_r of the sandpapers at a frequency of 150 GHz lay in the range from 3.6 to 4.9 (Table 5.1). In the case of real road surfaces, the relative permittivity value can vary within a much wider range, for example, from 4.27 to 15.20 at 4.8 GHz [136]. We can expect that certain similar differences will exist in the low THz frequency range. This will make the difference between the curves σ_{HH}° and σ_{VV}° more noticeable and simplify the task of classifying surfaces.

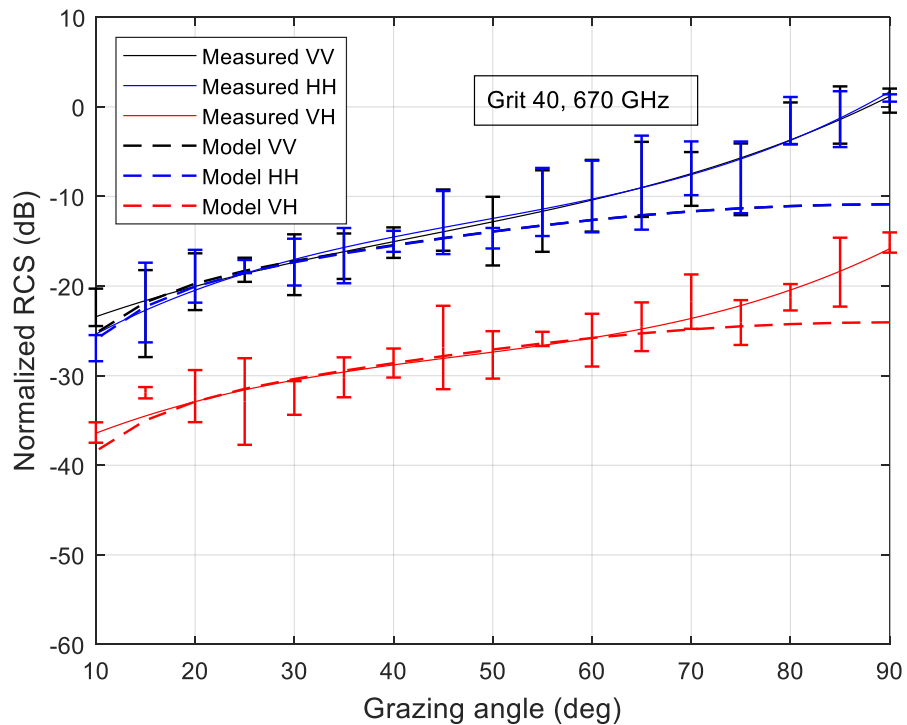
As can be seen from Figure 5.8a-d, at grazing angles less than about 50°, the experimental results are in good agreement with normalized RCS calculated according to (5.3) - (5.5). This allows us to draw a conclusion about the applicability of the empirical scattering model, introduced in Section 5.4.1, for the low THz range of signals. It should be noted that the empirical model could not be used for the cases of specular reflections which take place at high grazing angles. However, as already mentioned, the low grazing angles is interested, and therefore this limitation does not seem significant.

The normalized RCS for cross-polarized signal σ_{VH}° (σ_{HV}°) are significantly weaker than for co-polarized signal. In accordance with the empirical model, cross-polarized backscatter ratio q (equation (5.4)) does not depend on the grazing angle. Indeed, in the case of 40-grit sandpaper, at a signal frequency of 150 GHz in the range of angles

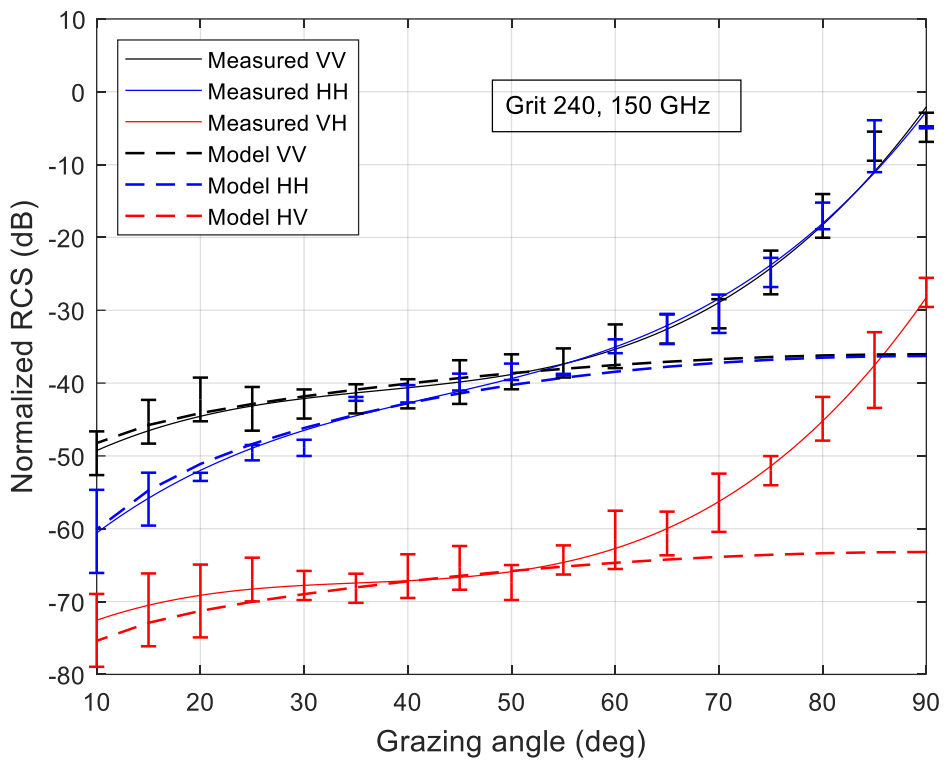
from 30° to 90°, the difference between the co-polarized and cross-polarized signal is about 16 dB (Figure 5. 8a). At a signal frequency of 670 GHz, this difference was about 14 dB (Figure 5. 8b)). Similar dependences are observed for paper with grit 240 (Figure 5. 8c-d).



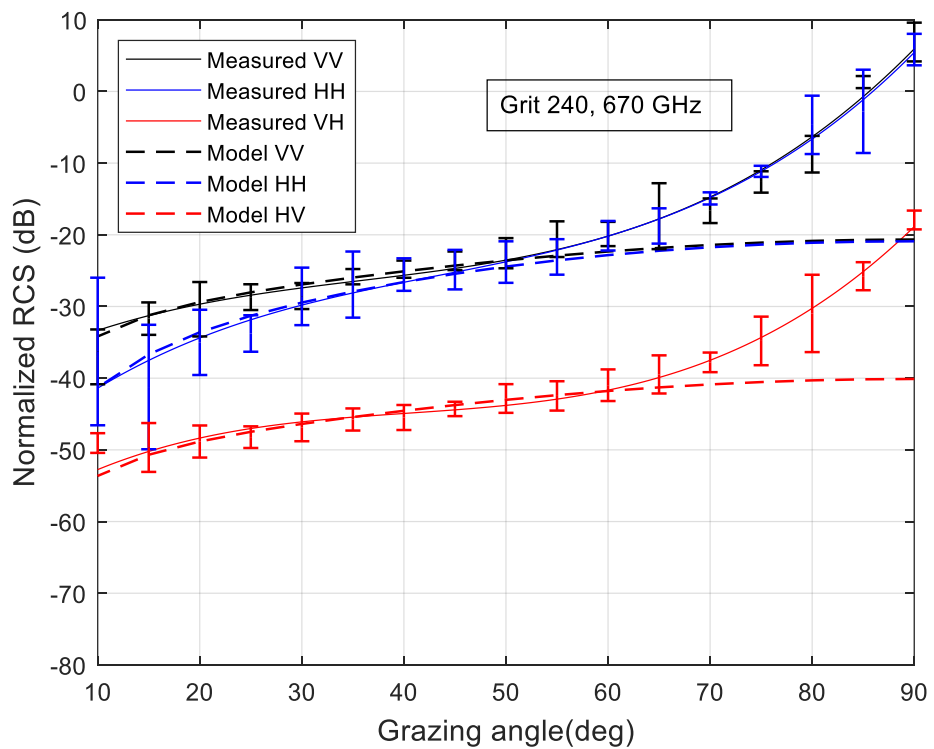
(a)



(b)



(c)



(d)

Figure 5.8: Measured and calculated normalized RCS: (a) grit 40 at 150 GHz, (b) grit 40 at 670 GHz, (c) grit 240 at 150 GHz, and (d) grit 240 at 670 GHz.

Table 5.4 shows the ratio q measured in the range from 30° to 90°. As can be seen from the table, for each sample and frequency, this ratio varies within relatively small limits over the specified range of grazing angles.

Table 5.4. Cross-polarized backscatter ratio q , dB

Grazing angle	30°	60°	90°
Grit 40, 150 GHz	-16	-16	-17
Grit 40, 670 GHz	-13	-14	-14
Grit 240, 150 GHz	-26	-26	-26
Grit 240, 670 GHz	-19	-20	-22

As can be seen from Figure 5. 8a–c, at low grazing angles, there was some difference between the model and the experiment. This may be the result of the backscattering return power approaching the noise floor of the instrument. This effect is especially noticeable when measuring cross-polarization returns σ_{VH}° (σ_{HV}°), since the power of the backscattered cross-polarized signal becomes very small. In addition, the sandpaper sample is not ideally flat which affects the accuracy of the measurements for small grazing angle wherein the sample’s unevenness becomes more relevant.

5.6.3 Discussion

The difference in the power of the vertically polarized and horizontally polarized signal allows us to conclude about the dielectric parameters of the surfaces. In real road conditions, due to different dielectric permittivity, the difference between signals backscattered from different surfaces will be significantly larger than in the experiment.

For example, in [140] it is shown that at a frequency of 94 GHz the effective dielectric constant of road surfaces varies from 2.5 for dirt road to 4.2 for concrete. If we assume that the roughness of these surfaces is the same, then in accordance with (5. 3) - (5. 5), due to a different dielectric constant, the difference between normalized RCS of these surfaces at 45° will be 6.5 dB. For comparison, the variations of ϵ_r measured at 150 GHz for sandpaper are in the range from 3.6 to 4.9 (see Table 5.1). This gives us the difference of normalized RCS due to ϵ_r of about 2.6 dB. In particular, the analysis of backscattered signals can be used to determine surface moisture to detect ice and water [19,133] .

The backscattered cross-polarized signal also carries information about the properties of surfaces (roughness and dielectric constant); however, its low power at low grazing angles can make it difficult to extract and analyze the parameters of such a signal. The ability to use such information will depend on the practical implementation of the radar.

The absolute values of the reflected signals cannot serve as a reliable basis for surface identification, since they depend on the individual parameters of the transmitter and the receiver, their installation accuracy, antenna radome contamination (dirt, mud, snow, etc.). Therefore, the use of co-polarization and cross-polarization ratios, together with other signal characteristics, will give more reliable classification results.

The ability to distinguish surfaces gives good prospects for imaging radar in recognizing road markings, which may be important when developing autonomous cars [35]. As shown in [131,132], wide band 79 GHz automotive radar allows sufficiently accurate image segmentation and classification of surfaces and obstacles which are the key technologies to provide valuable information for path planning in autonomous driving. From these results, it follows that increasing the frequency of the radar can potentially lead to more accurate discrimination of a larger number of surfaces.

Let us now consider the effect of surface clutter return on the recognition of road objects. The results of measuring surface RCS lead to important conclusions about the degree of this influence. The normalized RCS decreases rapidly with decreasing grazing angle (increasing distance). Therefore, the power of the signal reflected from the road surface which is proportional to σ/R_0^4 (equation (3. 9)) will decrease faster than the power of the signal reflected from the considered as point targets road objects which is proportional to $1/R_0^4$. This leads to an increase in signal-to-clutter ratio. Let us say that in the case of 40 grit sandpaper at a frequency of 300 GHz, this ratio was 0 dB at an angle of 45°. Then, as follows from Figure 5. 6c, with a decrease in the angle to 10°, due to a decrease in the normalized RCS, this ratio will increase to approximately 10 dB. Of course, we must consider that with a high-resolution radar, even road objects will be area scatterers so the simple $1/R_0^4$ rule does not really apply to them. However, the obtained results give us confidence that such techniques might be feasible and with the range of hundreds of metres, reflection from the road surface will not impede the recognition of objects.

5.7 Conclusion

The aim of this work was to study the characteristics of low THz signal reflection from surfaces with different roughness in terms of applicability in automotive radars. It should be noted that how the reflected signal from the road surfaces can be used to classify surfaces. The radar with frequencies: 79 GHz, 150 GHz, 300 GHz, and 670 GHz were examined and measured the backscattering from sandpaper with grit 40, 80, 120 and 240. The resulting frequency and grit combinations cover all possible variants, from very smooth to very rough surfaces.

In general, three areas can be distinguished in the graphs of normalized RCS of co-polarized signal:

1. The initial section of the graph relates to the dominant specular reflection region, where the reflected signal is weak and rapidly decreases with increasing distance (decreasing grazing angle). The power of such a signal is likely to be insufficient for the classification of surfaces.
2. The diffuse reflection region, the extent of which is determined by the Fraunhofer criterion, where the reflected signal is strong enough for distinguishing surfaces with different roughness. This region may be almost absent when the signal is reflected from a smooth surface when the power of backscattering signal is low.
3. The third distinctive region where the level of the reflected signal is maximum, its angular range depends on the beamwidth of the antenna. The smoother the surface, the more prominent this region. With a very rough surface, this region is barely visible.

The use of a signal in the low THz range allows us to obtain diffuse reflection from road surfaces, which are smooth surfaces at the usual frequencies of automobile radars (24 GHz or 79 GHz).

The results of proposed experiments showed that the Fraunhofer criterion could serve as a sufficiently accurate guideline for determining the surface roughness characterization in the low THz range. The empirical scattering model, discussed in Section 5.4.1, showed good accuracy in diffuse reflection area in comparison with our measured result in the low THz range; it provides an important understanding of the

features of radar signal backscattering. However, its use requires knowledge of the properties of surfaces, including roughness and the dielectric constant.

This work provides an insight into the effects of surface roughness on signal backscattering, which will play an important role in understanding the complex problem of signal reflection from actual road surfaces. The results obtained will allow selection of the features of the backscattered signal to effectively distinguish between road surfaces.

The novelty and importance of these results lie in the experimental demonstration of an advantage of moving higher in frequency for the automotive surface ID radar in terms of increased normalized RCS measured at various conditions and range of grazing angles, in confirmation of the applicability of the known models of signal backscattering to the region of low THz frequencies, and in substantiating the possibility of surface identification by analyzing the parameters of polarized backscattered signal.

5.8 Summary

This chapter reports the radar signal backscattering within the mm-wave and low THz frequency range of 79 GHz, 150 GHz, 300 GHz, and 670 GHz and from the sandpaper with grit 40, 80, 120 and 240 to demonstrate benefits of low THz radar for surface identification for automotive sensing.

In section 5.3 the Fraunhofer criterion was discussed as a guideline for determining the type of backscattering (specular and diffuse).

The responses of four sandpapers, made of similar material, but of different roughness were measured and their normalized radar cross sections were estimated as a function of grazing angle and polarization. The experimental technique developed in this work provides backscattering coefficient (normalized radar cross-section) measurement with high accuracy, as a function of frequency, polarization, and grazing angle.

The results show that the Fraunhofer criterion could serve as a sufficiently accurate guideline for determining the surface roughness characterization in the Low THz range. The empirical model showed good accuracy in comparison with measured results in the Low THz range; it provides an important understanding of the features of radar signal backscattering. However, its use requires knowledge of the properties of surfaces, including roughness and the dielectric properties of the surface material. The results obtained will provide reference information for creating remote surface identification systems for automotive use, which will be of particular advantage in surface classification, object classification and path determination in autonomous automotive vehicle operation.

Chapter 6: Surface classification based on low THz radar imaging using convolutional neural network

6.1 Overview

As mentioned in previous chapter the development of an automotive surface recognition system is an important and yet unsolved task. So, in this chapter, a novel approach to surface classification has been considered based on the analysis of the Low THz radar images, using convolutional neural networks (CNN). Firstly in section 6.3 it shows the promising results which were published in [151] in classification of surfaces (sandpapers) with known roughness in laboratory conditions using 150 GHz and 300 GHz radars. The proposed experimental technique in combination with a convolutional neural network provides high surface classification accuracy. And secondly in section 6.4 the novel approach has been applied to the data of actual road scenes collected during outdoor trials, obtained using 79 GHz scanning radar and creating the real road surface images. Finally in order to classify the surfaces with a neural network, the unique dataset based on the gained radar images has been produced. The proposed dataset contains different types of road surfaces which are labelled in six different classes for road surface classification tasks. The proposed study provides high surface classification accuracy and has been published in [152]. The work described in this chapter and in the mentioned publications [136,137] was carried out and both publications were written by the author of this thesis under supervision of the co-authors of the papers, Professor Gardner and Professor Gashinova and Dr Bystrov.

6.2 Introduction

The first works on the recognition of road surfaces using stationary radar appeared back in the 1980s and since then the topic has attracted constant attention by researchers and the automotive industry. Although during recent years there has been great progress in AV development, there are still some unsolved tasks, among them the development of surface identification (Surface ID) system. This system should remotely classify the road surfaces and alert the driver or AV computer to potentially hazardous road surfaces, ice, standing water or changes in road path, which will allow the vehicle to remain safely under control as it transitions from one surface to another, reducing costly damage, avoiding injury and saving lives. Automatically adapting vehicle speed to surface conditions is an essential step in providing autonomous driving. In four-wheel drive vehicles, Surface ID system will enable two or four-wheel drive to be selected as appropriate, therefore also helping to reduce CO2 emissions.

There are different sensor technologies for road surface classification, such as optic cameras [6-10], light detection and ranging (LIDAR)[11,12], sonar[5,13], and radar [14-22]. LIDAR uses laser light and because of high resolution has the advantage of detecting small objects. Optical cameras are cheap, lightweight, they produce an easily understandable colour image of the scene and they support sufficient range. In addition, stereo cameras provide a depth map where distance to the object can be evaluated by disparity of cameras. However, severe weather conditions negatively affect the performance of LIDAR and optical cameras. Furthermore, optical cameras require adequate visible radiation levels and have poor performance in limited lighting conditions. The advantages of sonar are the small size of a transceiver, simplicity and cheapness combined with high range resolution. On the other hand, the sonar has a low range (usually up to 6-8 meters), and it is mostly used in parking sensors. To provide partial or full autonomy, automotive sensors for surface classification should be operational under all weather conditions, including rain, snow and fog, and at any time of the day. Unlike LIDAR, optical sensors and sonar, radar sensors have the advantage of robust operation in harsh weather and lighting conditions [23-25].

As mentioned previously, because of the advantages of operating in high frequency ranges, currently, one of the trends in the development of automotive radars is to increase the operating frequency from 24 GHz to 79 GHz and higher. However by

increasing the operating frequency the signal backscattering from road surfaces needs to take into account.

Our research is based on the theory of electromagnetic signal backscattering from rough surface; Some of the important parameters which highly influence the surface backscattering are: surface roughness, characterized by root-mean-square (rms) height and correlation length; dielectric property of the surface material, which largely depends on its moisture content; and radar operational frequency. The backscattering coefficient of a distributed target as explained in equation (3.4) is an ensemble average of the radar cross section σ per unit of illuminated surface area A . In chapter 5 the results of experimental verification of this theory have been presented for low THz frequency range. For the considered case of automotive radar, the diffuse backscattering is of particular interest. Indeed, an increase in the power of the reflected signal occurring in this case allows a more accurate classification of the type of road surface. In contrast, the power of the signal backscattered from a smooth road surface is low and is not sufficient for surface differentiation. Most road surfaces are effectively smooth when low frequency radar signals are used. In order to evaluate the surface roughness relative to wavelength the Fraunhofer criterion (5.1) can be expressed in terms of electromagnetic roughness (kh) as explained in equation (5.2) and based on that surface may be considered relatively smooth if its $kh < 0.2$ and very rough if its $kh \geq 2$. From the Fraunhofer criterion it follows that with an increase in the frequency of the radar, its ability to distinguish surfaces improves. For example as its expressed in figure 5.2 rough asphalt with $h=0.90$ mm and smooth asphalt with $h= 0.33$ mm. For a radar with a frequency of 79 GHz (wavelength of 3.8 mm) with an incidence angle of over 82° , both of these surfaces will be smooth and indistinguishable (5.1). At the same time, a radar with a frequency of 300 GHz (wavelength of 1 mm) will be able to distinguish them even at an incidence angle of 88° . Let us assume that the radar is mounted at a height of 1 m above the road. An angle of 82° corresponds to only 7 m, and an angle of 88° - of almost 30 m.

In this chapter the performance of low THz imaging radar in the Surface ID task has been analyzed. This became possible by improving the resolution of the radar with increasing frequency, bandwidth, and using a signal wavelength commensurate with the roughness of the road surface. This work will allow us to subsequently move on to surface recognition using low THz radar.

As mentioned above, road surface classification using different sensor technologies has been investigated in many works, including those related to radars operating in the millimeter wave (mmWave) range up to 100 GHz [20-22], however there is no evidence of the study on recognition of different road surfaces based on the analysis of data obtained using imaging radar at frequencies corresponding to definition of low THz (0.1 THz-1 THz). The novelty of this work is the use of imaging radar to recognize road surfaces within the range of low THz radar and classify them by application of neural networks.

In [26,133], attention was focused on the practical implementation of the surface recognition system. In [133] the combination of 24 GHz polarimetric radar and 40 kHz sonar was used to classify different road surfaces (asphalt, grass, gravel, sand and bitumen) in various weather condition (ice, snow, and rain). Different statistical classification methods were used for surface identification, and the most accurate between them was multilayer perceptron (MLP), which is a class of feedforward artificial neural network (ANN). When using MLP, the classification accuracy of fourteen surfaces exceeded 95%.

6.3 Surface classification based on Low Terahertz Radar Imaging and Convolutional Neural Network

The new approach to road surface recognition considered here is based on analysis of surface images using a convolutional neural network (CNN). The novelty of this work is the use of imaging radar to recognize road surfaces. This became possible by improving the resolution of the radar with increasing frequency, bandwidth, and using a signal wavelength commensurate with the roughness of the road surface. In this section only the results obtained in controllable conditions are present at very short ranges due to currently limited power available from used instrumentations, as will be described in next sub section. In section 6.4 the results of actual road surface classification in outdoor trial are presented.

6.3.1 The experimental setup

The experiment was conducted at the Terahertz measurement facility of the University of Birmingham. The centrepiece of the facility is the Keysight N5247B vector network analyser (VNA), which is capable of measurement of the full two-port scattering parameters in the frequency range up to 1.1 THz using the frequency converter units as explained in section 3.2.1.3. The experimental setup is shown in Figure 6.1. The aim is to distinguish the patch of sandpaper of different roughness against the surface of the floor, which ultimately should lead to image segmentation and surface identification.

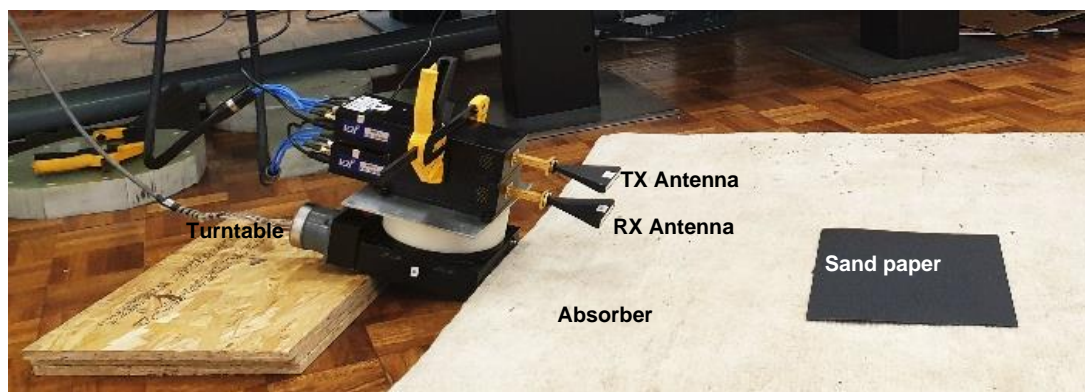
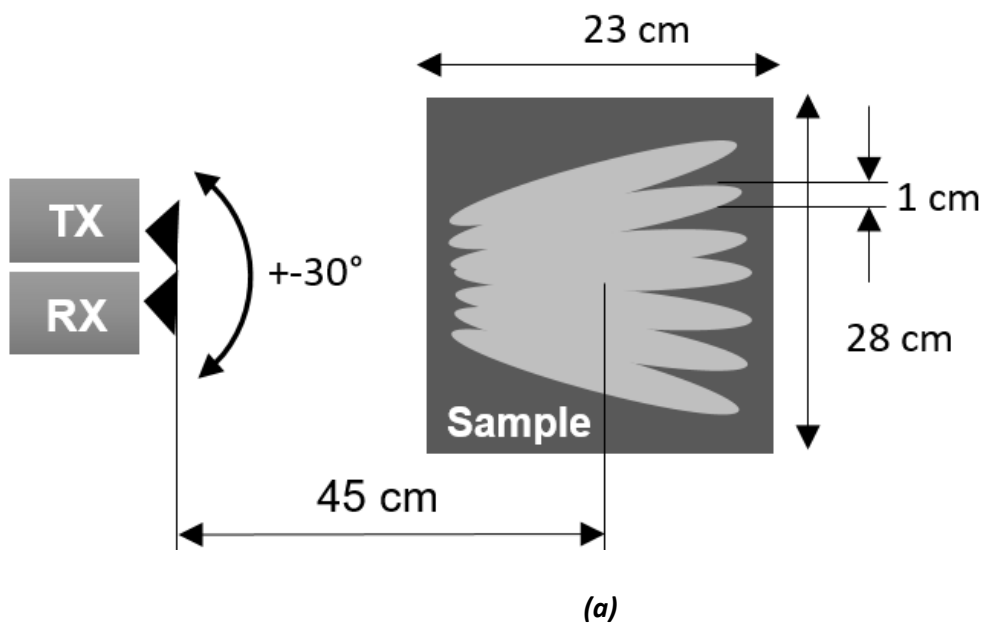


Figure 6.1: Experimental setup (a) system schematic (b) actual system configuration

In order to obtain high-resolution radar images, two fan-beam horn antennas were used, having a narrow beamwidth in azimuth direction to provide a high angular resolution in azimuth and a wider beamwidth in vertical direction to deliver the required wide illuminated footprint along the path. The bandwidth of the sweep is 8 GHz for 150 GHz and 16 GHz for 300 GHz radar to achieve the sub-cm range resolution. The antennas parameters and specifications of the measurement system components are provided in Table 6.1.

Table 6.1: Parameters of the measurement system

Parameters	150 GHz	300 GHz
Frequency Band	142-150 GHz	282-298 GHz
Sweep Bandwidth	8 GHz	16 GHz
Antenna Azimuth Beamwidth	22° (-3 dB)	22° (-3 dB)
Antenna Elevation Beamwidth	2.2° (-3 dB)	2.2° (-3 dB)
Antenna gain	30 dBi	29 dBi
Antenna External Dimensions	9x80 mm	9x65 mm
Far Field	6.4 m	8.19 m
Range resolution	18.7 mm	9.4 mm

As a test surface, the sandpaper with grits 40, 80, 120, 240 and 320 was used. The roughness parameters were measured in [150] and shown in Table 6.2. Using sandpaper allows carrying out experiments with surfaces, the roughness of which is known and lies within the controlled limits. The sandpaper is laid on the carpeted floor and located at an average distance of 45 cm from the antennas. Such a short distance is chosen only due to limited power of used THz VNA transmitter.

The test surface is stationary, the quasi-monostatic radar with two closely spaced Tx and Rx antennas rotates on a turntable which is controlled by computer and allows the radar system scanning in azimuth. The horn antennas azimuthal beamwidth is 2.2° one way, so the antennas increment angle is set to half the beamwidth (1.1°). In order to provide the image of the whole scene with the sandpaper with dimension of 23 cm x 28 cm, the scene was scanned from -30° to $+30^\circ$. Therefore, the number of azimuthal scans forming each image was 60.

Table 6.2: Sandpaper Parameters

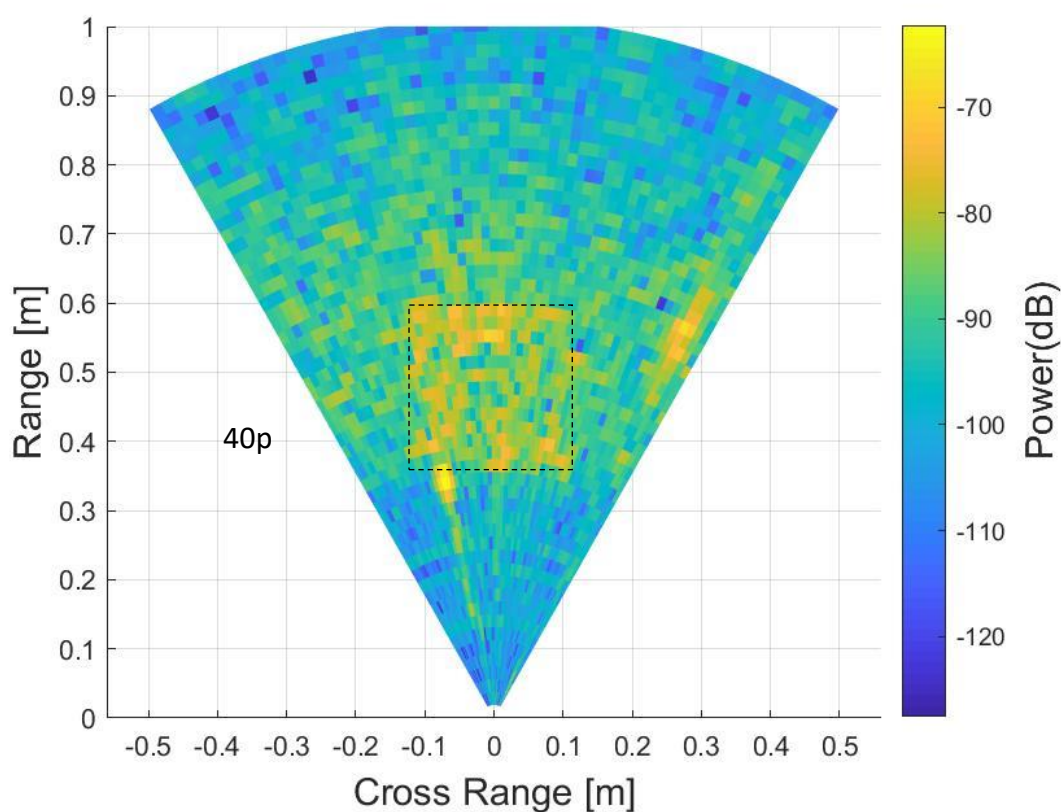
Grit	Surface rms, mm	Electromagnetic roughness kh			
		79 GHz	150 GHz	300 GHz	670 GHz
40	0.13	0.18	0.34	0.69	1.55
80	0.07	0.10	0.19	0.38	0.84
120	0.03	0.05	0.09	0.19	0.42
240	0.02	0.02	0.03	0.06	0.14
320	0.01		0.03	0.06	

The range profiles produced at each azimuth position are augmented to produce the image of the scene as explained in section 3.5 . The polar range profile is then converted to the Cartesian x-y surface. The intensity images were generated in MATLAB. In the next section, the radar images of sand paper with different roughness (grits of 40, 80, 120, 240, and 320) at 150 GHz and 300 GHz are presented and the results are discussed.

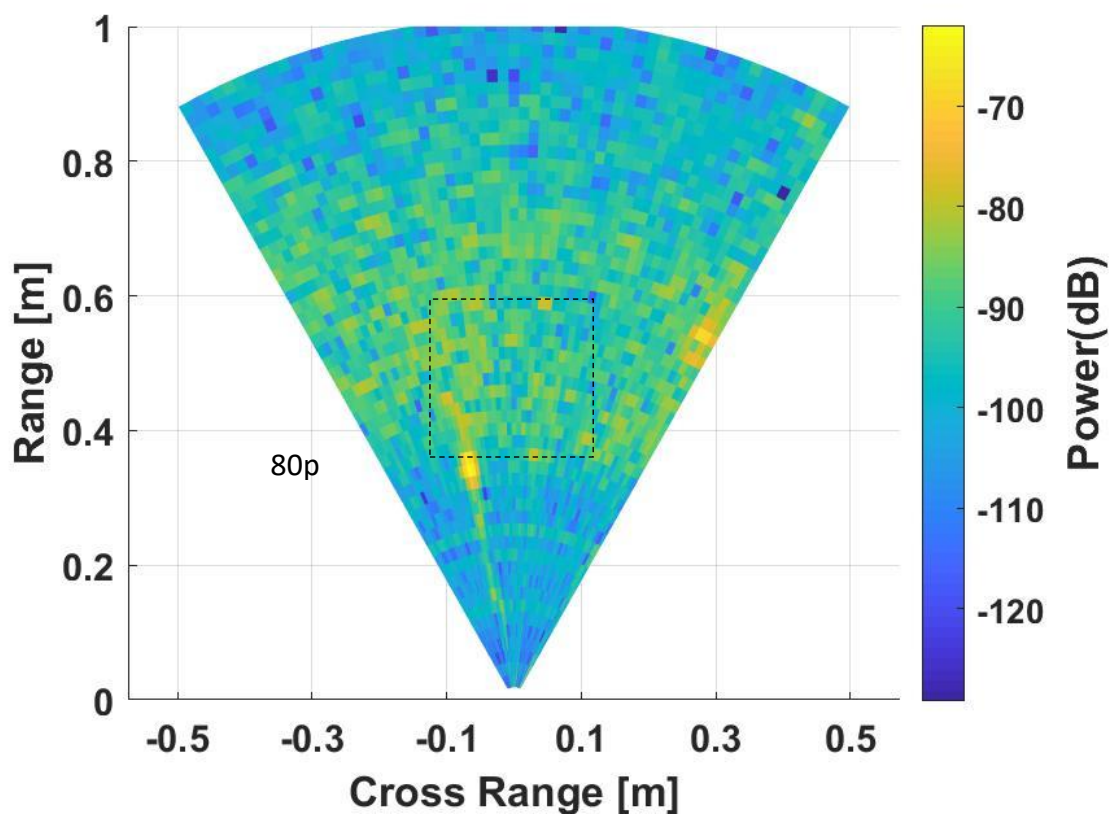
6.3.2 Experimental results and Analysis

6.3.2.1 Images of samples

From electromagnetic roughness values, presented in Table 6.2, it follows that at 150 GHz only 40 grit sandpaper can be considered as a rough surface and at 300 GHz both 40 and 80 grit sandpapers will generate diffuse reflections. This conclusion is confirmed by the images below. In figure 6.2, 150 GHz radar images of sandpaper with grit 40 and 80 are presented. The patch of sample with grit 40 is clearly distinguishable from the background, but the backscattering from the sandpaper with grit 80 is not. This effect is observed for remaining finer grade patches and not shown here.



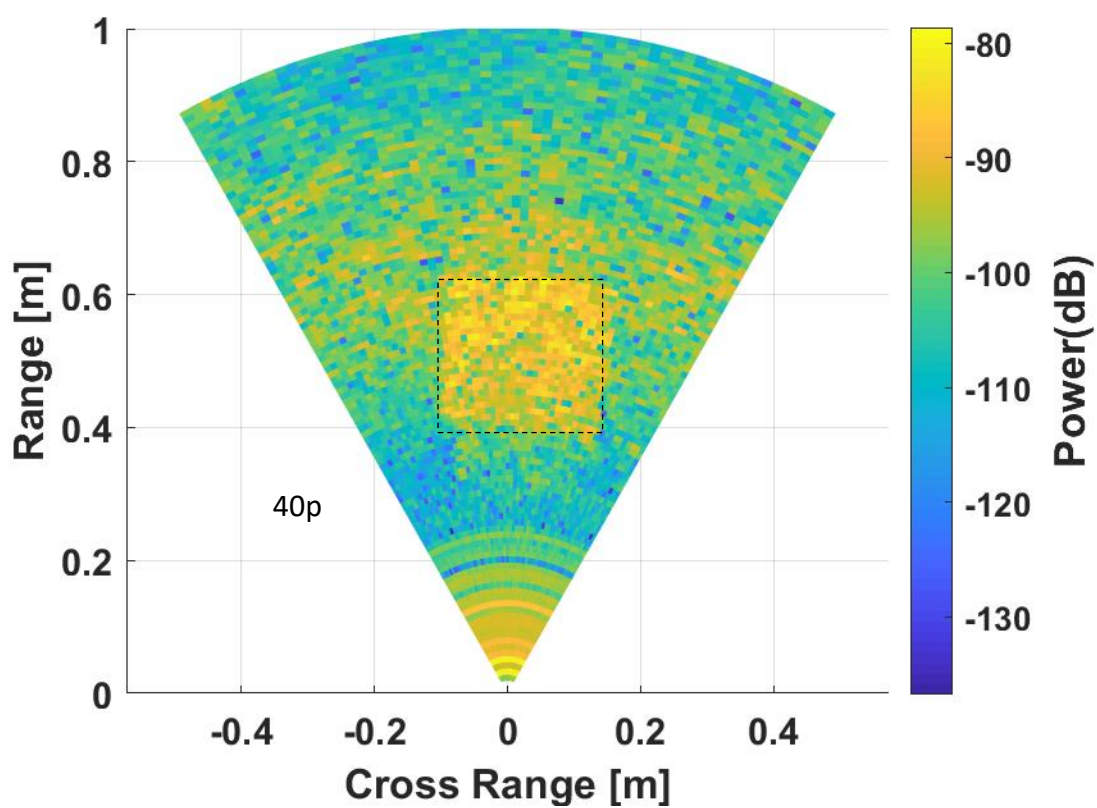
(a)



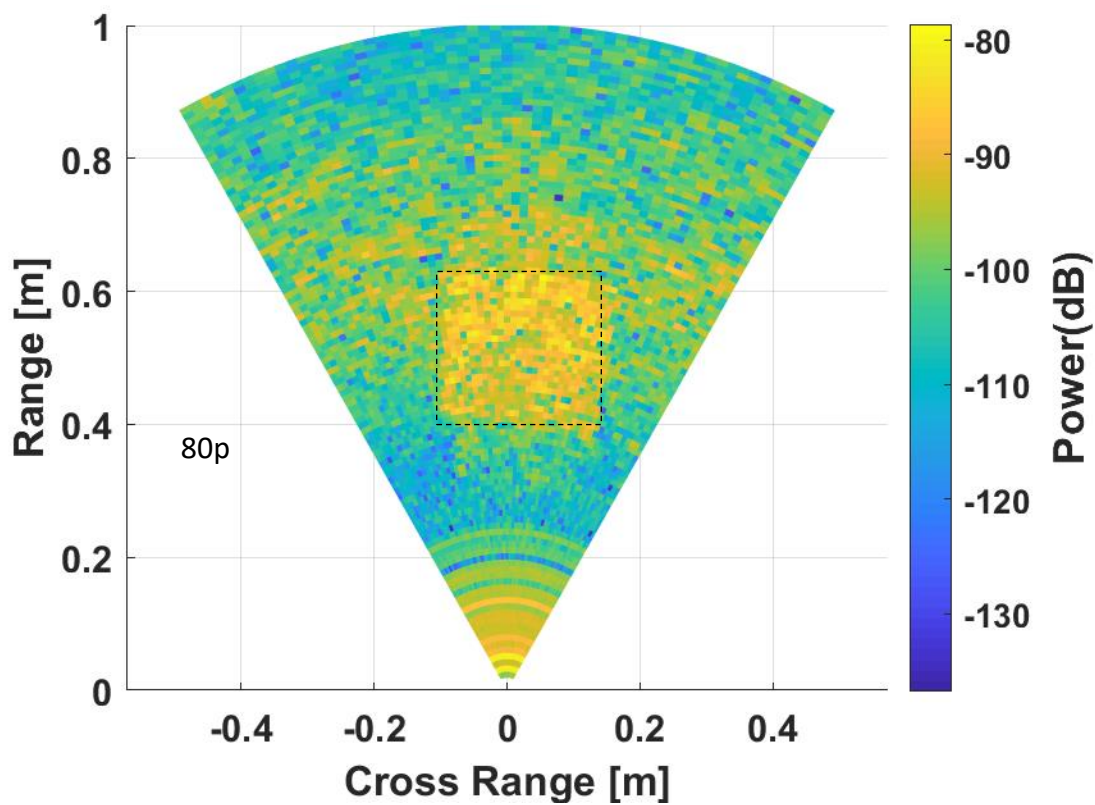
(b)

Figure 6.2: 150 GHz radar images of sandpaper with grit (a) 40 and (b) 80, the rectangle shows the position of the sample

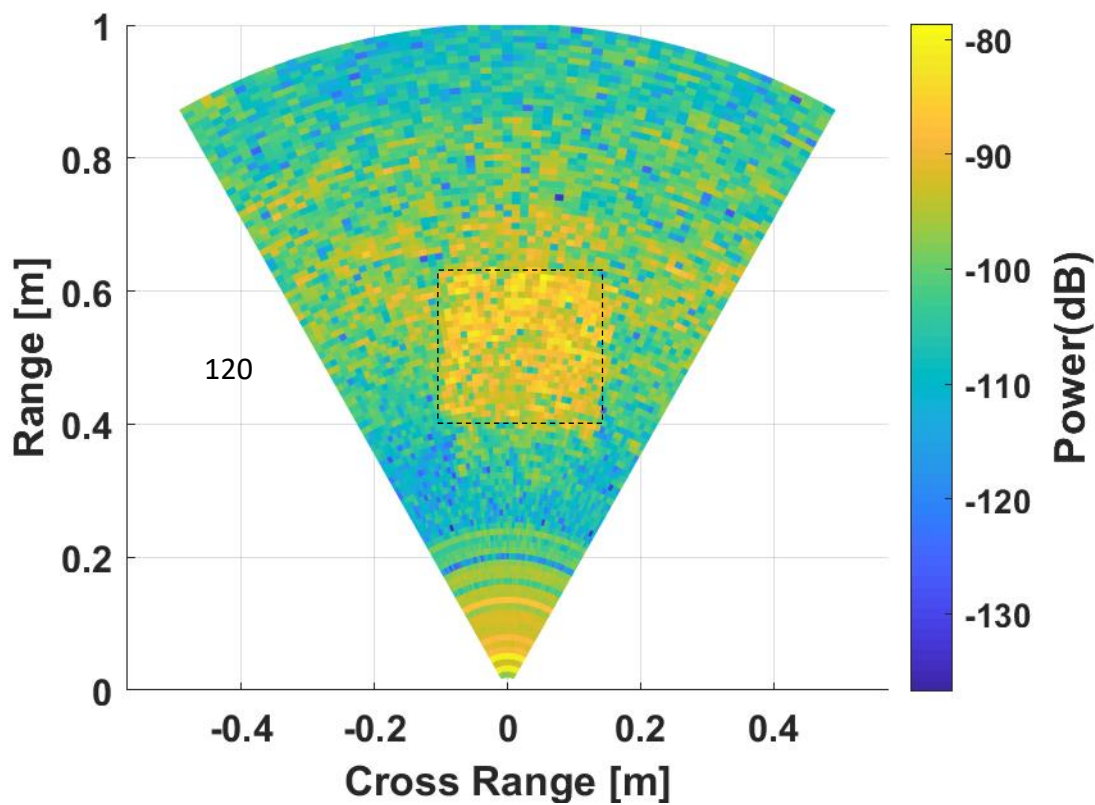
In Figure 6. 3, the images of sandpapers with grit 40, 80, 120, 240 and 320 obtained at 300 GHz are shown. In Figure 6. 3a-c sandpaper patches with grit 40, 80, and 120 are clearly seen due to their high diffuse backscattering effect. This effect is much less in the case of sandpaper with 240 grit and its image merges with the background. The appearance of specular reflection can be observed in Figure 6. 3e as can conclude from consideration of the low reflected power region within the bounding box corresponding to the patch.



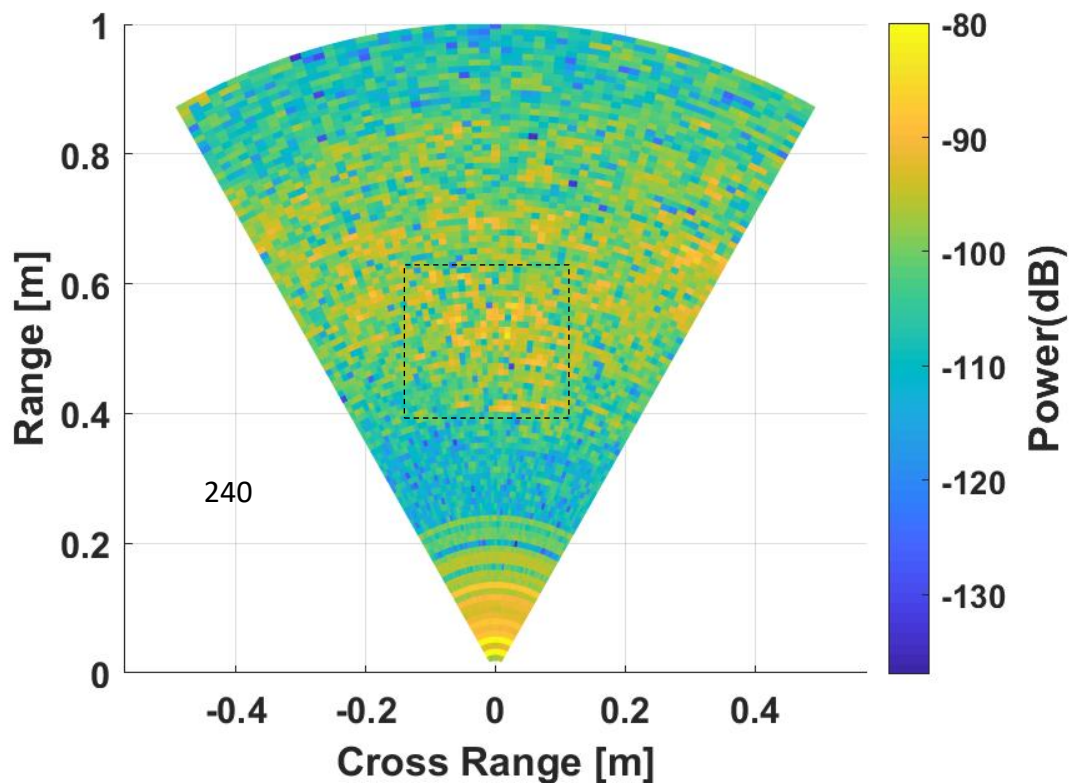
(a)



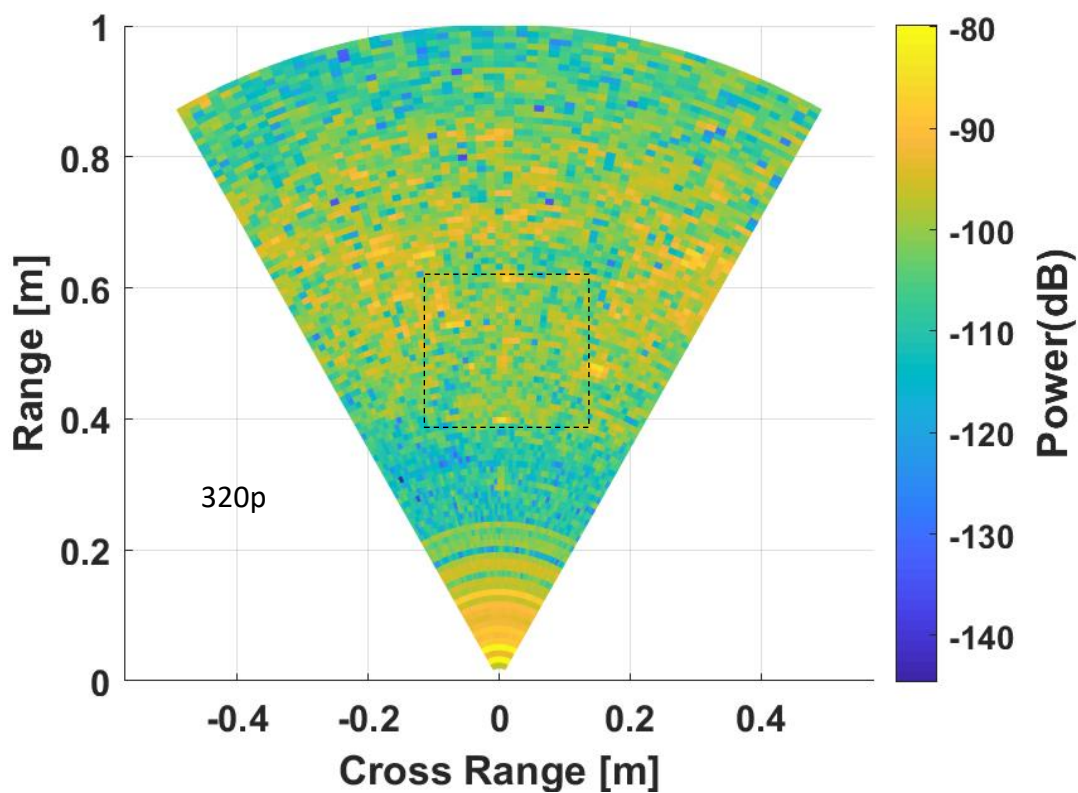
(b)



(c)



(d)



(e)

Figure 6.3: 300 GHz radar images of sandpaper with grit (a) 40, (b) 80, (c) 120, (d) 240, and (e) 320. the rectangle shows the position of the sample

6.3.2.2 Backscattering coefficient

The reflective properties of a surface are characterized by its backscattering coefficient. As mentioned in equation (3.8), the backscattering coefficient of a distributed target is an ensemble average of the radar cross section σ per unit of illuminated area A .

The VNA, used in our experiment, is primarily intended for measuring scattering in terms of S-parameters, which are complex matrix elements that show reflection/transmission characteristics (amplitude and phase) in frequency domain. As was shown in equation (3.9), the radar cross section can be calculated as

$$\delta = 4\pi R_0^2 \frac{|S_{21}|^2}{|S_{21f}|^2}$$

where S_{21} is the measured transmission coefficient and S_{21f} is the transmission coefficient in free space. Because the area A is the same in all our experiments, the radar cross section σ and the backscattering coefficient σ^0 are proportional to S_{21} .

As mentioned in section 5.4.1 one of the most well known empirical models for calculating the backscattering coefficients was proposed in [136]. This model which is applied for this study, is used to calculate the corresponding coefficients for the vertically polarized signal only and is compared with the measured values. The results are presented in Figure 6.4.

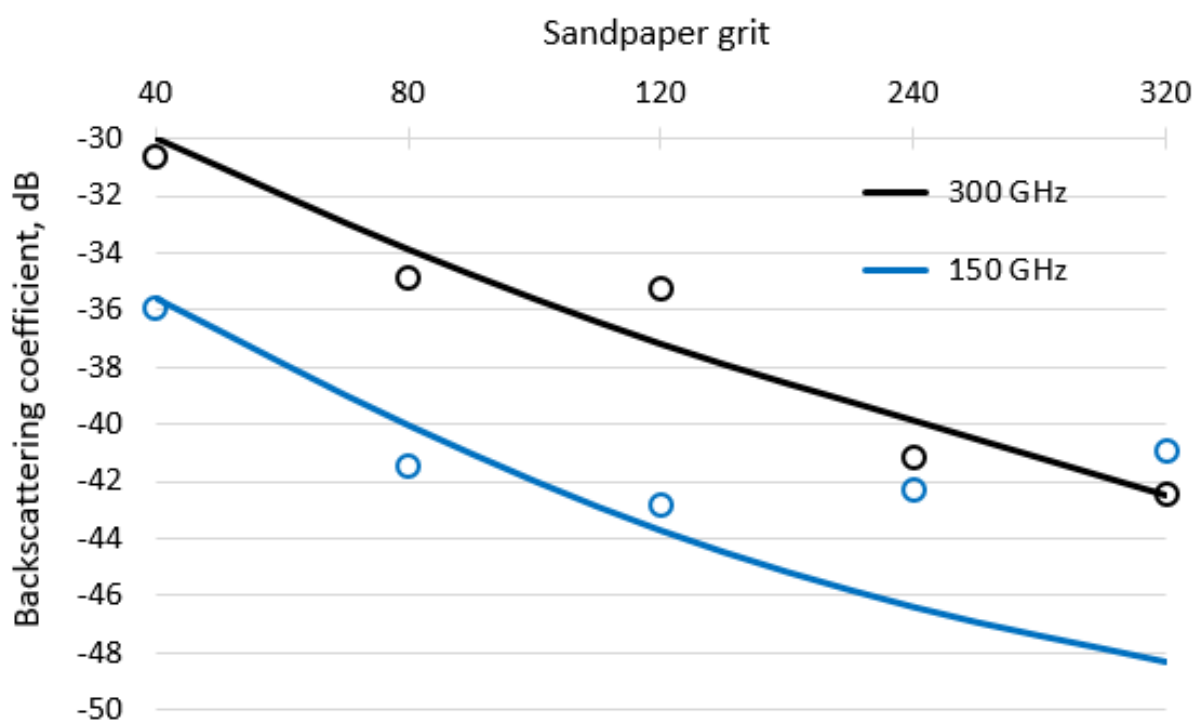


Figure 6.4: Backscattering coefficient for vertically polarized signal, lines represent the theoretically calculated curves, circles indicate the experimentally measured values

Overall correspondence is observed between the measured results and the theoretical calculations up to a backscattering coefficient level of approximately -40dB. Further, the signal-to-noise ratio drops, measurement accuracy decreases and finally the signal becomes indistinguishable from the noise. Deviations of the measured values from the theoretical calculations can be explained by the difference in the parameters of the used samples from those given in [150]. Since the parameters of the grit are not strictly standardized, each manufacturer allows some deviations from the generally accepted values of roughness.

Since the above images and theoretical analysis lead to the conclusion about the limited capabilities of a radar with a frequency of 150 GHz for the classification of the surfaces under study, for this purpose only 300 GHz radar data was used. In the next section, the preliminary results of the classification of surfaces using convolutional neural network (CNN) are presented.

6.3.3 Classification using CNN

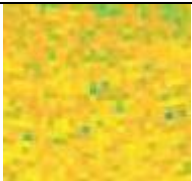
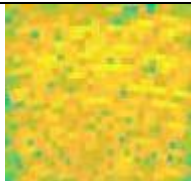
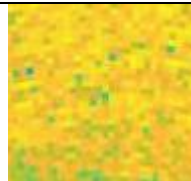
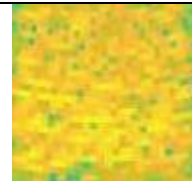

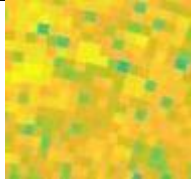
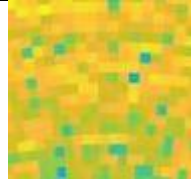
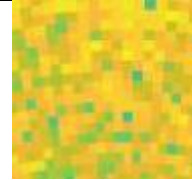
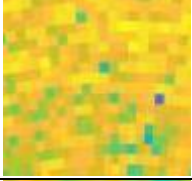
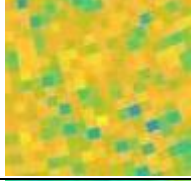
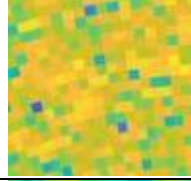
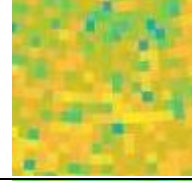
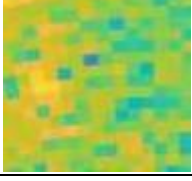
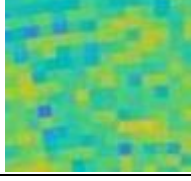
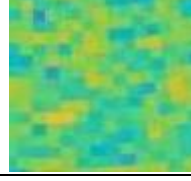
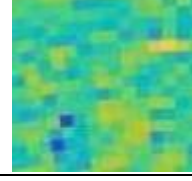
CNN is a type of artificial neural network (ANN) which can automatically extract the features of the sample and propagate them from a low layer to a high layer through multiple layers of convolutional operations and generate the output in the form of class. CNN has been successfully applied for many applications such as image and speech recognition, object detection and pattern recognition [153]. CNN utilizes weight-sharing which reduces the number of weights in comparison to ANN, therefore as a result the network is faster and has lower memory requirements. The 2-dimensional image can be fed to the CNN directly without converting to 1-dimensional image (which is necessary for ANN). This gives the benefit of maintaining the spatial properties of the image. By using actual raw image data as an input, the pre-processing of image is no longer needed. In this regard, among other autonomous vehicle path planning algorithms, such as [131,132], CNN have recently been widely used in processing data coming from optical [154] and radar sensors [155,156].

The main focus of this section is to classify sandpaper radar images, which simulate examples of various road surfaces, based on their roughness. Because of mentioned advantages of CNN in other applications of machine learning model, the CNN was chose to classify the sandpapers with different grits.

6.3.3.1 Data set

Our data set consists of the cropped sandpaper patches from raw radar images obtained from four types of sandpaper with various roughness: grits 40, 80, 120 and 320. Each patch is represented by an array of pixels (89×93) and their examples are illustrated in [table 6.3](#). The full dataset of radar imagery, consisting of 534 different cropped patch images, is divided into four folder which represent four classes: grit 40 (109 radar images), grit 80 (126 radar images), grit 120 (240 radar images), grit 320 (60 radar images). The training dataset has to be larger than the testing dataset in order to avoid underfitting, so the training set comprised 75% of images (400 images), which were chosen at random, and the remaining 25% (134 images) formed the test set. In Matlab code the "imageDatastore" function has been used which automatically labels the images based on their folder names.

Table 6.3: Road Surfaces Cropped Images, 89×93 pixel

sandpaper type	Sample 1	Sample 2	Sample 3	Sample 4
Grit 40				
Grit 80				
Grit 120				
Grit 320				

6.3.4 Network Architecture

The typical structure of the CNN is composed of convolution layers (CVL), subsampling layers (pooling layers), followed by fully connected (FC) layers. The feature extraction of input sample is performed by CVL and pooling layers, while the fully connected layers map the extracted features into final output, such as classification. The CNN architecture design for the proposed sandpapers radar images classification task is illustrated in Figure 6. 5. The output of both CVL and pooling layer calculated by equation (2. 53). The network architecture state of the art has massively vary by different choices of: number of CVL layer, the number of kernel and their size, as well as using some techniques for instance , activation functions, regularization, batch normalization, which can mainly influence the network performance efficiency.

For the proposed image classification, the CNN architecture has a form of:

Input→*CONV*→*Batch Normalization*→*ReLU*→*Pool*→*Drop out*→*FC*→*Softmax*→*Output*

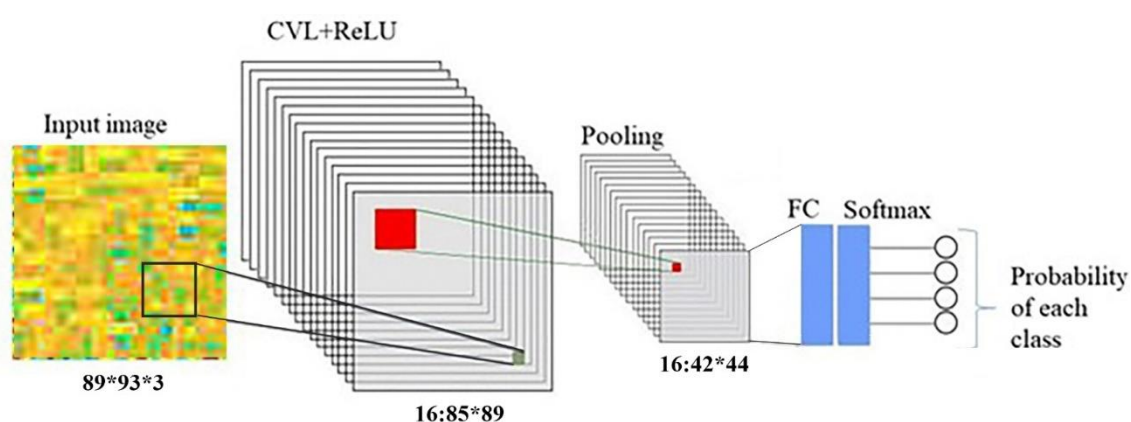


Figure 6.5: CNN schematic architecture for sand paper classification

Next, each component of this architecture and the implementation of the CNN as a

whole is describe and analysed in detail.

The 89×93×3 RGB pixel cropped sample from the raw radar image is presented as an input and fed to the network. The CNN performance is improved by using several techniques to speed up the training process and optimise the testing accuracy, such as batch normalization and dropout layer, which are outlined below. The parameters related to these learning techniques are selected based on typical values or chosen according to empirical studies.

To extract the certain features of the image which can help the model to learn specific characteristics of the image, a convolution layer with 16 kernel size of 5×5 is applied.

The batch normalization is applied on the outputs of CVL to speed up the network training and reduce the sensitivity to network initialization. Some recent studies [82] suggested that non-linear activation functions like Rectified Linear Unit (ReLU) $f(x) = \max(0, x)$ improves both learning speed and classification performance in comparison with traditional neuron models. Therefore, in our CNN the batch normalization is followed by non-linear ReLU activation function and our testing results showed that by using ReLU activation function the classification performance improves by 4% from 93% to 97%.

The max pooling layer with filter size of 2×2 and stride of 2 pixel is applied to reduce the number of dimensions of the image without losing important features or patterns to make the learning easier/faster and to avoid overfitting. Dropout is a regularization layer which zeroes-out the random number of neurons during training to prevent the overfitting.

In our proposed CNN model, the drop-out rate of 0.3 is applied during training, so the neuron activation output is multiplied by 0.7 during testing.

The convolutional and max pooling layers are followed by one fully connected neural layer with 4 neurons which correspond to the number of different sandpaper grits under consideration and combines all the features learned by the previous layers in order to classify the image. The SoftMax function [157] then generates a vector of probabilities with one value for each possible class.

The output result is a probability of the image belonging to one of four classes where

the maximum value indicates the predicted sandpaper grit.

After designing CNN network architecture, the network needs to be trained. In this study the stochastic gradient descent has been used with momentum (SGDM) optimizer [158] with the default value learning rate of 0.01 to speed up the training process. All the data processing and the CNNs training were performed in MATLAB which was written by author of this thesis.

Too many layers can add unnecessary complexity and may overfit the network without improving the performance. Our proposed shallow CNN with one convolutional layer provides less computation and training time and reduces the number of parameters to be learned, while achieving a suitable classification accuracy.

6.3.5 Sand paper classification result

The classification performance of the proposed CNN-based model was evaluated preliminarily on limited number of 300 GHz radar images of sandpaper with four different grits, namely 40, 80, 120, and 320. The images were precisely cropped by 89×93 pixels. As mentioned before the training set comprised 75% of images, which were chosen at random, and the remaining 25% formed the validation set. The model was trained over 50 epochs.

The accuracy A is the number of correct predictions made by CNN, divided by the total number of predictions [159]:

$$A = \frac{TP + TN}{TP + FP + TN + FN} \quad (6.1)$$

where TP is true positive which denotes items that are correctly identified. For example, for the reference class 'grit 40', TP are sandpaper images with grit 40 which correctly identified as 40 grit sandpaper. FP are false positives and they are items incorrectly identified, for example sandpaper image with grit 80 classified as 40 grit sandpaper. TN are true negatives and they are all the images correctly rejected from the 40 grit sandpaper reference class. Finally, FN are false negatives and they are items from the reference class which are wrongly classified (40 grit sandpaper classified as 80 grit sandpaper, for example).

The accuracy on the testing set is presented in the form of a confusion matrix in Table 6.4. The four columns refer to four sandpaper actual grits, and the rows represent the resulting grits to which the analysed sandpapers were attributed by the developed CNN-based model. As can be seen from the confusion matrix, in case of sandpapers with grits 320, all samples were correctly classified. Two samples with roughness of 40 grit were classified incorrectly as 120 grit and two 120-grit samples were classified incorrectly as having 40 grit roughness. Four samples of 80 grit sandpaper were classified incorrectly as having grit 120. Thus, the accuracy of the correct recognition of samples was on average 97 percent.

Table 6.4: Confusion Matrix of the Classification Results

		Grit 40	Grit 80	Grit 120	Grit 320
Actual Class	Grit 40	79	0	2	0
	Grit 80	0	90	0	0
	Grit 120	2	4	178	0
	Grit 320	0	0	0	45

The recall, precision, and F1-score [160] have been used in the performance analysis:

$$recall = \frac{TP}{(TP + FN)} \quad (6.2)$$

$$precision = \frac{TP}{(TP + FP)} \quad (6.3)$$

$$F_1 = \frac{2 \times recall \times precision}{(recall + precision)} \quad (6.4)$$

Applying the proposed approach within the existing set of data can result in achieved precision, recall, and F1-score of 97.7%, 97.5%, and 97%, respectively.

6.4 Road Surface Classification Based on Radar Imaging Using Convolutional Neural Network

In the previous section (6.3) an approach to surface identification based on the analysis of the sub-THz radar images using a convolutional neural network (CNN) has been presented. The promising results in classification of surfaces with known roughness were obtained in laboratory conditions using 150 GHz and 300 GHz radars.

In this section the performance of mmWave 79 GHz imaging radar in the Surface ID task is analysed. This work will allow us to subsequently move on to surface recognition using sub-THz radar. In this study the novel approach has been applied to the real road surface images, obtained using 79 GHz scanning radar. This technique makes it possible to solve an important outstanding task in the implementation of autonomous vehicles and classify different road surfaces (asphalt, mud, gravel, river, rocky road and uneven countryside road). Increasing radar frequency from 24 GHz to 79 GHz allows increasing radar bandwidth and therefore higher range resolution. Moreover, the shorter signal wavelength provides increased interaction with the physical surface texture, giving additional information due to more diffuse scattering. An experimental imaging radar with mechanically scanned fan beam antennas has been used. In this research, the dataset created from the 79 GHz scanned fan beam radar data. This dataset consists of cropped images of different types of road surfaces which are labelled in six different classes for road surface classification tasks.

In the following sub sections, the methodology of data collection is described, also the radar images of different road surfaces with various properties and roughness, captured with 79 GHz radar, are presented and analysed. In section 6.4.3, the six types of surfaces are classified with CNN based on their images.

6.4.1 Methodology of Data Collection

The purpose of this research was to test the performance of mmWave imaging radar in classification of different road surfaces with different characteristic such as rms roughness, texture, composition, and surface structure. In order to achieve the goal of

this research, the backscattered radar signal data from different road surfaces was recorded, the corresponding radar images were obtained by processing this recorded data, and finally, CNN was applied for classification.

The asphalt radar images were taken around the campus of the University of Birmingham in winter 2019. The radar images of different road surfaces, such as rocky, gravel, muddy, uneven countryside road, and a river were recorded in Scotland during autumn 2019. The river can be considered as an extreme model of water on the road (puddles or flooded road).

The frequency-modulated continuous-wave (FMCW) radar with a central frequency of 79 GHz which has been designed and built in collaboration with ELVA-1 [96] was used for image data collection. This is shown in Figure 6.6 along with aligned LIDAR and stereo camera for the ground truth optical imagery and control of the scene. The radar is placed in the rear of a test vehicle and approximately 1.35 m above the road surface.

is placed in the rear of a test vehicle and approximately 1.35 m above the road surface.

The radar signal bandwidth was set to 5 GHz to achieve about 3 cm range resolution and cover full automotive frequency allowance of 5 GHz (76–81 GHz). In order to obtain high-resolution radar images, two fan-beam horn antennas were used, having a narrow beamwidth in azimuth direction to provide a high angular resolution in azimuth and a wider beamwidth in vertical direction to deliver the required wide illuminated footprint along the path. The horn antennas azimuthal one-way beamwidth is 2.2° , so the antennas increment angle was set to half the beamwidth (1.1°). The 79 GHz antennas were placed approximately 1.6 m above the road surface.

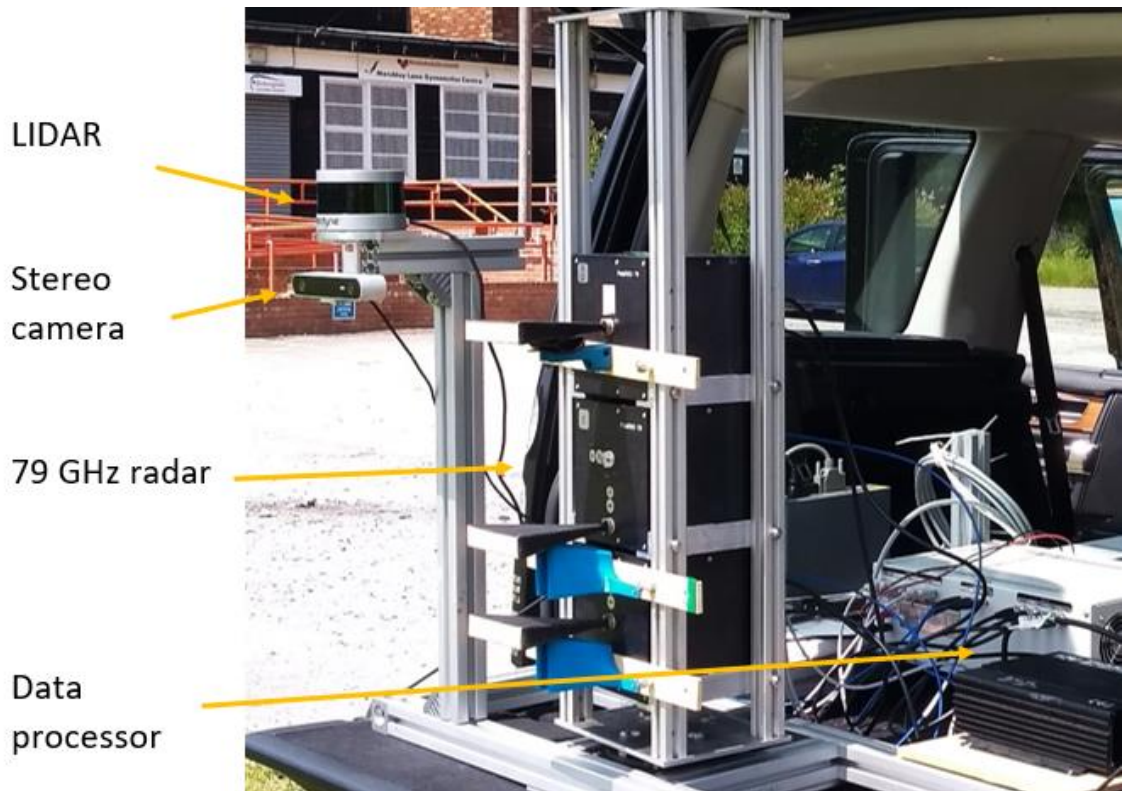


Figure 6.6: Experimental setup configuration

The antenna parameters and specifications of the measurement system components are provided in Table 6. 5. The experimental radar rotates on a turntable which is controlled by computer and allows the radar system scanning $\pm 30^\circ$ field of view with a frequency of 0.83 Hz in azimuth. The range profiles produced at each azimuth position are augmented to produce the image of the scene. The polar range profile is then converted to the Cartesian x-y surface. The final image is formed by creating a map showing the backscatter power received by resolution cells, whose dimensions are defined by the range and cross-range resolutions as shown in Figure 6. 7 and Figure 6. 8. The intensity images were generated in MATLAB.

Table 6.5: Parameters of the Measurement System

Parameters	
Frequency band	77-82 GHz
Wavelength	3.8 mm
Bandwidth	5 GHz
Output Power	15 dBm
Azimuth Beamwidth	2.2° (-3 dB)
Elevation Beamwidth	15° (-3 dB)
Range resolution	30 mm
Scan rate	0.83 Hz
Azimuthal step	1°
Total azimuthal scan angle	60°

In the next section, the radar images obtained using the equipment described above are presented and analysed in terms of surface classification.

6.4.2 Experimental results and analysis

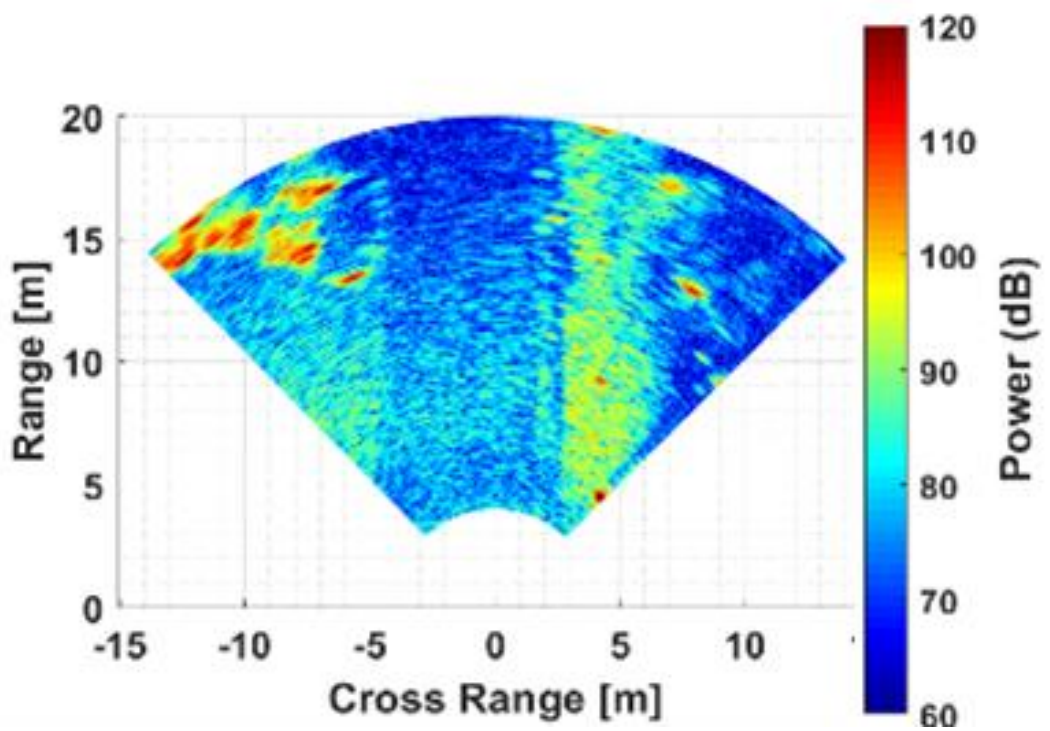
In Figure 6.7 the camera images of an asphalt road scene, even countryside road and muddy road are shown with corresponding 79 GHz radar imagery which shows the range, angular position, and intensity of reflection power. The colour bar in the following figures indicates the signal power in dB on an arbitrary scale.

The texture sensitivity and high resolution of the radar imagery are clearly visible and prove that the diffuse backscattering from road surface occurs at 79 GHz frequency. The road surface is clearly visible in Figure 6.7(b) and Figure 6.7(d) due to reduced backscattering from the smoother texture of the actual road in comparison with roadsides. This is not the case in Figure 6.7(f) as greater backscattering is observed from actual road surface than from roadsides. Probably this can be explained by relatively high dielectric permittivity of water and gravel mix which forms the muddy road.

Figure 6.8(a) is the camera image relevant to the radar image shown in Figure 6.8(b), where the sample area of river, gravel road, and rocky road were, respectively, illustrated in white box, red box, and blue box. The differences between the areas of gravel road, rocky road, and river can be seen clearly in Figure 6.8(b).



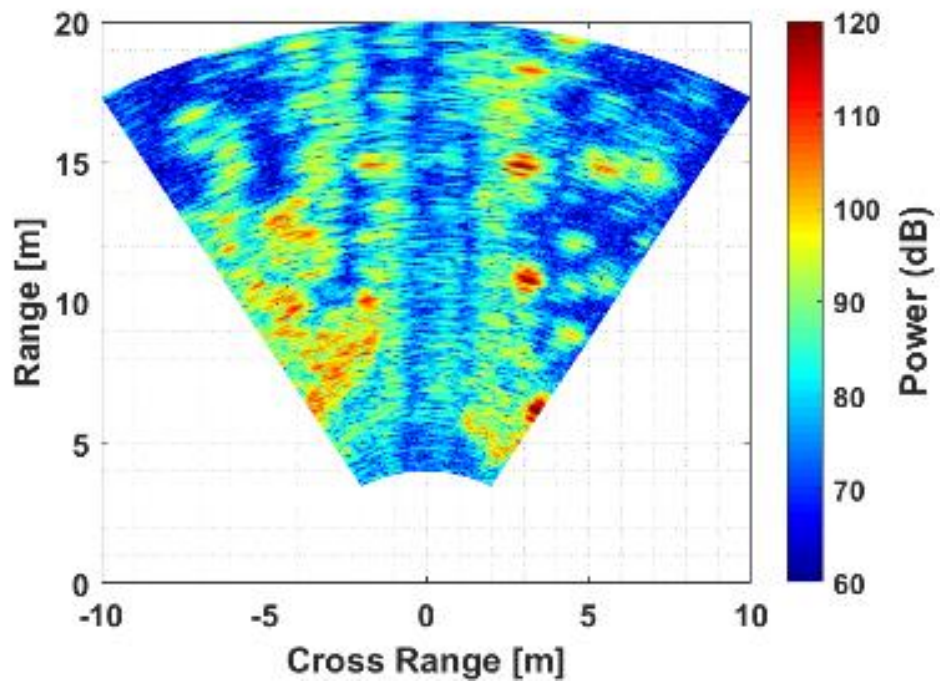
(a)



(b)



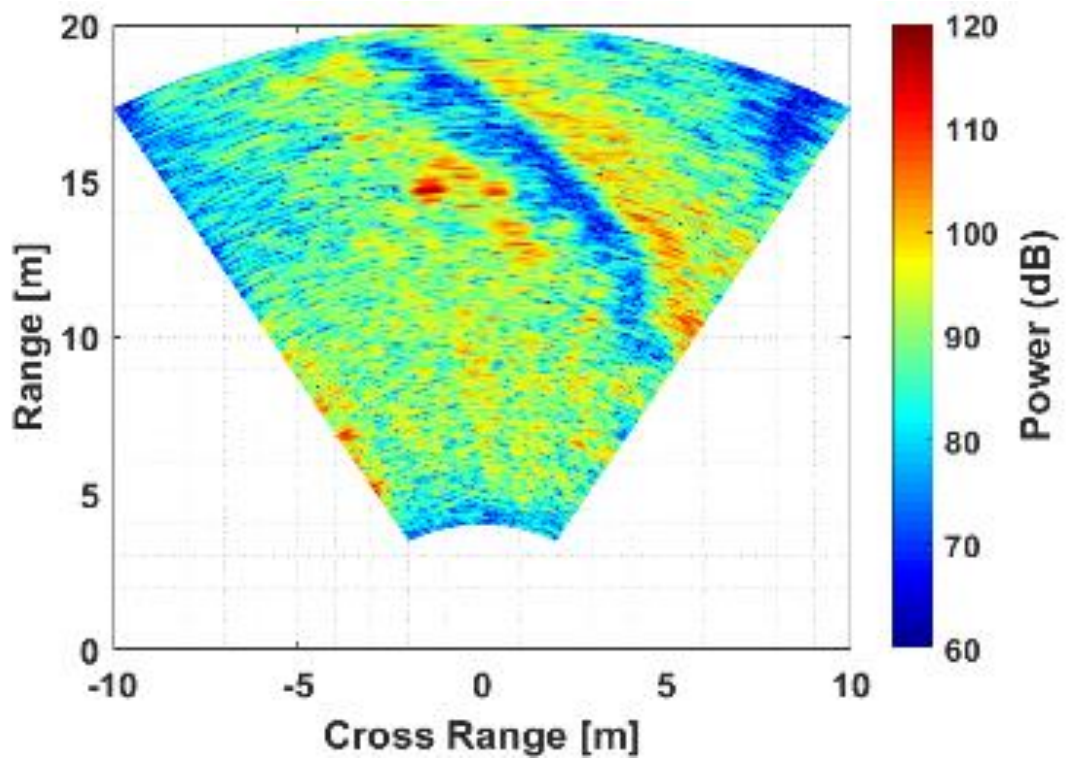
(c)



(d)



(e)

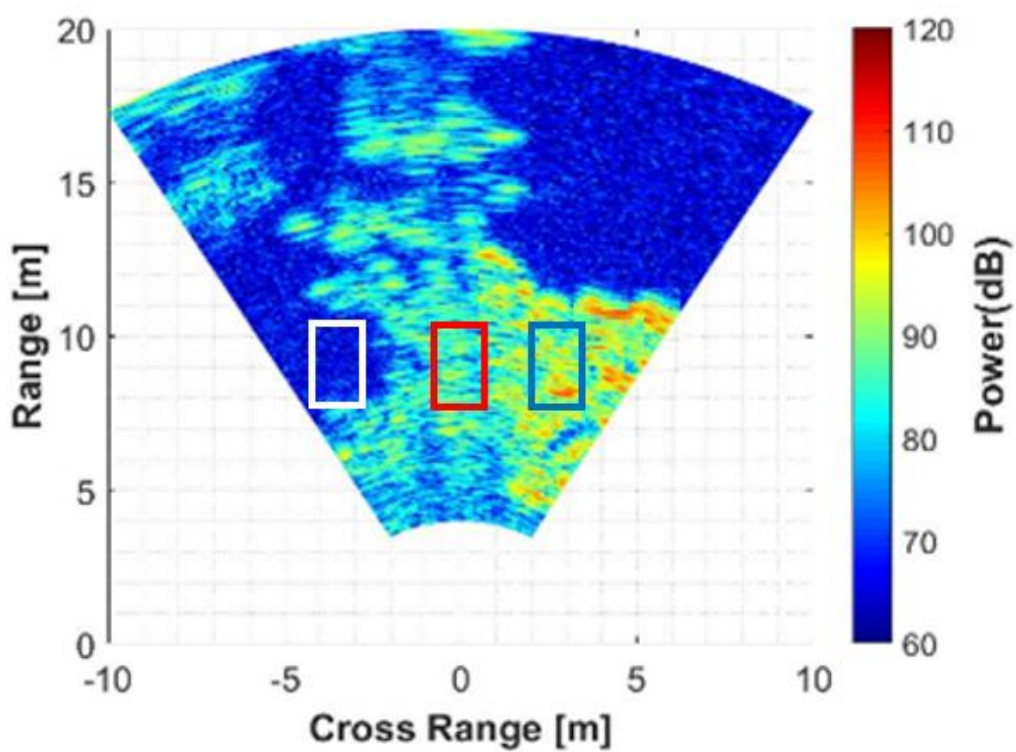


(f)

Figure 6.7: Photos and radar maps of asphalt road (a),(b), countryside road (c),(d), and muddy road (e),(f).



(a)



(b)

Figure 6.8: Riverside image scene: camera image (a), radar map (b); the white, red and blue boxes denotes to area of river, gravel and rocky road

The average reflected power (\tilde{P}_R), in dB on an arbitrary scale, of river, gravel, rocky, countryside, muddy road, and city road (asphalt) is presented in Table 6. 6. The results are averaged over ten or more surfaces measurements within $2 \times 3 \text{ m}^2$ cells. The range gating up to 10 m was used to account for variability of grazing angles (from 13.5° to nearly 2°) specific for automotive scenarios, to remove dependence of the power returns (normalized RCSs) on the grazing angle for the areas of the same surface.

Table 6.6: road surface parameters

	RIVER	ASPHALT	UNEVEN	GRAVEL	ROCKY	MUD
rms, mm	-	0.6	7	10	15	5
\tilde{P}_R , dB	65	77	83	84	90	91

Surface roughness was measured during the experiment by taking 20 depth readings on 20 cm of typical surface length. The impact of surface roughness on scattering is prominent and the reflection power is increasing by increasing the surface roughness. However, some other parameters like material permittivity can influence surface backscattering, as we can see in the case of a muddy surface which is a compound of gravel and water.

The absolute values of the reflected signals cannot serve as a reliable basis for surface identification, since they depend on the individual parameters of transmitter and receiver, their installation accuracy, radome contamination (dirt, mud, snow, etc.). Therefore, in our work, we use radar images for surface classification. As I mentioned in section 2.7 for image analysis the CNN class of neural networks is most commonly applied. Based on the results shown in section 6.3.5 of this thesis, these networks are well suited to the task and can be designed to be accurate, reliable and fast in terms of feature extraction and feature expression.

6.4.3 Road surface classification with CNN

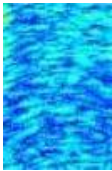
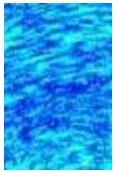
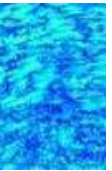
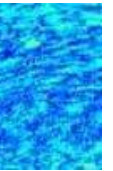
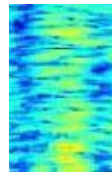
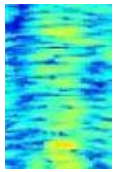
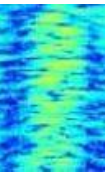
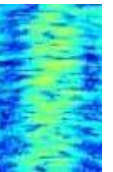
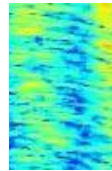
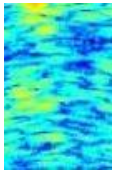
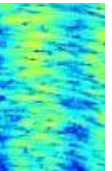
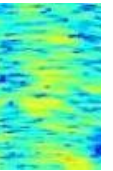
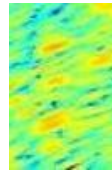
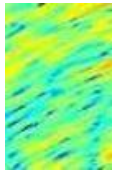
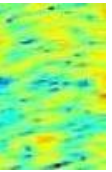
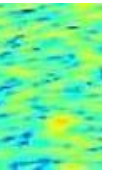
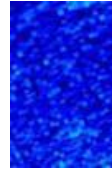
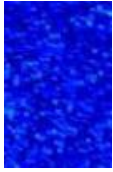
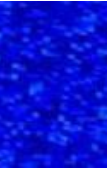
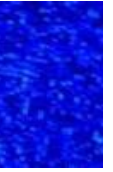
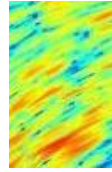
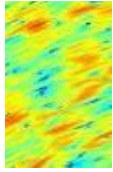
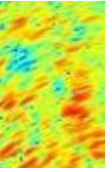
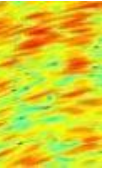
In section 6.3.3 radar images of different grits sandpapers were demonstrated which were obtained in laboratory conditions, to simulate examples of various road surfaces, based on their roughness, and then they were classified with CNN. In this section the main focus is on the classification of actual different road surfaces based on their radar images which have been taken in actual road scenarios. So, we create the dataset from the 79 GHz scanned fan beam radar data. Our data set consists of the cropped patches from raw radar images obtained from six different road surfaces with various roughness. Each patch is represented by an array of pixels (100×65) and their examples are illustrated in Table 6.7.

The full dataset of radar imagery, consisting of 2011 different cropped patch images, is divided into six classes:

- asphalt (190 radar images)
- uneven country side road (445 images)
- muddy road (225 images)
- gravel road (155 images)
- rocky road (354 images)
- river (642 images)

The training dataset has to be larger than the testing dataset in order to avoid underfitting, so the training set comprised 75% of images (1504 images), which were chosen at random, and the remaining 25% (501 images) formed the test set.

Table 6.7: Road Surfaces Cropped Images, 100×65 pixel

Surface type	Sample 1	Sample 2	Sample 3	Sample 4
Asphalt				
Uneven				
Gravel				
Mud				
River				
Rocky				

For our proposed road surface classification task, The specific CNN architecture has been designed to classify the different radar images of road surface and has been illustrated in Figure 6.9 . The CVL and pooling layer output have been calculated using equation (2.53). For our proposed image classification, the CNN architecture has a form of:

Input→CONV→Batch Normalization→ReLU→Pool→Drop out→FC→Softmax→Output

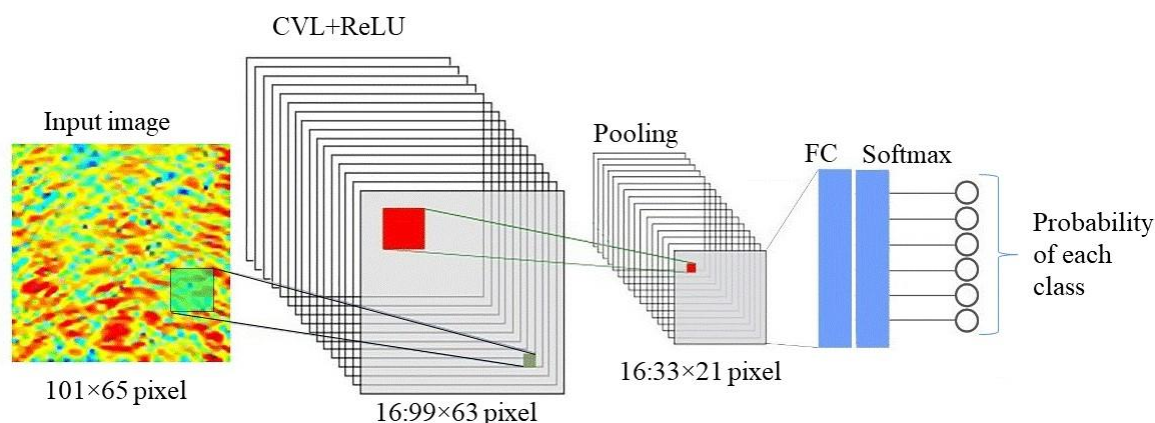


Figure 6.9: CNN simplified schematic structure for road surface classification task

The 101x65x3 RGB pixel cropped sample from the raw radar image is presented as an input and fed to the network. The CNN performance is improved by using several techniques to speed up the training process and optimise the testing accuracy, such as batch normalization and dropout layer, which are outlined below. The parameters related to these learning techniques are selected based on typical values or chosen according to empirical studies.

As mentioned before in order to extract the important features of the radar image which can help the model to learn specific characteristics of the image, a convolution layer with 16 kernel size of 3x3 is applied.

Like our previous model for classification of sandpaper radar images the batch normalization is applied on the outputs of CVL to speed up the network training and reduce the sensitivity to network initialization. In the CNN proposed here, the batch normalization is followed by non-linear ReLU activation function and our testing results showed that by using ReLU activation function the classification performance improves by 0.5% from 98.4% to 98.9%.

The max pooling layer with filter size of 3×3 and stride of 3 pixel is applied to reduce the number of dimensions of the image without losing important features or patterns to make the learning easier/faster and to avoid overfitting.

In our proposed CNN model, the drop-out rate of 0.2 is applied during training, so the neuron activation output is multiplied by 0.8 during testing. The convolutional and max pooling layers are followed by one fully connected neural layer with 6 neurons which correspond to the number of surfaces under consideration and combines all the features learned by the previous layers in order to classify the image. The SoftMax function [157] then generates a vector of probabilities with one value for each possible class. The output result is a probability of the image belonging to one of six classes where the maximum value indicates the predicted road surface.

After designing CNN network architecture, the network needs to be trained as it explained in section [6.3.4](#).

6.4.4 Road surface classification result

In this section the performance of the proposed CNN was evaluated with respect to classification of six different road surfaces radar based on 79 GHz radar images. The accuracy A which is shown in equation (6. 1) is the number of correct predictions made by CNN, divided by the total number of predictions.

For instance, for the reference class 'asphalt', TP are asphalt images correctly identified as asphalt. FP are false positives and they are items incorrectly identified, for example mud images classified as asphalt. TN are true negatives and they are all the images correctly rejected from the asphalt reference class. Finally, FN are false negatives and they are items from the reference class which are wrongly classified (asphalt classified as mud, for example).

Table 6. 9 shows the accuracy of the training set in the form of a confusion matrix .The columns in the matrix refer to predicted classes (five types of road surfaces and river), and the rows represent the actual classes of surfaces. As it's indicate in Table 6. 9 , all the samples of asphalt, mud, rocky road, and river was classified correctly, 332 out of 334 images of uneven road sample were classified correctly and only two samples were classified as gravel, 104 out of 116 samples of gravel road were classified correctly while 12 sample was classified incorrectly as a uneven road. This can be explained by similar structures of these surfaces. Thus, the classification accuracy was 98.9%, which shows the best surface classification performance.

Table 6.8: Confusion Matrix of the Classification Results

		Predicted Class					
		Asphalt	Uneven	Gravel	Mud	River	Rocky
Actual Class	Asphalt	142	0	0	0	0	0
	Uneven	0	332	12	0	0	0
	Gravel	0	2	104	0	0	0
	Mud	0	0	0	169	0	0
	River	0	0	0	0	481	0
	Rocky	0	0	0	0	0	265

The recall, precision, and F1-score as shown in equations (6. 2)-(6. 4) have been used in the performance analysis and we have achieved precision, recall, and *F1*-score of 99.1%, 98.1%, and 98.6%, respectively, which proves the potential of imaging radar in road surface classification based on the surface texture and profile of the road surfaces.

6.5 Summary and conclusion

In this chapter firstly, a novel approach has been explored to classify the surfaces based on the analysis of the image obtained using the Low Terahertz radar at two frequencies of 150 GHz and 300 GHz. The mentioned techniques demonstrate the benefit of high frequency radar which offers higher accuracy due to sensitivity of the microwave signal to the surface roughness. The convolutional neural network (CNN) has been applied in the classification of sandpaper with different roughness (grit). The proposed experimental technique in combination with CNN provides good surface classification accuracy which laid the foundation for the subsequent work on the development of automotive radar for surface classification.

In the next stage an approach considered to surface classification based on the analysis of the 79 GHz imaging radar data and classifying six types of road (asphalt, mud, gravel, river, rocky road and uneven countryside road) with different roughness and dielectric properties. The unique dataset which includes cropped images of different types of mentioned road surfaces are labelled in six different classes for road surface classification tasks. Although, the overall results show that the use of a 79 GHz scanning radar with subsequent image processing using a CNN allows achieving high accuracy of surface recognition, however this is not the fact for surfaces with similar structures, because as can be seen in table 6.8 12 samples of the gravel road (rms roughness of 10 mm) were classified incorrectly as an uneven road (rms roughness of 7 mm). Low THz radars, as have been demonstrated in the Section 6.3.2, are sensitive to small differences between surfaces parameter, which is an advantage over lower frequency radars. The use of 79GHz was due to availability of automotive radar, while low THz measurements currently could only be carried out in a laboratory, stationary.

Chapter 7: Conclusion and Future Work

7.1 Summary and Conclusion

This chapter will conclude the study by summarising the key research findings in relation to the research goals, as well as proposing future plans for this research study.

The aim of this PhD research is to study the feasibility of using low THz radar in the future AV. To achieve this goal the following objectives have been considered:

- Investigating the performance of low THz sensors in the presence of different radome contaminants and various weather conditions
- Studying the normalized RCS from surfaces with different roughness and dielectric properties for remote classification purposes.
- Studying the performance of low THz imaging radar for surface identification task
- Applying CNN to 79 GHz radar images in order to classify the real road surfaces, as a starting point for further classifications achievable with THz radar and CNN.

The novelty and importance of these objectives, which have been successfully met in this PhD programme, lie in the demonstration of an advantage of moving to higher frequency radar for the future autonomy. The possibility of using radars with a high frequency even in the case of radome contamination is shown, the improvement of surface recognition with increasing frequency is analysed, and a new method of surface recognition using imaging radar is proposed and confirmed.

To achieve the first objective of this PhD research, a set of practical and theoretical research work has been done which was described in details in [chapter 4](#). The signal reduction due to presence of uniform layers of leaves at 300 GHz was measured and analysed, and the results shows that the water inside the leaves is the main cause of signal reduction. The transmissivity through a uniform layer of pure water, salty water with different levels of salt and actual seawater were measured and analysed at 300 GHz and 670 GHz. The reduction in transmissivity has been observed when increasing water thickness along with an additional slight decrease in the transmissivity observed with increasing water salinity at both frequencies. Additionally the results indicate that the attenuation due to the presence of a uniform thickness of pure water, salty water and actual sea water, increases with frequency. Overall, based on the above experiments and other research carried out by MISL group, on the radome contaminants, it can be

concluded that water within the contaminants is the main cause of attenuation and its effect is in general more detrimental at higher frequencies.

Chapter 5 explores signal backscattering within the mm-wave and low Terahertz frequency range, represented by frequencies of 79 GHz, 150 GHz, 300 GHz, and 670 GHz, from surfaces with different roughness in regards to achieving the second objective of this thesis. The responses of four sandpapers, made of similar material, but with different roughness were measured and their normalized radar cross sections were estimated as a function of grazing angle and polarization. The obtained results show the advantages of low THz radar for surface discrimination for automotive sensing and provide reference information for creating remote surface identification systems for automotive use, in the field of surface classification, object classification and path determination.

In chapter 6, an approach has been considered to surface classification based on the analysis of the sandpaper image with different roughness using 150 GHz and 300 GHz imaging radar. The CNN has been applied to radar images of sandpapers (with different roughness) obtained at these two frequencies. The proposed experimental technique in combination with CNN provides good surface classification accuracy. The achieved high resolution radar imagery at two frequencies of 150 GHz and 300 GHz demonstrate that high frequency is more favourable to provide surface identification due to sensitivity of the wave to the surface texture and roughness. The gained high resolution radar imagery of sandpapers led to the next step of this PhD research which was the classification of actual road surfaces. The novel approach was applied to the real road surface images (asphalt, mud, gravel, river, rocky road and uneven countryside road), obtained using 79 GHz scanning radar. A similar CNN approach which was applied for classifying sandpaper radar images was applied to 79 GHz actual road surfaces. The gained results show that the use of a 79 GHz scanning radar with subsequent image processing using a CNN allows us to achieve high accuracy of surface recognition. As mentioned previously the main goal of moving to low THz frequency in surface ID tasks is to collect more information from road surfaces and it was demonstrated that (based on the gained results of sand paper images at 150 GHz and 300 GHz radar) the high frequency radar images provide more information about features of the road surfaces even with similar structure.

Chapter 7: Conclusion and Future Work

To sum up, this PhD research clearly demonstrates the great potential of using the low THz radar in future autonomous car instead of traditional radar. Considering the expansion of the radar equipped cars and the sharp increase in the use of radar technology in individual cars, there would be a high possibility of frequency interference and overcrowded spectrum at 77GHz, therefore the automotive radar operation could prosper by entering into a new era of higher frequency.

7.2 Future plan

Although, the theoretical and practical studies in this PhD research provide the solid basis for the expansion of low THz radar systems for the future autonomous car, undoubtedly, there are further research needed in this field.

Within the area of signal attenuation through radome covered with leaves, further research is needed to analysis the attenuation of non-uniform layers of randomly distributed wet leaves corresponding to realistic road scenarios at the range of low THz frequencies (150-700 GHz).

The study of signal reduction due to layer of water at low THz radar has focused on propagation through a uniform layer of water, which is a simplified approximation of a real-life scenario. Further studies on transmissivity through randomly distributed water droplets obscuring the radome (already completed at 150 GHz and 300 GHz) are needed at 670 GHz.

In the field of low THz radar signal backscattering for surface identification task, further investigation is necessary to study the signal reflection from asphalt, gravel, sand, grass, etc. at low THz frequencies, paying particular attention to the peculiarities of reflection from coatings formed by weather conditions (water, snow, ice). Knowledge of the patterns of low THz radar signal reflection from various surfaces and their dependence on the parameters of the measuring system will allow to select the features of the backscattered signal to effectively distinguish between road surfaces.

The results of imaging radar at low THz for surface classification task and using CNN, which are explained in details in chapter 6, lay the foundation for further work on the development of automotive Surface ID system. The future plan is to extend the dataset by measuring the road surfaces in various weather conditions (snow, rain, ice) and to apply 300 GHz imaging radar in order to obtain radar images with higher resolution.

References

- (1) Thomas P, Morris A, Talbot R, Fagerlind H. Identifying the causes of road crashes in Europe. *Annals of advances in automotive medicine* 2013;57:13.
- (2) Road deaths in the European Union – latest data. Available at: <https://etsc.eu/euroadsafetydata/>.
- (3) International S. Automated Driving Levels of Driving Automation are Defined in New SAE International Standard J3016. 2019. Available at: <https://www.sae.org/news/2019/01/sae-updates-j3016-automated-driving-graphic>
- (4) New Level 3 Autonomous Vehicles Hitting the Road in 2020. Available at: <https://innovationatwork.ieee.org/new-level-3-autonomous-vehicles-hitting-the-road-in-2020/>.
- (5) Bystrov A, Hoare E, Tran TY, Clarke N, Gashinova M, Cherniakov M. Automotive surface identification system. In *2017 IEEE International Conference on Vehicular Electronics and Safety (ICVES) 2017 Jun 27* (pp. 115-120). IEEE.
- (6) Shinmoto Y, Takagi J, Egawa K, Murata Y, Takeuchi M. Road surface recognition sensor using an optical spatial filter. In *Proceedings of Conference on Intelligent Transportation Systems 1997 Nov 12* (pp. 1000-1004). IEEE.
- (7) Yamada M, Oshima T, Ueda K, Horiba I, Yamamoto S. A study of the road surface condition detection technique for deployment on a vehicle. *JSAE Rev* 2003;24(2):183-188.
- (8) Jokela M, Kutila M, Le L. Road condition monitoring system based on a stereo camera. In *2009 IEEE 5th International conference on intelligent computer communication and processing 2009 Aug 27* (pp. 423-428). IEEE.
- (9) Yang HJ, Jang H, Jeong DS. Detection algorithm for road surface condition using wavelet packet transform and SVM. In *The 19th Korea-Japan Joint Workshop on Frontiers of Computer Vision 2013* (pp. 323-326). IEEE.
- (10) Jonsson P, Casselgren J, Thörnberg B. Road surface status classification using spectral analysis of NIR camera images. *IEEE Sensors Journal* 2014;15(3):1641-1656.
- (11) Hebert M, Vandapel N. *Terrain classification techniques from ladar data for autonomous navigation*. 2003.
- (12) Wang S, Kodagoda S, Ranasinghe R. Road terrain type classification based on laser measurement system data. In *Australasian Conference on Robotics and Automation, ACRA 2012 Dec 1*.
- (13) Smith PP, Zografos K. Sonar for recognising the texture of pathways. *Robotics and autonomous systems* 2005;51(1):17-28.

References

- (14) Tapkan BI, Yoakim-Stover S, Kubichek F. Active microwave remote sensing of road surface conditions. *Proceedings of the Snow Removal and Ice Control Technology 1997*:73-80.
- (15) Li ES, Sarabandi K. Low grazing incidence millimeter-wave scattering models and measurements for various road surfaces. *IEEE Transactions on Antennas and Propagation* 1999;47(5):851-861.
- (16) Finkle R, Schreck A, Wanielik G. Polarimetric road condition classification and data visualisation. In 1995 International Geoscience and Remote Sensing Symposium, IGARSS'95. Quantitative Remote Sensing for Science and Applications 1995 Jul 10 (Vol. 3, pp. 1786-1788). IEEE.
- (17) Snuttjer BR, Narayanan RM. Millimeter-wave backscatter measurements in support of surface navigation applications. In IGARSS'96. 1996 International Geoscience and Remote Sensing Symposium 1996 May 31 (Vol. 1, pp. 506-508). IEEE.
- (18) Rudolf H, Wanielik G, Sieber AJ. Road condition recognition using microwaves. In *Proceedings of Conference on Intelligent Transportation Systems 1997 Nov 12* (pp. 996-999). IEEE.
- (19) Viikari VV, Varpula T, Kantanen M. Road-condition recognition using 24-GHz automotive radar. *IEEE transactions on intelligent transportation systems* 2009;10(4):639-648.
- (20) Song IY, Yoon JH, Bae SH, Jeon M, Shin V. Classification of road surface status using a 94 GHz dual-channel polarimetric radiometer. *Int J Remote Sens* 2012;33(18):5746-5767.
- (21) Kees N, Detlefsen J. Road surface classification by using a polarimetric coherent radar module at millimeter waves. In 1994 IEEE MTT-S International Microwave Symposium Digest (Cat. No. 94CH3389-4) 1994 May 23 (pp. 1675-1678). IEEE.
- (22) Schneider R, Didascalou D, Wiesbeck W. Impact of road surfaces on millimeter-wave propagation. *IEEE Transactions on Vehicular Technology* 2000;49(4):1314-1320.
- (23) Daniel L, Phippen D, Hoare E, Stove A, Cherniakov M, Gashinova M. Low-THz radar, lidar and optical imaging through artificially generated fog. 2017.
- (24) Yang Y, Mandehgar M, Grischkowsky DR. Broadband THz signals propagate through dense fog. *IEEE Photonics Technology Letters* 2014;27(4):383-386.
- (25) Federici JF, Ma J, Moeller L. Review of weather impact on outdoor terahertz wireless communication links. *Nano Communication Networks* 2016;10:13-26.
- (26) Bystrov A, Hoare E, Tran TY, Clarke N, Gashinova M, Cherniakov M. Sensors for automotive remote road surface classification. In 2018 IEEE International Conference on Vehicular Electronics and Safety (ICVES) 2018 Sep 12 (pp. 1-6). IEEE.

References

- (27) ETSI ET. Electromagnetic compatibility and radio spectrum matters (erm); short range devices (srd); radio equipment to be used in the 25 mhz to 1 000 mhz frequency range with power levels ranging up to 500 mw. European harmonized standard EN 2012; 300(220)
- (28) FCC 47 CFR 15.249 - Operation within the bands 902-928 MHz, 2400-2483.5 MHz, 5725-5875 MHz, and 24.0-24.25 GHz.
- (29) Vizard DR, Gashinova M, Hoare EG, Cherniakov M. Portable low THz imaging radars for automotive applications. In 2015 40th International Conference on Infrared, Millimeter, and Terahertz waves (IRMMW-THz) 2015 Aug 23 (pp. 1-2). IEEE.
- (30) Norouzian F, Hoare EG, Marchetti E, Cherniakov M, Gashinova M. Next generation, Low-THz automotive radar—the potential for frequencies above 100 GHz. In 2019 20th International Radar Symposium (IRS) 2019 Jun 26 (pp. 1-7). IEEE.
- (31) Carpintero G, Garcia-Munoz E, Hartnagel H, Preu S, Raisanen A. Semiconductor terahertz technology: devices and systems at room temperature operation. : John Wiley & Sons; 2015.
- (32) Laboratory of Terahertz Spectroscopy. Available at: <http://lts.fzu.cz/en/intro.htm>. Accessed 20/12/, 2020.
- (33) Cooper KB, Dengler RJ, Lombart N, Thomas B, Chattopadhyay G, Siegel PH. THz imaging radar for standoff personnel screening. IEEE Transactions on Terahertz Science and Technology 2011;1(1):169-182.
- (34) Hejase JA, Rothwell EJ, Chahal P. A multiple angle method for THz time-domain material characterization. IEEE Transactions on Terahertz Science and Technology 2013;3(5):656-665.
- (35) Jasteh D, Hoare EG, Cherniakov M, Gashinova M. Experimental low-terahertz radar image analysis for automotive terrain sensing. IEEE Geoscience and Remote Sensing Letters 2016;13(4):490-494.
- (36) Daniel L, Phippen D, Hoare E, Cherniakov M, Gashinova M. Image segmentation in real aperture Low-THz radar images. In 2019 20th International Radar Symposium (IRS) 2019 Jun 26 (pp. 1-8). IEEE.
- (37) Gishkori S, Wright D, Daniel L, Gashinova M, Mulgrew B. Forward scanning automotive SAR with moving targets. In 2019 International Radar Conference (RADAR) 2019 Sep 23 (pp. 1-4). IEEE.
- (38) O'Hara J.F., Grischkowsky DR. Comment on the veracity of the ITU-R recommendation for atmospheric attenuation at terahertz frequencies. IEEE Transactions on Terahertz Science and Technology 2018;8(3):372-375.
- (39) Moon E, Jeon T, Grischkowsky DR. Long-path THz-TDS atmospheric measurements between buildings. IEEE Transactions on Terahertz Science and Technology 2015;5(5):742-750.

References

- (40) Gashinova M, Hoare E, Stove A. Predicted sensitivity of a 300GHz FMCW radar to pedestrians. In 2016 46th European Microwave Conference (EuMC) 2016 Oct 4 (pp. 1497-1500). IEEE.
- (41) Skolnik MI. Introduction to radar systems. New York 1980.
- (42) White P. Radar Waveforms for A&D and Automotive Radar White Paper.
- (43) Richards MA, Scheer J, Holm WA, Melvin WL. Principles of modern radar. : Citeseer; 2010.
- (44) Skolnik MI. Radar handbook. : McGraw-Hill Education; 2008.
- (45) Kingsley S, Quegan S. Understanding radar systems. : SciTech Publishing; 1999.
- (46) Ulaby F, Long D. Microwave radar and radiometric remote sensing. : Artech House; 2015.
- (47) Uluisik C, Cakir G, Cakir M, Sevgi L. Radar cross section (RCS) modeling and simulation, part 1: a tutorial review of definitions, strategies, and canonical examples. IEEE Antennas and Propagation Magazine 2008;50(1):115-126.
- (48) Fuhs AE. Radar cross section lectures. : American Institute of Aeronautics and Astronautics, Inc; 1984.
- (49) Frezza F, Mangini F, Tedeschi N. Introduction to electromagnetic scattering: tutorial. JOSA A 2018;35(1):163-173.
- (50) Knott EF. Radar cross section measurements. : Springer Science & Business Media; 2012.
- (51) Jankiraman M. Design of multi-frequency CW radars. : SciTech Publishing; 2007.
- (52) Stove AG. Linear FMCW radar techniques. In IEEE Proceedings F-Radar and Signal Processing 1992 Oct (Vol. 139, No. 5, pp. 343-350). IET.
- (53) Salous S. Radio propagation measurement and channel modelling. : John Wiley & Sons; 2013.
- (54) Barrick DE. FM/CW radar signals and digital processing. 1973.
- (55) Einstein TH. Generation of high resolution radar range profiles and range profile auto-correlation functions using stepped-frequency pulse train. 1984.
- (56) Barton DK. Modern radar system analysis. Norwood 1988.
- (57) Greco MS, Watts S. Radar clutter modeling and analysis. Academic Press Library in Signal Processing: Elsevier; 2014. p. 513-594.

References

- (58) Sector IR. Recommendation itu-r p. 676–10, attenuation by atmospheric gases. International Telecommunications Union 2013.
- (59) Rappaport TS. Wireless communications: principles and practice. : prentice hall PTR New Jersey; 1996.
- (60) Ulaby FT, Moore RK, Fung AK. Microwave remote sensing: Active and passive. volume 1-microwave remote sensing fundamentals and radiometry. 1981.
- (61) Fung AK. Microwave scattering and emission models and their applications. Norwood, MA: Artech House, 1994 1994.
- (62) Richards MA, Scheer J, Holm WA, Melvin WL. Principles of modern radar. : Citeseer; 2010.
- (63) Mittleman DM, Hunsche S, Boivin L, Nuss MC. T-ray tomography. Optics letters. 1997 Jun 15;22(12):904-6.
- (64) Federici JF, Gary D, Barat R, Michalopoulou Z. Detection of explosives by terahertz imaging. Counterterrorist Detection Techniques of Explosives: Elsevier; 2007. p. 323-366.
- (65) Gomez-Sepulveda A, Hernandez-Serrano AI, Radpour R, Koch-Dandolo CL, Rojas-Landeros SC, Ascencio-Rojas LF, et al. History of Mexican easel paintings from an altarpiece revealed by non-invasive terahertz time-domain imaging. Journal of Infrared, Millimeter, and Terahertz Waves 2017;38(4):403-412.
- (66) Medical applications of terahertz imaging: a review of current technology and potential applications in biomedical engineering. : IEEE; 2004.
- (67) Jasteh D, Gashinova M, Hoare EG, Tran TY, Clarke N, Cherniakov M. Low-THz imaging radar for outdoor applications. In 2015 16th International Radar Symposium (IRS) 2015 Jun 24 (pp. 203-208). IEEE.
- (68) Stove A. Potential applications for low-Tera-Hertz radar. In 2015 16th International Radar Symposium (IRS) 2015 Jun 24 (pp. 191-196). IEEE.
- (69) Bryllert T, Drakinskiy V, Cooper KB, Stake J. Integrated 200–240-GHz FMCW radar transceiver module. IEEE Trans Microwave Theory Tech 2013;61(10):3808-3815.
- (70) Reck T, Jung-Kubiak C, Siles JV, Lee C, Lin R, Chattopadhyay G, et al. A silicon micromachined eight-pixel transceiver array for submillimeter-wave radar. IEEE Transactions on Terahertz Science and Technology 2015;5(2):197-206.
- (71) Siegel PH. Terahertz technology. IEEE Trans Microwave Theory Tech 2002;50(3):910-928.
- (72) Microwave Journal. Available at: <http://www.microwavejournal.com>.

References

- (73) N. T.S.B, Special Investigation Report. Vehicle-and Infrastructure-Based Technology for the Prevention for Rear-End Collisions. 2001; Available at: <https://www.nts.gov/safety/safety-studies/Pages/SIR0101.aspx>.
- (74) Hasch J, Topak E, Schnabel R, Zwick T, Weigel R, Waldschmidt C. Millimeter-wave technology for automotive radar sensors in the 77 GHz frequency band. IEEE Trans Microwave Theory Tech 2012;60(3):845-860.
- (75) Brooker GM. Mutual interference of millimetre-wave radar systems. IEEE Trans Electromagn Compat 2007; 49(1):170-181.
- (76) Mitchell TM, Learning M. Mcgraw-hill science. Engineering/Math 1997; 1:27.
- (77) Yegnanarayana B. Artificial neural networks. : PHI Learning Pvt. Ltd; 2009.
- (78) Jain AK, Mao J, Mohiuddin KM. Artificial neural networks: A tutorial. Computer 1996; 29(3):31-44.
- (79) Russell S, Norvig P. Artificial intelligence: a modern approach. 2002.
- (80) Hinton GE. A practical guide to training restricted Boltzmann machines. Neural networks: Tricks of the trade: Springer; 2012. p. 599-619.
- (81) Ramachandran P, Zoph B, Le QV. Searching for activation functions. arXiv preprint arXiv:1710.05941 2017.
- (82) Krizhevsky A, Sutskever I, Hinton GE. Imagenet classification with deep convolutional neural networks. Advances in neural information processing systems 2012;25:1097-1105.
- (83) Delving deep into rectifiers: Surpassing human-level performance on imagenet classification. ; 2015.
- (84) Nielsen MA. Neural networks and deep learning. : Determination press San Francisco, CA; 2015.
- (85) Nwankpa C, Ijomah W, Gachagan A, Marshall S. Activation functions: Comparison of trends in practice and research for deep learning. arXiv preprint arXiv:1811.03378 2018.
- (86) Goodfellow I, Bengio Y, Courville A. Deep learning. : MIT press; 2016.
- (87) Sharma S, Sharma S, Athaiya A. Activation functions in neural networks. towards data science 2017;6(12):310-316.
- (88) Ruder S. An overview of gradient descent optimization algorithms. arXiv preprint arXiv:1609.04747 2016.
- (89) Kandel ER. An introduction to the work of David Hubel and Torsten Wiesel. J Physiol (Lond) 2009;587:2733.

References

- (90) Albelwi S, Mahmood A. A framework for designing the architectures of deep convolutional neural networks. *Entropy* 2017;19(6):242.
- (91) Ciregan D, Meier U, Schmidhuber J. Multi-column deep neural networks for image classification. In 2012 IEEE conference on computer vision and pattern recognition 2012 Jun 16 (pp. 3642-3649). IEEE.
- (92) Yamashita R, Nishio M, Do RKG, Togashi K. Convolutional neural networks: an overview and application in radiology. *Insights into imaging* 2018;9(4):611-629.
- (93) VivaTechSARL. Available at: Available: <http://www.vivatechmmw.com>. Accessed February, 2021.
- (94) Sabery S, Norouzian F, Gardner P, Hoare E, Cherniakov M, Gashinova M. Signal reduction by tree leaves in low-THz automotive radar. In 2018 48th European Microwave Conference (EuMC) 2018 Sep 23 (pp. 1445-1448). IEEE.
- (95) Terahertz Measurement Facility. Available at: <https://www.birmingham.ac.uk/research/activity/eese/communications-sensing/terahertz-measurement-facility>.
- (96) elva-1. Available at: <http://elva-1.com/>.
- (97) Pico technology. Available at: <https://www.picotech.com/oscilloscope/5000/flexibleresolution-oscilloscope>.
- (98) Marchetti E. Study of electromagnetic wave propagation and scattering in Low-THz automotive radar. 2020.
- (99) Hayt Jr W,H., Buck JA, Akhtar MJ. *Engineering Electromagnetics | (SIE)*. : McGraw-Hill Education; 2020.
- (100) Walser RM. Electromagnetic metamaterials. In *Complex Mediums II: beyond linear isotropic dielectrics* 2001 Jul 9 (Vol. 4467, pp. 1-15). International Society for Optics and Photonics.
- (101) Naftaly M. *Terahertz metrology*. : Artech House; 2015.
- (102) Sabery S, Norouzian F, Gardner P, Bystrov A, Gashinova M. Signal Reduction Due to Layer of Water at Low-THz Frequency for Automotive Radar Applications. England; January 2022.
- (103) Du R, Norouzian F, Marchetti E, Willetts B, Gashinova M, Cherniakov M. Characterisation of attenuation by sand in low-THz band. In 2017 IEEE Radar Conference (RadarConf) 2017 May 8 (pp. 0294-0297). IEEE.
- (104) Norouzian F, Du R, Marchetti E, Gashinova M, Hoare E, Constantinou C, Gardner P, Cherniakov M. Transmission through uniform layer of ice at low-THz frequencies. In 2017 European Radar Conference (EURAD) 2017 Oct 11 (pp. 211-214). IEEE.

References

- (105) Norouzian F, Du R, Marchetti E, Gashinova M, Hoare E, Constantinou C, et al. Low-THz transmission through liquid contaminants on antenna radome. 2018.
- (106) Jördens C, Scheller M, Breitenstein B, Selmar D, Koch M. Evaluation of leaf water status by means of permittivity at terahertz frequencies. *J Biol Phys* 2009;35(3):255-264.
- (107) Hadjiloucas S, Karatzas LS, Bowen JW. Measurements of leaf water content using terahertz radiation. *IEEE Trans Microwave Theory Tech* 1999;47(2):142-149.
- (108) Looyenga H. Dielectric constants of heterogeneous mixtures. *Physica* 1965;31(3):401-406.
- (109) Norouzian F, Du R, Hoare EG, Gardner P, Constantinou C, Cherniakov M, et al. Low-THz transmission through water-containing contaminants on antenna radome. *IEEE Transactions on Terahertz Science and Technology* 2017;8(1):63-75.
- (110) EasyLogEL-USB-2. Available at: www.lascarelectronics.com.
- (111) Norouzian F, Marchetti E, Gashinova M, Hoare E, Constantinou C, Gardner P, et al. Rain attenuation at millimeter wave and low-THz frequencies. *IEEE Transactions on Antennas and Propagation* 2019;68(1):421-431.
- (112) Norouzian F, Marchetti E, Hoare E, Gashinova M, Constantinou C, Gardner P, et al. Experimental study on low-THz automotive radar signal attenuation during snowfall. *IET Radar, Sonar & Navigation* 2019;13(9):1421-1427.
- (113) Anderson I. Measurements of 20-GHz transmission through a radome in rain. *IEEE Transactions on Antennas and Propagation* 1975;23(5):619-622.
- (114) Arage A, Kuehnle G, Jakoby R. Measurement of wet antenna effects on millimetre wave propagation. In 2006 IEEE Conference on Radar 2006 Apr 24 (pp. 5-pp). IEEE.
- (115) Blevis BC. Losses due to rain on radomes and antenna reflecting surfaces. 1964.
- (116) Brissinger D, Parent G, Boulet P. Experimental study on radiation attenuation by a water film. *Journal of Quantitative Spectroscopy and Radiative Transfer* 2014;145:160-168.
- (117) Chen N, Gourova R, Krasnov OA, Yarovoy A. The influence of the water-covered dielectric radome on 77ghz automotive radar signals. In 2017 European Radar Conference (EURAD) 2017 Oct 11 (pp. 139-142). IEEE.
- (118) Beneduci A. Which is the effective time scale of the fast Debye relaxation process in water? *Journal of molecular liquids* 2008;138(1-3):55-60.
- (119) Buchner R, Barthel J, Stauber J. The dielectric relaxation of water between 0 C and 35 C. *Chemical Physics Letters* 1999;306(1-2):57-63.
- (120) Kaatze U. Complex permittivity of water as a function of frequency and temperature. *J Chem Eng Data* 1989;34(4):371-374.

References

- (121) Koeberg M, Wu C, Kim D, Bonn M. THz dielectric relaxation of ionic liquid: water mixtures. *Chemical physics letters* 2007;439(1-3):60-64.
- (122) Liebe HJ, Hufford GA, Manabe T. A model for the complex permittivity of water at frequencies below 1 THz. *Int J Infrared Millim Waves* 1991;12(7):659-675.
- (123) Ellison WJ. Permittivity of pure water, at standard atmospheric pressure, over the frequency range 0–25 THz and the temperature range 0–100 C. *Journal of physical and chemical reference data* 2007;36(1):1-18.
- (124) Ray PS. Broadband complex refractive indices of ice and water. *Appl Opt* 1972;11(8):1836-1844.
- (125) Meissner T, Wentz FJ. The complex dielectric constant of pure and sea water from microwave satellite observations. *IEEE Trans Geosci Remote Sens* 2004;42(9):1836-1849.
- (126) Afsar MN, Birch JR, Clarke RN, Chantry GW. The measurement of the properties of materials. *Proc IEEE* 1986;74(1):183-199.
- (127) Buis A, Lynch P, Cook-Anderson G, Sullivant R. Aquarius/SAC-D: Studying Earth's salty seas from space. Jun 2011.
- (128) Vinh NQ, Sherwin MS, Allen SJ, George DK, Rahmani AJ, Plaxco KW. High-precision gigahertz-to-terahertz spectroscopy of aqueous salt solutions as a probe of the femtosecond-to-picosecond dynamics of liquid water. *J Chem Phys* 2015;142(16):164502.
- (129) Qiao W, Yang K, Thoma A, Dekorsy T. Dielectric relaxation of HCl and NaCl solutions investigated by terahertz time-domain spectroscopy. *Journal of Infrared, Millimeter, and Terahertz Waves* 2012;33(10):1029-1038.
- (130) Sabery SM, Bystrov A, Navarro-Cía M, Gardner P, Gashinova M. Study of Low Terahertz Radar Signal Backscattering for Surface Identification. *Sensors* 2021;21(9):2954.
- (131) Xiao Y, Daniel L, Gashinova M. Image segmentation and region classification in automotive high-resolution radar imagery. *IEEE Sensors Journal* 2020;21(5):6698-6711.
- (132) Daniel L, Xiao Y, Hoare E, Cherniakov M, Gashinova M. Statistical image segmentation and region classification approaches for automotive radar. In 2020 17th European Radar Conference (EuRAD) 2021 Jan 10 (pp. 124-127). IEEE.
- (133) Bystrov A, Hoare E, Tran T, Clarke N, Gashinova M, Cherniakov M. Automotive system for remote surface classification. *Sensors* 2017;17(4):745.
- (134) Nagy LL. Electromagnetic reflectivity characteristics of road surfaces. *IEEE Transactions on Vehicular Technology* 1974;23(4):117-124.

References

- (135) Strutt JW, Rayleigh B. The Theory of Sound... Revised and Enlarged. : Macmillan & Company; 1894.
- (136) Oh Y, Sarabandi K, Ulaby FT. An empirical model and an inversion technique for radar scattering from bare soil surfaces. *IEEE Trans Geosci Remote Sens* 1992;30(2):370-381.
- (137) Jansen C, Priebe S, Moller C, Jacob M, Dierke H, Koch M, et al. Diffuse scattering from rough surfaces in THz communication channels. *IEEE Transactions on Terahertz Science and Technology* 2011;1(2):462-472.
- (138) Ma J, Shrestha R, Zhang W, Moeller L, Mittleman DM. Terahertz wireless links using diffuse scattering from rough surfaces. *IEEE Transactions on Terahertz Science and Technology* 2019;9(5):463-470.
- (139) Grossman EN, Popovic N, Chamberlin RA, Gordon J, Novotny D. Submillimeter wavelength scattering from random rough surfaces. *IEEE Transactions on Terahertz Science and Technology* 2017;7(5):546-562.
- (140) Nashashibi AY, Ibrahim AA, Cook S, Sarabandi K. Experimental characterization of polarimetric radar backscatter response of distributed targets at high millimeter-wave frequencies. *IEEE Trans Geosci Remote Sens* 2015;54(2):1013-1024.
- (141) Bystrov A, Hoare E, Gashinova M, Cherniakov M, Tran TY. Experimental study of rough surface backscattering for low terahertz automotive radar. In 2019 20th International Radar Symposium (IRS) 2019 Jun 26 (pp. 1-7). IEEE.
- (142) Nathanson FE, Reilly JP, Cohen MN. Radar design principles-Signal processing and the Environment. NASA STI/Recon Technical Report A 1991;91:46747.
- (143) Komarov VV. Handbook of dielectric and thermal properties of materials at microwave frequencies. : Artech house; 2012.
- (144) Scheller M, Jansen C, Koch M. Analyzing sub-100- μm samples with transmission terahertz time domain spectroscopy. *Opt Commun* 2009;282(7):1304-1306.
- (145) Ma M, Wang Y, Navarro-Cia M, Liu F, Zhang F, Liu Z, et al. The dielectric properties of some ceramic substrate materials at terahertz frequencies. *Journal of the European Ceramic Society* 2019;39(14):4424-4428.
- (146) Nelder JA, Mead R. A simplex method for function minimization. *The computer journal* 1965;7(4):308-313.
- (147) Camacho M, Boix RR, Kuznetsov SA, Beruete M, Navarro-Cía M. Far-field and near-field physics of extraordinary THz transmitting hole-array antennas. *IEEE Transactions on Antennas and Propagation* 2019;67(9):6029-6038.
- (148) Freer S, Camacho M, Kuznetsov SA, Boix RR, Beruete M, Navarro-Cía M. Revealing the underlying mechanisms behind TE extraordinary THz transmission. *Photonics Research* 2020;8(4):430-439.

References

- (149) Freer S, Gorodetsky A, Navarro-Cia M. Beam profiling of a commercial lens-assisted terahertz time domain spectrometer. *IEEE Transactions on Terahertz Science and Technology* 2020;11(1):90-100.
- (150) Leroux P. Sandpaper roughness measurement using 3D profilometry (Technical Report). 2014.
- (151) Sabery SM, Bystrov A, Gardner P, Gashinova M. Surface classification based on low terahertz radar imaging and deep neural network. In 2020 21st International Radar Symposium (IRS) 2020 Oct 5 (pp. 24-27). IEEE.
- (152) Sabery SM, Bystrov A, Gardner P, Stroescu A, Gashinova M. Road Surface Classification Based on Radar Imaging Using Convolutional Neural Network. *IEEE Sensors Journal* 2021.
- (153) LeCun Y, Bengio Y, Hinton G. Deep learning. *Nature* 2015;521(7553):436-444.
- (154) Nolte M, Kister N, Maurer M. Assessment of deep convolutional neural networks for road surface classification. In 2018 21st International Conference on Intelligent Transportation Systems (ITSC) 2018 Nov 4 (pp. 381-386). IEEE.
- (155) Stroescu A, Cherniakov M, Gashinova M. Classification of high resolution automotive radar imagery for autonomous driving based on deep neural networks. In 2019 20th International Radar Symposium (IRS) 2019 Jun 26 (pp. 1-10). IEEE.
- (156) Stroescu A, Daniel L, Gashinova M. Combined Object Detection and Tracking on High Resolution Radar Imagery for Autonomous Driving Using Deep Neural Networks and Particle Filters. In 2020 IEEE Radar Conference (RadarConf20) 2020 Sep 21 (pp. 1-6). IEEE.
- (157) Bridle JS. Probabilistic interpretation of feedforward classification network outputs, with relationships to statistical pattern recognition. *Neurocomputing: Springer*; 1990. p. 227-236.
- (158) Liu Y, Gao Y, Yin W. An improved analysis of stochastic gradient descent with momentum. *arXiv preprint arXiv:2007.07989* 2020.
- (159) Tharwat A. Classification assessment methods. *Applied Computing and Informatics* 2020.
- (160) Sammut C, Webb GI. *Encyclopedia of machine learning*. : Springer Science & Business Media; 2011.

